Thèse n° 9894

Linear and nonlinear applications of miniaturized silicon nitride microresonators

Présentée le 23 juin 2023

Faculté des sciences et techniques de l'ingénieur
Laboratoire de photonique et mesures quantiques (STI/SB)
Programme doctoral en photonique

pour l'obtention du grade de Docteur ès Sciences

par

Arslan Sajid RAJA

Acceptée sur proposition du jury

Prof. F. Carbone, président du jury
Prof. T. Kippenberg, directeur de thèse
Prof. T. Herr, rapporteur
Prof. C. Koos, rapporteur
Prof. C. S. Brès, rapporteuse

École
polytechnique
fédérale
de Lausanne

2023

Read! In the Name of your Lord Who created.
Quran (96:1)

To my grandparents (late) and parents, who gave me constant love and support.

Acknowledgements

I would like to extend my gratitude to Prof. Tobias Kippenberg for his support and guidance throughout my stay in his lab as a part of my Master's and Ph.D. theses. The milestones achieved in my thesis would not have been possible without his visionary perspective and understanding of various disciplines. I am grateful for the opportunities he provided me to collaborate with external and internal collaborators. I would like to express my appreciation to Prof. Christian Koos, Prof. Tobias Herr, and Prof. Camille-Sophie Brès for their valuable contributions as members of my Ph.D. defense committee.

I am grateful to Antonella Ragnelli and Kathleen Vionnet for their support, dedication, and expertise in resolving administrative/grant(funding) issues and organizing events.

I extend my thanks to Michael Geiselmann and Martin H. Pfeiffer, for their assistance in imparting a diverse range of experimental skills at the beginning of my journey. The diligent work of the K-lab fabrication team, including Junqiu Liu, Rui Ning Wang, Bahareh Ghadiani, and Zheru Qiu, in the clean room and fabrication of essential samples for my Ph.D. research is appreciated. Special thanks are given to Michael Gorodetsky, Hairun Guo, John Jost, Andrey Voloshin, and Sofya E. Agafonova for their contributions to our collaborative project with the Russian Quantum Center (RQC), including training and assistance in various project aspects. During my internship at Cambridge, where I engaged in collaborative research with Microsoft Research, I am grateful for the support and assistance of Sophie Lange, Kai Shi, Hitesh Ballani, Paolo Costa, and Istvan Haller in conducting diverse experiments. Sincere thanks go to the EPFL team, including Maxim Karpov, Xin Fu, Anton Lukashchuk (sample design), and Alexandre Goy, for their significant contributions to constructing the microcomb breadboard. I am truly grateful to Erwan Lucas for introducing me to locking schemes and phase noise characterization, which played an important role in multiple internal projects. I would like to express my sincere thanks to Claus Ropers, Jan-Wilke Henke, Armin Feist, Germaine Arend, F. Jasmin Kappert, and Ofer Kfir from the University of Göttingen for their crucial role in introducing me to this new field during the final phase of my Ph.D. Their hospitality during our joint experiments in Göttingen is appreciated. Additionally, I extend my thanks to Yujia Yang, Huang Guanhao, Junqiu Liu, and Zheru Qiu (electron-photon EPFL team) for their assistance. The individuals in the BM lab (my good friends), especially Nils Johan Engelsen, Jijun He, Marta Divall, Amirali Arabmoheghi, Wenle Weng, Sergey Fedorov, Johann Riemensberger, Miles Anderson, Grigory Likhachev, Nikolay Pavlov, Alberto Beccari, John Jost, Huang Guanhao, and Mohammad Bereyhi, are deeply appreciated for making BM lab a wonderful place to work. Similarly, I would like to extend a big thanks to all the wonderful people, including Anat Siddharth, Sina Khorasani, Martin H. Pfeiffer, Romain Bouchand, Weng

Wenle, and Yujia Yang with whom I have shared my office. Their presence has made this journey pleasant. A big thanks go out to all members of the K-lab, both past and present, for their generosity in sharing their knowledge and expertise throughout this journey.
I am truly grateful to my family, including my parents, brother, sisters, Aqeel Ahmed, and Ianina Kosse for their unconditional support and understanding of my absence on numerous family occasions. My current thesis is dedicated to my late grandparents (Dada and Dadi), as I was unable to bid them a final farewell. May Allah bless them with the highest place in Jannah-tul-Firdaus. I would like to thank Amir Youssefi for his invaluable guidance and for teaching me Arabic. Last but not least, a big thanks goes to Sachin Verleker, a friend and brother from India, for our multiple joint ventures such as finding new restaurants, playing badminton, introducing me to F1/Chess, etc.

Lausanne, June 2023 Arslan

Abstract

Photonic integrated circuits (PICs) are the subject of massive interest due to the range of applications they can provide at a huge scale while building on well-established CMOS technologies. One of the critical parameters defining a technology's maturity level is its implementation in an operational environment. Optical frequency combs (microcombs) generated using on-chip microresonators have proved vital for multiple industrial and research applications. However, like many other technologies, microcombs based on PICs are restricted to a well-stabilized lab environment. The full photonic integration of soliton microcombs in a single, compact, and electrically-driven package would allow mass-manufacturable devices compatible with emerging high-volume applications such as laser-based ranging (LIDAR), or sources for dense wavelength division multiplexing for data center based optical interconnects. Another obstacle is establishing optical packaging protocol allowing the miniaturization and portability of this platform. The current thesis work aims at the miniaturization of the microcombs system based on ultra-low loss Si_3N_4 microresonator providing a path toward its applicability at a broader scale. Two approaches have been established for miniaturization based on application requirements.

The first approach uses fast optical feedback originating from a Si_3N_4 microresonator known as "self-injection-locking." By directly coupling a multi-frequency laser diode to the Si_3N_4, self-injection locking first leads to narrow linewidth single-mode lasing and subsequently enables the generation of the optical frequency comb. Moreover, the soliton state is initiated by changing the current simplifying conventional soliton generation mechanism and reducing the overall footprint to 1 cm^3.

In the second approach, a more generic protocol of optical packaging is implemented, enabling the interfacing of Si_3N_4 based microcomb with standard fiber modules. The requirements of high input power and broadband coupling for frequency comb generation separate microresonator packaging from conventional packaging. Initially, packaging protocols are established, enabling device operation at high power (> 2.5 W) and low temperature. In parallel, a cost-effective fiber-based mode converter is developed to enhance coupling efficiency.

The first application of a packaged soliton microcombs module demonstrates ultra-fast (nanoseconds timescale) circuit switching for the data center in collaboration with Microsoft Research (MSR), Cambridge. This study carried out at MSR Cambridge, shows the potential of a soliton microcomb as a multiwavelength source for future datacenter and the importance of optical packaging to enable the demonstration on a system level.

Further validation of the generic optical packaging approach is done by interfacing a photonic integrated Si_3N_4 based microresonator inside a transmission electron microscope (TEM) to modulate the electron beam with the linear and nonlinear intracavity field. The introduction of integrated photonics, facilitated by optical packaging, has enabled highly efficient interactions in the continuous wave (CW) regime of the transmission electron microscope (TEM). Previously, achieving such efficiency was only possible using an advanced version of TEM known as ultrafast TEM (U-TEM), which has limited availability worldwide. Furthermore, the reliability of the packaging is confirmed through the successful generation of a soliton microcomb in the TEM.
The packaging further assists different applications, including stabilization of microwave generated via soliton, optical accelerometer, and integrated photon pair sources. Moreover, current work contributed to soliton generation without an amplifier (butterfly DFB (Morton laser) and external cavity laser diode) and via on-chip ALN actuators.

Keywords: Photonics integration, optical frequency comb, nonlinear photonics, optical packaging, self-injection locking, ultra-fast circuit switching, soliton microcomb, datacenter, transmission electron microscope, Photon-Induced Near-field Electron Microscopy, integrated photonics

Résumé

Les circuits intégrés photoniques (PIC) font l'objet d'un intérêt massif en raison de la gamme d'applications qu'ils peuvent fournir à grande échelle tout en s'appuyant sur des technologies CMOS bien établies. L'un des paramètres critiques définissant le niveau de maturité d'une technologie est sa mise en œuvre dans un environnement opérationnel. Les peignes de fréquence optiques (microcombs) générés à l'aide de microrésonateurs sur puce se sont avérés essentiels pour de nombreuses applications industrielles et de recherche. Cependant, comme beaucoup d'autres technologies, les microcombs basés sur des PIC sont limités à un environnement de laboratoire bien stabilisé. L'intégration photonique complète des microcombes à solitons dans un boîtier unique, compact et à commande électrique permettrait de fabriquer en masse des dispositifs compatibles avec les applications émergentes à grand volume telles que la télémétrie à base de laser (LIDAR) ou les sources de multiplexage dense par répartition en longueur d'onde pour les interconnexions optiques basées sur les centres de données. Un autre obstacle est l'établissement d'un protocole d'emballage optique permettant la miniaturisation et la portabilité de cette plateforme. Le présent travail de thèse vise à miniaturiser le système de microcombs basé sur un microrésonateur à très faible perte Si_3N_4, ouvrant ainsi la voie à son applicabilité à plus grande échelle. Deux approches ont été établies pour la miniaturisation en fonction des exigences de l'application.

La première approche utilise une rétroaction optique rapide provenant d'un microrésonateur Si_3N_4 connu sous le nom de "verrouillage par auto-injection". En couplant directement une diode laser multifréquence à l'Si_3N_4, le verrouillage par auto-injection conduit d'abord à un laser monomode à largeur de raie étroite et permet ensuite de générer le peigne de fréquences optiques. En outre, l'état de soliton est initié en changeant le courant, ce qui simplifie le mécanisme conventionnel de génération de soliton et réduit l'empreinte globale à 1 cm^3.

Dans la seconde approche, un protocole plus générique de conditionnement optique est mis en œuvre, permettant l'interfaçage des microcombinaisons à base de Si_3N_4 avec des modules de fibre standard. Les exigences de puissance d'entrée élevée et de couplage à large bande pour la génération de peignes de fréquence distinguent l'emballage des microrésonateurs de l'emballage conventionnel. Dans un premier temps, des protocoles de conditionnement sont établis, permettant le fonctionnement du dispositif à haute puissance (> 2,5 W) et à basse température. En parallèle, un convertisseur de mode à base de fibre rentable est développé pour améliorer l'efficacité du couplage.

La première application d'un module de microcombs à solitons emballés démontre une commutation de circuit ultra-rapide (à l'échelle de la nanoseconde) pour le centre de données en

collaboration avec Microsoft Research (MSR), Cambridge. Cette étude réalisée au MSR de Cambridge montre le potentiel d'un microcombe à solitons en tant que source à longueurs d'onde multiples pour les futurs centres de données et l'importance de l'emballage optique pour permettre la démonstration au niveau du système.
Une validation supplémentaire de l'approche générique du conditionnement optique est effectuée en interfaçant un microrésonateur photonique intégré à base de Si_3N_4 à l'intérieur d'un microscope électronique à transmission (TEM) pour moduler le faisceau d'électrons avec le champ intracavité linéaire et non linéaire. L'introduction de la photonique intégrée, facilitée par le conditionnement optique, a permis des interactions très efficaces dans le régime d'ondes continues du microscope électronique à transmission (MET). Auparavant, il n'était possible d'atteindre une telle efficacité qu'en utilisant une version avancée du TEM, connue sous le nom de TEM ultrarapide (U-TEM), dont la disponibilité est limitée à l'échelle mondiale. En outre, la fiabilité de l'emballage est confirmée par la génération réussie d'un microcombinant de soliton dans le TEM.
L'emballage contribue également à différentes applications, notamment la stabilisation des micro-ondes générées par soliton, l'accéléromètre optique et les sources de paires de photons intégrées. En outre, les travaux actuels ont contribué à la génération de solitons sans amplificateur (DFB papillon (laser Morton) et diode laser à cavité externe) et par le biais d'actionneurs ALN sur puce.

Mots clés : Intégration photonique, peigne de fréquences optiques, photonique non linéaire, emballage optique, verrouillage par auto-injection, commutation de circuits ultra-rapide, micro-combinaison de solitons, centre de données, microscope électronique à transmission, microscopie électronique à champ proche induite par photons, photonique intégrée

Publication List

Main publications [1]

- **Arslan S. Raja*,** et al. “Electrically pumped photonic integrated soliton microcomb." Nature Communications 10(1), 1-8 (2019)
- **Arslan S. Raja*,** et al. “Ultrafast optical circuit switching for data centers using integrated soliton microcombs." Nature Communications 12(1), 1-7 (2021)
- Jan-Wilke Henke*, **Arslan S. Raja*,** et al. “Integrated photonics enables continuous-beam electron phase modulation." Nature, 600(7890), 653-658 (2022)
- Y. Yang*, J-W. Henke*, **Arslan S. Raja***, F. J. Kappert et al. “Free electron interaction with nonlinear optical states" In preparation (2023)
- **Arslan S. Raja*,** et al. “Chip-based soliton microcomb module using a hybrid semiconductor laser." Optics Express, 28(3), 2714-2721 (2020)
- J. Liu*, **Arslan S. Raja*,** et al. “Ultralow-power chip-based soliton microcombs for photonic integration." Optica, 5(10), 1347-1353 (2019)
- J. Liu*, E. Lucas*, **Arslan S. Raja*,** et al. “Photonic microwave generation in the X-and K-band using integrated soliton microcombs." Nature Photonics, 14(8), 486-491 (2020)
- J. Liu*, H. Tian*, E. Lucas*, **Arslan S. Raja*,** et al. “Monolithic piezoelectric control of soliton microcombs." Nature, 583(7816), 385-390 (2020)
- J. Liu*, **Arslan S. Raja*,** et al. “Double inverse nanotapers for efficient light coupling to integrated photonic devices." Optics letters 43.14 (2018)

Patent applications

- T. Kippenberg, M. L.Gorodetsky, **Arslan S. Raja**, H. Guo.“Generating optical pulses via a soliton state of an optical microresonator coupled with a chip-based semiconductor laser."US11513419B2 (2022)
- T. LaGrange, P. Cattaneo, F. Carbone, B. Weaver, A. Sapozhnik, Y. Yang, **Arslan S. Raja,** T. Kippenberg. ‘Electron spectrometer calibration method ."Application submitted.

[1] * equal contribution

Additional contributions

- A. Feist, G. Huang, G. Arend, Y. Yang, J-W. Henke, **Arslan S. Raja**, et al. “Cavity-mediated electron-photon pairs." Science 377.6607 (2022)
- J. Feldmann, N. Youngblood, M. Karpov, H. Gehring, X. Li, M. Stappers, M. Le Gallo, X. Fu, A. Lukashchuk, **Arslan S. Raja**, et al. “Parallel convolutional processing using an integrated photonic tensor core." Nature 589.7840 (2021)
- M. HP. Pfeiffer, J. Liu, **Arslan S Raja**, et al. “Ultra-smooth silicon nitride waveguides based on the Damascene reflow process: fabrication and loss origins." Optica 5.7 (2018)
- J. Liu, G. Huang, R. N. Wang, J. He, **Arslan S Raja**, et al. “High-yield, wafer-scale fabrication of ultralow-loss, dispersion-engineered silicon nitride photonic circuits." Nature communications 12.1 (2021)
- T. Brydges, **Arslan S Raja**, et al. “An Integrated Photon Pair Source with Monolithic Piezoelectric Frequency Tunability." arXiv preprint arXiv:2210.16387 (2022))
- F Samara, N Maring, A Martin, **Arslan S Raja**, et al. “Entanglement swapping between independent and asynchronous integrated photon-pair sources." Quantum Science and Technology 6.4 (2021)
- J. Hu, J. He, J. Liu, **Arslan S Raja**, et al. “Reconfigurable radiofrequency filters based on versatile soliton microcombs." Nature communications 11.1 (2020)
- F. Gyger, J. Liu, F. Yang, J. He, **Arslan S Raja**, et al. “Observation of stimulated Brillouin scattering in silicon nitride integrated waveguides." Physical review letters 124.1 (2020)
- E. Lucas, G. Lihachev, R. Bouchand, N. G Pavlov, **Arslan S Raja**, et al. “Spatial multiplexing of soliton microcombs." Nature Photonics 12.11 (2018)
- G Huang, E Lucas, J Liu, **Arslan S Raja**, et al. “Thermorefractive noise in silicon-nitride microresonators." Physical Review A 99.6 (2019)

Contents

Acronyms

AFG - arbitrary function generator
AOM - acousto-optic modulator
ARDE - aspect-ratio-dependent etch
ASE - amplified spontaneous emission
AWG - arbitrary waveform generator
AWGR - arrayed waveguide grating router

BER - bit error ratio

CMP - chemical mechanical polishing
CTE - coefficient of thermal expansion
CW - continuous wave

DFB - distributed feedback
DKS - dissipative Kerr soliton
DLA - dielectric laser accelerator
DP-MZM - dual-parallel Machzhener modulator
DSP - digital signal processing
DTU - data transmission unit
DUV - deep ultraviolet

EAM - electro-absorption modulator
ECDL - external cavity diode laser
EDFA - erbium doped fiber amplifier
EEGS - electron energy gain spectroscopy
EFTEM - energy-filtered transmission electron microscopy
EOM - electro-optical modulator
ER - extinction ratio
ESA - electrical spectrum analyzer

FBG - fiber Bragg grating
FEC - forward error correction
FCG - frequency comb generator
FDTD - finite difference time domain
FEM - finite element method
FP - Fabry-Pérot
FSR - free spectral range
FWHM - full width at half maximum
FWM - four-wave mixing

GVD - group velocity dispersion

HR - high-reflection

IELS - inelastic electron-light scattering
IL - insertion loss
InP - Indium phosphide

LLE - Lugiato-Lefever equation
LiDAR - light detection and ranging
LPCVD - low-pressure chemical vapor deposition
LTO - low-temperature oxide

MCMC - Markov chain Monte Carlo
MI - modulation instability
MZI - Mach-Zehnder interferometer
MZM - Mach-Zehnder modulator

N.A. - numerical aperture
NRZ - non-return to zero

OADM- optical add-drop multiplexer
OBF- optical band-pass filter
OCS - optical circuit switching
OCT - optical coherence tomography
OEIC - optoelectronics integrated circuit
O-E-O - opto-electronic-opto
OSA - optical spectrum analyzer
OSC - oscilloscope
OSNR - optical signal-to-noise ratio
OSU- optical switching unit

PAM - pulse amplitude modulation
PC - polarization controller
PCB - printed circuit board
PD - photodiod
PDH - Pound-Drever-Hall
PhC - photonic crystal cavities
PIC - photonic integrated circuit
PID - proportional-integral-derivative
PINEM - photon-induced near-field electron microscopy
PM - polarization-maintaining
PNA - phase noise analyzer
PSC - perfect soliton crystal

RF - radio frequency
RIN - relative intensity noise
ROP - received optical power

SC-SSB - suppressed-carrier single-sideband modulation
SEM - scanning electron microsope
SFWM - spontaneous four-wave mixing
SFG - sum frequency generation
SMSR - side mode suppression ratio
SMF - single-mode optical fiber
SOA - semiconductor optical amplifier
SPM - self-phase modulation
SSB - single-sideband

TDC - time-to-digital converters
TE - transverse electric
TEC - thermoelectric cooler
TEM - transmission electron microscope
TEOS - tetraethylorthosilicate
TIA - trans-impedance amplifier
THG - third-harmonic generation
TL - tunable laser
TOR - top of rack
TRN - thermo-refractive noise

UHNA - ultrahigh numerical aperture fiber
ULN - ultra-low noise laser
UTEM - ultrafast-transmission electron microscope

VCO - voltage controlled oscillator
VNA - vector network analyzer
VOA - variable optical attenuator

WGM - whispering gallery mode
WDM - wavelength division multiplexing

XPM - cross-phase modulation

1 Introduction

Silicon photonics (or photonics integrated circuits (PICs)) has emerged as a potential candidate to facilitate and replace conventional electronic-based functionalities by leveraging the existing fabrication capabilities, providing access to high bandwidth and compact devices at relatively low power. The data communication domain, specifically data center interconnects, has benefited greatly from silicon photonics [2, 3]. However, recent trends indicate PIC can boost the overall efficiency of multiple emerging applications such as LiDAR, sensing, and quantum computing by miniaturizing the overall architecture required for these applications and, more importantly, by reducing the cost and power consumption [4]. The fabrication of silicon photonic structures is being done on a relatively massive scale in external foundries, indicating the maturity of photonic integrated circuits. Moreover, a lot of attention has been paid to integrating all functionalities such as source (laser) [5, 3, 2, 6], active components (modulators [7, 8], optical amplifiers integration [9, 10], and detector [11], etc.) and passive components (splitter and combiner) [12] to mimic an actual counterpart of an integrated electron circuit. This is partially since a major portion of the cost contributes toward integrating PIC, hindering its implementation on a massive scale. The die-level chip design and fabrication cost is one-fifth of the cost occurring from testing, integration, and packaging sub-photonic systems. One primary ingredient of photonic packaging is fiber-to-chip, and laser die-to-chip packaging, which is currently done on a small scale and adds excessive cost to the whole integration cycle [13]. Further, it requires considering the electrical connection and thermal and mechanical stability to meet the standard to be operated in an external environment. Currently, the coupling from an external source to the chip is not well standardized, e.g., using an on-chip or off-chip mode converter for adiabatic mode conversion. A wide range of established methods, such as grating couplers [14, 15], inverse tapers [16, 14, 15], and on-chip microlensing [17], is implemented to couple the light into the photonic integrated circuits efficiently.

Most of the academic's research currently relies on testing and executing the photonic sub-module via probe stations and well-stabilized optical setups to show the feasibility of many photonic applications. However, transforming photonic circuit-based applications from the lab to the external environment requires integrating all components optimally to survive and function in

ambient conditions. This mostly leads to additional prototyping as the photonic packaging part is not considered during the initial study.

In the current thesis, a portion of the study is devoted to establishing packaging protocols that facilitate the applicability of the multi-wavelength laser sources based on Si_3N_4 microcomb [18] outside the lab. The main focus of packaging's development is initially put on the high optical power handling capability with Si_3N_4 device able to sustain up to 2.5 to 3 W optical power. The core idea of this study revolves around the miniaturization of soliton microcombs for practical and scientific applications. For this purpose, two approaches are adopted;

- The first miniaturization approach is based on the unique effect of self-injection-locking, enabling an ultra-compact and electrically driven soliton microcomb by directly coupling the multi-frequency laser diode to Si_3N_4 [19].
- The second approach takes advantage of a fiber pigtailed Si_3N_4 microresonator driven via an external laser and amplifier to generate an optical frequency comb [20], leading to two main applications performed in this study.
  - In the first application, the soliton microcomb module is used to show ultra-fast optical circuits switching for data center application at Microsoft Research Cambridge [21].
  - Moreover, photonic packaged Si_3N_4 is further utilized for modulation of electron beam in CW-mode [22]. Later, the same platform is used to study the interaction of solitons with an electron beam [23] (chapter 7).
  - Similarly, the packaged Si_3N_4 device facilitates the stabilization of microwave repetition rate soliton [24], photon-pair generation [25], and matrix multiplication [26].
  - In addition, some efforts are dedicated to soliton generation via a laser diode and a DFB ultra-low noise laser (ULN) [20, 27], microwave generation via a soliton [24], and soliton initialization via on-chip ALN [28].

1.1 Need for miniaturization of soliton microcomb system

An optical frequency comb consists of equally spaced discrete frequency components over a large bandwidth. In the temporal domain, it corresponds to ultrashort pulses with round trip time $T_R = \frac{1}{f_{rep}}$. The spectral position of the n-th line of a frequency comb can be represented as:

$$f_n = n.f_{rep} + f_{ceo} \tag{1.1}$$

Where f_{rep} represents the spacing between comb lines and f_{ceo} is the offset frequency that arises due to the carrier-envelope offset phase ($f_{ceo} = \frac{\Delta\phi}{2\pi T_R}$). After the initial demonstration in passively modelocked lasers, several practical utilities of frequency combs have been developed, ranging from optical spectroscopy [29], astronomy [30] to optical metrology [31]. These modules are commercially available from the Menlo system in tabletop systems (Figure 1.1). The mode lock

laser module is highly attractive for multiple scientific applications. However, the widespread applicability is limited due to the large size of the module.

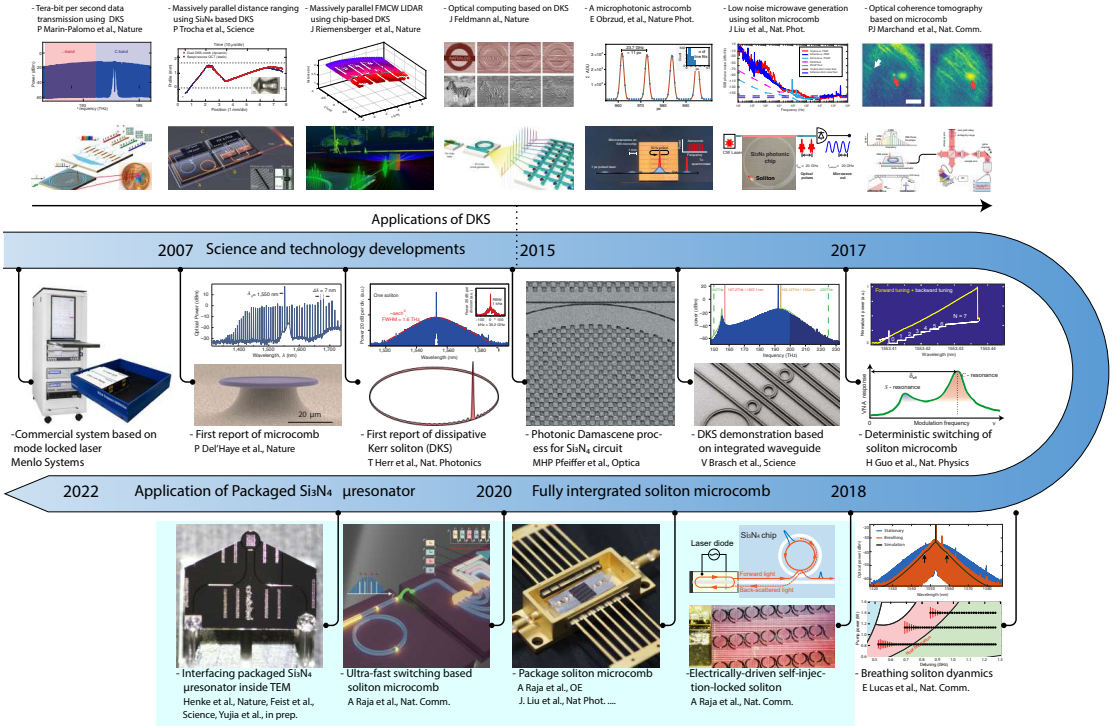

Figure 1.1: **The scientific and technological development overview of Si_3N_4 microresonator based soliton microcomb.** Development of optical frequency comb started with the commercialization of mode lock laser-based module and later discovery of soliton microcomb leading to multiple application demonstrations ranging from telecom to optical coherence tomography (OCT). In addition to application demonstration, considerable efforts are made to improve the fabrication quality of Si_3N_4 microresonators to enhance power efficiency. These improvements played a major role in paving the way for photonic integrated soliton mircocomb, which are relatively compact and electrically driven overall, improving the readiness level of technology.

In 2007, a new microresonator [32] based platform emerged, paving the way for the compact chip-scale frequency comb generation utilizing the Kerr nonlinearity (Figure 1.1). Optical microresonators have gained a lot of interest due to tight spatial confinement and high-quality factor (Q – factor) in the order of 10^6-10^{10} [33, 34, 35, 36, 37, 38]. The compactness enables a high repetition rate (10 [24] to 1000 GHz [39]) frequency combs compared to modelocked laser combs where repetition rates higher than 10 GHz are challenging to achieve, requiring interleaving via external MZM modules [40]. Demonstration of dissipative Kerr soliton (DKS) in microresonators proved that ultrashort pulses [41] can be generated similarly to modelocked lasers. DKS in microresonators arises due to the balance of the cavity's dispersion (anomalous) and the Kerr nonlinearity, as well as the loss in the cavity is compensated by parametric gain [18, 42]. The physics explaining the dynamics of dissipative soliton microcombs is well studied experimentally and analytically, mainly underlying the generation and probing of multiple nonlinear states

such as breathing, crystals, and Multiple soliton states, etc [41, 43, 44, 45, 46, 47, 48, 49]. Octave spanning combs can be generated by tailoring the dispersion of the microresonator hence allowing for the direct self-referencing (f − 2f) [50, 51, 52]. However, self-referenced soliton microcombs are relatively difficult to achieve in low repetition rate (< 300 GHz) [53] microresonators compared to high (~ 1 THz) [51]. An alternative pumping scheme relying on an external pulse (pulse pumping) to initiate a soliton state is proposed to enhance conversion efficiency and improve the soliton generation mechanism [54]. This pumping architecture could allow fully self-referenced micromb in a low repetition rate regime [55, 56], without needing an additional combs module for repetition rate measurements [51].

Till now, optical microresonators fabricated using silica [32, 34], diamond [57], crystalline (MgF_2 [41] & CaF_2 [33, 58]), Si_3N_4 [59, 36, 60, 35], AlGaAs [61], Lithium Niobate ($LiNbO_3$) [62, 63], GaP [64], and SiON [65] etc. are being studied intensively for different comb applications (see Figure 1.2). Each platform has unique advantages and drawbacks, including heterogeneous integration with lasers, ultra-low loss, and high power handling capability. For example, $LiNbO_3$-based microresonators are a highly attractive platform for soliton microcomb due to the intrinsic capability of modulation and self-referencing via f-2f ($\chi^{(2)}$) on the same device [62, 66]. But, efficient light coupling and high yield fabrication are some challenges that are being investigated, and further improved [67].

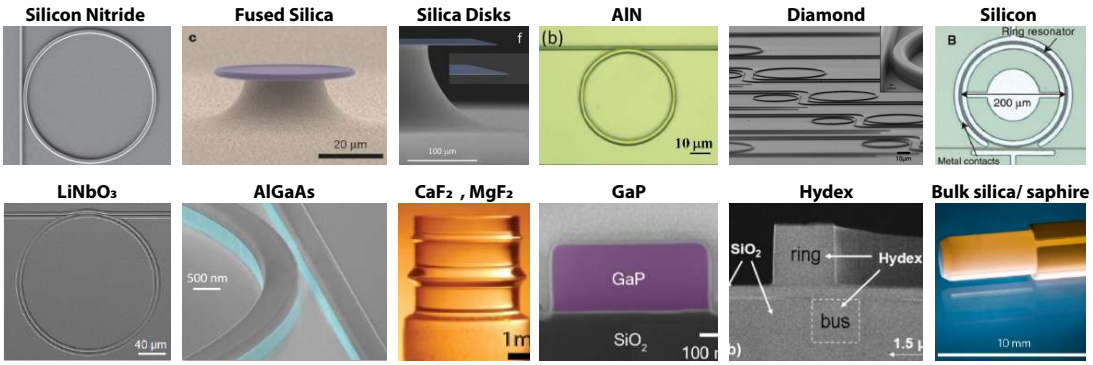

Figure 1.2: **The overview of multiple materials platforms utilized to demonstrate the nonlinear frequency conversion-based optical frequency comb.** Figure adapted from [68, 69, 70, 57, 33, 71, 54, 72, 64, 63, 73, 74, 75, 76]. An important goal for any platform used to perform nonlinear photonics is to achieve low-loss fabrication. The other crucial parameters are higher nonlinearity, active capabilities, integration (CMOS compatibility), transparency window, etc. The current thesis work is based on ultralow loss Si_3N_4 photonic circuits [59, 77, 27, 35].

The main focus of this thesis lies on the Si_3N_4 based microresonators due to the following advantages: planer waveguide and microresonator geometry [78, 79] with low-loss fabrication [35], dispersion engineering [80, 52], high power handling [81] and high repetition rate devices are easily achievable [52]. One of the main advantages of integrated photonic-based microresonators compared to crystalline ones is the ease of coupling light to the cavity (Figure 1.2). Using lithographic techniques, this is done via a bus waveguide directly placed next to the cavity. Coupling light to the bus waveguide is difficult due to a high index contrast ($\Delta_n \sim 0.55$) as the mode is

well confined in the waveguide. Mode confinement is important for the nonlinear phenomenon, but coupling the light from an external source is challenging due to a big mismatch between the waveguide and input fiber modes. After the initial soliton demonstration [82], proof of principle applications were shown based on Si_3N_4 microcomb in coherent telecommunication [83, 84], astronomical spectrograph calibration [85], precise distance measurement [86] (FMCW-LiDAR [87]), optical coherence tomography [88, 89], data center circuit switching [21], convolutional processing [26], low noise microwave [24] and frequency synthesis [51](Figure 1.1). The diverse range of applications demonstrated by soliton microcomb shows the technology's potential impact and usefulness while emphasizing the module's further miniaturization to facilitate operation in on-field applications. The soliton initiation mechanism is slightly complicated because the soliton exists on the effective red side cavity, and thermal effects hinder soliton generation [43]. Multiple schemes have been designed to generate the soliton using a well-stabilized single-mode laser [43, 82, 84, 86]. The core generation idea is to scan the laser wavelength at the optimum speed to balance the thermal effect leading to shifting of cavity resonance due to a change in power. The scanning is performed either internally by changing the laser wavelength via PZT or externally (modulators) to generate the soliton state [90]. In addition, schemes based on dual-laser pumping and intensity modulation of the pump to use mode as an auxiliary pump to compensate for the thermal effect are used to initiate the soliton [91, 92]. Moreover, on-chip actuators could initiate the soliton by heating and stress-optic effect [93, 94].

The chip-based lasers are an attractive solution for fully integrated soliton generation; however, power and frequency agility requirement poses the biggest obstacle. To this end, a unique effect known as self-injection-locking is used to relax the soliton generation thanks to "fast optical feedback" originating from the cavity and eventually locking the laser [95, 96, 97]. Moreover, this effect allows soliton generation from a multi-frequency laser diode, further easing the requirement of the single-frequency pump laser [19, 98, 99]. Indeed, after the first demonstration of self-injection locking on an integrated platform, this approach is later implemented via DFB to generate solitons in a low repetition rate microresonator [100, 101]. Building on ongoing improvement, a heterogeneously integrated soliton microcomb source is demonstrated [6].

Generally, higher power per comb line is desired for different practical applications >-10 dBm especially related to telecommunication [84, 86, 87]. Even though chip-based soliton microcombs are attractive solutions, the maximum power provided by DFB is ~ 200 mW [101, 100]. In addition, the insertion loss is high, exceeding 4 dB due to the elliptical shape of the laser diode mode, further reducing power reaching the bus waveguide. In this direction, a different approach based on optical packaging is adopted [20], facilitating the integration of soliton microcomb modules into standard fiber components. Different solutions have been proposed to reduce the coupling losses when coupling light from an external source to a photonic chip [102, 17, 13]. A piezo precision stage is used in a laboratory environment to couple light into the bus waveguide by actively aligning the fiber. The coupling efficiency is affected by vibration movements as the misalignment tolerance (30 % coupling loss) is very low (< 0.5 μm). To stabilize the input and output, coupling fibers should be fixed to the chip. Different techniques based on welding [103, 104, 105] and fiber fusion (Glasspack) [104] relying on CO_2 laser to fix the fiber on the chip

have been demonstrated. Optical epoxy provides better handling and freedom while attaching the fiber to the chip. But epoxy has some disadvantages, i.e., a large coefficient of thermal expansion (CTE) mismatch between glass (fiber) and epoxy, linear shrinkage, and low transmission. Large CTE mismatch and linear shrinkage are the main issues due to operation at high power (500 mW to 1.5 W). Careful selection of the different parameters is required for the epoxy to maintain coupling not only at low power but at high power as well. Permanently connecting the fiber to the chip will stabilize the coupling and help make the platform attractive for applications outside the laboratory and integration into standard fiber modules. Moreover, as demonstrated in this study, the fiber integrated Si_3N_4 photonic devices enable the demonstration of electron beam modulation, where implementation is generally extremely challenging [22, 106, 23]. These results opened a new domain where integrated photonics showed its potential and the importance of fiber-integrated devices.

The following section focuses on the fundamental properties of microresonators and frequency comb generation. The first part initially covers the phenomena of light coupling for optical microresonators. Furthermore, a short overview of different third-order nonlinear processes is presented. Moreover, some basic coupled-mode equations and dispersion relevant to optical microresonators are discussed. Then a general overview of self-injection locking and Si_3N_4-based photonic integrated circuits is provided.

1.2 Optical microresonators

An integrated optical microresonator consists of a ring placed close to a straight waveguide for coupling light in and out of the microresonator [107] (Figure 1.3). However, the actual shape of microresonators can be circular, racetrack, or arbitrary. The field inside the microresonator builds up when an incoming field interferes constructively with the field inside the cavity after one round trip. The Si_3N_4-based microresonator exhibits strong temporal (ultra-low propagation loss [38, 35, 37, 36]) and spatial confinement giving rise to nonlinear frequency conversion at relatively low threshold power [27, 36]. The spatial confinement factor ($\Gamma = \frac{P_{\text{core}}}{P_{\text{total}}} = \frac{\int\int_A |\vec{E}|^2 dA}{\int\int_\infty |\vec{E}|^2 dA}$) refers to the fraction of power inside core area (A) compared to the total waveguide (clore+cladding).

1.2.1 Input/output coupling

An integrated microresonator uses a bus waveguide to couple into the microresonator evanescently. The external coupling into the microresonator is analytically described by coupled mode theory [108, 52]. The field inside the microresonator is given by $a = a_0(t)e^{-i\omega_0 t}$ while an input driving field propagates with $s = s(t)e^{-i\omega_p t}$. The driving field and cavity field amplitudes are normalized such that $|s|^2$ and $|a_o|^2$ correspond to the number of photons in the cavity and input energy, respectively. The equation of motion for the cavity coupled to the waveguide with coupling rate κ_{ex} and intrinsic loss rate κ_0 is the following:

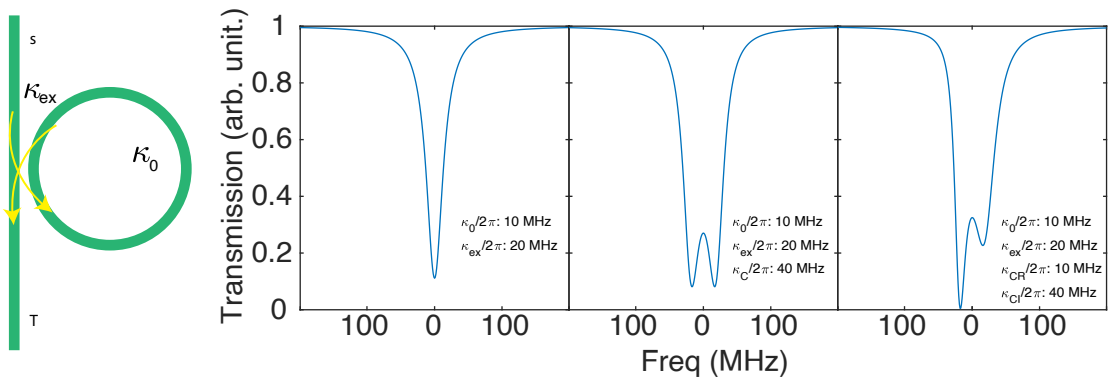

Figure 1.3: **Overview of different models to fit the transmission signal of the cavity.** An integrated microresonator with intrinsic loss rate κ_0 and external coupling rate κ_{ex}. The transmission (T) through the bus waveguide coupled to the microresonator is analyzed for three cases, considering different parameters κ_0, κ_{ex}, κ_C, κ_{CR} and κ_{CI}.

$$\frac{da_0(t)}{dt} = -\left(\frac{\kappa}{2}\right)a_0 + s\sqrt{\kappa_{ex}}e^{-i(\omega_p-\omega_0)t} \tag{1.2}$$

Where $\kappa = \kappa_0 + \kappa_{ext}$ is the total cavity decay rate. The above equation is in the rotating frame of the microresonator (ω_0), transforming the equation into a driving laser frame by applying transformation $a_o(t) = A(t)e^{-i(\omega_p-\omega_0)t}$:

$$\frac{dA(t)}{dt} = i\Delta A(t) - \left(\frac{\kappa}{2}\right)A(t) + s\sqrt{\kappa_{ex}} \tag{1.3}$$

where the detuning is $\Delta = (\omega_p - \omega_0)$. For the steady state ($\frac{dA(t)}{dt} = 0$) and constant input, the cavity amplitude and photon number are given by:

$$A(t) = \frac{-s\sqrt{\kappa_{ex}}}{\left(i\Delta - \frac{\kappa}{2}\right)}, \qquad |A(t)|^2 = \frac{|s|^2\kappa_{ex}}{\left(\Delta^2 + \frac{\kappa^2}{4}\right)}$$

Transmission is calculated by considering energy conservation and the transmitted amplitude is given by:

$$t = s - \sqrt{\kappa_{ex}}A(t), \qquad T = \left|\frac{t}{s}\right|^2$$

$$T = \left|1 - \frac{\kappa_{ex}}{-i\Delta + \frac{\kappa}{2}}\right|^2, \qquad T(\Delta = 0) = \left|\frac{\kappa_0 - \kappa_{ex}}{\kappa_0 + \kappa_{ex}}\right|^2$$

The interference between input and cavity field is represented as transmission (T), corresponding to the Lorentzian profile with full width at half maximum (FWHM) equal to $\kappa/2\pi$. The quality factor of a microresonator as a function of the relative linewidth ($\delta\omega$) can be defined as:

$$Q = \frac{\omega_o}{\delta\omega} = \frac{2\pi\omega_0}{\kappa} \tag{1.4}$$

However, the surface Rayleigh or bulk scattering in the microresonator arising due to waveguide sidewall roughness leads to the coupling of clockwise and counter-clockwise modes. This requires the introduction of a real coupling parameter (κ_C) and modifying the coupled mode equation mentioned above [109, 110] leading to transmission from the cavity,

$$T = \left| 1 - \frac{\kappa_{\text{ex}}(-i\Delta + \frac{\kappa}{2})}{(-i\Delta + \frac{\kappa}{2})^2 + (\frac{\kappa_C}{2})^2} \right|^2 .$$

The κ_{C} is critical for achieving a good locking range in self-injection-locking devices. A more accurate model with the second-order coupling mechanism in counter-propagating modes is presented in [111]. A complex coupling ($\kappa_{\text{C}} = \kappa_{\text{CR}} + i\kappa_{\text{CI}}$) parameter is incorporated inside the coupled mode equation to explain the asymmetric lineshapes arising due to the direct and indirect scattering process,

$$T = \left| 1 - \frac{\kappa_{\text{ex}}(-i\Delta + \frac{\kappa}{2})}{(-i\Delta + \frac{\kappa}{2})^2 + (\frac{(\kappa_{\text{CR}}+\kappa_{\text{CI}})}{2})^2} \right|^2 .$$

The three models mentioned above are compared in Figure 1.3. The first graph shows a typical Loreztioan shape transmission profile without scattering (mode coupling). At the same time, the two graphs on the right show the impact of scattering leading to a doublet resonance profile considering a simple [109, 110], and advanced [111] model to explain the asymmetry in resonance doublets. Depending upon the ratio of κ_{ex} and κ_0 different coupling regimes can be defined [112, 52]. In under-coupled regimes, the intrinsic loss dominates the external coupling rate ($\kappa_0 > \kappa_{\text{ex}}$). The linewidth value approaches κ_0 in this scenario. In critical coupling, the transmission drops to zero as the intrinsic loss rate equals the coupling rate ($\kappa_0 = \kappa_{\text{ex}}$). In over coupled situation, the coupling rate is higher than the intrinsic loss rate ($\kappa_{\text{ex}} > \kappa_0$), and the linewidth is determined by $\frac{\kappa}{2\pi}$. These different coupling regimes can be realized by changing the distance between the bus waveguide and the microresonator. The three models mentioned above are used rigorously to characterize the loss properties of Si_3N_4 microresonators [77, 27, 35].

1.3 Dispersion

Dispersion plays an important role in optical frequency comb generation using microresonators. Generally, material dispersion is defined as the dependence of the refractive index on frequency. In addition to intrinsic material dispersion, waveguide dispersion arises due to frequency-dependent guiding effects and depends upon the geometrical parameters of the microresonator. In microresonators, dispersion is presented as an offset of equidistant resonances relative to the FSR. Without dispersion, a microresonator's resonances (single mode family) would be separated by a constant FSR. The dispersion in the microresonator is described by expanding the resonance around the

pump [113]:

$$\omega_\mu = \omega_0 + \sum_{j=1}^{\infty} \frac{D_j}{j!}\mu^j \tag{1.5}$$

Where ω_0 is pump angular frequency, $D_1/2\pi$ is the FSR of a microresonator, D_2 is linked to

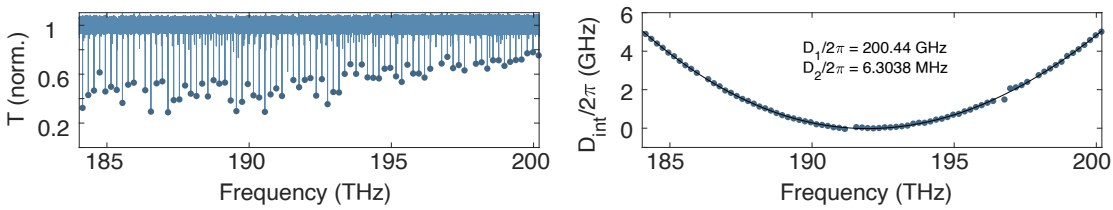

Figure 1.4: Measured integrated dispersion D_{int} of 200 GHz FSR Si_3N_4 microresonator from calibrated transmission. The fitting shows $D_1/2\pi$ and $D_2/2\pi$ correspond to ~ 200.44 GHz and 6.3038 MHz respectively.

group velocity dispersion (GVD) and $D_{j>2}$ are higher order dispersion terms.

$$D_1 = 2\pi FSR \qquad D_2 = -\frac{cD_1^2\beta_2}{n_g}$$

where β_2 is GVD for fiber and n_g is group index. GVD is anomalous and normal for positive and negative values of D_2 respectively. For bright dissipative soliton generation, the dispersion of the microresonator should be anomalous. It is more convenient to express the dispersion terms in a single expression (integrated dispersion):

$$D_{\text{int}} = \sum_{j=2}^{\infty} \frac{D_j\mu^j}{j!} = \frac{D_2\mu^2}{2!} + \frac{D_3\mu^3}{3!} + ... \tag{1.6}$$

Figure 1.4 shows the calibrated transmission scan measured by using a widely tunable laser diode (1500 nm to 1630 nm) referenced to a fiber-based mode lock laser [114, 115]. From the calibrated transmission, the integrated dispersion is fitted. In the absence of dispersion, all the blue dots in Figure 1.4 right graph should lie on the straight line (0 GHz line). The fitted dispersion profile yields a $D_2/2\pi > 0$, indicating the microresonator possesses anomalous dispersion.

1.4 Kerr nonlinearity

Optical frequency comb generation via a microresonator relies on Kerr nonlinearity when pumped at relatively high optical power (threshold). This section provides a short overview of the third-order nonlinear processes. When considering the intense field interaction with the dielectric medium, a simple harmonic oscillator model requires modification, such as adding a quadratic or cubic electric field displacement. The induced polarization of a media considering the nonlinear

medium and instantaneous response (memoryless) to the electric field is given by [116, 117].

$$P(z,t) = \varepsilon_0\chi^{(1)}E(z,t) + \varepsilon_0\chi^{(2)}E^2(z,t) + \varepsilon_0\chi^{(3)}E^3(z,t) + ... \tag{1.7}$$

$$P^{(3)} = \varepsilon_0\chi^{(3)}E^3(z,t) \tag{1.8}$$

ε_0 is vacuum permittivity, $\chi^{(3)}$ is 3rd order susceptibility (tensor) and $P^{(3)}$ represents nonlinear polarization (3rd order). Consider the superposition of three different plane waves with frequencies ω_i, ω_j and ω_k in the nonlinear medium:

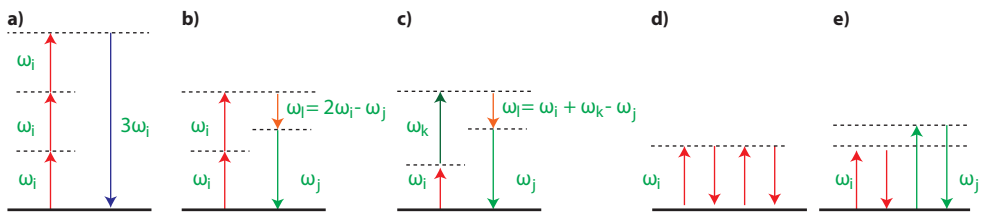

Figure 1.5: **Energy level description of different processes in a third-order nonlinear medium. a)** THG **b)** Degenerate FWM **c)** Non-degenerate FWM **d)** SPM **e)** XPM. Dashed lines represent virtual energy levels with a short lifetime (corresponding to the quantum mechanical uncertainty relation) [117].

$$\begin{aligned}
P^{(3)} = \frac{1}{2}\varepsilon_0\chi^{(3)}\Bigg[&\frac{1}{2}E_i^3 e^{-i(3\omega_i t - 3k_i z)} + ... + c.c. \\
&+ \frac{3}{4}E_i^2 E_j e^{-i((2\omega_i+\omega_j)t-(2k_i+k_j)z)} + ... + c.c. \\
&+ \frac{6}{4}E_i E_j E_k e^{-i((\omega_i+\omega_j+\omega_k)t-(k_i+k_j+k_k)z)} + ... + c.c. \\
&+ \frac{3}{4}|E_i|^2 E_i e^{-i(\omega_i t - k_i z)} + ... + c.c. \\
&+ \frac{6}{4}|E_j|^2 E_i e^{-i(\omega_i t - k_i z)} + ... + c.c. \\
&+ \frac{3}{4}E_i^2 E_j^* e^{-i((2\omega_i-\omega_j)t-(2k_i-k_j)z)} + ... + c.c. \\
&+ \frac{6}{4}E_i E_j E_k^* e^{-i((\omega_i+\omega_j-\omega_k)t-(k_i+k_j-k_k)z)} + ... + c.c.\Bigg]
\end{aligned} \tag{1.9}$$

The first term in Equation 1.9 represents the third harmonic generation (THG) in which three waves produce a single wave with three times the energy of the incoming wave (3 ω_i). The second/sixth and third/seventh terms represent degenerate and non-degenerate fourth wave mixing (FWM) respectively. In degenerate/non-degenerate FWM two/three waves with different frequencies interact to generate a new wave. Degenerate and non-degenerate FWM are also known as third-order sum frequency generation (SFG). The fourth term represents self-phase modulation (SPM) in which the incoming wave changes its own phase. If the phase of the

incoming wave is being changed by another wave this effect is known as cross phase modulation (XPM) as indicated in the fifth term. The value, in fraction, before each term is the degeneracy factor calculated from the number of permutations of input waves e.g. following permutation possible for degenerate FWM (ω_i,ω_i, ω_j), (ω_i,ω_j, ω_i) and (ω_j,ω_i, ω_i). And "..." in each term corresponds to the ensemble of all expressions by considering different combinations of electric fields.

Phase shift induced by SPM and XPM can be represented as the intensity-dependent refractive index of the nonlinear medium. The extra factor, 2 I, is due to the degeneracy factor as shown in Equation 1.9 indicating XPM is a 2 times stronger process than SPM.

$$n(\omega_i) = n_0(\omega_i) + n_2 I(\omega_i) \qquad n(\omega_i) = n_0(\omega_i) + n_2(I(\omega_i) + 2I(\omega_2))$$

n_2 is the Kerr coefficient and is represented as: $n_2 = \frac{3Z_0}{4n_0^2}\chi^{(3)}$. Whereas Z_0 is free space wave impedance. Both processes (XPM and SPM) are intrinsically phase-matched ($k_i - k_i + k_i - k_i = 0$), ($k_j - k_j + k_i - k_i = 0$). Phase mismatch (angular momentum and energy not conserved) interactions lead to lower conversion efficiency due to destructive interference from nonlinear fields [118]. Phase-matched interactions are achieved by taking advantage of the intensity-dependent refractive index, which shifts the resonance position of the microresonator opposite to dispersion (anomalous dispersion).

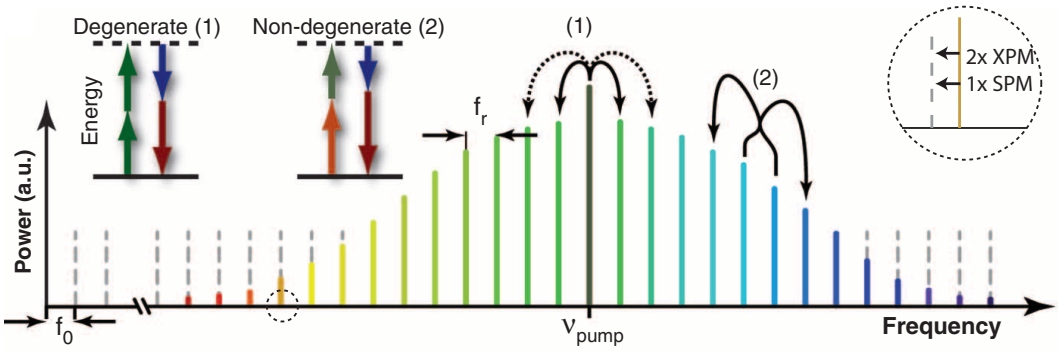

Figure 1.6: **Optical comb generated using microresonators with high** Kerr **nonlinearity.** Degenerate and non-degenerate FWM combine inside the nonlinear microresonator to generate the optical frequency comb. f_r is the frequency spacing between two comb lines and f_0 is the offset frequency. Figure adapted from: [119].

The two main processes responsible for generating the comb in a microresonator are degenerate and non-degenerate FWM. When a CW laser is tuned into one of the resonances of the microresonator at high power, degenerate FWM takes place to generate two sidebands. In degenerate FWM, two pump photons in the microresonator interact to generate a signal and an idler. Afterward, cascaded non-degenerate FWM takes place to produce the optical comb spectra (Figure 1.6). Due to the intrinsic dispersion of the microresonator (Figure 1.4), the cavity modes around the pump mode (ν_{pump}, Figure 1.6) are not symmetric ($2 \times \omega_{pump} \neq \omega_{singnal} + \omega_{idler}$), requires energy conservation for efficient interaction. The energy conservation condition is fulfilled with the help

of SPM and XPM by shifting of resonance (Figure 1.6 circle inset). In the following section, a brief introduction will be provided regarding the analytical models that explain the generation of optical frequency combs.

1.5 Coupled mode equation

Kerr nonlinearity dynamics can be studied in a microresonator by extending Equation 1.2 to all modes. The electric field inside the microresonator with third-order nonlinearity can be described by a nonlinear wave equation [116, 117]:

$$\left[\Delta - \frac{n^2}{c^2}\frac{\partial^2}{\partial t^2}\right] E(r,z,\phi,t) = \mu_0 \frac{\partial^2 P_{NL}(r,z,\phi,t)}{\partial t^2} \tag{1.10}$$

Expressing the electric field inside the microresonator with circular geometry in the angular coordinates is more convenient. The following ansatz can be used for the electric field inside the microresonator:

$$E(r,z,\phi,t) = \sum_{\mu} \frac{1}{2}\{E_\mu(r,z).a_\mu(t)e^{-i(\omega_\mu t - \mu\phi)} + c.c,\} \tag{1.11}$$

Where E_μ is one of the eigenmodes of the microresonator with azimuthal index μ and amplitude a_μ. The approximation in Equation 1.11 is valid in microresonators due to high Q − factor (low losses) and negligible nonlinear coupling between modes during one round trip time. The slow varying envelope approximation (SVEA) (Equation 1.12) is valid as a_μ is not changing significantly.

$$|\frac{\partial^2 a_\mu}{\partial t^2}| << |2i\omega_\mu \frac{\partial a_\mu}{\partial t}| << |-\omega_\mu^2 a_\mu| \tag{1.12}$$

The equation is obtained by inserting Equation 1.11 into Equation 1.10 and using SVEA approximation and $\sum_\mu a_\mu \left[\Delta - \frac{n^2}{c^2}\frac{\partial^2}{\partial t^2}\right] E_\mu = 0$:

$$\frac{n^2}{c^2}(-2i\omega_\mu)E_\mu e^{-i\omega_\mu t}\frac{\partial a_\mu}{\partial t} = \frac{3\omega_{\mu 1}^2}{8}\mu_o\varepsilon_0\chi^{(3)} \sum_{\mu'\mu''\mu'''} E_{\mu'}E_{\mu''}E^*_{\mu'''}a_{\mu'}a_{\mu''}a^*_{\mu'''}e^{-i(\omega_{\mu'}+\omega_{\mu''}-\omega_{\mu'''})t} \tag{1.13}$$

Coupled wave equation (Equation 1.13) is only valid for terms fulfilling the angular momentum conservation $\mu = \mu' + \mu'' - \mu'''$. This condition is satisfied for FWM, SPM, and XPM in a WGM microresonator. Equation 1.13 can be further simplified by projecting on the mode E_μ by multiplying $E^*_\mu e^{i\omega_\mu t}$ and integrating over the volume and using a normalized factor $a_\mu = \sqrt{\frac{2\hbar\omega_\mu}{\varepsilon_0 n_0^2 V_{\text{eff}}}}A_\mu$ such that $|A_\mu|^2$ corresponds to number of photons. After introducing the nonlinear coupling term to the coupled mode equation (Equation 1.2), the full coupled mode equation is

equal to [120]:

$$\frac{\partial A_\mu}{\partial t} = -i\frac{\kappa}{2}A_\mu + ig\sum_{\mu'\mu''\mu'''} A_{\mu'}A_{\mu''}A^*_{\mu'''}e^{-i(\omega_{\mu'}+\omega_{\mu''}-\omega_{\mu'''}-\omega_\mu)t} + \delta_{0\mu}s\sqrt{\kappa_{\text{ex}}}e^{-i(\omega_p-\omega_0)t} \tag{1.14}$$

Where g is the nonlinear coupling coefficient given by:

$$g = \frac{\hbar\omega_\mu^2 c n_2}{n^2 V_{\text{eff}}}$$

and V_{eff} is equal to the length of the microresonator multiplied by the effective nonlinear mode area ($V_{\text{eff}} = L_{\text{R}} \times A_{\text{eff}}$). The pump is associated with mode index zero ($\mu = 0$). Equation 1.14 contains loss term κ, nonlinear coupling of the modes and the driving pump. Dimensionless equations can be obtained from Equation 1.14 by applying the phase transformation $a'_\mu = A_\mu\sqrt{\frac{2g}{\kappa}}e^{-i(\omega_\mu-\omega_p-\mu D_1)t}$ and the following scaling terms [43]:

$$f = \sqrt{\frac{8g\eta P_{in}}{\kappa^2\hbar\omega_o}} \qquad \tau = \frac{\kappa t}{2}$$

where η corresponds to coupling efficiency $\eta = \frac{\kappa_{\text{ext}}}{\kappa}$, $P_{in} = |s|^2\hbar\omega_0$ and resonance frequency $\omega_\mu = \omega_0 + D_1\mu + \frac{2}{2}D_2\mu^2 + \frac{1}{6}D_3\mu^3 + ...,$. Using the scaling terms and applying the phase transformation the dimensionless equation is given by:

$$\frac{\partial a'_\mu}{\partial \tau} = -(1+i\zeta_\mu)a'_\mu + i\sum_{\mu'\mu''\mu'''}(2-\delta_{\mu'\mu''})a'_{\mu'}a'_{\mu''}a'^*_{\mu'''} + \delta_{0\mu}f \tag{1.15}$$

In Equation 1.15 a'_μ represents fields on equidistant frequency lines and ζ_μ corresponds to detuning (normalized) ($\zeta_\mu = \frac{2(\omega_\mu-\omega_p-\mu D_1)}{\kappa}$). All the parameters (field magnitudes, detuning, and frequencies) are measured in the unit of $\kappa/2$. Different nonlinear dynamics in a microresonator are studied numerically (simulation) using Equation 1.15. This equation can be used to analytically derive the shift of the resonance (pump mode) due to nonlinear effects and the threshold power for the first sideband generation. In the absence of the g term ($g = 0$) in Equation 1.14, a Lorentzain shape is observed (Figure 1.3). The threshold input power for the generation of a first pair of sidebands can be derived only considering three modes (pump, signal, and idler) ($P_{\text{th}} = \frac{\kappa^2 n_0^2 V_{\text{eff}}}{8\eta\omega_0 c n_2}$) [43]. The P_{th} depends on the V_{eff}, κ and n_2. More importantly, P_{th} scales inversely with Q^2 (κ^2), indicating the improvement required to reduce losses in integrated devices for power-efficient nonlinear conversion. In addition, the location of the first sideband (signal and idler) can be estimated analytically using the following expression:

$$\mu_{th} \sim \sqrt{\frac{\kappa}{D_2}(\sqrt{\frac{P_{\text{in}}}{P_{\text{th}}}-1}+1)}.$$

The first sideband or gain lobe position ($\sim \sqrt{\kappa/D_2}$) for parametric oscillation typically depends on the microresonator's linewidth (κ) and second-order dispersion (D_2). When threshold power is reached inside the microresonator, parametric oscillation occurs after the gain overcomes the loss, generating two comb lines around the pump. This state is generally known as a primary comb or Turing roll exhibiting low radio frequency intensity noise [41]. Further increasing the power inside the cavity increases the nonlinear gain and, eventually, the generation of the secondary comb. As first reported in [41], the primary, also referred to as type-1 combs, have spacing (Δ) that is multiple of the free spectral range (FSR) of the microresonator. In contrast, the spacing of the secondary comb is not always equal to an integer multiple of Δ. The secondary comb starts merging once the power inside the cavity is further increased. This particular state is known as modulation instability (MI), with low RF noise higher than primary and secondary combs.

Even though coupled mode equation (Equation 1.14) can provide valuable insight into nonlinear dynamics of the microresonator-based optical frequency comb generation. But, the analytical modeling using the technique is not considered efficient, especially considering many modes (N). In this regard, a more efficient analytical scheme is used to understand the nonlinear dynamics of the cavity via a fast Fourier transform.

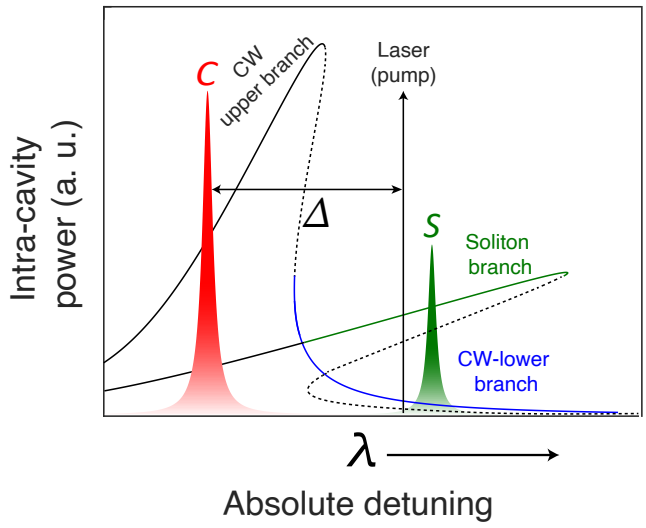

Figure 1.7: **Nonlinear response of the Kerr microresonator when subjected to high power.** Bistable resonance is measured when pumping the microresonator above the threshold power. The nonlinear dissipative states that can be accessed on the upper CW branch when scanning the laser from the blue to the red side of the cavity are primary combs, secondary combs, and modulation instability. A soliton state is only accessible on the effective red-detuned side of the cavity resonance. When initiating soliton via forward scanning, the system undergoes a bi-stable regime, where soliton exists on the upper branch (soliton branch, green line) while the weak background (CW) exists on the lower branch (CW-lower branch, blue part).

1.6 Lugiato Lefever equation

To transform the full coupled mode equation (Equation 1.14) from the frequency domain into the time domain following phase transformation is used (angular mode function, $G(\phi, t) = \sum_u A_\mu e^{i\mu\phi - i\omega\mu t} e^{i(\omega_p + \mu D_1)t}$) and Fourier transform property ($\sum_u (i\mu)^n A_\mu e^{i\mu\phi - i\omega\mu t} e^{i(\omega_p + \mu D_1)t} = \frac{\partial^n G(\phi,t)}{\partial \phi^n}$, a full coupled mode equation can be transformed into:

$$\frac{\partial G(\phi, t)}{\partial t} - i\frac{1}{2}D_2\frac{\partial^2 G(\phi, t)}{\partial \phi^2} = -\{\frac{\kappa}{2} + i(\omega_0 - \omega_p)\}G(\phi, t) + ig|G(\phi, t)|^2 G(\phi, t) + \sqrt{\kappa_{\text{ex}}}s_{in} \quad (1.16)$$

Equation 1.16 can be transformed into a dimensionless equation by using the following scaling terms:

$$\psi = G(\phi, t)\sqrt{\frac{2g}{\kappa}} \qquad \zeta_0 = \frac{2(\omega_0 - \omega_p)}{\kappa} \qquad \tau = \frac{\kappa t}{2}$$

Where dimensionless dispersion is given by $d_2 = D_2/\kappa$.

$$\frac{\partial \psi}{\partial \tau} - id_2\frac{\partial^2 \psi}{\partial \phi^2} = -\{1 + i\zeta_0\}\psi + i|\psi|^2\psi + f \quad (1.17)$$

Now introducing the dimensionless longitudinal coordinate ($\theta = \phi\sqrt{\frac{1}{2d_2}}$):

$$\frac{\partial \psi}{\partial \tau} - i\frac{1}{2}\frac{\partial^2 \psi}{\partial \theta^2} = -\{1 + i\zeta_0\}\psi + i|\psi|^2\psi + f \quad (1.18)$$

Equation 1.18 is similar to the Lugiato Lefever equation (LLE) equation which is used to study spatial dissipative structure in passive nonlinear optical systems [121]. This equation describes the evolution of the pulse and multiple nonlinear dissipative states inside an optical microresonator. It is equivalent to a damped-driven nonlinear Schödinger equation (NLSE). The time t (slow time) indicates the evolution of the intra-cavity average over multiple round trip times, while τ (fast time) refers to the evolution of the field with respect to group velocity. For steady state ($\partial\psi/\partial\tau = 0$) the following expression is an approximate solution:

$$\psi = \psi_0 + \psi_1 \simeq \psi_0 + Be^{i\phi_0}\text{sech}(B\theta)$$

The above-approximated solution corresponds to a single soliton with a continuous pump background (ψ_0) where B (real number) defines the width and amplitude of the soliton, and ϕ_0 defines the phase angle. As the pulse (soliton) inside the cavity experiences losses, it is known as dissipative Kerr soliton (DKS). Losses inside the cavity are compensated by parametric gain, and the Kerr nonlinearity balances anomalous dispersion while maintaining the width of the pulse. Dissipative Kerr solitons were first discovered in fiber-loop cavities [122] and later found in microresonator-based cavities [43]. The two parts in steady solution are indicated in the nonlinear response measurement of the microresonator (Figure 1.7). One important point that needs to be highlighted is that a soliton exists on the effective red-detuned side of the cavity as

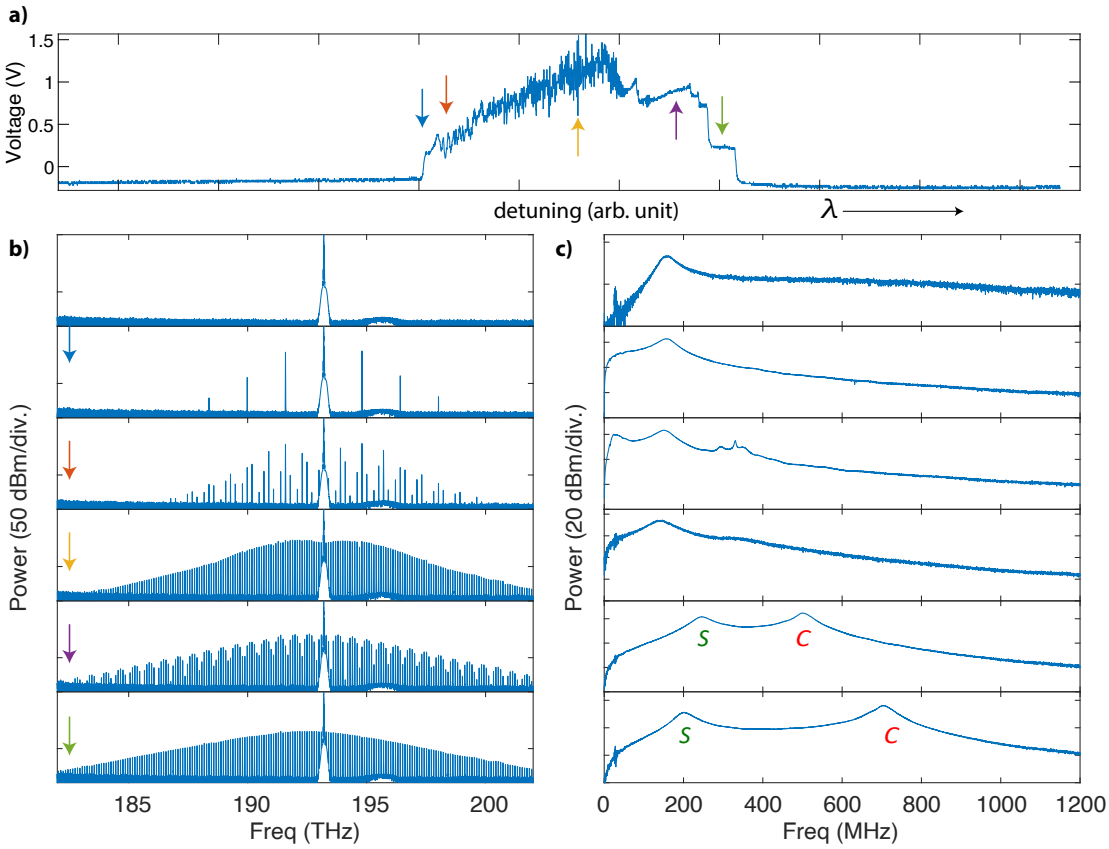

Figure 1.8: **Non-destructive experimental probing of different states generated in a 100 GHz Si_3N_4 microresonator. a** Generated light signal is measured by scanning the pump laser across the cavity resonance at an input power of 274 mW. **b** The optical spectrum of different optical nonlinear states generated by changing the laser detuning. The arrows mark the location of the spectrum in the generated light signal (**a**). The probing of different nonlinear by using a vector network analyzer performs weak phase modulation of the pump via an electro-optic modulator. The multiple and single solitons state leads to a double resonance response ($\mathscr{S}$ and $\mathscr{C}$).

initially experimentally validated in ref [43] (Figure 1.7). Furthermore, this has been verified experimentally by weakly phase modulating the pump mode to probe the cavity nondestructively [123]. One other important property of a soliton that links to effective detuning ($\delta\omega = 2\pi\Delta$) is pulse duration ($\tau_{\text{pulse}}$)

$$\tau_{\text{pulse}} \approx \frac{1}{D_1}\sqrt{\frac{D_2}{2\delta\omega}}. \tag{1.19}$$

Moreover, the soliton generation process is stochastic, meaning various solitons states (N=1,2,3,4, ...) can be generated when scanning over the resonance. (Figure 1.8 a show a single trace of the generated light, indicating multiple low noises ladders (light magenta and light green) corresponding to two and single soliton. Generally, a single soliton is desired for the low line-to-line power variation and smooth envelope (sech^2(f)) to practical application (Figure 1.8 bottom

graph). The deterministic soliton generation is proposed initially via backward switching along with non-destructive probing in Ref [123]. The underlying phenomenon is associated with nonlinear thermal switching from a higher soliton to a lower number. Figure 1.8 b & c shows one example when a two soliton is switched to a single soliton via backward switching. This method has been implemented in the current thesis in multiple projects, but mainly in chapter 2, chapter 5, and chapter 7. As the soliton state can exist over a relatively long detuning range ($\sim 10 \times \kappa_o$) when changing detuning (pump wavelength), the generated comb lines follow the pump. This enables the concurrent tuning of all soliton lines when tuning the pump wavelength externally (or tuning cavity [93]) as demonstrated in FMCW LiDAR experiments [87].

The existence of the soliton state on the effective red side of the resonance and sudden drop of intracavity power when initiating complicate the soliton access due to thermal effects. Due to these reasons, multiple schemes have been implemented to access the soliton reliably and deterministically. One simple method to access the soliton is forward tuning, relying on scanning the pump laser at a speed (10-50 Hz) lower than the thermal response of the microresonator [43]. An advanced version of forward tuning is realized using an external Dual-parallel Machzhener modulator (DP-MZM), enabling the pump's scanning faster than the cavity's thermal relaxation [124]. Similarly, another scheme relies on the rapid increase of pump power when generating a soliton, which leads to heating to compensate for the drop in power with the help of acoustic optics modulators [125]. A dual-pumping method utilizing an extra pump laser to compensate for thermal effects is also used to access the soliton in devices where simple laser piezo tuning does not work. The current thesis uses the forward tuning method in most projects, either via simple laser tuning (chapter 3, chapter 2) or fast tuning via DP-MZM (chapter 3, chapter 7).

Generally, the soliton generation via chip-based lasers was difficult to implement due to the requirement of well-stabilized single-mode lasers with narrow linewidth. In addition, the required threshold power for initiating the soliton was not in the range of what chip-based can achieve. Impressive fabrication method improvements done by the EPFL team, led by Junqiu Liu, throughout the thesis study have enabled the ultra-low loss Si_3N_4 photonic microresonator [35, 77, 27]. First, a 99 GHz FSR soliton microcomb is generated without the amplifier(chapter 3). Then, a unique approach is adopted to demonstrate the soliton generation using the self-injection-locking, enabling the true chip-based and electrically driven soliton microcomb.

As part of the current thesis study focuses on soliton generation via self-injection locking, a short overview of the effect is provided in the next section.

1.7 Self-injection-locking

Recently, substantial efforts have been made to improve the linewidth of the on-chip laser via self-injection locking thanks to advances enabling ultra-low Si_3N_4 microresonators [37, 126, 127]. In the past, a master-slave configuration has been implemented to transfer the low-noise laser's (low-power) coherence into the high-power laser diode by injecting a small portion of optical

feedback [128]. However, this scheme is sensitive to the external environment, and full chip integration would require additional elements such as on-chip isolators. Alternatively, a reduction in linewidth can also be achieved by locking the laser with an external high-Q cavity. There are two possible implementations of this locking method; the first is a more traditional one known as Pound-Drever-Hall (PDH), [129, 130] which relies on active stabilization via phase modulation and electric locking loops. Moreover, a similar method without phase modulation is also used but requires a stable reference level for optimum locking [131]. In comparison, laser stabilization can also be achieved by passive optical feedback from optical components which are external to the laser cavity [132, 133, 134, 135, 136, 137, 138] such as diffraction gratings [139, 140, 141, 142, 143] and optical low loss cavities [134, 144, 145, 146, 147, 148]. The direct optical feedback originating from high-Q cavity leads to an effect known as "self-injection-effect," a known phenomenon in radio physics [149]. When a radio-frequency generator is connected with a (reference) resonant load with a relatively high-Q compared to the generator, it leads to better frequency stability [149]. The parameter that dictates the frequency stabilization is the ratio of the Q-factor of the load and the Q-factor of the generator (oscillator). Similarly, this concept is implemented via optical Fabry-Pérot (FP) cavities to stabilize the laser. Indeed, this high-Q FP has enabled laser with linewidth in the order ~ 6.2 Hz (FP cavity Q-factor $\sim 1.5 \times 10^{1}0$) [147] and 125 Hz (FP cavity Q-factor $\sim 1.5\times10^{7}$) [150]. The high-Q FP cavities require special coating and, more importantly, are bulky. In parallel, whispering gallery mode (WGM) microresonators are implemented to improve the laser properties providing the possibility of direct integration of the laser while giving access to low propagation losses (high-Q factor, $\sim 10^{8}$-10^{11}) [97, 151, 152].

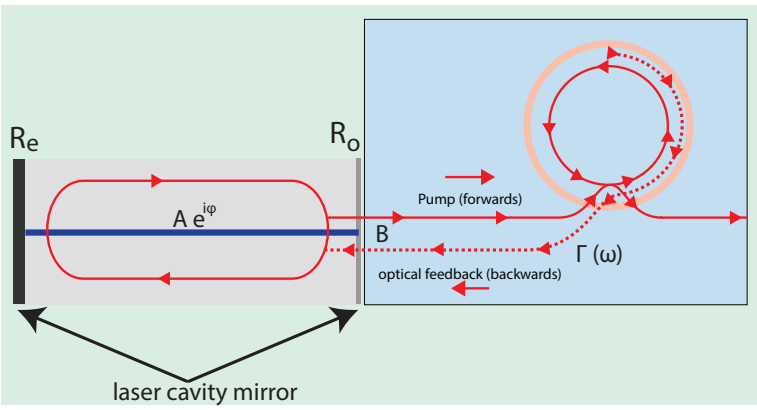

Figure 1.9: **Concept of self-injection-locking effects** The intra-cavity field A(t) of the laser is the sum of light reflected from both mirrors and light back-scattered light from microresonator (B). The inhomogeneous surface and sidewall roughness lead to bulk and Rayleigh scattering, assisting with locking a free-running laser diode with a high-Q microresonator.

When laser light is coupled to WGM microresonator with the help of a prism, tapered fiber, or bus waveguide, a fraction of resonant light is scattered back to the laser due to internal and surface inhomogeneities leading to Rayleigh scattering. This fast optical feedback stabilizes the laser and improves its linewidth, as shown in the first study on a silica microsphere [151]. Similar

laser stabilization is performed using a fiber loop laser [153], and distributed feedback laser in conjunction with high-Q WGM microresonators [154]. An instantaneous linewidth of 200 Hz [95] and sub-Hz levels [154] for semiconductor lasers is achieved, showing improvement on a scale of $\sim 10^4$-10^7 (intrinsic linewidth $\sim$ MHz).

The main focus of all the studies mentioned above is stabilizing single-frequency lasers. Recently, a study utilizing a multi-frequency (FP) laser diode demonstrated a self-injection locking to the crystalline microresonator leading to linewidth improvement and single-frequency operation [98, 155]. In addition, self-injection-locking could lead to more power in the single-frequency mode. Indeed, this has been demonstrated by using a multi-frequency diode could even lead to optical frequency comb generation along with single-mode lasing in a crystalline microresonator [98]. However, due to prism/tapered fiber coupling, crystalline microresonators are unsuitable for photonic integration. In this regard, in the current study chapter 4, multi-frequency laser diode-based self-injection locking is implemented via a photonic integrated Si_3N_4 microresonator in collaboration with the Russian Quantum Center (RQC). This led to an electrically driven chip-based soliton microresonator source, paving the way for full integration as discussed in more detail (chapter 4). In parallel to our study, an electrically driven photonic integrated source based on on-chip vernier filters and gain chip (pump) is shown in Ref.[99].

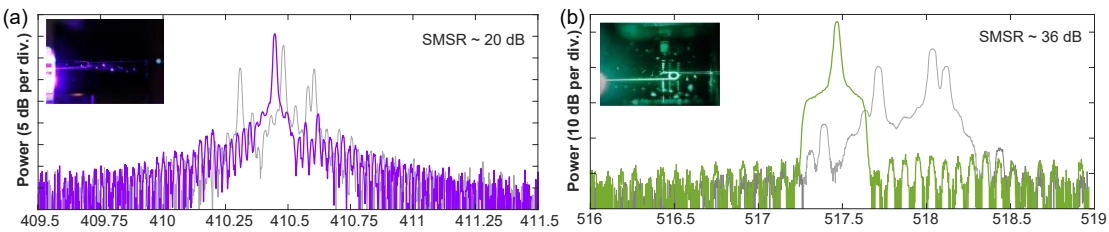

Figure 1.10: **Self-inejection locking based single mode laser at two different wavelengths. Figure adapted from [156]**. **a** Optical spectrum of free running laser (grey) multi-frequency laser diode and self-injection locked single mode lasing with 20 dB side mode suppression ratio (SMSR). A low loss Si_3N_4 based microresonator enables single-mode lasing via optical feedback. **b** Single-mode laser at 517 nm via self-locking to a Si_3N_4 microresonator.

The theoretical model describing a laser diode's locking/pulling effects in FP cavities is well established [146]. The analytical model describing the self-injection locking effect in microresonators' cavities is first reported in Ref. [157]. The model considers the FP laser cavity with two mirrors (input and output mirror) coupled to a microresonator with a certain back reflection constant. The time-dependent field inside the FP laser cavity is the sum of fields reflected from the cavity mirrors and the microresonator due to backscattering (Figure 1.9),

$$A(t)e^{i\varphi(t)} = iT_oB(t) + R_eR_oA\left(t-\tau_d\right)e^{i\omega\tau_d+2(\gamma-\alpha)L+i\varphi(t-\tau_d)} \tag{1.20}$$

Where $A(t)$ is the amplitude of the intra-cavity field of the laser, τ_d round trip time ($\tau_d = \frac{2nL}{c}$, laser cavity length: L), R_o & R_e are reflection coefficients of the laser cavity, T_o is transmission coefficient of output mirror, ω is instantaneous laser frequency, α is loss, and γ is gain coefficient.

While the field reflected from the microresonator is given by:

$$B(t) = \frac{iT_o}{R_o}\Gamma(\omega)A\left(t-\tau_s\right)e^{i\omega\tau_s+i\varphi(t-\tau_s)} \tag{1.21}$$

Where τ_s is the time for light to propagate from the laser cavity to the microresonator cavity and back to the laser, $\Gamma/2\pi$ is the reflection coefficient of the microresonator. By considering laser cavity resonance ($\omega_d\tau_d = 2\pi$ M, M is an integer) close to generation frequency, using Taylor expansion in Equation 1.20 and inserting Equation 1.21 leads to a set of equations similar to Lang-Kobayashi equations [158]:

$$\dot{A} = \left(\frac{g\left(|A|^2\right)}{2} - \frac{\kappa_d}{2}\right)A - \frac{\kappa_{do}}{R_o}|\Gamma(\omega)|A\left(t-\tau_s\right)\cos(\psi)$$

$$\dot{\varphi} = \alpha_g\frac{g\left(|A|^2\right)}{2} + (\omega-\omega_d) - \frac{\kappa_{do}}{R_o}|\Gamma(\omega)|\frac{A\left(t-\tau_s\right)}{A(t)}\sin(\psi).$$

Using the stationary value condition ($\dot{A} = \dot{\varphi} = 0, A\left(t-\tau_s\right) = A(t), \varphi\left(t-\tau_s\right) = \varphi(t), \psi = \arg(\Gamma) + \omega\tau_s$) lead to relation between generated laser frequency (ω) and laser cavity frequency (ω_d)

$$\omega - \bar{\omega}_d = |\Gamma(\omega)|\bar{\kappa}_{do}\sin\left(\psi - \arctan\left(\alpha_g\right)\right).$$

This relation provides an overview of how the generation frequency is linked to the reflection coefficient of the microresonator. By inserting the value of reflection co-efficient ($\Gamma(\omega)$) [109, 110] and using assumptions [157], a relation between free running and self-injection locked laser's linewidth is calculated which is given by,

$$\frac{\delta\omega}{\delta\omega_{\text{free}}} = \frac{Q_{\text{LD}}^2}{Q^2}\frac{\left(1+\beta^2\right)^4}{\left(1+{\alpha_g}^2\right)(8\eta\beta)^2}$$

Whereas $\delta\omega_{\text{free}}/2\pi$ is the linewidth of the free-running laser, $\delta\omega/2\pi$ is self-injection-locked laser linewidth, α_g is the linewidth enhancement factor, β is the normalized mode coupling rate (κ_C/κ) and Q_{LD} (Q) is the quality factor of the laser diode (microresonator). This result shows that the photonic integrated microresonators with a higher Q factor improve free-running (not locked) laser linewidth. Indeed, the recent implementation of self-injection-locking via low- and high-confinement Si_3N_4 microresonators with ultra-low propagation loss enables sub-Hz level linewidth on-chip lasers [37, 126], and more recent demonstration matches fiber laser performance [127]. Also, a heterogeneously integrated soliton microcomb based on Si_3N_4 microresonators and semiconductor lasers (InP/Si) module has been demonstrated recently [6]. In addition, the analytical description of self-injection-locking is extended to incorporate the nonlinear terms to better understand the soliton generation mechanism in recent studies [101, 100].

The other key advantage of self-injection locking is translating this effect to other spectral regions

where achieving single-mode lasing, or narrow linewidth is difficult, e.g., 400 nm (near UV), visible, and mid-infrared (mid-IR). A recent demonstration from our group extended the self-injection of multi-frequency laser to the near UV and green wavelength range [156] (Figure 1.10). Moreover, a similar demonstration is done at multiple wavelengths ranging from 400 to 780 nm by utilizing fast optical feedback [159]. Even a self-injection locked laser is shown in the mid-IR region around 3 μm ([160]), further indicating the potential of this scheme.

1.8 Integrated silicon nitride (Si_3N_4) microresonators

The current thesis study is primarily based on applications of the Si_3N_4 microresonators with a height ranging from 650 nm to 900 nm (Figure 1.11). The fabrication of Si_3N_4 is done and improved by my colleague Junqiu Liu during this study [27, 35]. These advances played a major role in performing multiple projects, such as self-injection locking and optical circuit switching. The samples in this study are fabricated using the photonic Damascene process with reflow. First, a 4-inch silicon substrate with 4 μm thick thermal wet SiO_2 cladding is used. Then, the substrate is coated with a deep-ultraviolet (DUV) photoresist, and microresonators and bus waveguides are patterned on the substrate via DUV stepper photolithography (248 nm KrF excimer laser). The pattern is then dry-etched into the SiO_2 cladding using $C_4H_8/O_2/He$ etchants to create waveguide preforms. Next, stoichiometric Si_3N_4 film is deposited on the patterned substrate via low-pressure chemical vapor deposition (LPCVD) to fill the waveguide preforms and to form the waveguide cores. Afterward, etch-back and chemical-mechanical polishing [28] is used to planarize the substrate and to remove excess Si_3N_4. The entire substrate is further annealed at 1200°C to remove the residual hydrogen content in Si_3N_4, to reduce hydrogen-induced absorption loss in Si_3N_4 waveguides. This high-temperature annealing is critical to fabricate low propagation losses waveguides at telecommunication bands around 1550 nm. Then top SiO_2 cladding is deposited before etching the chip for dicing via backside griding. More details about fabrication can be found in the following Refs [77, 27, 35].

1.8.1 Si_3N_4 photonic integrated circuit design

Photonic devices with a high index contrast, e.g., Si_3N_4 and Si, etc., have gained a lot of interest due to high confinement of the optical mode, CMOS fabrication compatibility (Si), compact size, and low losses at telecommunication band (Si_3N_4) [161, 59, 35, 36]. However, coupling light efficiently into this type of waveguide is still challenging. Different solutions have been proposed depending on operational requirements and fabrication processes. Broadband coupling is also critical for Si_3N_4 microresonators-based frequency comb generation. Higher coupling efficiency is needed to reduce the input power, especially for nonlinear processes, as power-efficient devices are important for next-generation photonic elements.

Mode Engineering: The main reasons behind coupling losses are mode mismatch, effective

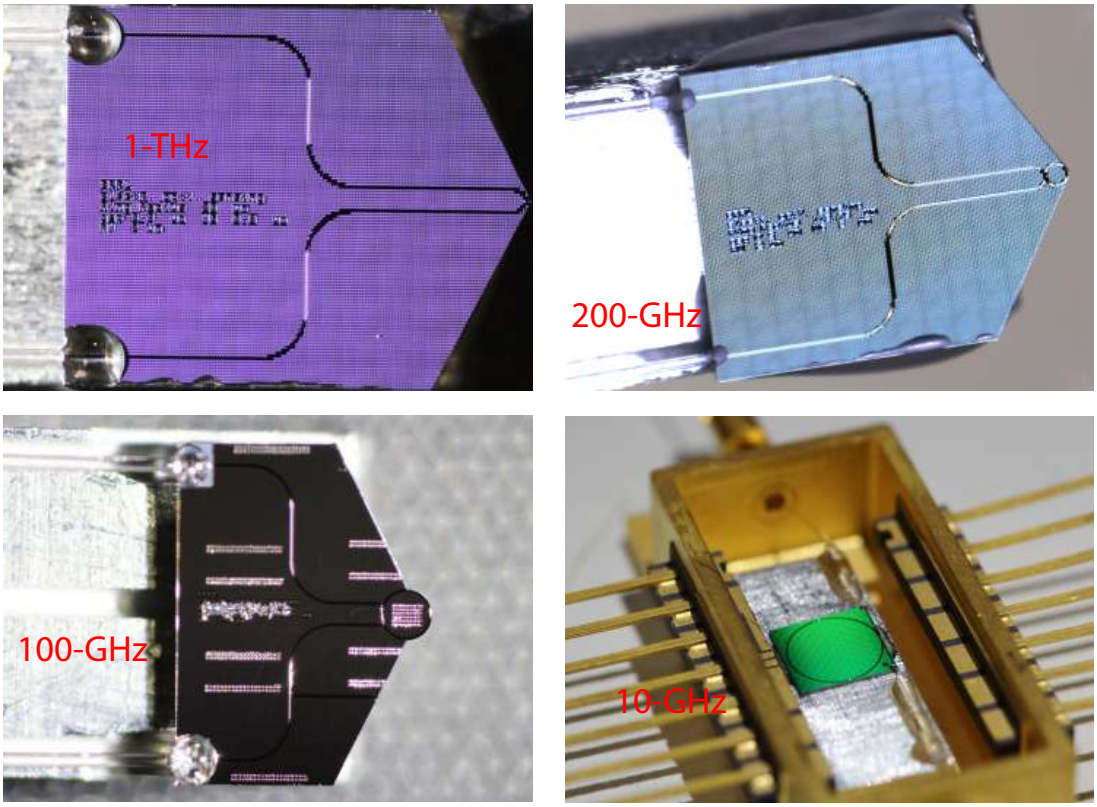

Figure 1.11: **Overview of the Si_3N_4 sample used in the thesis.** Images of four packaged devices with FSR ranging from 10 GHz to 1 THz are used for multiple projects to study the interaction of electrons with photons, data center optical circuit switching, and low-noise microwave generation. Image credit: Top left (Jijun He), Top right (A. Feist), and bottom right (E. Lucas).

index mismatch, and alignment tolerance. It is important to understand these issues to optimize coupling efficiency.

Mode mismatch is due to the different mode profiles of the waveguide (Figure 1.12 c, top inset) and coupling fiber (Figure 1.12 c, top inset). Coupling efficiency from the input mode to the waveguide mode can be computed using the orthogonality relation (scalar mode expansion) [162]:

$$\eta = \frac{\left|\int\int_{-\infty}^{\infty} \phi(x,y,0)\psi_0^*(x,y)dxdy\right|^2}{\left|\int\int_{-\infty}^{\infty} |\psi_0(x,y)|^2 dxdy \int\int_{-\infty}^{\infty} |\phi(x,y,0)|^2 dxdy\right|} \tag{1.22}$$

where ψ_0 represents the mode field of the waveguide and ϕ represents the excitation mode field. As shown in the numerator of Equation 1.22, efficient coupling is only possible when the incoming fiber mode completely overlaps with the waveguide mode. Due to the big difference in the waveguide and fiber modes, mode conversion is one key point to increase the coupling in well-confined waveguides.

Effective index mismatch is responsible for the back reflection of light as it travels from one medium to another. For example, while coupling, the light travels from the air (lensed fiber) or silica (butt coupling) to Si_3N_4, which causes back reflection loss. Effective index mismatch can be avoided by using an index-matching gel between the optical fiber and waveguide to reduce the index contrast. This loss can be calculated using Snell's law:

$$T = \frac{4n_1n_2}{(n_1 + n_2)^2} \tag{1.23}$$

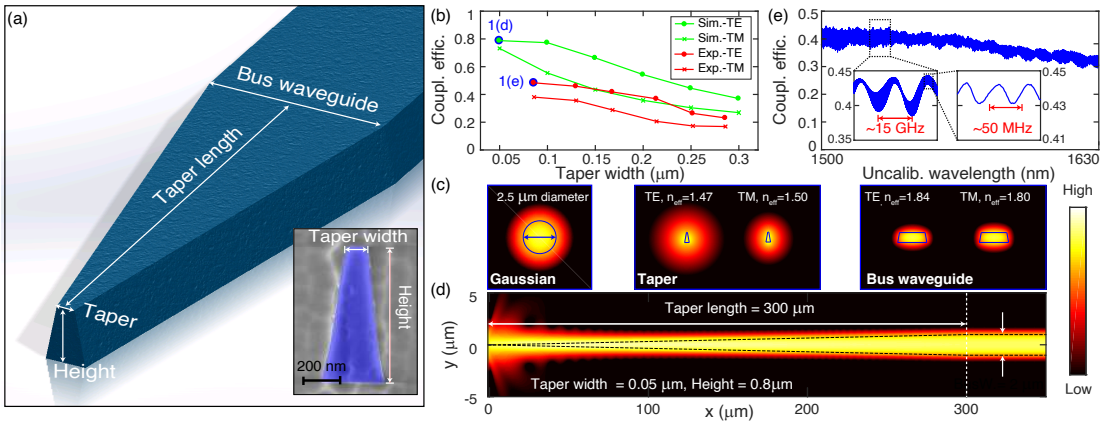

Figure 1.12: **Schematic, simulation and characterization of the regular 1D inverse tapers. a** Schematic of the 1D-taper. Inset: SEM image of the taper cross-section (Si_3N_4 is blue shaded) of 80 nm width and 820 nm height, at the chip facet, buried in SiO_2 cladding. The taper width is defined as the trapezoid's top side width. **b** Simulated coupling efficiency (including two chip facets) versus different taper widths for both the TE and TM polarizations (green), in comparison with the experimentally measured data (red). Blue-shaded data points are studied in more detail in (d) and (e). **c** Simulated mode profiles of the incident Gaussian mode, 0.1-μm-width taper's TE and TM modes, and 2-μm-width bus waveguide's TE and TM fundamental modes, to illustrate the taper's working mechanism as a mode transformer. n_{eff}: effective refractive index. **d** Simulated mode coupling profile in the case of ~80% coupling efficiency marked in (b). **e** Characterized coupling efficiency from 1500 to 1630 nm, of the taper marked in (b). Two Fabry-Perot interference patterns are observed. The ~15 GHz one is due to the reflection between two chip facets (5 mm cavity length), and the ~50 MHz one is likely due to the reflection between the input chip facet and the laser (2 m cavity length).

T is the transmission of normally incident light from the medium with a refractive index n_1 to the medium with a refractive index n_2. For light traveling from the air (n=1) to the Si_4N_3 (n=1.98) with normal incidence, 89% will be transmitted ignoring absorption, and 11% will be back-reflected at the interface of both mediums.

To improve the coupling efficiency mode, fabrication engineering can be implemented. Different methods have been reported to improve the coupling efficiency [16, 14, 15, 17]. Tapering of

waveguide [163], grating couplers [14, 15], prisms [164], and graded index couplers [165] are some of the commonly used techniques. One of the previously mentioned methods can be implemented depending on the requirements. A grating-assisted coupler, also known as a surface coupler, has a decent coupling efficiency of 60%, but the bandwidth is limited. Similarly, a prism coupler can achieve good coupling efficiency, but the operational bandwidth is limited. On the other hand, graded index couplers can have a broad operating bandwidth, but the coupling efficiency is low. Due to high coupling efficiency, easy fabrication, and high operational bandwidth, taper couplers are mainly used for mode conversion in Si_3N_4 for nonlinear conversion applications [166]. Perfect fiber alignment with the waveguide is also important, as misalignment can lead to losses. Misalignment loss is prominent in Si_3N_4 based waveguides as tolerance is less than 0.5 µm due to high index contrast. Coupling loss due to alignment is not critical for active alignment but can play a significant role in passive alignment, e.g., Si-photonic packaging.

The mode field diameter of lensed fiber at the focusing point is 3 µm ± 0.5 µm and the waveguide mode for Si_3N_4 waveguide having dimension 2 µm × 900 nm is approximately 1 µm. The mode field of the Si_3N_4 waveguide is increased using the inverse taper to attain optimum coupling efficiency. By decreasing the width of the waveguide, the mode is not well confined in the core and leaks out into the cladding; eventually making the mode field bigger (Figure 1.12,c). Adiabatic mode conversion requires proper simulation to calculate the taper width and length for adequate mode coupling to the waveguide. This work uses a commercial software package Lumerical [167] to conduct the simulations. Finite difference time domain (FDTD) [168] is a powerful and simple technique to solve the electromagnetic waves in the temporal domain using a central approximation. The basic working principle behind this technique is to discretize the Maxwell equations in space and time by a central approximation. This method can sweep a wide range of frequencies using a single run. This technique was first reported by Yee back in 1966 [169, 170].

Different geometrical structures are already defined in Lumerical. But, custom structures can be implemented using programming or importing the structures made in Solidworks [171] or GDS file. A linear taper waveguide (100 nm wide at chip edge) ensures an adiabatic mode conversion from input fact to Si_3N_4 waveguide with a dimension of 2µm × 790 nm (width × height). After defining the structure properties, the mesh region is defined along with the boundary condition, which in our case is PML. As in FDTD, resolving the magnetic/electric fields and the geometrical structure requires very fine meshing, which increases computational power. Artificial boundaries can be used depending on the waveguide's polarization and symmetry to reduce computational power and time. The source is defined by a Gaussian beam with a radius of 1.25 µm at 1550 nm as it is similar to a lensed fiber (1.25 ± 0.25 µm). Afterward, different monitors are placed in the simulation region to extract parameters such as transmission, power, and effective index in the specific region. Power coupled to the fundamental or specific modes can be calculated from mode projection. Lumerical implements the orthogonality relation to find the power from the total transmitted power in a specific mode. The total power and the power coupled to the

fundamental mode are given by [162]:

$$P_{\text{tot}} = \frac{1}{2}\int_{-\infty}^{\infty}\int_{-\infty}^{\infty} \text{Re}\left[\mathbf{E}(x,y,0)\times\mathbf{H}^*(x,y,0)\right] e_z dxdy \tag{1.24}$$

$$P_{\text{fund}} = |a_0|^2 \frac{1}{2}\int_{-\infty}^{\infty}\int_{-\infty}^{\infty} Re\left[E_0(x,y)\times H_0^*(x,y)\right] e_z dxdy \tag{1.25}$$

The amplitude of fundamental mode a_0 is calculated using the orthogonality relation:

$$a_0 = \frac{1}{P_0}\int_{-\infty}^{\infty}\int_{-\infty}^{\infty} \left(\mathbf{E}(x,y,0)\times H_0^*(x,y) + E_0^*(x,y)\times\mathbf{H}(x,y,0)\right) e_z dxdy \tag{1.26}$$

Besides this, the transmission or coupling efficiency can be calculated using $\eta = \frac{P_{fund}}{P_{tot}}$. Figure 1.12 b shows the simulated and measured transmission efficiency for different taper widths, following similar trends. The offset can be associated with slightly different mode field diameters of lensed fiber (± 0.5 µm) and not considering additional loss due to fiber connectors in calibration for this set of measurements. The optimum coupling can be achieved for taper width < 200 nm, which is difficult to achieve with a UV-stepper lithography instrument that can print a minimum feature size of ~ 225 nm or wider reliably. To optimize the coupling for the Si_3N_4 structure used in this study, a double inverse taper structure is implemented that allows the tapering of waveguides in both directions (height and width) (Figure 1.13 a,d). This unique structure is possible thanks to aspect-ratio-dependent etch (ARDE) of SiO_2 during preform step [27, 35, 77] (Figure 1.13 b). More importantly, the optimum coupling can be moved to a higher taper width, alleviating the need for a high-resolution lithographic instrument as shown in Figure 1.13 c.

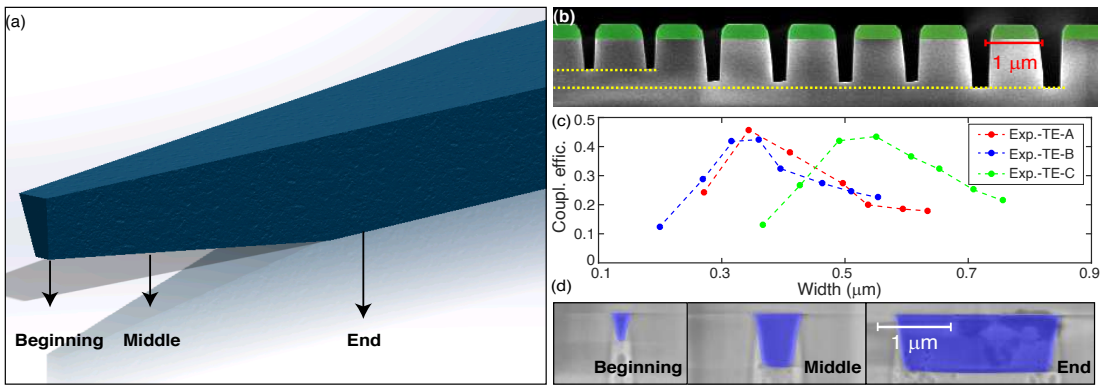

Figure 1.13: **Schematic and characterization of regular 2D inverse taper. a** Schematic of the 2D-taper. **b** SEM image of the ARDE effect on a SiO_2 substrate with Si etch mask (green shaded). The height varies depending on the trench width. **c** Measured coupling efficiency of 2D-taper chips at 1550 nm wavelength for both the TE polarizations for three different etching rates. **d** SEM images of the taper cross-sections (Si_3N_4 is blue shaded) at the taper beginning (chip facet side), middle, and end (bus waveguide side) are shown.

In addition to optimizing the transmission into a Si_3N_4 waveguide from an external source, FDTD-based (Lumerical) simulations are also used to calculate the coupling rate (κ_{ex}) [172]). Moreover, the broadband integrated dispersion (D_{int}) of a Si_3N_4 microresonator is calculated by using commercial software (COMSOL) via finite element method (FEM) simulation.

1.8.2 Experimental characterization of Si_3N_4 devices

Optical characterization is a crucial step in evaluating the performance of a single chip and the whole wafer consisting of more than 100 chips. Quick quantitative analysis of different optical parameters, i.e., coupling efficiency, Q – factor, and dispersion, is required to improve further the chip's performance by optimizing the design and the fabrication process [77, 27, 35]. The core idea behind the characterization of Si_3N_4 devices takes advantage of broadband spectroscopy via an optical frequency comb, as reported in Ref [114]. However, the characterizations scheme has been improved by Martin Pfeiffer [77], Junqiu Liu [115], and Johann Riemensberger [173].

A set of three external cavity diode lasers (ECDLs) capable of scanning from 1280 to 1630 nm is used to measure broadband transmission. Each laser has a 5-nm overlapping wavelength region allowing stitching of transmission spectrum, e.g., laser 1: 1355 nm to 1505 nm & laser 2: 1500 nm to 1630 nm [115]. The lasers are calibrated against a fiber mode-locked laser (after broadening via highly nonlinear fiber) and a 42 MHz fiber MZM interferometer. The absolute calibration is performed via gas cell spectroscopy [77]. The characterized data is analyzed using three models (normal Lorentzian, split mode [109, 110], and advanced split model [77]) explained in subsection 1.2.1.
Design of Si_3N_4: The silicon nitride samples are designed using a Python-based Gdspy module. The script was initially developed by Arne Kordts and later improved by Mikhail Churaev, Johann Riemensberger, and Junqiu Liu.

2 High-power, low-temperature, and vacuum-compatible optical packaging

This chapter provides an overview of packaging solutions built for multiple projects. In addition, it provides a summary of advances focused on improving the splicing loss of ultrahigh numerical aperture fiber (UHNA) with single-mode fiber (SMF, SMF-28) used for performing the packaging. The packaging protocols described in this chapter enable the demonstration of various applications, including wavelength switching for the data center [21], packaged-soliton module [20, 24], and electron-photon interaction (continuous wave (CW) [22], soliton [23]).

2.1 Introduction

Photonic integration has emerged quickly in the last two decades by replacing many conventional electronic technologies (optical communication and information technology). Efforts are being made in both industry [17], and academia [13] to tackle the packaging issues and to realize the practical use of photonic elements. Optical frequency comb generated from a microresonator covers a wide range of applications from astronomical spectrometer calibration [30, 85, 174] to molecular detection [175, 88]. But most applications are still in the research phase and demonstrated in laboratory environments. The problems discussed in this study differ slightly from conventional optical packaging issues and have not yet been completely explored in the industry. High input power up to 3 W, mode mismatch, and broadband coupling are the main challenges that must be surpassed. Improving the coupling efficiency is as important as maintaining it for a long time and at high power. In addition, quantum applications such as microwave to optical conversion [176] require operation at cryogenic temperatures (4-mK), making low-temperature compatible packaging solutions an important requirement. Moreover, fully packaged devices could potentially allow the interfacing of chip-scale devices to an instrument such as a transmission electron microscope (TEM) [177, 178], which remained out of reach due to restricted operation and size limitations. This interfacing allowed the demonstration of many new avenues of scientific and technical applications, discussed in more detail later [22, 106].

2.2 Levels of packaging

Photonic packaging usually consists of different single-chip to multi-chip integration levels, also known as an optoelectronics integrated circuit (OEIC). Integrating different optical elements on a single platform will reduce complexity and implementation on a wider scale. Photonic packaging can be divided into four levels as defined below [179]:

- Zero-level: Single-chip packaging
- First-level: One or more chips integrated into a module
- Second-level: From module to printed circuit board (PCB)
- Third-level: PCB to motherboard level

Currently, the main focus for multiple applications, such as optical transceivers inside data centers, requires third-level integration to meet future bandwidth and energy-efficiency requirements [180]. Moreover, integrating different materials via heterogeneous [181], or hybrid is vital for many applications, such as high data-rate transmission transceivers [182], frequency agile lasers [126], and fully integrated comb sources[19, 99, 101]. However, this work focuses on the zeroth level, also known as optical packaging (at the die level). This level serves as a basis for high-level packaging. Most of the fundamental challenges are explored and solved at this stage. The main difficulties while packaging a chip with dimensions 5mm x 5mm are the following:

- Optimum coupling via fiber and protection of the optical path
- Mechanical strength (fiber)
- Heat management due to operation at high input optical power
- Vacuum compatibility (dilution fridge and TEM)

2.3 Coupling via UHNA fiber

Due to the strong confinement of light in Si_3N_4 waveguides, coupling the light from a fiber into these waveguides is challenging. This is one of the main challenges for this project and the overall integration of different photonic elements. By improving coupling efficiency, the input power level required for nonlinear effects can be reduced, hence making packaging more feasible. Even after implementing mode engineering [16, 166], the maximum mode field diameter that allows efficient coupling is 3.5 to 4 µm (lensed or UHNA fiber); however, making misalignment tolerances in the order of less than 0.5 µm. This renders passive alignment difficult to use. Usually, active alignment is implemented to couple the light. Recently IBM Nano-photonics Packaging department demonstrated polymer-based adiabatic fiber coupling assembly [17] compatible with

the equipment used for microelectronics. Similarly, the Tyndall institute showed parallel planner fiber coupling using grating couplers, and direct integration of VSCELs on the chip using the flip chip method [13]. Many other techniques, such as interposer [183], photonic wire-bonding [184], lensed fiber, micro-optics lens array [102] etc., have been devised to address the coupling issues for different applications. Typically, lensed fibers with mode field diameter of 2 to 3 µm and a working distance of 16 to 20 µm are used to couple light to the chip. Alternatively, a chip-based mode converter fabricated via doping the silicon oxide can couple the light [1]. This work uses ultrahigh numerical aperture (UHNA) fiber from Nufern to couple the light into Si_3N_4 waveguides. Using UHNA is favorable due to the following:

- Splicing with the standard SMF-28
- Direct gluing of fiber to chip facet (butt coupling) as shown in Figure 2.1 b is possible
- No strict working distance requirement
- Cost effective as compared to lensed fiber

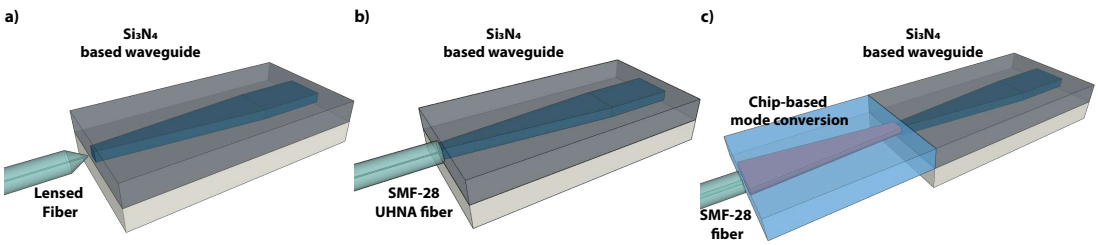

Figure 2.1: **Coupling to a high index contrast waveguide (Si_3N_4) using lensed, SMF-28, UHNA fiber, and an on-chip mode converter. a** Optimum working distance should be maintained, along with horizontal and vertical alignment for efficient coupling via lensed fiber. **b** Alternatively, a standard SMF or ultrahigh numerical aperture (UHNA) fibers can be used to couple the light by positioning them in close vicinity of the waveguide facet (butt coupling). UHNA fibers can be glued to the chip directly, providing a more convenient packaging solution. **c** On-chip mode converters based on low index contrast material (SiO_2)), thin Si_3N_4 (height ~ 100-300 nm) or polymer cladding can be used to couple light. These mode converters are commercially available.

Different UHNA fibers have been characterized to find an optimum packaging fiber and validate the mode conversion. A commercial beam profiler measures the fiber's mode profile and numerical aperture. A small piece of UHNA-7 fiber (2 cm) is spliced (Figure 2.4) with SMF-28. The UHNA-7 spliced fiber is placed at a pre-defined distance (~ 10-15 cm) from the beam profiler. Afterward, the beam profiler, attached to the moveable stage, is moved in small steps (~ 5 mm) to record the far field of fiber or waveguide mode. The far field measured at a pre-defined distance is fitted with a Gaussian function to extract full width at $\frac{1}{e^2}$ to calculate the effective numerical aperture (N.A.) or divergence angle. SMF's measured effective measured N.A. is around ~ 0.083,

matchings well with measured value [185] [1]. Similar measurements are performed on UHNA-3, UHNA-7, lensed fiber, SiO_2 doped mode converter, and Si_3N_4 waveguides with a cross-section of 250 nm × 700 nm to estimate the effective N.A (Figure 2.2). As evident from measurements, UHNA-7 fiber effective N.A. is close to Si_3N_4 waveguide compared with UHNA-3 fiber, making it an ideal candidate for packaging.

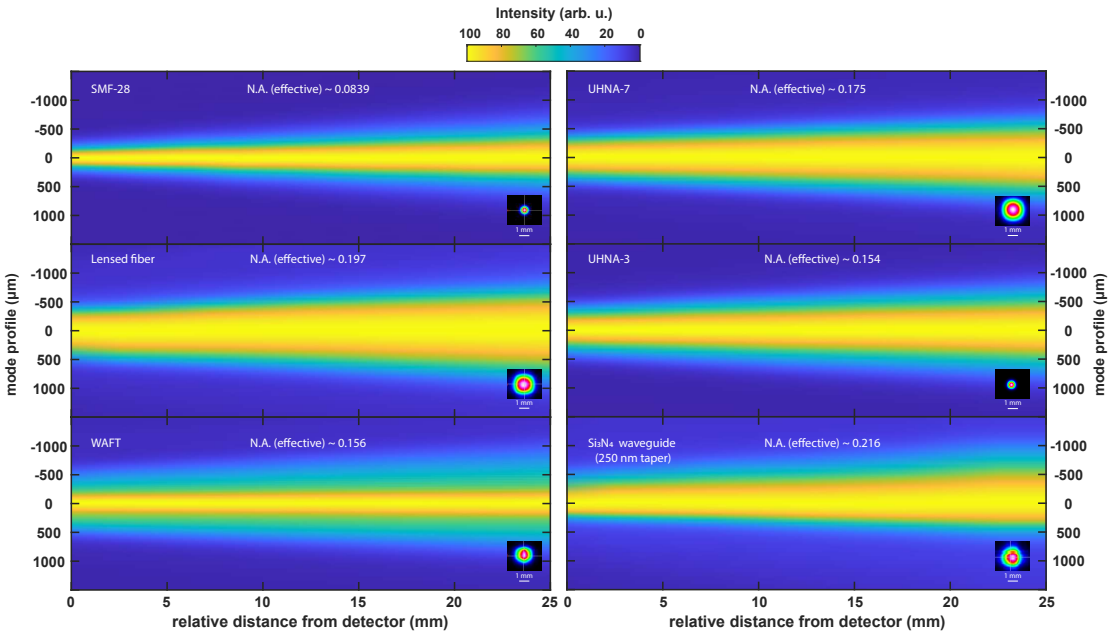

Figure 2.2: **Far-field mode profile imaging via beam profiler to estimate the effective numerical aperture (N.A.) of optical fibers**. Overview of effective N.A. measurements of SMF-28, Lensed fiber, UHNA-7, UHNA-3, and waveguides (Si_3N_4 and doped SiO_2 waveguide). These quantitative measurements provide insight into efficient external coupling from fiber to the photonic integrated chip (Si_3N_4).

The loss due to direct splicing or mode conversion from SMF to UHNA fiber can be calculated as shown in Equation 2.1. It is also essential to have a minimum splicing loss due to the spatial offset of the fiber cores, which might lead to the burning of the spliced region when operating at high input power (2-3.5 W).

$$L(\mathrm{dB}) = 20 \log \left[\frac{w_{\mathrm{smf}}^2 + w_{\mathrm{uhna}}^2}{2\, w_{\mathrm{smf}}\, w_{\mathrm{uhna}}} \right] \tag{2.1}$$

where ω_{smf} is the mode field radius of SMF and ω_{uhna} is the mode field radius of UHNA fiber. The loss from the above formula [186] considering direct (no adiabatic mode conversion) splice will be around 3 dB which implies that 50 to 60 % of input power will be lost while propagating from SMF to the UHNA7 fiber (Figure 2.3 d). Optimized splicing can be designed by looking at

[1] Effective N.A. (13.5 %) is different from nominal N.A. (1-5%) as specified by manufacturer

the structure of UHNA fiber [187] to perform adiabatic mode conversion (Figure 2.3 a (bottom inset)). The UHNA fiber is a double-clad fiber having a core diameter of 1.8 µm. The core is made of germanosilicate to increase the refractive index. In contrast, the outer core (inner cladding) is made of fluorosilicate and has a refractive index slightly lower than the core region. The outer cladding is silica and has a lower refractive index than the inner cladding. Using this geometry, the mode can be confined well inside the core compared to the conventional SMF. During splicing, the generated heat spreads fluorine into the core part, which is doped with germanium. Moreover, germanium diffuses out to the inner cladding making it compatible with low N.A. fibers by matching mode field diameter (allowing adiabatic mode conversion). Two splicing methods are used to reduce the splicing loss below <0.1 dB as part of the packaging project in the current study.

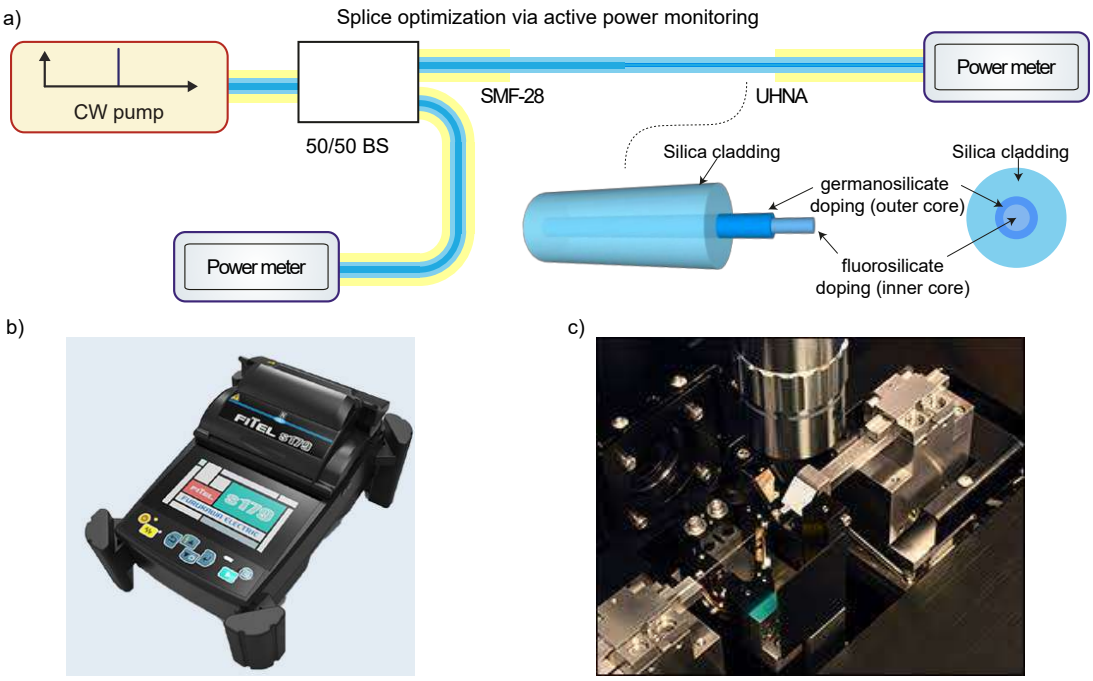

Figure 2.3: **The active monitoring of power during the splicing process to optimize the splicing loss. a** Experimental setup used to optimize the splicing mechanism for both instruments, standard splicer **b)** and vytran **c)**. images adapted from [188, 189]. The inset in **a)** shows the structure of the UHNA fiber, which consists of two cores and one cladding.

2.4 Standard splicer

A standard fiber fusion splicer uses the principle of electric discharge to generate heat to fuse the bare glass (without polymer coating) fiber (Figure 2.4 d). Generally, fusing similar fibers or fibers with the same mode field diameters requires a single arc to melt the fibers' ends and subsequently merge them. While splicing fibers with different mode field diameters requires

multiple arcs, in order of 1 to 3 seconds, for thermal diffusion. Multiple arcs also help in reducing the tension during splicing [190]. By optimizing the different parameters, such as the number of arcs, power of arc, and duration of the arc, the splicing loss can be improved [2]. Generally, the splicing algorithm used is based on two major steps. First, joining two fibers (SMF and UHNA) by melting the fibers' end at predefined arc power as shown in Figure 2.4 d. The splicing loss till this step is around 1-2 dB as mode conversion is not adiabatic (Equation 2.1). In the second step, multiple arcs (re-arc) are applied to reshape the inner/outer core of UHNA fiber via heat diffusion for adiabatic mode conversion. Observing optical power during splicing is important to find the optimum re-arc power and duration (Figure 2.3 a). The higher re-arc power and longer duration could taper the fiber shape at the splicing region, leading to higher splicing loss or damaged fiber. This instrument (Figure 2.3 b) reduces the splicing loss to 0.2 to 0.4 dB deterministically.

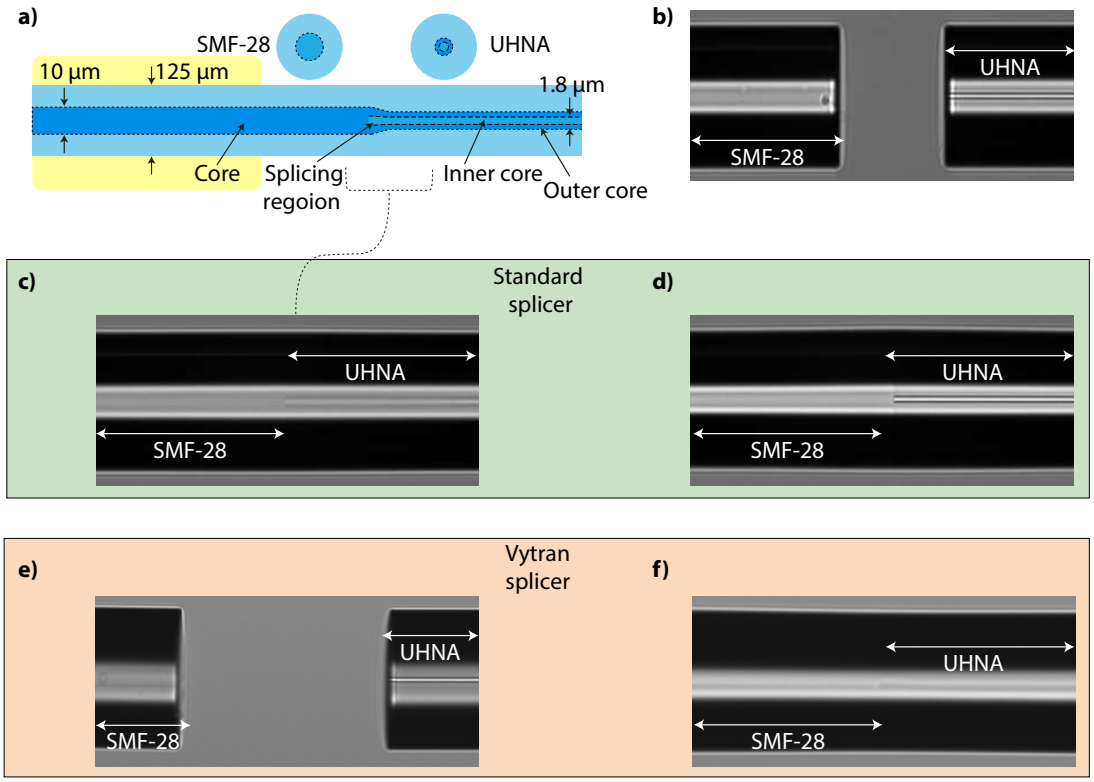

Figure 2.4: **Direct splicing of SMF and UHNA fiber for mode conversion. a** Direct splicing introduces some losses, and a special multi arcs program is used to introduce a tapered region for adiabatic mode conversion (see splicing region). **b** The core diameter of both fibers differs by more than 7 µm, as seen in the microscope images inside the splicer. **c** In this figure, the taper is not visible at the splicing interface for adiabatic mode conversion, but an experimentally low loss is observed. **d** A spliced fiber without using a multiarc program leads to higher loss (2 to 3 dB). **e, f** The images are taken when splicing fibers (SMF and UHNA) using a vytran splicer.

[2] A special thanks to Simon Hönl (IBM) for useful discussion to assist with programming

2.5 Vytran splicer

To further improve the splicing loss (< 0.1 dB), a special splicing instrument based on filament fusion, known as a vytran splicer, is used. The key parameters linked to splicing loss are filament power, on-duration, and fire polishing (duration and area covered). Fire polishing is the key aspect that separates vytran from the standard splicer to push the splicing loss down to 0.03 dB. The main reason is that the stage linked to the filament moves across spliced fiber, leading to thermal diffusion in the larger part of UHNA fiber. As shown in Figure 2.3 a, an optical setup is used to optimize the splicing loss with active power monitoring. For most of UHNA-7-SMF fiber splicing, the arc duration on time is kept around 90 seconds. The filament on-duration could be reduced by increasing the filament power or reducing the distance between filament and fibers (which effectively means higher power). However, it is found that 90 seconds on duration led to higher yield than other lesser on-durations (higher filament power). More importantly, the fire polishing power is kept higher than the first-stage filament power, as it led to lower losses. The filament power, on-duration, and fire polishing are optimized for each fiber UHNA-1, UHNA-3, and UHNA-7 as these fibers are based on different core compositions and hence have different thermal diffusion properties.

Generally, for prototyping the packaging procedure, a standard splicer (Figure 2.3 b) is used, while for actual experiments vytran special (Figure 2.3 b) splicer is implemented to minimize the coupling losses.

2.6 Optical adhesive

The next step is to find an appropriate epoxy which is critical for gluing the fibers. Gluing is preferred as it is easy to handle in comparison to solutions like direct fusion [104] and laser welding [103, 105], which require a high power CO_2 laser. But there are some disadvantages of glue. As most of the optical glues are polymer based, they have a coefficient of thermal expansion higher than glass (SiO_2) which becomes crucial at high power and can lead to misalignment of the fiber. Moreover, CTE mismatch becomes even more critical for low-temperature packaging as different CTEs lead to loss of adhesion. A proper balance of the different properties of optical adhesive is required for optimum results. Some properties of optical adhesives or epoxies are the following [191]:

- **Viscosity**: Viscosity is defined as resistance to fluid flow and is usually expressed in centipoise (cps). Low-viscosity adhesives have a low resistance to flow and are easy to dispense but difficult to handle. Medium viscosity glue (transparent [3]) is easy to dispense, flows quickly, and also has high transmission. At the same time, high-viscosity glue (opaque) is difficult to dispense and transmission is also low.
- **Coefficient of Thermal Expansion (CTE)**: Temperature increase results in the expansion

[3] Based on the epoxies used in this study

of not only adhesive but all materials. It is crucial as a significant mismatch of CTE between two materials can lead to cracking when the temperature increases. The CTE of silica is approximately 7 ppm/K, while epoxies have a typical CTE of approximately 40-125 ppm/K. This CTE mismatch must be kept low to avoid any cracks at the adhesion point due to operation at high power.

- **Linear Shrinkage**: Describes how much the epoxy will shrink after UV or thermal curing. This parameter is also kept as low as possible to avoid any coupling losses due to shrinkage, which leads to the misalignment of fibers from the optimum coupling. The best achievable value for linear shrinkage is around 0.1 % to 0.3 % which means the material will shrink 0.1 % to 0.3 % of its original length.

- **Refractive Index**: The refractive index of epoxy also plays a significant role as it can act as an index-matching gel when dispensed between the fiber and the waveguide. The refractive index of optical epoxies ranges from 1.4 to 1.6, closer to silica (index-matching gel).

- **Transmission**: Light transmission through these adhesives for optical packaging is important. Most of the optical adhesives (low to medium viscous) are transparent, having transmission of more than 96 % in the broad spectrum range covering 600 to 2000 nm.

- **Curing**: Optical epoxies are usually cured thermally or using a UV light. Thermal curing is unsuitable as active alignment is required during curing, and it is difficult to increase or decrease the temperature quickly. UV light curing is preferred as active alignment can be performed during the curing process, and the intensity of UV light can be changed easily to control the curing process.

- **Shelf life (not UV cured)**: This is the lifetime of epoxy before it expires or different parameters like refractive index and viscosity change. Storing epoxies at specified temperatures is essential as some epoxies have more lifetime at low temperatures while others can easily survive at room temperature. Usually, epoxy's lifetime is around 6 to 12 months.

- **Storage modulus**: This particular property of the epoxy measured its stiffness. It is extremely important for low temperature (≈ 4-Kelvin or lower) compatible optical packaging. The lower the storage modulus (200,000-300,000 psi), the better it is suited to low-temperature compatible packaging.

2.7 Dispensing valve system

A very precise system is required to dispense epoxy with accuracy in the µm range (dispensing). For this purpose, a microdot dispensing valve, as shown in Figure 2.5, is used based on pneumatic valve actuators. Air pressure is applied on the piston to move the piston stem linearly, controlling the valve needle's opening and closing. Air pressure to the piston is controlled via an electronic

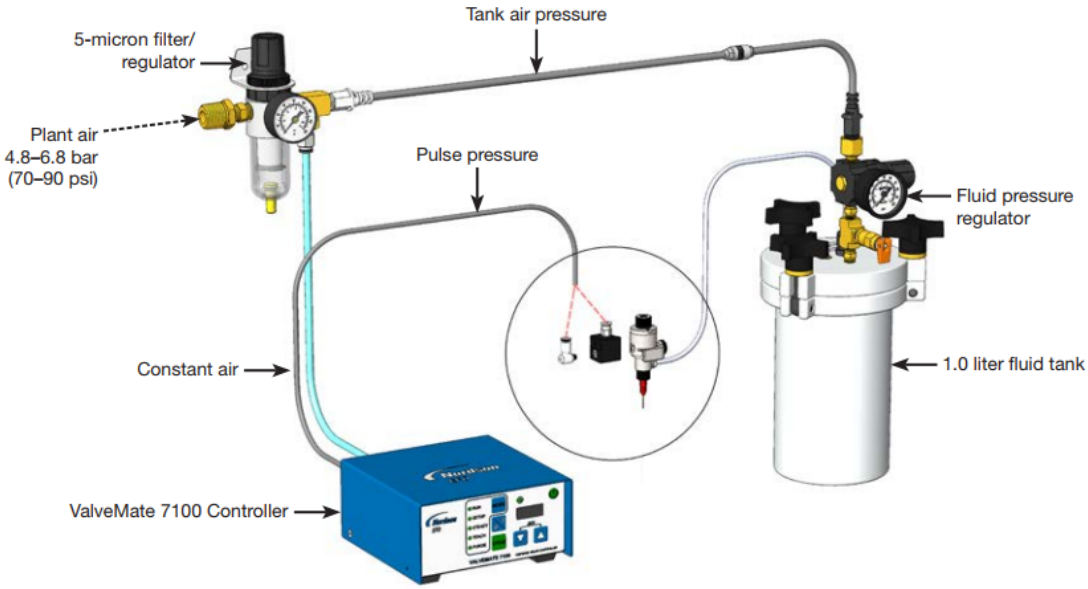

Figure 2.5: **The working principle of the dispensing valve.** Air pressure is used to control the glue as well as the opening of the valve piston via an electronic controller unit. A 10cc opaque epoxy barrel stores the epoxy, and air pressure forces the glue inside the valve during operation. The needle size, the viscosity of the glue, and air pressure control the drop size. Two regulators are used to maintain air pressure for precise dispensing. Figure adapted from [192].

controller for a defined amount of time. The epoxy is placed inside the high-pressure opaque 3cc syringe barrel. Air pressure is also used to push the glue inside the valve during operation. Depending upon the requirement, different needles can be used, e.g., for high viscosity, it is better to use a needle with a big opening as a small needle will clog. In contrast, a small needle should be preferred for low viscosity, enabling precise drop size control. An optimal drop size can be achieved by choosing appropriate combinations of syringe size, glue viscosity, air pressure, and valve opening time, as shown in Figure 2.6. The amount of glue at the adhesion point of the fiber and chip can be changed by changing the dispensing positions. It is also important that the drop size is repeatable, as observed during the experiment, and the deviation is very small.

2.8 Optical packaging setup

An optical setup has been designed and implemented in order to carry out the optical packaging experiment as shown in Figure 2.7. The optical setup consists of an external cavity diode laser (ECDL) laser with an operating range from 1500 nm to 1630 nm, split by a 3 dB splitter. The output from port 1 of the splitter is used to monitor the input light coupled to the chip, and another port is used to couple the light into the chip. A polarization controller is used to optimize the coupling of the TE mode family, which is more relevant for pumping the chip at high power for nonlinear frequency conversion. A special stage has been designed to hold the sample. The

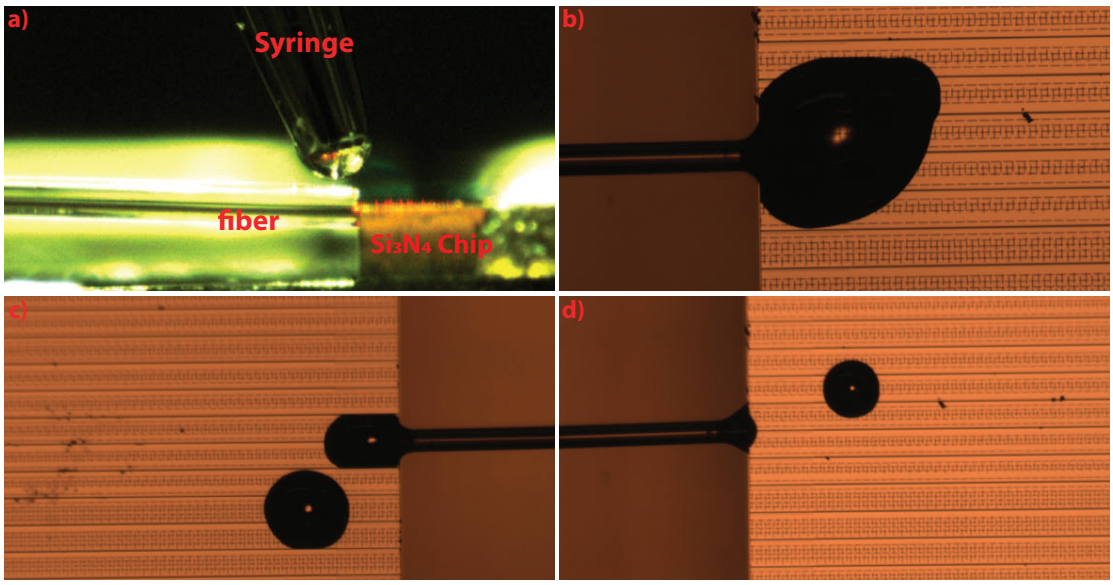

Figure 2.6: **Different dispensed glue dots deposited on the chip facet and butt coupled fiber. a** The camera image is taken just before dispensing the epoxy. The syringe is placed in the closed vicinity of the fiber and chip, requiring a -scale resolution stage to avoid damage to the chip/fiber. As shown in **c** and **d**, the amount of medium viscous glue to join the fiber and chip facet can be changed depending on the dispensing position. **b** A big drop of dispensed glue as compared to **c** and **d** is achieved by using low viscous glue.

sample holder is connected to the vacuum pump to hold the sample firmly during the packaging process, as it is critical to keep the sample in a stable position. A power meter monitors the power on the output side while coupling the light. The dispensing valve is mounted on a 3-axis motorized mechanical stage with sub-micron resolution. It is critical to control valve movement when the needle is very close to the fiber, as it can damage the fiber or chip facet (Figure 2.6, a). As the dispensing valve is placed right above the chip, it is difficult to use the top camera to see the chip while dispensing the glue. For dispensing the glue, a separate camera is installed at around 45 degrees to keep track of the needle when it is close to the optical fiber (Figure 2.6 a). The purpose of the top camera is to align the fibers actively while coupling the light before dispensing the glue. For active alignment, normal Thorlab Nanomax mechanical stages have been used. For curing the glue, a UV lamp is used, and the intensity of UV light can be tuned by changing the current.

Table 2.1: Initial experimental results (optical epoxies)

No.	Viscosity	Handling	T in VIS – IR	CTE mismatch	Linear Shrinkage
Dymax OP-67-LS	High	Very difficult	Bad	Medium	Very low
OG-142, OG-154-1 and OG-198-55 (Epotek)	Medium	Easy	Good	High	Low
NOA81 (Norland)	Low	Difficult	Good	High	High

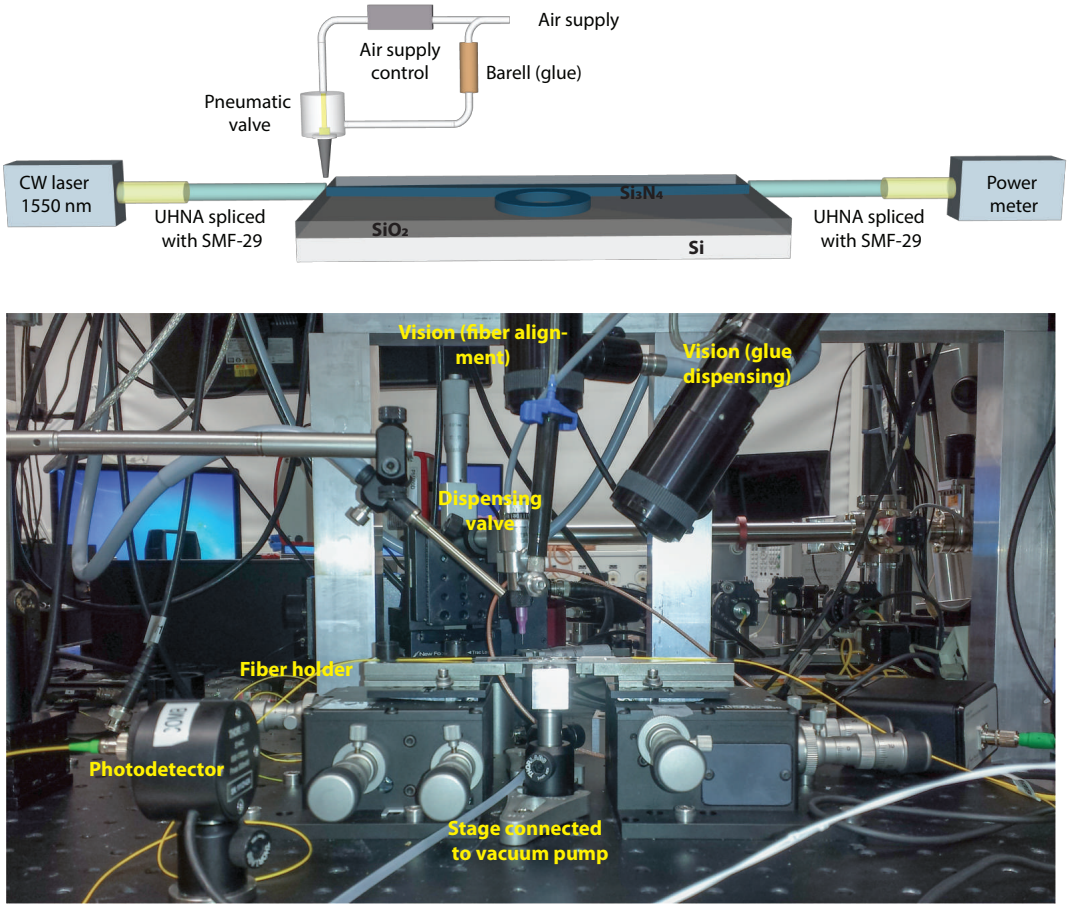

Figure 2.7: **An optical setup for packaging of the** Si_3N_4 **microresonators.** An external cavity diode laser (ECDL) is used to couple the light into the chip. A polarization controller optimizes the TE polarization before active alignment. The chip is placed on a specially designed sample holder for better stability during the experiment. UV light is used to cure the glue after dispensing. An extra camera is placed at approximately 45 degrees for better vision while dispensing.

Different glues have been tested on straight waveguides to find the best glue that can handle high power and shrinks less during and after curing. Their performance is compared by checking coupling stability for a long time (20-30 hours). High-viscosity glue usually has low shrinkage and CTE mismatch and is ideal for our experiment. Still, it is difficult to handle this type of glue due to clogging inside the valve and very low transmission (impact only if the glue comes in the path of light). The initial experiments used low and medium-viscosity epoxies with high transmission in the VIS – NIR – IR range. Initial measurements are summarized in Table 2.1.

2.9 Packaging procedure

The packaging steps can be summarized in the following steps (Figure 2.8):

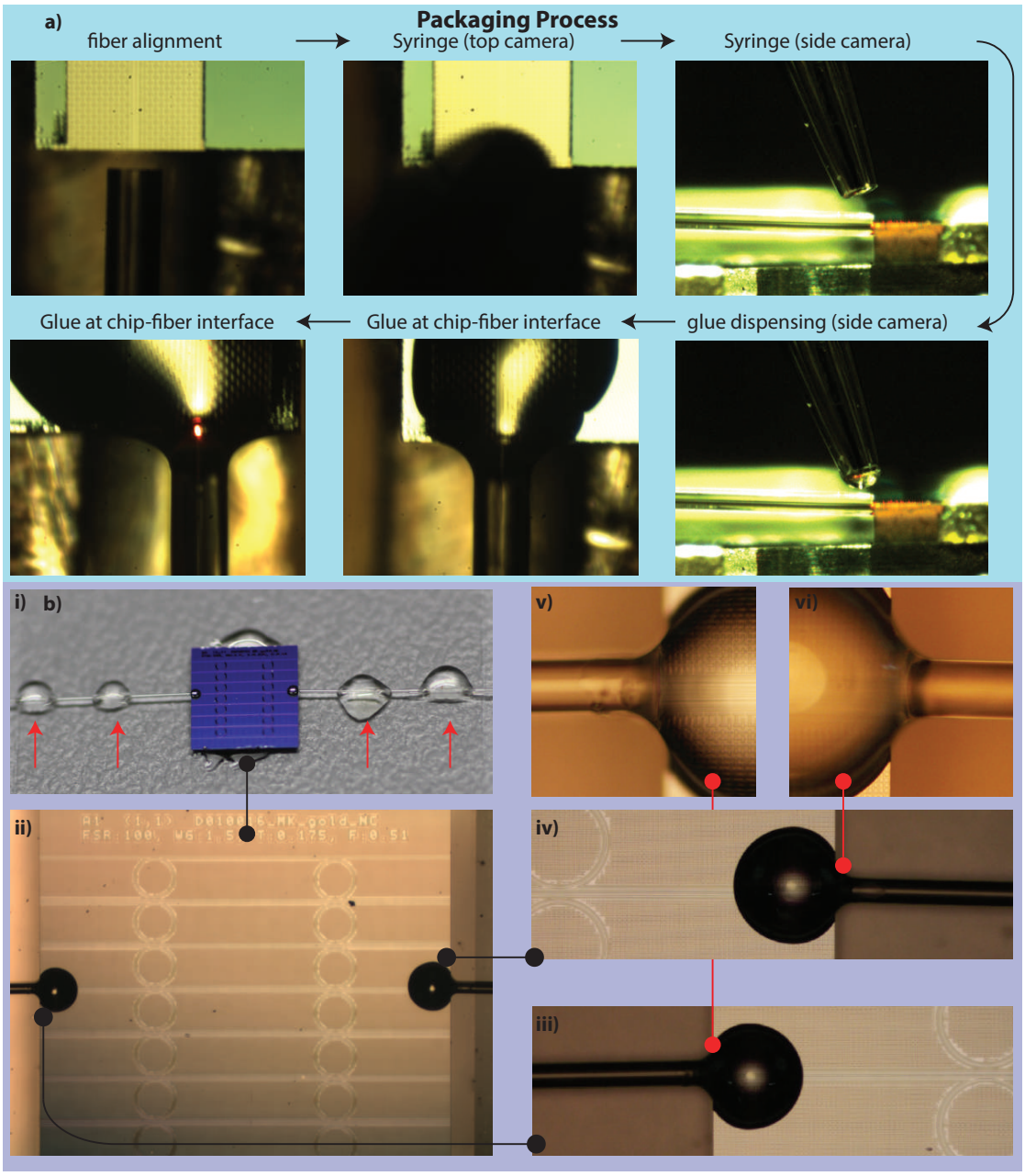

Figure 2.8: **Overview of the packaging process based on fiber alignment, glue dispensing, and curing. a** first step requires the alignment of optical fiber via the top camera. After coupling alignment, the dispensing valve is aligned via a motorized stage and side camera. Then a drop of glue is dispensed, which sometimes leads to fiber drift and requires realignment. After realignment, if required, the epoxy is cured via UV light. **b** Optically packaged chip on glass substrate using UHNA fibers. Microscope image of the packaged chip (ii), fiber-chip interface (iii, iv), and zoomed-in view of glue drop (v, vi).

- Characterization of chips using the setup mentioned in subsection 1.8.2 [115, 173] and selection of proper chips and waveguides.

- Gluing the chip to glass, Aluminum (Al), and Copper (Cu) substrate with dimension 22 mm x 22 mm. This provides mechanical stability to the chip and the fibers after packaging. Different mounts have been used depending on the projects' requirements, e.g., a Cu mount is preferred for low-temperature experiments. Similarly, different glues are used to attach the chip to the substrate, e.g., chip interfacing inside the TEM requires a special silver paste to reduce the charging (chapter 7, Figure 7.1).

- The SMF is directly spliced with UHNA3 fiber using a special program in the splicing machine to minimize loss during mode conversion. The size of UHNA fiber after the splice region is kept short so that it can be directly glued to the glass substrate away from the chip facet for compactness. This will provide the advantage of not having the spliced region outside the packaged device in a fiber sleeve. Keeping the small UHNA fiber enables polarization-maintaining packaging devices (see section 2.12).

- Fibers and chips on the glass substrate are carefully placed on the setup. The vacuum pump is turned on to hold the sample firmly.

- Initially, a fiber can be aligned near the chip facet using a visible alignment laser. Afterward, the coupling is optimized by actively aligning the fiber. A polarization controller optimizes TE polarization (Figure 2.8 a).

- Once the fibers are perfectly aligned, the dispensing valve dispenses the epoxy to the left facet of the chip. An appropriate time for valve opening and the air pressure is adjusted for specific drop sizes. It is important to keep the drop size as small as possible near the facet for better results (Figure 2.8 a).

- Most of the time, after dispensing the drop at the chip-fiber interface, the coupling changes due to misalignment. This requires again realignment of fiber actively. The key step here is to ensure that the fiber touches the chip facet so that it does not move while curing.

- UV light having 365 nm is used to cure the glue. UV lamp with set intensity levels at 100 $mWcm^{-2}$, 200 $mWcm^{-2}$ and 284 $mWcm^{-2}$ is used to cure for 1 min, 1 min, and 2 min respectively. If the epoxy is directly cured at maximum intensity, this may cause abrupt changes in fiber position due to shrinkage and lower coupling efficiency.

- Then, a single drop is dispensed on the right side, away from the chip facet, to hold the fiber in a stable position as the fiber glued to the chip is very fragile (Figure 2.8 b, i, red arrow).

- The last three steps are repeated for gluing the right side of the chip facet to the fiber.

- Afterward, the fiber clamps are removed (strain relief), and the glue is exposed to UV light for more than 120 minutes for shadow curing.

- Automatic monitoring of coupling efficiency as complete curing takes up to 24 hours.

2.10 Straight waveguide packaging

A straight waveguide has been packaged using the method described in section 2.9. The reason for packaging a straight waveguide is to compare the performance of different glues at low and high power. Initial study about epoxy mentioned in Table 2.1 showed that medium viscosity epoxies are good for packaging. The next step is to find an optimum epoxy that can be used throughout the project from a group of medium-viscous epoxies. It is critical to characterize the devices before packaging and only package better-performing chips to compare performance properly. It should also be considered that coupling efficiency with the UHNA and the lensed fiber can not be the same as they have different mode field diameters (Figure 2.2). The first tests will act as a benchmark to evaluate the performance of the packaged device. Chips containing straight waveguides are characterized, and the best-performing chips are selected for packaging. At this point, the selection criterion are restricted to coupling efficiency. Dimension of the packaged device as shown in Figure 2.9 a) initial taper width 230 nm and waveguide width is 2.1 µm (Chip A[4]) b) initial taper width 200 nm and waveguide width 2.1 µm (Chip B[5]) and height of both waveguides is 790 nm. Dispensed epoxy drop size is important near the chip, but not away from the chip, relieving strain and providing mechanical stability to the fiber (Figure 2.9, Figure 2.8 b (i, red arrows)). Some initial observations are the following:

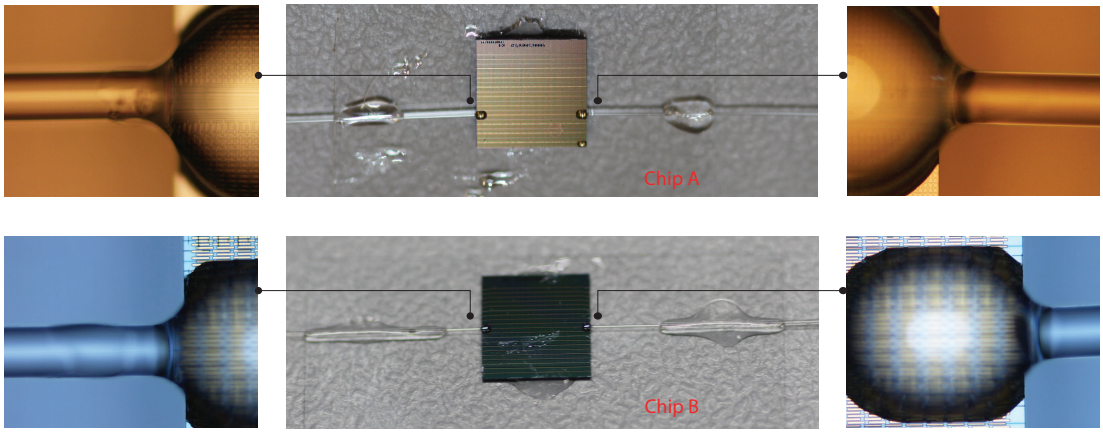

Figure 2.9: **Two packaged straight waveguides to find the optimum packaging glue and observe the coupling efficiency.** The magnified view shows the area covered by glue to join the chip facet with the UHNA fiber. The amount of glue should be kept small for better performance. Some degradation in coupling efficiency is observed due to the low transmission of glue in the path of light and stress leading to misalignment. Both chips were glued to the glass substrate. The epoxy used to protect fiber far away from the chip facet covers a bigger region in chip B than in chip A. This is due to the lower viscosity of OG-142 (15,000 cps) compared to OG-154 (36,00 cps), leading to the easy flow of epoxy on the glass substrates.

- Minimal glue drop should be dispensed to maintain coupling efficiency during UV curing

[4]glue used: OG-154-1
[5]glue used: OG-142

- Glue dispensing leads to slightly better coupling in comparison to without glue on the fiber-chip interface due to index matching (without curing)
- As curing takes up to 24 hours, within this period, the performance of epoxy can be estimated (Figure 2.10)
- It is important to monitor the coupling efficiency variation while performing the UV curing. In case of a sudden change in the coupling efficiency, UV curing must be stopped until the coupling efficiency stabilizes
- Coupling efficiency varies more (2 to 3 %) in the initial 24 hours due to the refractive index change of epoxy. Also, linear shrinkage (strain) shifts the fiber away from the optimum coupling point
- The coupling is stable after 24 hours of UV curing (Figure 2.10 c)

A 2-4 % coupling loss is observed after packaging due to glue dispensing and post-curing. Moreover, the epoxy can act as an index-matching material leading to higher coupling and reduced back-reflection due to index mismatch. The coupling efficiency of chip A with the lensed fibers is 22% (before gluing), while after the epoxy dispensing, the coupling efficiency is approximately 18.5%. Chip B coupling efficiency with the lensed fibers is 19% (before gluing), and after packaging, the coupling efficiency is approximately 17 %. Two different epoxies have been used for chip packaging. Initial coupling efficiency degradation is the same after UV cure, which is usually done in steps of 5 minutes. The coupling stability during post-UV curing tells whether the glue is useful for packaging. As shown in Figure 2.10 the decrease in the coupling efficiency of the chips is different in both chips. For chip A, input power, output power, and coupling were 217W, 55 W, and 22%, respectively. Chip B had a coupling efficiency of 17% with input and output power around 241 W and 43.14 W, respectively. As stated earlier, UV curing takes up to 24 hours, as shown in Figure 2.10, during which the coupling efficiency changes. The behavior of the packaged device is stable for 30 hours after UV curing, which can be seen in Figure 2.10 c. At the same time, a chip with a bad fiber-chip epoxy interface could lead to fluctuating output coupling even though coupling seems stable during the curing (Figure 2.11). Bad chip packaging could happen due to the following reasons:

- One main reason for bad optical packaging is expired or bad epoxy. Even though the shelf life of most of the epoxy used in this study is one year at 5 °C. The lifetime varies for different epoxies once exposed to room temperature for a longer time, and it is difficult to predict the exact lifetime. But, throughout this study, a generic lifetime is established (OG-154: 1-1.5 weeks, OG-142: 3 to 4 weeks).
- The proper cleaning of the dispensing valve after changing the epoxy is necessary. If not done properly, this could lead to intermixing new epoxy with old epoxy. Current cleaning protocols are the following: first, sonicating the valve with acetone for 10 (20) minutes for

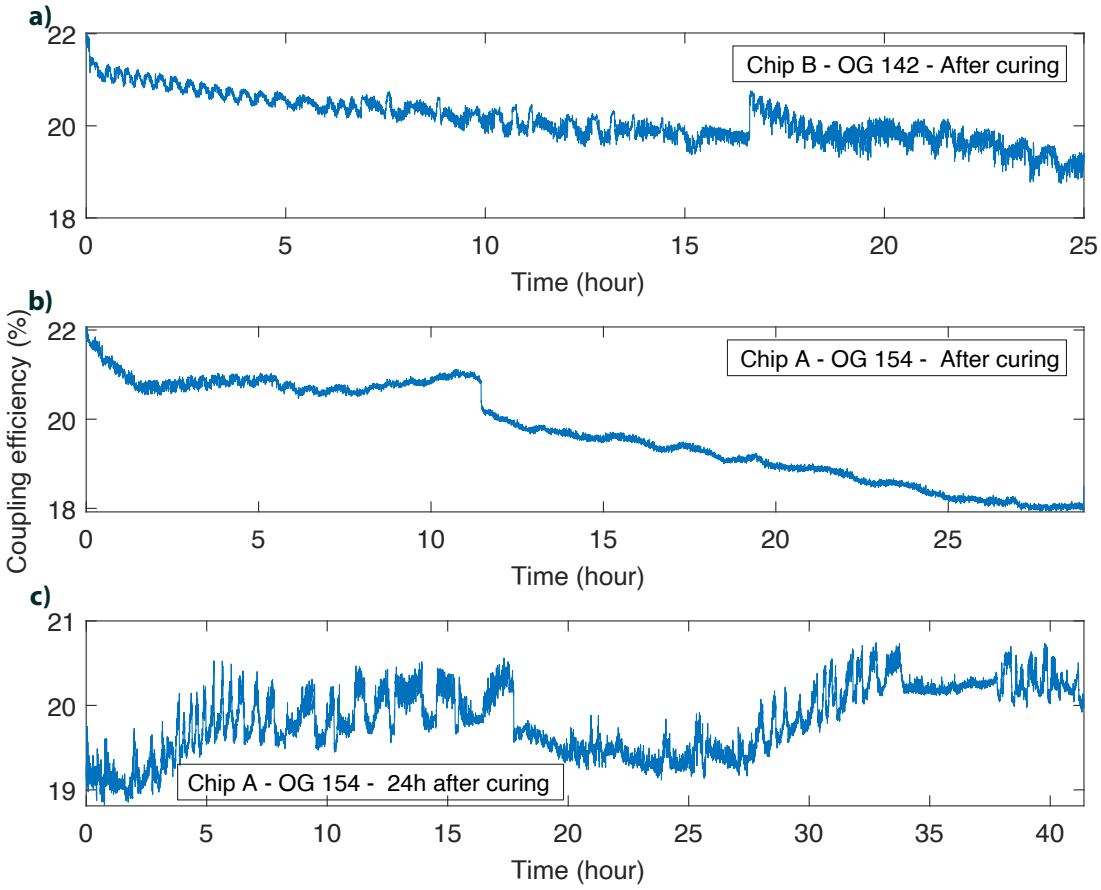

Figure 2.10: **The post-curing coupling monitoring of packaged chips.** The coupling efficiency of both chips degrades (2-3 %) during the initial 24 hours (**a & b**). This coupling drift comes from stress on fiber due to cured epoxy or changes in epoxy properties post-curing. **c** The packaged chip coupling stabilizes after 24 hours of epoxy curing. The fluctuations in output power follow the changes in input power (Figure C.2).

low (high) viscous epoxy and then performing the second sonication using isopropanol for 5 minutes. After sonication, the dispensing is dried thoroughly to ensure the remaining isopropanol does not mix with fresh epoxy.

- When a drop of epoxy is dispensed on the fiber-chip interface after active alignment. Most of the time, a drift of fiber from the optimum butt-coupling position takes place and hence requires realignment while epoxy is present on the fiber-chip interface. Sometimes, predicting whether fiber is touching the chip facet is difficult. Resistance to medium viscous epoxy can be misunderstood as a sign of fiber touching the facet. Moreover, if the fiber facet is not cleaved at 90 degrees (flat cleaved), this issue can persist when epoxy is present, leading to a worse vision for active alignment.

The same characterizations have been performed on the same glues with different chips to verify

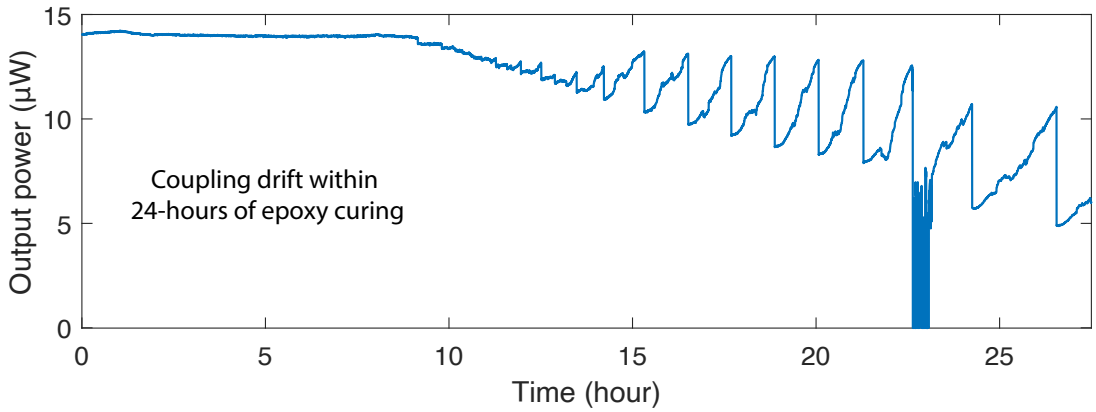

Figure 2.11: **The post-curing coupling monitoring of chip with bad fiber packaging.** The coupling seems stable till ~ 9 hours (after epoxy curing), and later coupling is degraded in small steps. This could arise due to multiple reasons, such as the utilization of expired epoxy, fiber not attached to the chip facet (free to move), and fiber pushed strongly against the chip facet leading to tension before curing. (Input power ~ 50 μW)

the glues' performance better. Approximately the same results have been reproduced on other chips.

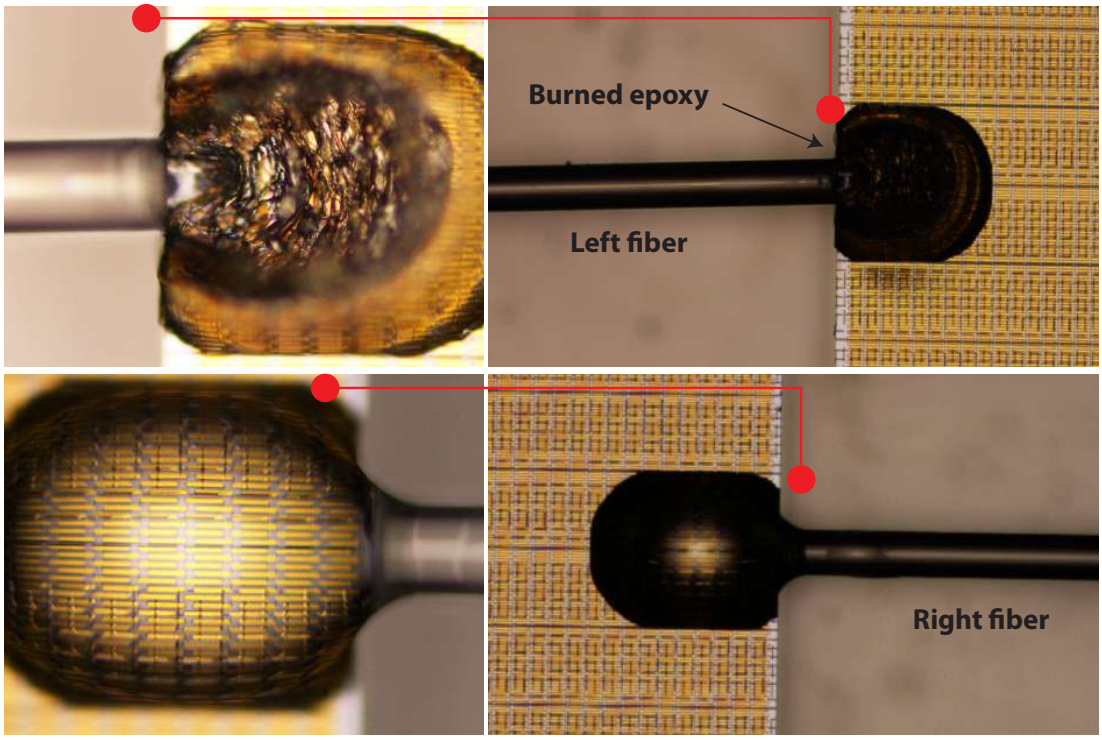

Figure 2.12: **High power testing of a packaged chip.** The chip/glue burned at optical power around 2.8 W. While the output fiber did not get any damage, as shown by two microscope images of the chip (bottom).

2.11 High power coupling stability

Since generating a frequency comb, with high conversion efficiency (overcoupled $\kappa_{ex} >> 3\times \kappa_0$), in a microresonator requires slightly higher power (> 150 mW), the packaged chip is tested at high input power. After selecting the suitable coupling fiber (UHNA3 and UHNA7) and the optical epoxies, high-power testing is done to check the performance of the glue. The first question is to determine the threshold power for the glue damage as it is based on polymer. An optical amplifier is used after the Toptica seed laser to characterize the high-power packaged device. A built-in isolator inside the amplifier avoids strong back reflection if the packaged chip (glue) gets damaged. Afterward, the output light is split by a 99 to 1 ratio; 1% light is used to monitor the input light while the remaining light is coupled to the chip. The output light is detected by a high-power photodetector that can handle up to 20 W of optical power.

The package is placed inside a laser radiation-safe box (glass) for eye safety. These box windows are made of anodized aluminum. The packaged chip is tested by increasing the power in small steps and monitoring coupling efficiency. The results are summarized in Table 2.2. The coupling efficiency degrades as power increases after 1 W. This is due to glue expansion at higher power. The increased temperature shifts the fiber from the optimum coupling point, which causes a loss of coupling efficiency. The first chip got damaged as soon as power is increased from 2.7 W to 2.8 W. From Figure 2.12, it is difficult to tell whether the chip is burned or the glue. However, 2.5 W is still adequate power to operate without burning the chips. Generally, the power used to produce combs with a low repetition rate and high efficiency (over-coupled) is around 1-1.5 W [84, 24, 27], two times lower than the damage threshold.

Table 2.2: Coupling efficiency at high input power

No.	Input power mW	Output power mW	Coupling efficiency (%)
1	100	18.3	18.3
2	500	90.1	18.02
3	1000	178.5	17.8
4	1500	254.3	16.9
5	2000	331.2	16.56
6	2500	396.8	15.8

The next question after high-power testing is whether coupling efficiency can be stabilized at high power. To answer this question, long-term stability at high power is tested. Again, a straight waveguide is packaged with an initial taper width of 260 nm and a waveguide width of 2 μm. The coupling efficiency of the device after packaging is 24 % which is much better than what was achieved in the first run. The device is tested at 2.6 W, slightly lower than the previous 2.7 W at which the last packaged device burned. The coupling efficiency at 2.6 W input power is around 23 %, slightly lower than low power coupling efficiency. Table 2.2 shows the coupling stability of the packaged straight waveguide at 2.6 W input power. The coupling efficiency seemed stable for the first 40 minutes but decreased and increased afterward. The expansion of glue, a polymer with

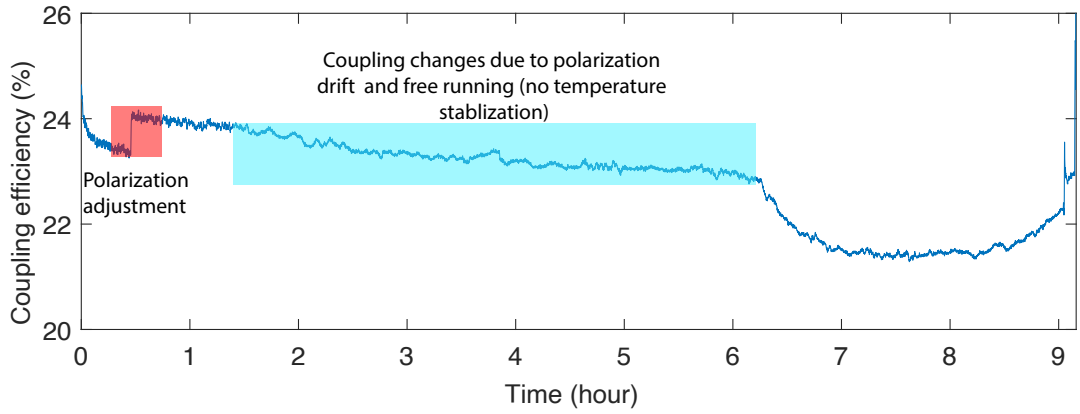

Figure 2.13: **Long-term coupling stability at input power 2.6 W.** Input power of 2.6 W, output power of 630 mW, and coupling efficiency ~ 24 % are observed at the beginning of the experiment. Four to five percent coupling fluctuations are observed during the experiment due to the heating effect and polarization drift (marked in red). Overall performance seems stable and could be improved by using a cooling element.

a higher CTE than glass, can explain this phenomenon. Moreover, polarization drift is another factor that plays an important role in coupling fluctuation. The sharp changes in output power (marked in red) are due to manual polarization adjustment. This can be improved by gluing the device to a better thermally conductive material and using a cooling element.

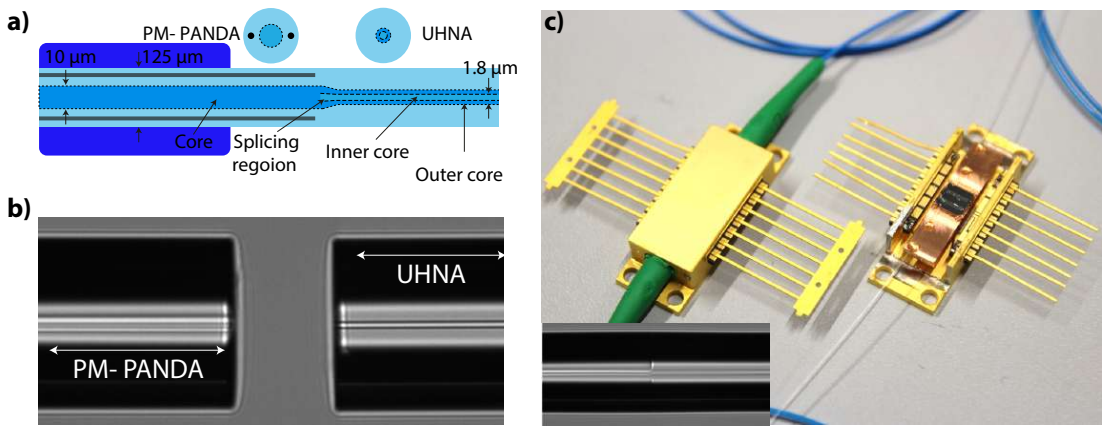

Figure 2.14: **Polarization maintaining packaging of Si_3N_4. a** A small piece of UHNA fiber splice with the polarization maintaining (PM, PANDA) fiber. The PM fiber has two rods applying stress to the core, leading to birefringence properties and eventually allowing single polarization transmission. Even though a non-PM UHNA fiber is spliced with PM fiber, the device maintains its polarization as this non-PM piece is strongly glued or attached to the chip carrier. **b)** A microscopic image inside the splicer showing PM and UHNA fiber. **c** A Si_3N_4 photonic chip packaged using PM fiber with an inset showing the PM fiber spliced with UHNA. Image credit: Andrey Voloshin.

2.12 Polarization maintaining packaging

Polarization-insensitive packaging requires chip interfacing via polarization-maintaining (PM) fiber. This particular packaging is useful for harsh environment where fiber polarization drift. More importantly, it eliminates the need to use bulk and expensive motorized fiber polarizers to adjust polarization automatically for on-field applications. Usually, the PM-UHNA fiber exists with mode field diameter > 5.3 m at 1550 nm but requires substantial engineering for efficient light coupling. A unique alternative approach is presented here while taking advantage of the already established non-PM UHNA fiber. The underlying idea is to splice a short (4 to 6 mm) non-PM UHNA fiber to a standard PM fiber (PANDA, 10.1 m mode field diameter at 1550 nm) as indicated in Figure 2.14 a. After splicing the fiber; the polarization is calibrated using a free-space linear polarizer (LPVIS050) along with the fiber rotator stage. Alternatively, a free space polarization splitter could be utilized to adjust the polarization of spliced fiber. The small piece of spliced non-PM UHNA will be glued to the chip carrier and can not be moved or stretched (Figure 2.14 a & c). Therefore, this part of the fiber, which is not PM, will not play any role in polarization drift.

A Si_3N_4 photonic chip with 200 GHz FSR is packaged using calibrated PM fibers spliced to UHNA and following the steps mentioned in section 2.9 (Figure 2.14). The polarization stability of packaged devices is verified using a polarization-maintaining laser and optical power splitter. The laser frequency is scanned constantly via an arbitrary frequency generator (AFG) and aligned to one of the cavity's resonances. As shown in Figure 2.15 b, the input light is oriented to the quasi-TE mode (critically coupled light). To determine the long-term stability of polarization drift, the laser remained aligned to the cavity's resonance for more than 18 hours. During this duration, the polarization did not drift while free running in these conditions, indicating the robustness of the PM-packaged device.

2.13 Low-temperature compatible packaging

Quantum computing based on superconducting circuits requires operating at low/cryogenic temperatures (~ 800 mK). Conventionally, the interconnects used for the superconducting quantum circuit are based on electrical wires. The rise in electrical connections inside the dilution fridge increases the heat load. This poses a significant hurdle to the scalability of cryogenic computing architectures. One attractive alternative is a photonic-based solution to mitigate the heat and scalability issue. Recent demonstration [193, 194] showed the control and reading of superconducting quantum circuits via the fiber-based electro-optic device. Moreover, the microwave to optical transducer could allow interfacing of multiple quantum computers by taking advantage of ultra low-loss of optical fiber [176]. In addition to finding the perfect technology for microwave-to-optical conversion, one key challenge is establishing a suitable packaging solution (fiber interfacing). As the epoxies utilized in optical packaging are polymer based, it is important to characterize them for low-temperature compatibility. At low temperatures, the changes in adhesion properties become different due to stress and CTE mismatch between SiO_2 surface.

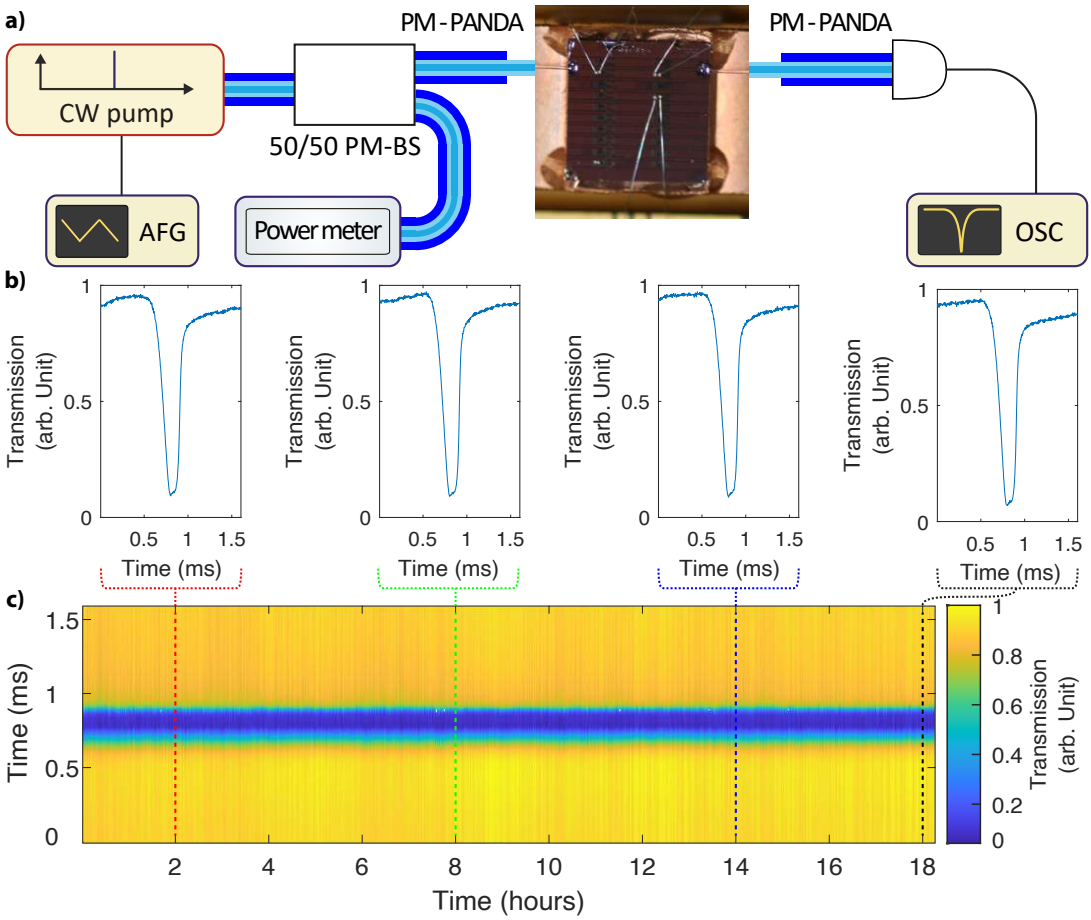

Figure 2.15: **PM-fiber-based packaged chip characterization. a** A Polarization maintaining CW laser is used to characterize the polarization stability of the packaged device. An arbitrary frequency generator (AFG) scans the wavelength (~ 2 GHz) by driving the laser's PZT. **b** Transmission spectrum captured via oscilloscope (OSC) shows that resonance is critically coupled, which is a good indication that photonic chip polarization is aligned to quasi-TE mode. **c** Long-term observation of resonance spectrum while driving the laser PZT constantly for 18 hours. The spectrum slices at different time intervals (2,8,12,18 hours) in **b** show the polarization of the device does not drift. Image credit: Andrey Voloshin.

A copper (Cu) metal-based chip carrier is prepared for low-temperature packaging. The epoxy (OG-142 and OG-154) used before for photonic packaging (room temperature) is more suitable for Aluminum and glass-based chip carriers. These epoxies do not work optimally if used with a Cu-based chip carrier. A glass strip is mounted on a Cu-based chip carrier to glue the fiber far away from the chip facet (Figure 2.16 a). For the first test, OG-142 is used to glue the fiber to the chip facet and far away. First, room temperature transmission stability is performed before inserting it in the dilution fridge. The chip is inserted inside a dilution fridge and interfaced with an external CW-laser and photodetector via fiber feedthrough to measure transmission at different temperatures (Figure 2.16 e). As shown in Figure 2.16 d, transmission is stable when

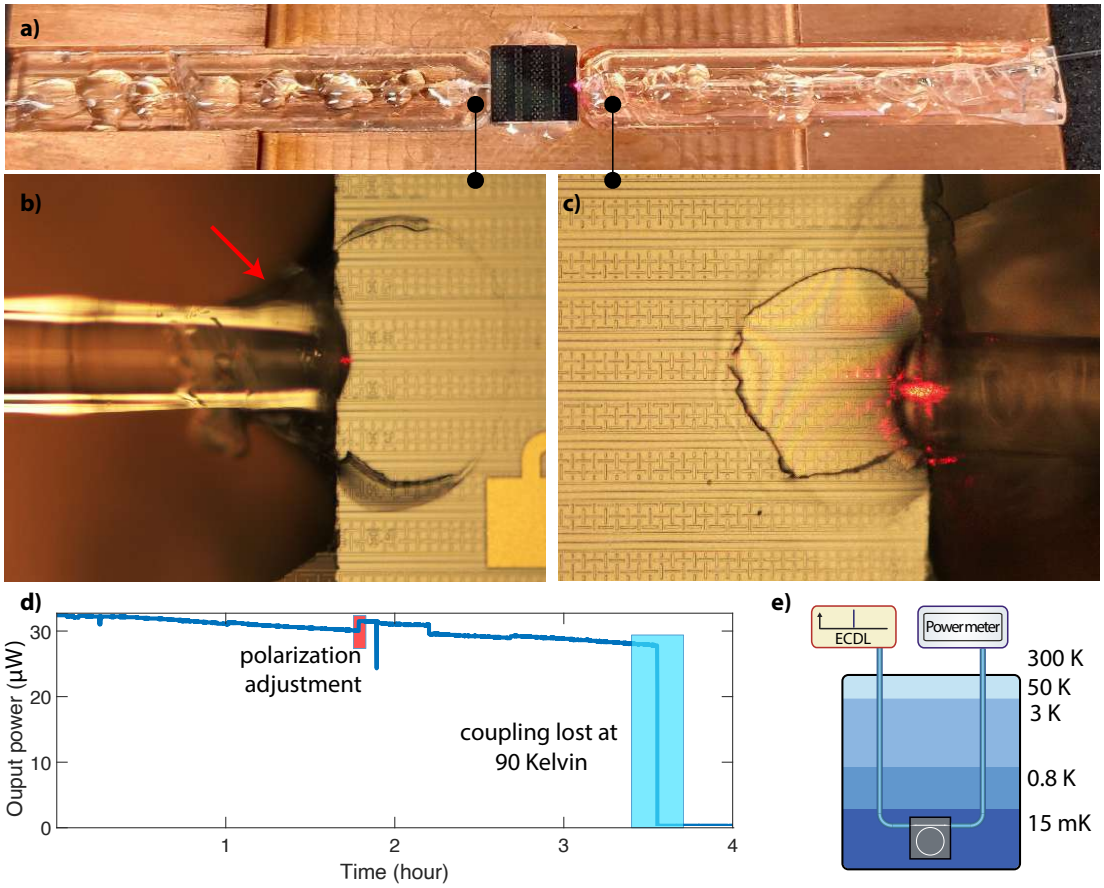

Figure 2.16: **Packaged photonic chip for testing the stability at low temperature. a** Photonic chip (Si_3N_4) is mounted on copper (Cu) while the fiber is glued on a long glass slide. The fiber is glued to glass because OG-142 has strong adhesion. **b & c** The zoomed-in picture of the photonic chip-fiber interface after going through the low-temperature cycle (300 K to 80 mK). The epoxy is removed from the fiber-chip interface to both chip ends. **d** The transmission through the chip is recorded during the cooldown cycle inside the dilution fridge. The chip coupling is lost at 90K due to excess stress applied to the epoxy resulting in its removal (**b & c**). **e** Schematic of dilution fridge showing the different temperature levels. The packaged chip is placed at the 80 mK stages and interfaces to the external components via fiber feedthrough. Note: Installation and data taken with the assistance of the Microwave team (T. Blésin, W. Kao, A. Youssefi, Y. Joshi, and M Chegnizadeh.)

the temperature drops from 300K to 150K. A slight decrease in transmission is associated with polarization drift (Figure 2.16 d, red shaded region). The coupling dropped to zero abruptly at 90 K. After inspecting the damaged chip, two things were observed; First, the glue drops at the fiber-chip interface are detached. Even though fibers are still attached to the chip via the remaining small glue on the left/right and bottom sides. Second, the big drop of epoxy has weak adhesion to the glass surface (far away from the chip facet). The fiber glued to glass can be detached by applying a small force post-cryogenic cycle. One possible reason for damage at low temperatures to this epoxy could be high storage modulus (>555,000 Psi) or stiffness,

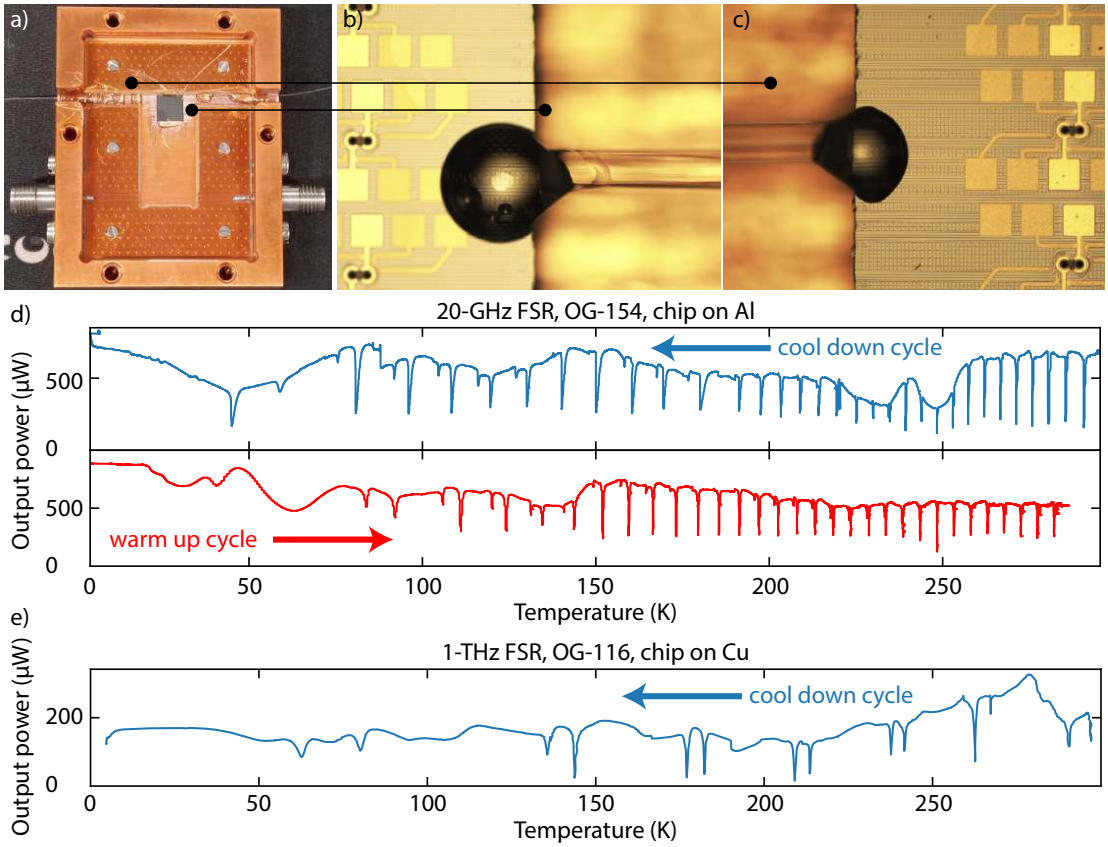

Figure 2.17: **Optical chip packaging using epoxy with low stiffness (storage modulus) for better stability at cryogenic temperature. a** 1 THz coupled microresonators packaged using OG-116 inside Copper (Cu) based chip carrier. **b & c** Magnified view of the fiber-chip interface. The epoxy did not lose adhesion to the chip facet after going through the cryogenic temperature cycle (see **e**). **d** The transmission observation during the cool (top) and the warm (bottom) cycle of 20 GHz FSR on Aluminum (Al) chip carrier. Multiple dips (resonance) in transmission can be observed during decreasing (top) and increasing (bottom) temperatures due to changes in the refractive index. **e** The transmission stability observation of a coupled-THz photonic chip packaged using OG-116 on a Cu chip carrier. Note: Installation and data taken with the assistance of the Microwave team (T. Blésin, W. Kao, A. Youssefi, Y. Joshi, and M. Chegnizadeh.)

yielding high stress. Moreover, the big CTE mismatch could have also led to the loss of adhesion. While the loss of adhesion to the chip surface and the glass surface is challenging to predict as it involves molecular binding chemistry and requires more in-depth surface analysis. The crack propagation could be another potential candidate for loss of binding, as the glue is not removed at every interface (Figure 2.16 b, red arrow).

To further consolidate the understanding of cryogenic optical packaging, OG-154, and OG-116 epoxies are further explored. The main criterion at this point is to use epoxies with lower stiffness (< 260,000 Psi). OG-154 (OG-116) is used on Al (Cu) chip carrier. The OG-116 requires a slightly different UV-curing procedure, as it cures much slower (x10 lower, ~ 5-10 min.) than

OG-154 and OG-142. Moreover, although the viscosity is similar, OG-116 offers strong resistance when dispensing. Proper curing of glue (OG-116) at the fiber-chip interface is critical. The glue drop dispensed far away from the chip facet to avoid fiber ripping off could give a strong shock and eventually loss in coupling. The packaging procedure mentioned in section 2.9 is followed for both epoxies (OG-154 & OG-116). After packaging, transmission stability is measured and verified at room temperature. Then both devices were installed inside the dilution fridge at the 800-mK stage (Figure 2.16 d). Both types of glue survived at low temperatures as shown in Figure 2.17 e & f at least two cooldowns and one warm-up cycle. A set of dips in the transmission is observed at different temperatures arising due to refractive index and cavity length changes due to temperature. As the laser frequency is fixed during the measurement, changes in the effective index lead to resonance frequency changes. Additionally, these measurements allow estimation of the $\frac{dn}{dT}$ at different temperatures, e.g. $\frac{dn}{dT}$ (50 K) < $\frac{dn}{dT}$ (300 K).

A drop in transmission ranging from 5 % to 8% is observed, which can be further improved by using a unique structure at the chip facet (section C.3). Nevertheless, the package survived the 3× cryogenic temperature cycles (300-K to 4mK). The damage generally occurs due to fiber losing adhesion far away from the chip facet. As mentioned earlier, the number of cryogenic temperature cycles sustained by packaged chips can be further increased by using rough surfaces instead of fine polished or flat surfaces. Another potential solution that could be implemented is using additional epoxy that is well-established for cryogenic operation but can not be used during regular optical packaging either because it is too viscous or linear shrinkage is too high. This epoxy can be applied on top of OG-154 and OG-166 (far away from the chip facet) after optical packaging is performed and stabilized (section 2.9). This will assist in maintaining adhesion to the chip carrier surface for multiple cryogenic cycles.

3 Soliton generation and stabilization in microresonators

Different soliton microcomb generation methods will be discussed in the first part of this chapter.

- Soliton generation via forward scanning
  - Laser internal PZT scan
  - external scanning via dual parallel Mach–Zehnder modulator
  - On-chip AlN acutator to initiate soliton
- Current initiated soliton generation
  - Self-injection-locking based soliton generation
  - Hybrid semiconductor ultra-low noise (ULN) laser

Then we will extend the discussion by showing the soliton generation in the packaged devices and its stability, paving the way for the compact module. These packaged devices have been used in multiple projects, including ultra-fast circuit switching for data center[20], continuous wave photon-induced near-field electron microscopy (CW-PINEM) [22], electron-photon pair generation [106], electron soliton interactions [23], convolutional processing [26], Brillouin scattering [81], photon pair generation [25] and on-chip accelerometer.

The results presented in the current chapter are based on the following published studies: **1:** [J. Liu*, A. S. Raja* [1] et al., Optica 5, 1347 (2018)] I was responsible for conducting experimental (chip characterization, optical setup construction, and soliton generation measurements) with assistance from J. Liu and M. Karpov. **2:** [J. Liu*, E. Lucas*, A. S. Raja*, J. He* et al., Nature Photonics, 14(8), 486-491 (2020)], I was responsible for experimental parts (optical setup construction, and soliton generation measurements) with assistance from J. He and assisting E. Lucas with the microwave characterization and stabilization part. **3:** [J. Liu*, H. Tian*, E. Lucas*, A. S. Raja*, et al., Nature, 583(7816), 385-390 (2020)], I was responsible for experimental parts

[1] *:equal contribution

(optical setup construction (installing probes), and soliton generation measurements) assistance from J. Liu, and assisting E. Lucas with stabilization methods. **4:** [A. S. Raja*, J. Liu* et al., Optics Express, 28(3), 2714-2721 (2020)], I was responsible for chip characterization, soliton generation, and packaging parts.

3.1 Soliton generation

Integrated optics and, more recently, silicon photonics have profoundly influenced the use of optics in conventionally electronic-dominated applications. The development of compact optical frequency combs, using soliton microcombs, provides a platform to make such optical combs ubiquitous and sufficiently compact to be applied to applications beyond laboratories. Compact frequency combs can impact a wide range of optical technologies from light detection and ranging (LiDAR) to wavelength division multiplexing laser sources for coherent communications (WDM), or future high bandwidth optical data-center interconnects to spectroscopy, low noise microwave generation or generation of entangled photon pairs for QKD and secure quantum communication [18, 42]. Microcombs realized in integrated Si_3N_4 microresonators are particularly promising, as Si_3N_4 has relatively high material nonlinearity and low light propagation loss. In addition, CMOS-compatible fabrication process and wafer-scale integration are utilized to fabricate Si_3N_4 microresonator devices. One of the main factors hindering the full integration of Si_3N_4 DKS combs functionalized by pump laser was the high required power budget, which crucially depends on: (1) the Q-factor of Si_3N_4 microresonator, (2) device coupling efficiency, and (3) the DKS tuning mechanism. Microcomb generation in Si_3N_4 microresonators relies on external power amplifiers for providing sufficient pump power [82, 52, 84, 86]. Moreover, the soliton exits on the red side of the resonance, which is thermally unstable. The soliton state is accessed by scanning the laser across the resonance using a method known as forward scanning [43]. Different variations of these schemes have been used to generate the soliton. Some widely adopted techniques are based on scanning the laser's wavelength using PZT (internal) [43], acoustic optic modulator [125], single sideband modulator [90], on-chip heaters [94], and on-chip piezoelectric actuators [93] to initiate the solitons. The following sections will explain some of these schemes performed in the current study.

3.2 Forward scanning via internal laser PZT

The scheme requires a frequency agile laser and has been widely adopted [43, 27, 18]. A custom-designed waveform is generated via an arbitrary frequency generator (AFG) to drive the internal PZT to scan the laser wavelength. This scheme works efficiently for microcavities with low losses (e.g., silica microdisks and crystalline microresonators, Q-factors > 500 million) [195, 43] due to low threshold powers, longer soliton existence range and weaker generated thermal effect due to light absorption. But, cavities with relatively lower Q-factor (< 1 million, Si_3N_4) require higher threshold power leading to strong thermal effects. However, a microresonator with larger spacing would require lower threshold power as the soliton initiation power scales linearly with

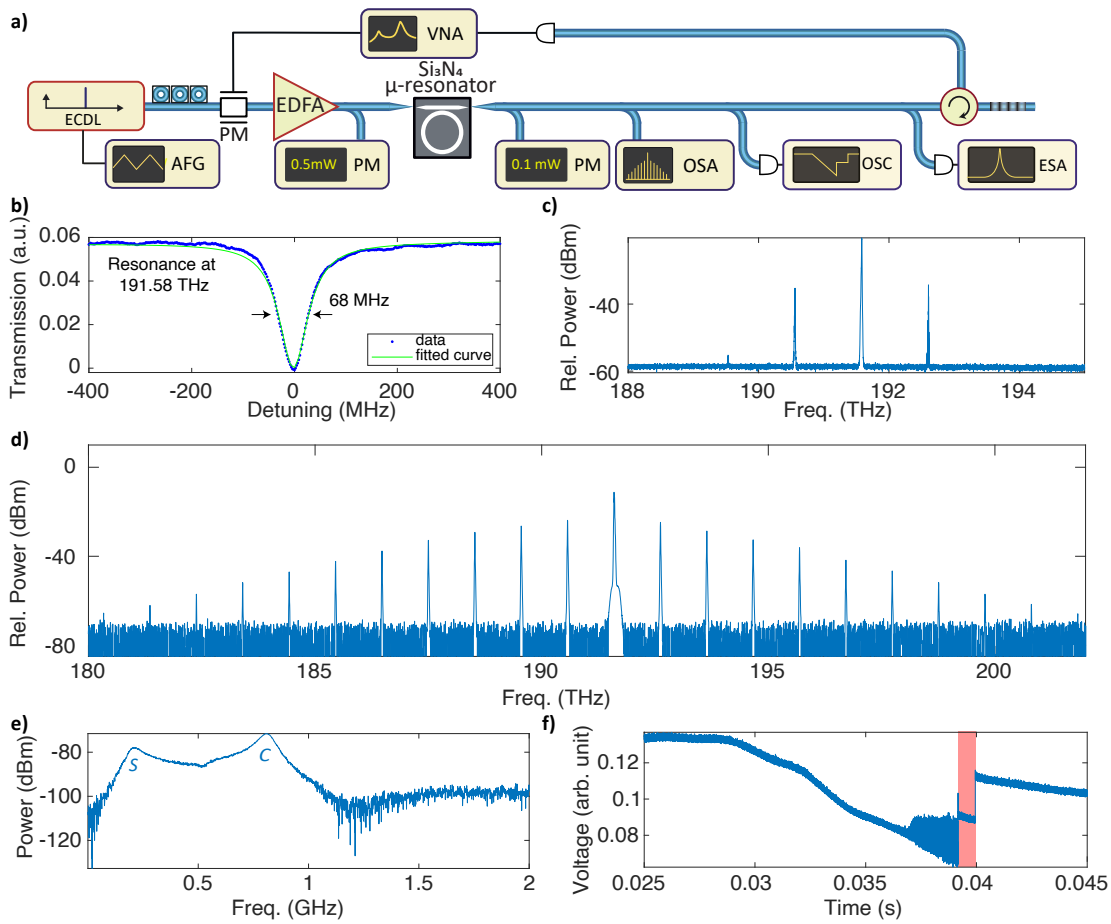

Figure 3.1: **The soliton generation via forward scanning.** **a** Optical setup to generate the soliton by scanning the laser wavelength. The soliton generation verifications can be done either by probing the cavity via a vector network analyzer (VNA) or observing a step in the transmitted signal via an oscilloscope (OSC) and measuring the amplitude noise via an electrical spectrum analyzer (ESA). ECDL: External cavity laser diode, PM: Power meter, OSA: optical spectrum analyzer, EDFA: Erbium-doped fiber amplifier, and EOM: electro-optic modulator. **b** The microresonator's resonance with total linewidth $(\frac{\kappa}{2\pi}) \approx 68$ MHz. **c** Optical parametric sidebands generated at an input power 50 μW in bus waveguide. **d** Optical spectrum of a soliton with THz repetition rate measured using OSA. **e** The VNA response of the cavity is performed by applying a weak modulation to the pump with an EOM. In the soliton state, two peaks are observed corresponding to the cavity ($\mathscr{C}$)) and the soliton ($\mathscr{S}$)) response. **f** The transmitted light signal is recorded on OSC and measured with a photodiode. The red-shaded region corresponds to a low noise state and signals soliton formation inside the microresonators. Dimension of microresonator (Waveguide width=0.55 μm, Resonator's waveguide width = 1.475, waveguide height ~ 750 nm and coupling gap= 1.025 μm)

cavity length. In the first part, Si_3N_4 microresonators with THz free spectral range (FSR) have been used to generate the soliton by forward scanning due to lower threshold power requirements. The Si_3N_4 based microresonators with THz spacing provide access to octave-spanning frequency

combs [51, 52].

An optical pumping setup is constructed to generate the soliton at different repetition rates ranging from 10 GHz [24] to 1 THz [27]. An external cavity laser diode (ECDL) with wide wavelength tunability is coupled to an electro-optic modulator. The weak modulation of the pump allows non-destructive probing of the cavity soliton states along with a vector network analyzer (VNA). A portion of the light is tapped on the input (output) side via optical splitters to estimate the chip's input (output) power. A photodetector measures the transmitted signal on an oscilloscope (OSC). The optical spectrum is observed on an optical spectrum analyzer (OSA). A fast photodiode (bandwidth > 5 GHz) is used to measure the cavity's VNA response. The lensed fibers couple the light in and out of Si_3N_4 photonic chips. The fiber-based polarization controller (PC) manually adjusts the input light polarization to the mode family under consideration.

At low optical power (< 10 µW), a Lorentzian shape resonance is observed (Figure 3.1, b). When optical power is increased, Lorentzian shape resonance switches to a triangular shape due to thermal and nonlinear effects (Figure 3.1, f). The threshold power for parametric oscillation can be estimated by using the following expression

$$P_{\text{th}} = \frac{\kappa^2 n^2 V_{\text{eff}}}{4\omega c n_2}, \tag{3.1}$$

where $\kappa/2\pi$ is the total linewidth of the microresonator, n is the linear refractive index, V_{eff} corresponds to the effective modal volume, ω is the angular frequency of light, c the speed of light in vacuum, and n_2 is the nonlinear intensity-dependent refractive index. The parametric oscillation threshold for Si_3N_4 microresonator with $V_{\text{eff}} \sim 1.4 \times 10^{-16}\text{m}^3$ (radius ~ 22.5 µm), n ~ 1.99, $\kappa/2\pi \sim 68$ MHz, $n_2 \sim 2.14 \times 10^{-19}\ \frac{\text{m}}{\text{W}}$ and $\omega \sim 1.20 \times 10^{15}\ \frac{\text{rad}}{\text{s}}$ is around 0.484 mW. While the experimentally measured parametrical threshold power is ~ 0.5 mW matching relatively well with the theoretical value (Figure 3.1,c). Further increase in power (~15 mW, bus waveguide) inside the microresonator, a noisy signal can be seen on the transmitted indicating modulation instability (MI) (Figure 3.1,c). The sharp transition to a low noise step after the MI state shows soliton generation. The tuning into the primary combs (parametric sidebands) and MI states can be done by tuning the laser wavelength in discrete steps. The soliton generation requires a single scan (typical scanning rate ~ 2 - 200 GHz/s) over resonance from the blue to red side (increasing wavelength) to tune into the soliton state. The single soliton spectrum generated by scanning the laser wavelength with AFG is shown in Figure 3.1, d. The optical spectrum has a characteristic shape featuring $\text{sech}^2(f)$ dependence. In addition, a double dip in VNA response is another distinctive indication of soliton generation (Figure 3.1 e).

However, devices with lower repetition rates require higher optical power to initiate the soliton due to longer cavity length (higher V_{eff}). A 100 GHz microresonator with intrinsic linewidth ($\frac{\kappa_0}{2\pi}$) of ~ 46 MHz and external coupling rate ($\frac{\kappa_{\text{ex}}}{2\pi}$) around 19 MHz is initially characterized using the method explained in subsection 1.8.2 (Figure 3.2 a). The microresonator's waveguide has a width of 1.5 µm and a height ~ 750 nm (radius ~ 235 µm). The bus waveguide has the exact dimensions of the microresonator. The gap between the bus waveguide and the microresonator is

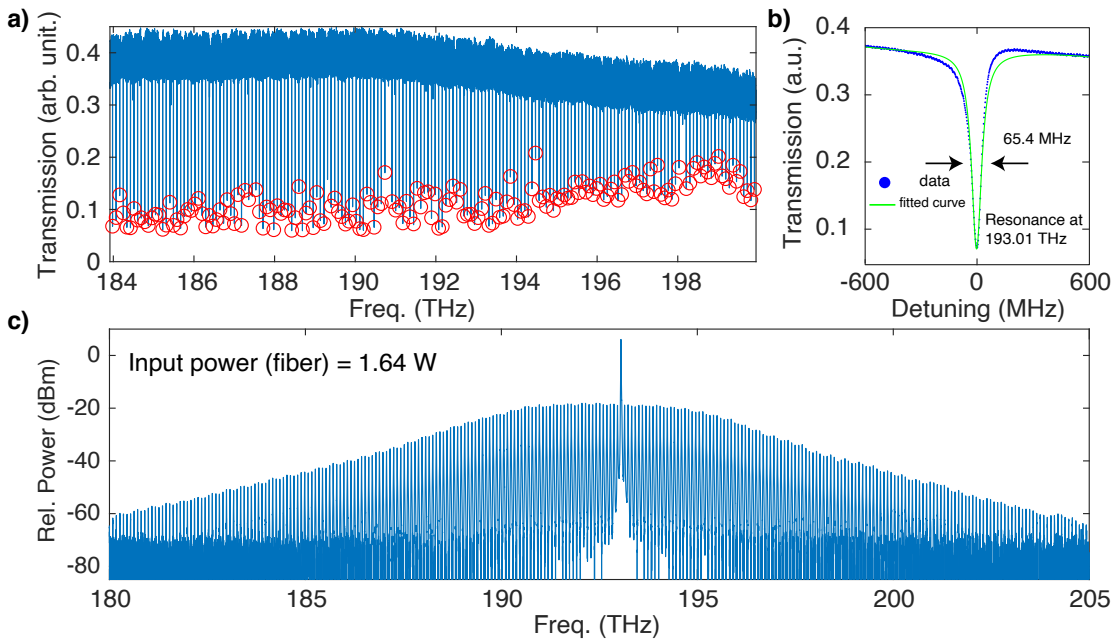

Figure 3.2: **Frequency comb generation in a Si_3N_4 microresonator with ~ 90 GHz line spacing.** **a** The broadband frequency transmission scan is measured by calibrating the laser against the self-reference fiber mode lock laser and Mach-Zehnder interferometer [115, 173]. **b** The microresonator's resonance with total linewidth ($\frac{\kappa}{2\pi}$) ~ 65 MHz (slightly undercoupled). **c** Optical frequency generated in 100 GHz FSR microresonators at an input power of 1.65 W. The strong thermal effects hindered the soliton generation via forward tuning (scanning laser PZT).

800 nm. The Si_3N_4 microresonator side cladding is SiO_2 while the top cladding is air. The MI state can be generated by pumping the microresonator at a higher input power (~ 150 mW). The soliton generation is impossible in this sample, even at an input power of > 1.65 W, mainly due to strong thermal effects. Then, a more advanced approach can initiate soliton generation where the laser wavelength can be scanned externally at a much higher rate (> 1 THz/s). The thermal effects can be stabilized by scanning the laser at the optimum speed to find a balance between the soliton existence range and thermal changes caused by the transition from MI to soliton.

3.3 Forward scanning via dual parallel Mach–Zehnder modulator (DP-MZM)

A more advanced pumping setup [2] is made by incorporating the dual parallel Mach–Zehnder modulator (DPMZM) to observe samples with strong thermal effects. A DPMZM is used to perform suppressed-carrier single-sideband modulation (SC-SSB). The voltage-controlled oscillator drives both MZM modulators along with a 90° hybrid. The hybrid provides microwave carriers with a 90 ° phase shift driving the MZM separately. The optimum suppression of the

[2] with M Karpov and E Lucas assistance

pump (carrier) with respect to the sideband requires adjustment of different DC biases applied to the main MZM (central) and sub MZMs (upper and lower) (Figure 3.3, a). The scheme enables the fast scanning (typical speed ~ up to 250 kHz) of modulated sideband (optical carrier) compared to internal laser PZT (~ 1-200 Hz). The demonstration of soliton along with DP-MZM is shown in a

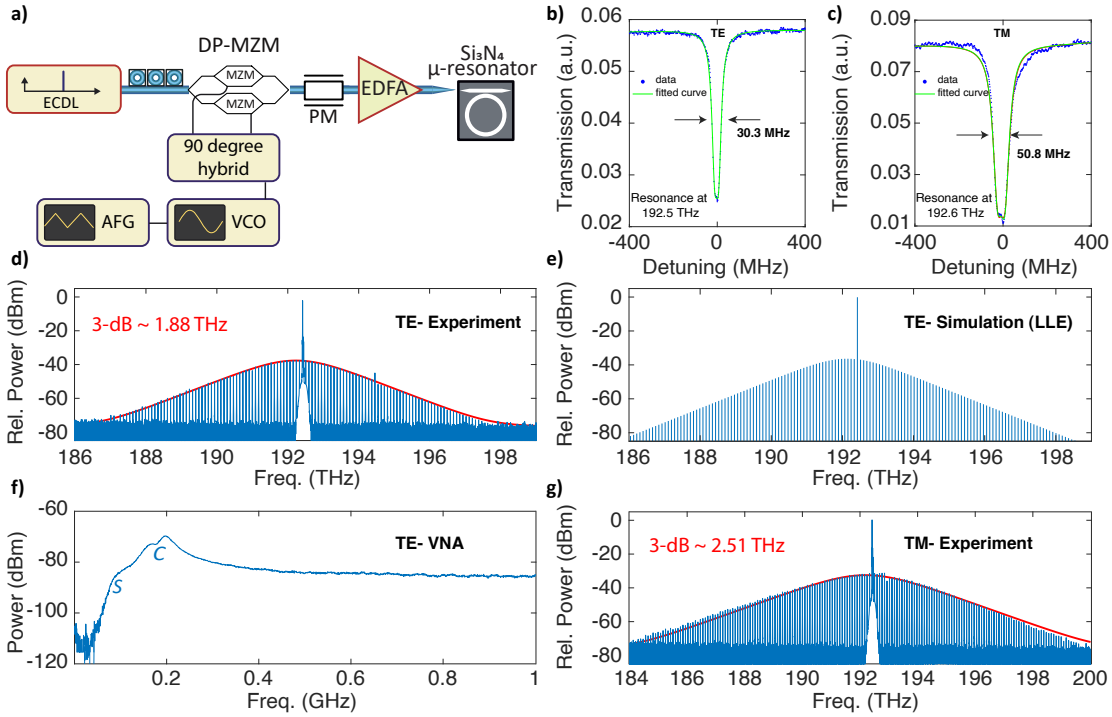

Figure 3.3: **The soliton generation by fast frequency shifting with a dual parallel Mach–Zehnder modulator (DP-MZM). a** Optical setup containing DPMZM to scan the laser wavelength to tune into a soliton state. A voltage-controlled oscillator (VCO) with a typical frequency tuning from 5 GHz to 15 GHz when applying 0 to 10V. The output of the oscillator is fed into a 90-° microwave hybrid generating two output signals having a 90-degree phase shift ($\cos(\omega t)$ and $\sin(\omega t)$). These signals drive the DPMZM in each branch separately. In addition, the DC bias in the upper, lower, and central MZMs is adjusted to suppress the carrier. The typical scanning speed up to ~ 250 kHz is used in experiments performed in this study to generate the soliton. **b & C** The resonances used to generate the soliton in 88 GHz microresonator in TE (TM) mode with total linewidth ($\frac{\kappa}{2\pi}$) of ~ 30.3 (50.8) MHz. **d** A single soliton generated in TE mode at an input power of ~ 50 mW via fast frequency tuning. The fitted spectrum with sech^2 has a 3 dB bandwidth of ~ 1.88 THz (15.2 nm). **c** The simulated optical spectrum produced by Lugiato Lefever equation (LLE) simulations while using experimental parameters matches well with the actual spectrum (d). **f** The ($\mathscr{C}$)) and ($\mathscr{S}$)) response measurement is used to verify the soliton generation using a phase modulator (PM). **g** The fast scanning via (DP-MZM) further enables the soliton generation in TM at an input power of ~ 80 mW. The optical spectrum has a 3 dB bandwidth of ~ 2.51 THz (20.3 nm). Dimension of microresonator (Waveguide width=1.575 μm, Resonator's waveguide width = 1.575, waveguide height ~ 750 nm and coupling gap= 800 μm)

microresonator with repetition rates below 90 GHz. Generally, achieving soliton in these devices (Si_3N_4) is relatively difficult due to high threshold power and thermal effects (Figure 3.2). Here,

we have used Si_3N_4 microresonators with intrinsic linewidth ($\frac{\kappa_0}{2\pi}$) of ~ 23 MHz for fundamental quasi-TE mode with 88 GHz FSR (Figure 3.3, b). The integrated dispersion second-order ($\frac{D_2}{2\pi}$) and third-order ($\frac{D_3}{2\pi}$) elements are 1.10 MHz and $\mathcal{O}(1)$ kHz respectively. A single soliton is generated by performing a single scan over the resonance via DPMZM driven by AFG and stopping at the soliton step (Figure 3.1, f). The optical power required to initiate the soliton is ~ 37 mW in the bus waveguide (~ 50 mW in the fiber). Moreover, weak phase modulation of the sideband generated via DPMZM is done to probe the soliton state non-destructive (Figure 3.3, f). In addition, the optical spectrum is fitted with characteristics of $sech^2$ shape yielding a 3 dB bandwidth of ~ 1.88 THz and pulse duration of ~ 167 fs. Similarly, the optical spectrum is generated using realistic parameters concerning experimental values and device dimensions using Lugiato Lefever Equation LLE simulations. The soliton spectrum based on simulation agrees with experiments. Compared to earlier studies employing DKSs in Si_3N_4 with a repetition rate of less than 100 GHz, the required input power was > 2 watts. The current device already presents significant improvements thanks to fabrication advances made by Junqiu Liu, and more detail on fabrication can be found in Ref. [27].

Moreover, this scheme further provides access to soliton generation in the second mode family (quasi-TM) with an intrinsic linewidth ($\frac{\kappa_0}{2\pi}$) of ~ 28 MHz (same device). The integrated dispersion first-order ($\frac{D_1}{2\pi}$), second-order ($\frac{D_2}{2\pi}$) and third-order ($\frac{D_3}{2\pi}$) elements are ~ 86.3 MHz, ~ 0.967 MHz and ~ 5.4 kHz respectively for fundamental TM mode. The quasi-TM mode is critically coupled with external coupling rate ($\frac{\kappa_{ex}}{2\pi}$) around 23 MHz and intrinsic linewidth ($\frac{\kappa_0}{2\pi}$) ~ 28 MHz (Figure 3.3,c). When pumping the resonance at 192.6 THz, a single soliton is generated when putting an input power of ~ 50.6 mW in the bus waveguide (80 mW at input fiber) (Figure 3.3, g). The fitted spectrum has a 3 dB bandwidth of ~ 2.51 THz and a pulse duration of 125 fs. The wider spectrum in this mode (quasi-TM, Figure 3.3, g) as compared to quasi-TE (Figure 3.3, d) is due to stronger strong external coupling rate (TM $\frac{\kappa_{ex}}{2\pi}$ > TE $\frac{\kappa_{ex}}{2\pi}$), higher input power ($P_{TM} > P_{TE}$) and weaker second-order dispersion element (TM $\frac{D_2}{2\pi}$ < TE $\frac{D_2}{2\pi}$).

Note: In the context of this thesis study, this scheme becomes extremely important for devices fabricated for soliton-electron interaction (see chapter 7). In these devices, soliton generation was only possible via this scheme.

3.4 Soliton generation without optical amplifiers

Soliton generation in Si_3N_4 microresonators relies on an external power amplifier for sufficient pump power and external phase modulators (DP-MZM) for tuning into DKS states (section 3.3 & section 3.2). Besides, constant efforts are being made to improve the Si_3N_4 microresonator Q-factor to relax the power requirement for DKS comb generation. Although Si_3N_4-based integrated DKS combs have progressed significantly in the past years, including the realization of Si_3N_4 microresonators in the ultrahigh-Q regime [36], DKS combs have not been demonstrated at low power levels compatible with on-chip lasers which operate with <100 mW power. For this reason, all existing experiments on Si_3N_4-based soliton microcombs have utilized amplifiers.

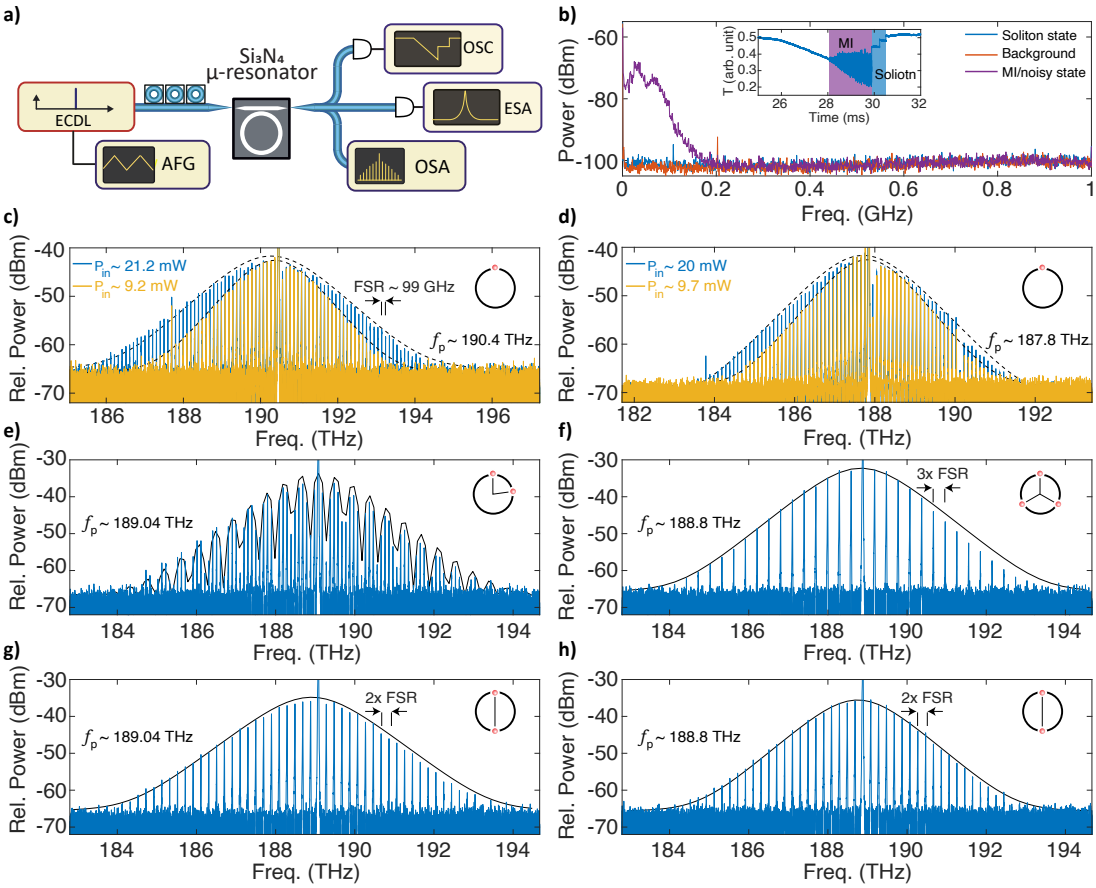

Figure 3.4: **Soliton generation in a Si_3N_4 microresonator directly using an external cavity diode laser (ECDL) and without an external amplifier.** **a** The schematic of the optical setup to generate the soliton by directly using a widely tunable ECDL. The nonlinear states are probed using an optical spectrum analyzer (OSA), an electrical spectrum analyzer (ESA), and an oscilloscope (OSC). The soliton state is initiated by performing a single scan over the resonance via arbitrary frequency generated (typical scanning speed ~ 1-50 Hz). **b** The low radio-frequency (RF) amplitude noise of different states to verify the soliton generation. The transmitted signal measured using OSC indicates Modulation instability (MI) and soliton states (single and multiple). **c & d** The single soliton generated at ~ 9.2 mW (9.7 mW) of optical power while pumping the resonance at ~ 190.4 THz (187.8). The wider spectrum is generated while pumping the microresonator with the maximum laser power (~ 21 mW). **e** Multi-soliton state is generated in the same device while pumping at different a resonance (P_{opt} ~ 20 mW). Two soliton states with an angular spacing of ~ 82° between them result in a complex spectrum shape due to interference. **f** Three soliton states with an angular spacing of 120° among each soliton result in a perfect soliton crystal (2 comb lines missing). **g & h** Perfect two soliton crystal states generated in the same device. Dimension of microresonator (Waveguide width ~ 1.5 μm, Resonator's waveguide width ~ 1.5 μm, waveguide height ~ 800 nm and coupling gap= 810 -850 μm)

Moreover, due to the increase in power with repetition rate, applications such as dual-comb coherent telecommunication [84] or ultrafast distance measurements [86], which utilize line spacing of 100 GHz or less, require amplifiers to supply several watts of power, posing a hindrance to the photonic integration of soliton sources.

The sample used in the previous sections (section 3.3) suffers from hydrogen absorption, hindering soliton initiation at optical power below 15 mW. Hydrogen can be introduced to Si_3N_4 wafers due to incomplete thermal annealing or water vapors forming a thin layer of water on the surface. The modified fabrication method of Si_3N_4 photonic integrated circuits, as reported in more detail [27, 77], first utilized more optimum annealing cycles. In addition, the top SiO_2 cladding is deposited as a combination of tetraethylorthosilicate (TEOS) and low-temperature oxide (LTO) to avoid a thin layer of water vapor. The Si_3N_4 microresonator, fabricated with modified annealing cycles and top SiO_2 deposition, exhibits an intrinsic linewidth ($\frac{\kappa_0}{2\pi}$) of ~ 14 MHz. The integrated dispersion first-order ($\frac{D_1}{2\pi}$), and second-order ($\frac{D_2}{2\pi}$) elements are ~ 98.9 GHz and ~ 1.23 MHz respectively for fundamental quasi-TE mode. Previously, Si_3N_4 based microresonators exhibiting Q-factor > 10^7 with anomalous dispersion ($\frac{D_2}{2\pi} > 0$) have been demonstrated [36]. But, a single soliton generation was not shown in these studies mainly due to weak $\frac{D_2}{2\pi}$ resulting in high threshold powers (> 100 mW) requiring external amplifiers. The wider waveguides (width > 2.5 µm) lead to less scattering losses due to strong confinement within the Si_3N_4 waveguide, but at the expense of weaker GVD (D_2) [36]. Here, a single soliton is generated while pumping the microresonator using an external cavity diode laser (ECDL, Toptica CTL) and tuning into soliton states via ECDL's internal PZT (forward scanning [43], section 3.2). A typical transmitted signal is observed on an oscilloscope using a photodetector, as shown in Figure 3.4 b inset, indicating noisy and soliton states. The VNA probing of soliton ($\mathscr{S}$) could not be performed in this experiment. The electro-optic modulator modulating the pump has a 3 dB insertion loss. However, a low-frequency (RF) amplitude noise arising due to the beating of combs lines is measured to verify further the soliton generation (Figure 3.4, b). This measurement is valid for low repetition rates (< 200 GHz) soliton states verification but might not be a suitable indicator for 1 THz devices [52]. The optical amplifier elimination enables accessing soliton generation outside the gain region (C-band) of optical amplifiers (typical ~ 1535 nm - 1570 nm). A single soliton is generated at an optical power < 10 mW (in fiber) when pumping resonances centered at 187.8 THz (Figure 3.4 c, R_{ring} ~ 228.41 µm). Similarly, another low-power initiated single soliton is generated in a different microresonator (R_{ring} ~ 228.43 µm) on the same chip (Figure 3.4, d). Increasing the power up to ~ 21 mW leads to a wider optical spectrum. Interestingly, the resonances next to mode crossing provide soliton generation at much lower optical power than the absence of mode crossing. Indeed, spatial mode interaction via mode crossing facilitates single soliton generation, as reported previously [196]. Moreover, adjacent resonances are also investigated in the same microresonator, which results in multiple soliton states (Figure 3.4 e,f,g,h). These states are initiated at an input power ~ 22 mW.

Furthermore, single soliton generation across the whole range of ECDL is demonstrated to show the reliability of the fabrication process. First, single solitons are generated in the C-band (centered frequencies ~ 194 - 195 THz). Afterward, more than ten solitons are generated in

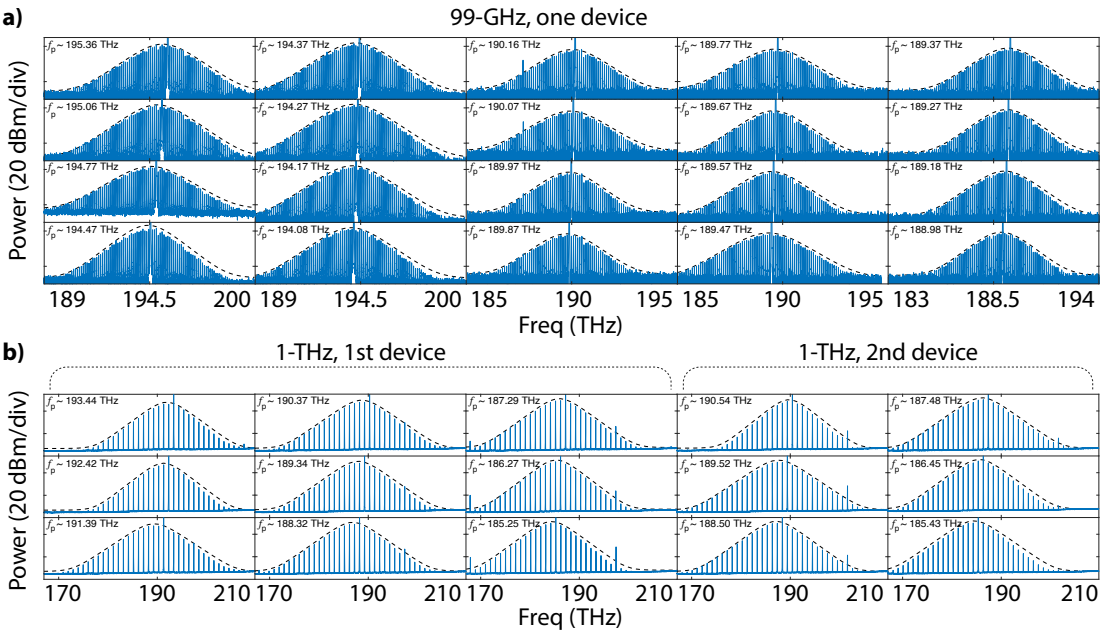

Figure 3.5: **Soliton generation in consecutive resonances in 99 GHz and 1 THz Si_3N_4 microresonators. a** More than 20 99 GHz FSR single soliton generated in one Si_3N_4 microresonator pumped directly using an external cavity diode laser (ECDL) (C & L bands). The maximum optical power utilized in these measurements is ~ 20 mW. The optical spectrums are fitted using $\text{sech}^2(f)$. **b** The 1 THz FSR solitons are generated in two microresonators by directly pumping with ECDL. Dimension of microresonator (Waveguide width ~ 1.5 µm (a), 550 nm (b) & , Resonator's waveguide width ~ 1.5 µm (a) & 1.475 µm and 1.4 µm (b) , waveguide height ~ 800 nm and coupling gap= 810µm (a) & 1 µm (b))

consecutive resonances centered at ~ 189 to 190 THz (Figure 3.5, a). All the measurements are done at maximum optical power (~ 22 mW) to show a broader spectrum, even though the soliton initiation might be lower (not performed in this set). However, some resonances lead to multi-soliton generation, similar to the one shown in Figure 3.4 e, f, g, and h. Moreover, similar measurements are performed in two THz FSR Si_3N_4 showing soliton generation in 9 and 6 consecutive resonances (Figure 3.5, b). The soliton generation across multiple resonances could be beneficial for the localized spectral features, e.g., avoided mode crossing. Overall, the soliton generation in consecutive resonances demonstrates the robustness of Si_3N_4 microresonators for soliton generation in a stable and reproducible way. It also offers the flexibility of the wavelength range of the pump laser for soliton initiation, which is important for future full photonic integration.

3.5 Soliton generation via ultra-low noise laser (ULN)

Advances in ultralow-loss Si_3N_4 waveguide fabrication processes [36, 27, 77], and state-of-art high-Q Si_3N_4 microresonators enable single soliton states generation with repetition rates below

100 GHz without needing an optical amplifier (Figure 3.4, Figure 3.5). It should be noted that, for practical applications using soliton microcombs, soliton pulses at electronically detectable repetition rates, with average pulse power of more than one mW, are still preferred. At the same time, recent reports show that packaged, semiconductor-based, fiber-coupled lasers [197] can provide sufficient output power and frequency stability for soliton microcomb generation on silica microdisks [198]. Though fragile tapered fibers to couple the silica microdisks are still required, hybrid semiconductor lasers with high output power (~100 mW) are a promising component to build compact, portable soliton microcomb devices for practical applications that require high soliton power. In addition, this hybrid semiconductor laser features excellent noise properties, with low relative intensity noise and narrow linewidth with low relative intensity noise (–160 dBc/Hz at $f_{offset} \sim 100$ kHz) and narrow linewidth (~ 15 Hz) [197]. These semiconductor lasers can potentially be a key building block for low-noise integrated soliton-based microwave photonics [24].

The Si_3N_4 microresonator chips used in this project are fabricated using the photonic Damascene reflow process [39], and feature microresonator Q-factors exceeding 1.5×10^7 across the telecom C- and L-band [27]. Key steps to achieve such high-Q include waveguide preform reflow to reduce scattering losses [39], and thermal annealing to reduce hydrogen absorption losses [27]. On the Si_3N_4 chip, the microresonator is coupled to a bus waveguide, and both waveguides are 1.50 m wide and 700 nm high, to achieve high coupling ideality [172]. Light is coupled into and out of the Si_3N_4 bus waveguide via double-inverse tapers on the chip facets [166], with > 25% total coupling efficiency (fiber-chip-fiber). The Si_3N_4 chips were characterized using a diode laser spectroscopy technique [114, 115] calibrated by a fully stabilized commercial optical frequency comb system. Each resonance was fitted [109] to extract intrinsic linewidth $\kappa_0/2\pi$, coupling strength $\kappa_{ex}/2\pi$, and backscattering rate $\gamma/2\pi$. The microresonators show an intrinsic Q-factor of $Q_0 \sim 1.5 \times 10^7$ across the telecom C- and L-band (Figure 3.6 f) [27], based on the statistics of more than 1000 resonances. The calibrated transmission spectrum allows measurement of the dispersion profile showing the deviation of equidistant resonances from each other. The fitting reveals a FSR ($D_1/2\pi$) of ~ 98.3 GHz and a second order dispersion ($D_2/2\pi$) equals to 1.22 MHz (Figure 3.6 e & f). Single soliton states with 99 GHz repetition rate have already been demonstrated in these high Q-factor Si_3N_4 microresonators, using only a diode laser at a record-low output power of 9 mW [27] (Figure 3.4). However, that scheme required a well-stabilized bulk laser diode (Toptica CTL 1550) which is not feasible in a compact package and not compatible with further potential photonic integration.

First, without using an EDFA, we use the semiconductor laser directly coupled to the Si_3N_4 chip, as shown in Figure 3.6. The laser shown in Figure 3.6 b & c, consists of two parts. The first part is a semiconductor-based gain chip that facilitates high-power operation. It features a highly reflective facet on one side, and an angled facet on the other for out-coupling [197]. The second part is a customized fiber Bragg grating (FBG) that supports single frequency and narrow linewidth operation. The light from the gain chip is coupled efficiently to the FBG via a polarization-maintaining (PM) lensed fiber. The laser power and frequency can be tuned via current control on the gain chip and temperature control on either the gain chip or the FBG. The

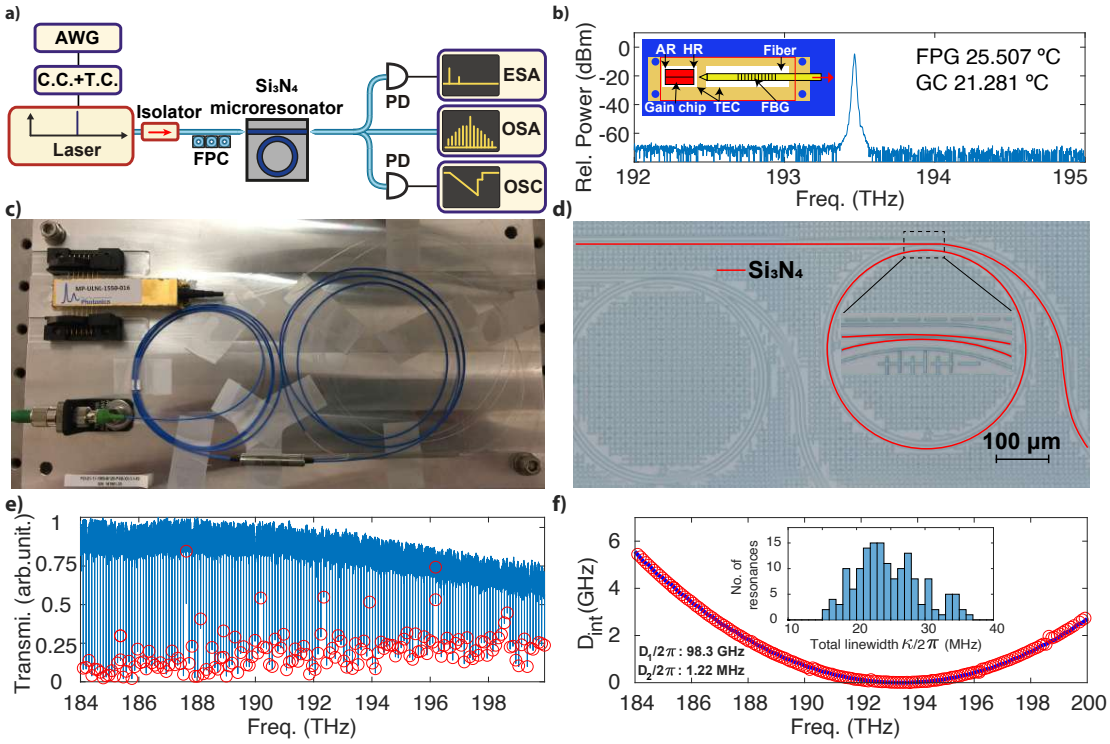

Figure 3.6: **Experimental setup for soliton microcomb generation using the semiconductor laser. a** The semiconductor laser is coupled to a Si_3N_4 microresonator chip. The laser is operated via a current and a temperature controller (C.C. and T.C.). An arbitrary waveform generator (AWG) scans the laser frequency over the resonance by directly modulating the laser current. The generated soliton microcomb spectrum is analyzed by an optical spectrum analyzer (OSA) and an electrical spectrum analyzer (ESA). OSC: Oscilloscope. FPC: Fiber polarization controller. **b** The optical spectrum of the semiconductor laser consists of a gain chip, a FBG, and an external fiber cavity (inset). AR: Anti-reflective coating. HR: Highly reflective coating. TEC: Thermoelectric cooler. **c** A butterfly-packaged ultra-low noise semiconductor laser mounted on an aluminum breadboard. **d** A microscope image showing a Si_3N_4 integrated microresonator. The inset shows a zoomed-in image of the coupling section between the bus waveguide and the microresonator. The bus waveguide and microresonator are red-shaded. **e** The transmission spectrum is measured using a widely tunable laser diode calibrated via a self-referenced fiber mode lock laser. **f** The dispersion profile (D_{int}) of the microresonator with second-order dispersion equals to 1.21 MHz. The linewidth ($\kappa/2\pi = \kappa_0/2\pi + \kappa_{\text{ex}}/2\pi$) distribution of the microresonator extracted from calibrated transmission scan using a fully stabilized frequency comb (inset).

maximum laser output power is around ~ 100 mW. The laser center frequency is approximately 193.4 THz and has a tuning range of ~ 100 GHz (Figure 3.6 b). An isolator is used at laser output to avoid back reflection into the laser. Light coupling to the Si_3N_4 bus waveguide via optical fibers impacts the phase difference between the pumped and the back-reflected (feedback due to intrinsic scattering) light and leads to unstable operation. This resonant feedback has been recently used in chip-based microcomb systems to access the soliton[157, 99, 19]. Moreover, a single soliton generation requires a large detuning from the pump laser, which is difficult to achieve,

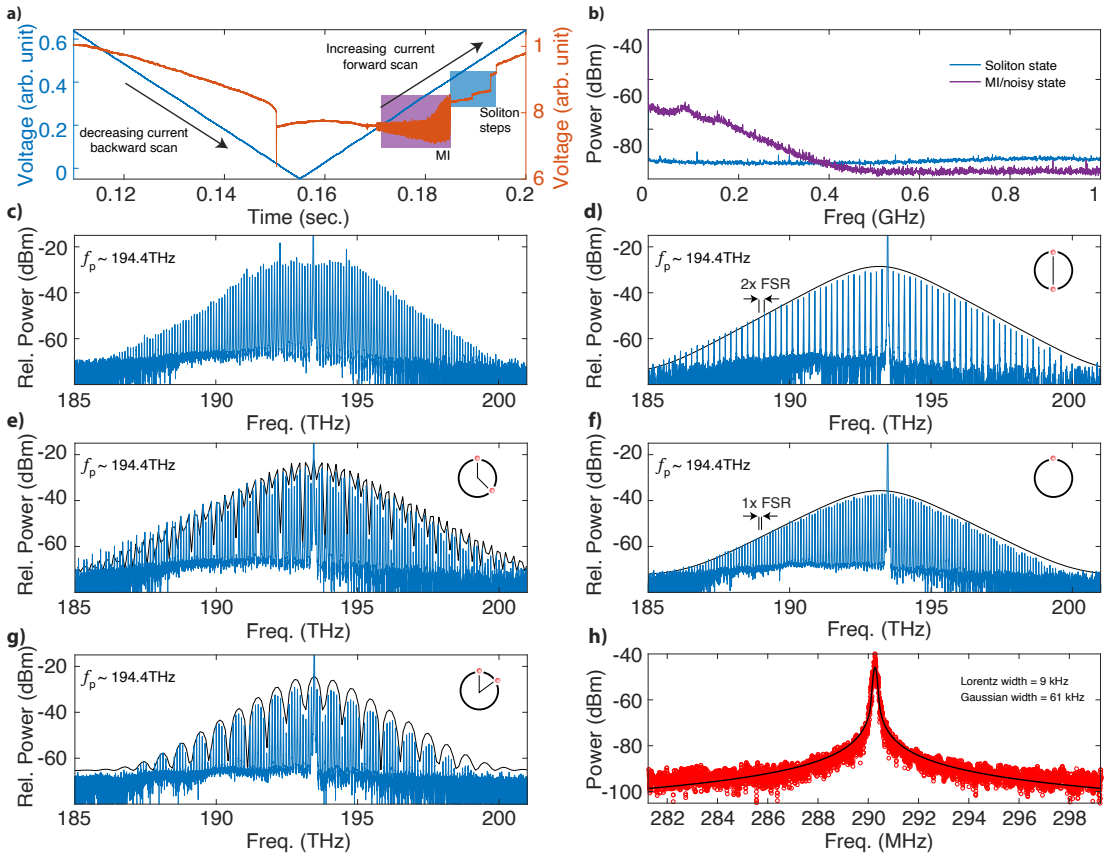

Figure 3.7: **Different microcomb states of 99 GHz repetition rate in a Si_3N_4 microresonator driven by the semiconductor laser.** **a** The transmitted signal is recorded by modulating the current applied to the gain section of the semiconductor laser. In the forward scan part, low noise steps (light blue shaded region) correspond to multiple and single solitons. At the same time, the noisy region (light magenta-shaded region) indicates the modulation instability state. **b** A low RF spectrum is recorded to access the coherence properties of different comb states (MI and soliton). **c** An MI comb is generated by scanning the laser frequency over a microresonator resonance from the effective blue-detuned side to the red-detuned side and stopping at a light magenta-shaded region (a). **d, e, f, & g** By optimizing the scan endpoint, a low-noise two soliton crystal state (d), multi-soliton state (e & g), and a single soliton state (f) are generated. The single soliton state (f) with a characteristic $\text{sech}^2(f)$ profile features a 3 dB bandwidth of 19 nm and a pulse duration of 131-fs. **h** Heterodyne beat note signal fitted with a Voigt profile shows a Lorentzian linewidth of 9 kHz and a Gaussian linewidth of 61 kHz.

and critically depends on the backscattered light and phase difference [101]. While the current method does not require precise control, and a single soliton can be accessed deterministically via current tuning.

The laser frequency is tuned into a microresonator resonance by controlling the FBG temperature in small steps until a full resonance profile is observed on the microresonator transmission spectrum. Then, the laser power is increased by increasing the current (~ 300 mA) applied to the gain chip until a step-like pattern is observed in the transmission signal, indicating the formation of solitons (Figure 3.7 a). As the laser frequency changes simultaneously with the output power change due to the current increase, the FBG temperature is controlled accordingly for the laser frequency to remain on resonance. Benefiting from the high microresonator Q and reduced thermal effect in Si_3N_4, the single soliton state is initiated deterministically via current tuning of the gain chip, which significantly reduces the system complexity compared with other soliton tuning techniques using "power kicking" [125], single sideband modulators [124] and dual lasers [199]. In the present work, the soliton state is generated by the simple forward laser frequency tuning method [43]. Conventionally, a triangular shape voltage signal is applied to the laser piezo to scan over the resonance. However, laser frequency tuning is limited by the piezo scan speed. Here, we directly modulate the current applied to the gain chip, allowing fast scan over resonance at kHz rate, which in turn modulates the laser frequency and power for soliton tuning [43] and switching [123]. The soliton existence range is sufficiently long, as shown in Figure 3.7 a, due to the high Q-factor and the reduced thermal effects. Therefore simultaneous modulation of laser frequency and power does not add extra complexity to soliton tuning. The reason is that, as the soliton exists on the effectively red-detuned side, the current increase applied to the gain chip leads to an increase in the laser wavelength as well as the optical power. In contrast, the input power increase can increase the soliton existence range. A baseband radio-frequency (RF) spectrum, shown in Figure 3.7 b, is recorded to verify the coherence of different comb states. A modulation instability (MI) comb state is generated initially by adjusting the endpoint of the voltage scan signal, which modulates the laser current (Figure 3.7c). Then, multiple multi-soliton states are initiated by increasing the current and performing a scan over resonance from the blue-detuned to the red-detuned side (Figure 3.7 c, d, & g). A low-intensity noise is observed on the electrical spectrum analyser (ESA), indicating the coherent nature of the soliton state (Figure 3.7 b & f). Once all parameters are known, such as the current applied to the gain chip and the temperatures of the gain chip and the FBG, a soliton can be generated deterministically by performing an optimized current scan, which significantly simplifies the soliton initiation process. Heterodyne beat note measurements are carried out further to confirm the intrinsic coherence of the soliton state. A narrow-linewidth (~ 10 kHz) reference laser is used to generate a beat note with a comb tooth. The measured beat note is fitted with a Voigt profile and shows a Lorentzian linewidth of 9 kHz and a Gaussian linewidth of 61 kHz, as shown in Figure 3.7 h (Appendix A). The linewidth is likely limited by the current and the temperature fluctuations of the laser driver as the main contribution to beat note comes from Gaussian lineshape (flicker noise). The single soliton spectrum is fitted with a hyperbolic secant squared ($sech^2$) function, showing a pulse duration of 131-fs and a 3 dB bandwidth of 19 nm.

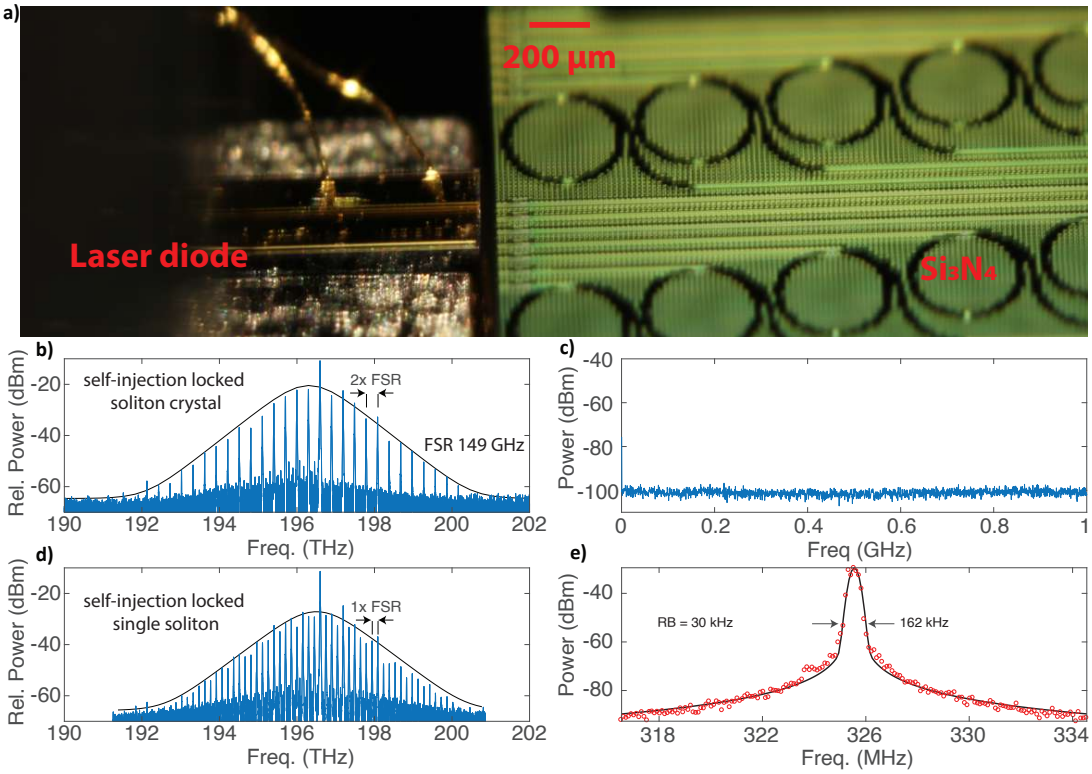

Figure 3.8: **Soliton generation via self-injection locking effects.** **a** A multi-frequency laser diode is coupled to a Si_3N_4 microresonator. When one of the laser modes is aligned to cavity resonance, fast optical feedback arises due to the intrinsic scattering of the microresonator coupled back to the laser diode via the same bus waveguide. **b** A soliton crystal is generated by tuning the current of the laser diode. **c** A low noise radio-frequency (RF) intensity is measured to verify the coherence of the state of the soliton crystal (b). **d** A single soliton is initiated via self-injection locking with manual tuning of laser diode current. **e** A heterodyne beat note is measured by beating on of single soliton line in **d** to show the low noise of the state.

3.6 Soliton generation via self-injection locking

The soliton generation via current/electrical control, in conjunction with a compact laser diode module (section 3.5), is critical for implementation in practical applications. But, the wider implementation of such systems, such as data centers and LiDAR modules, requires further integration into the chip-based module. However, these lasers suffer from the limited output power of the gain chips or laser diodes, typically below 50 mW output power. Recent improvements in the fabrication process have enabled soliton generation at an optical power of < 10 mW making soliton generation possible with a chip-based laser diode (section 3.4). When CW light from a laser diode is coupled to a microresonator via an optical waveguide, a portion of light from the microresonator starts traveling in the backward direction due to scattering in the microresonator (inhomogeneous and sidewall roughness). This feedback locks the pump to a microresonator and stabilizes it. This phenomenon is known as self-injection locking [157, 98]. Simultaneously,

direct feedback allows generating the soliton via tuning of current by maintaining a constant phase difference, optimized for specific locking regimes, between pumped and back-propagated light (covered in more detail in chapter 4).

Here, a chip-based laser is directly coupled to a microresonator with no elements in between, such as modulators, amplifiers, and isolators, as used in previous sections (Figure 3.8 a). Self-injection-locking allows using a multi-frequency laser which was never used to initiate the soliton in the previous demonstration using a Si_3N_4 microresonator. Single and crystal soliton states are generated by simply tuning the current applied to the multi-frequency laser diode without any complex tuning mechanism (Figure 3.8 b & d). Low-noise radio frequency (RF) intensity and heterodyne beat note measurements are performed to verify the coherence properties of the soliton states (Figure 3.8 c & f). This scheme provides a lead towards a fully integrated on-chip low-noise multi-wavelength source.

3.7 Soliton generation via on-chip heterogeneously integrated AlN

Access to on-chip actuation and laser frequency control is important for applications such as chip-based frequency combs and narrow linewidth lasers [87]. The ultra-low noise lasers, on-chip microwave source and frequency synthesizers are phase-locked to reference cavities. The conventional approaches for phase stabilization are based on bulk external components, e.g., acousto-optic and phase modulators [200, 201, 202]. The external components limit the photonic integration of chip-based microcomb systems. The on-chip high-speed actuators could bring disruptive improvement in the soliton microcomb and laser based on integrated platforms (Si_3N_4). Previously, this has been achieved by using graphene, ferroelectric lead-zirconate-titanate, and on-chip heaters [94, 203]. However, these methods suffer from high power consumption (heaters), low-speed (few kHz, heaters), and maintaining low-loss in Si_3N_4 waveguide (with graphene). These challenges are eliminated by integrating bulk acoustic resonators monolithically on ultralow-loss Si_3N_4 waveguides. The detailed fabrication is reported elsewhere [204]. Alternatively, direct soliton generation in materials exhibiting the Pockels effect, such as AlN [205, 206, 207, 208] and $LiNbO_3$ [209, 63, 62], allows simultaneous high-speed actuation; however, these platforms are not yet as mature as Si_3N_4. The AlN-based on-chip actuators are operated with ultralow power (< 300 nW), high speed (~ MHZ), bi-directional tuning, and are free from hysteresis. The piezoelectric AlN-based actuators are based on the stress-optic effect.

A CW laser is coupled to the microresonator. The soliton is initiated by strain-tuning the resonance to the laser [94] via varying the voltage, using the setup shown in Figure 3.9 a. The laser is initially set blue-detuned by 0.3 GHz from a microresonator resonance and launches 15 mW of power into the waveguide (60% coupling efficiency per chip facet). Though not required for soliton initiation, we monitor the resonance-laser detuning using an electro-optic modulator (EOM) and a vector network analyzer (VNA) [44]. As shown in Figure 3.9 c, the resonance is initially tuned to the laser (130 V→83 V), and subsequently generates modulation instability (MI, 50 V) and a multi-soliton state (MS, 44 V). Next, the AlN voltage is increased, so the backward

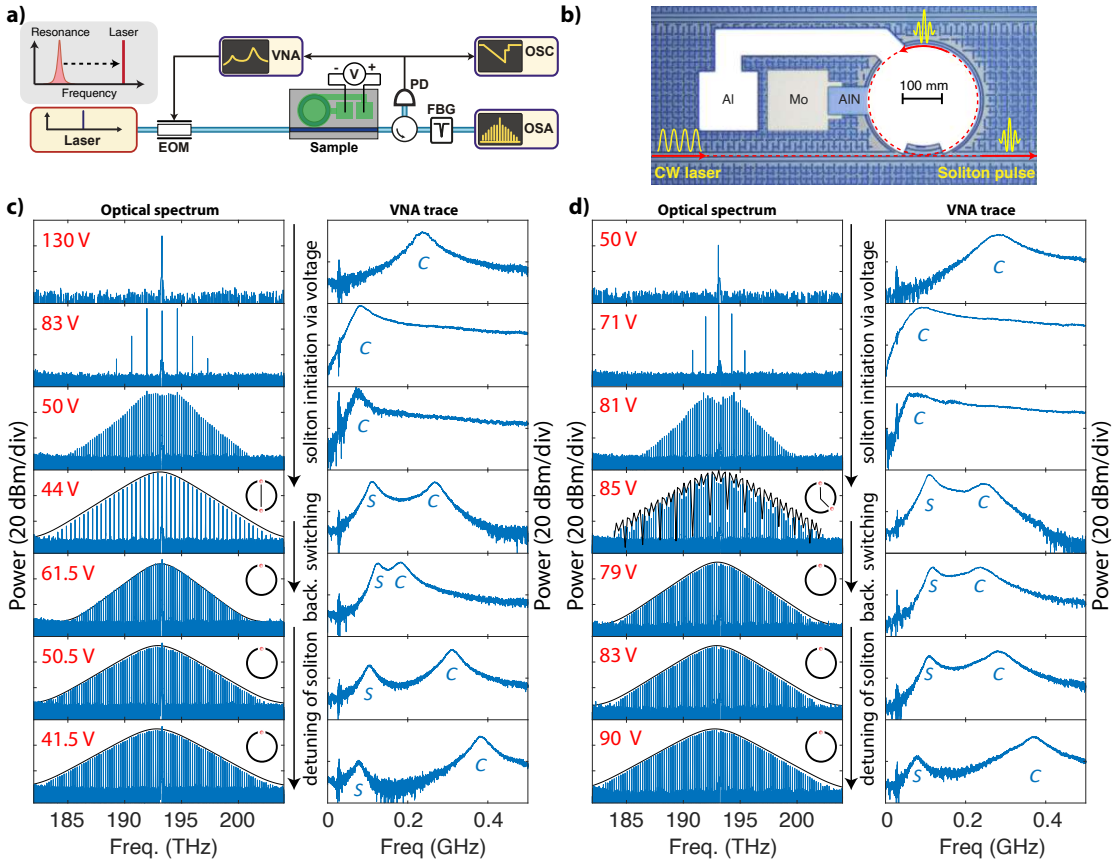

Figure 3.9: **Voltage controlled soliton initiation, switching, and control via AlN. a** Optical setup used to generate and control soliton by using a pair of DC-probes driven by a high-voltage source. VNA: vector network analyzer, OSC: Oscilloscope, OSA: optical spectrum analyzer, FBG: fiber Bragg grating-based filter, and PD: photodiode. **b** Microscope image showing the Si_3N_4 microresonator with a disk-shaped AlN actuator. **c** Soliton detuning control via AlN actuation. Left: Initially, the resonance is 0.3 GHz red-detuned (VNA signal) from the laser (130 V). The resonance is tuned to the laser and generates primary comb (83 V), modulation instability (MI, 50 V) and a perfect soliton crystal (PSC) state (MS, 44 V). Once the PSC is generated (44 V), the voltage is increased to switch to enable switching to a single soliton state (SS, 61.5 V). The soliton detuning, as well as the bandwidth, is further increased by decreasing the voltage (41.5 V). **d** Soliton detuning control via AlN actuation. Left: Initially, the resonance is 0.3 GHz red-detuned (VNA signal) from the laser (50 V). The resonance is tuned to the laser and generates primary comb (71 V), modulation instability (MI, 81 V) and a multi-soliton state (MS, 85 V). Once the multi-soliton is generated (85 V), the voltage is decreased to switch to enable switching to a single soliton state (SS, 79 V). The soliton detuning, as well as the bandwidth, is further increased by increasing the voltage (90 V).

tuning enables switching [44] to the single soliton state (SS, 61.5 V). The voltage is reduced again (41.5 V) to increase the soliton bandwidth. Figure 3.9 d shows different soliton states with different applied voltages.

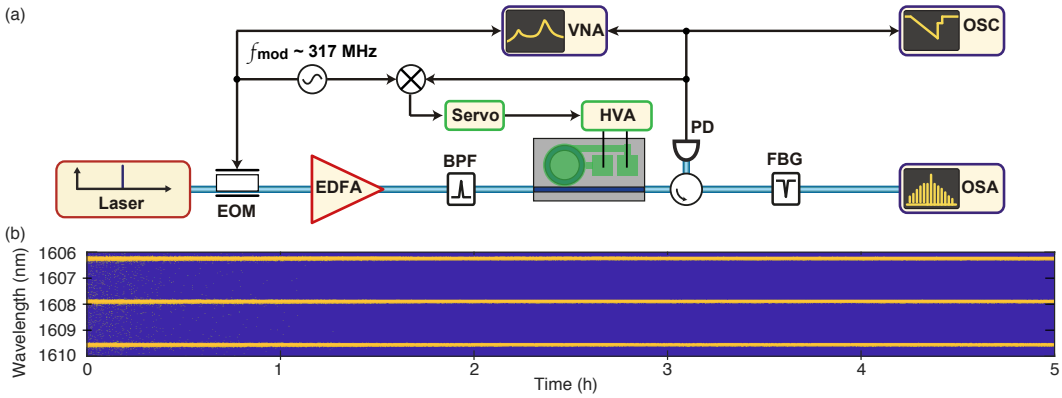

Figure 3.10: **a** Experimental setup and result for Long-term stabilization of the soliton microcomb. OSC: oscilloscope, VNA: vector network analyzer, HVA: high voltage amplifier, BPF: bandpass filter, and FBG: fiber Bragg grating. **b**Soliton stabilization over 5 hours, realized by locking the resonance to the laser and maintaining the soliton detuning.

In addition to soliton generation and switching, the soliton can be stabilized by locking the cavity to an external laser. The experimental setup to stabilize the soliton microcomb over 5 hours is shown in Figure 3.10 a. A feedback loop is applied in order to fix the soliton detuning at 317 MHz and eliminate the detuning fluctuation over a long-term. The VNA is used only to monitor soliton detuning over a long term. Figure 3.10 b shows the evolution of three soliton comb lines over 5 hours. The on-chip actuator further allows the locking of the repetition rate to an external reference, as mentioned in more detail in paper [93].

3.8 Soliton generation at microwave repetition rate

One of the most promising applications using soliton microcombs is to build ultra-low-noise photonics-based microwave oscillators [96]. This requires a comb repetition rate operating in the microwave domain, such as below 20 GHz in the microwave K- and X-band. However, soliton microcombs at microwave repetition rates have only been attained in silica [210] and crystal resonators [43], not an integrated platform such as Si_3N_4. Realizing full photonic integration based on silica and crystals is very challenging. For example, silica requires suspended structures in the air, while crystals are not amenable to wafer-scale processing, both of which require absolute isolation from contamination and moisture. The main challenges compounding soliton microcomb in Si_3N_4 at microwave repetition rate are all related to the optical losses in Si_3N_4 waveguides caused by the fabrication process. Low microresonator Q factor, corresponding to high waveguide loss, requires power amplifiers to reach the sufficient power level for comb generation and complex schemes to access the soliton state from the chaotic comb state. High Q is strictly required for future Si_3N_4 – based soliton microcombs integrated with other on-chip functionalities such as lasers and modulators.

The principle of microwave generators based on integrated soliton microcombs is depicted in

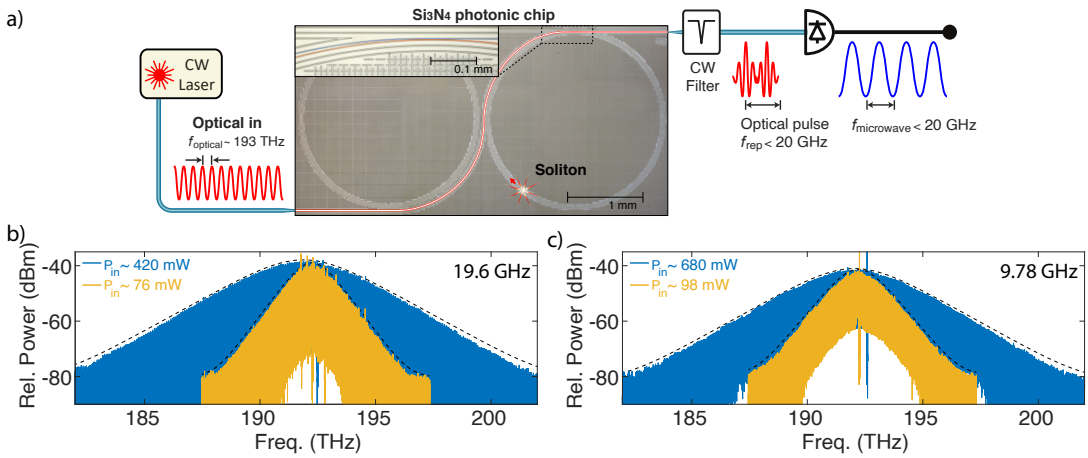

Figure 3.11: **Si_3N_4 based microwave repetition rate soliton generation.** .**a** Concept of microwave generation using an integrated Si_3N_4 soliton microcomb driven by a CW laser. The microscope image of the Si_3N_4 photonic chip highlights the bus-waveguide-to-ring-resonator coupling and stress-release patterns to prevent Si_3N_4 film cracks. **b** Single soliton spectra of 19.6 GHz repetition rate with 76 mW power in sample A (yellow, 3dB-bandwidth of 11.0 nm), and with 420 mW power in sample B (blue, 3dB-bandwidth of 26.9 nm), and their spectrum fit (black dashed). **c** Single soliton spectra of 9.78 GHz repetition rate with 98 mW power in sample C (yellow, 3dB-bandwidth of 12.5 nm), and with 680 mW power in sample D (blue, 3dB-bandwidth of 25.8 nm), and their spectrum fit (black dashed).

Figure 3.11 a. A photonic integrated microresonator is driven by a near-infrared continuous-wave (CW) laser to produce an optical pulse stream, which upon photodetection, generates a microwave signal whose frequency depends on the microresonator FSR.

Using the setup shown in Figure 3.1 a, single solitons are generated via simple laser piezo frequency tuning [44]. As shown in Figure 3.11 b, in sample A (yellow), the single soliton is generated with 38 mW power in the bus waveguide on-chip (76 mW power in the input lensed fiber). At the same time, parametric oscillations are observed at 7 mW. The single soliton spectrum fit shows a 3dB-bandwidth of 11.0 nm, corresponding to a pulse duration of 232 fs. Not only is this the first single soliton of a K-band repetition rate among all integrated platforms, but it also represents an extremely low threshold power for soliton formation, on par with the power values in silica and crystalline microresonators. We also generate single solitons at a 9.78 GHz repetition rate in the X-band, as shown in Figure 3.11 (c), with a power of 56 mW in sample C (yellow) and 340 mW in sample D (blue). The 3dB-band widths are 12.5 nm (yellow, 158 comb lines, 203 fs pulse duration) and 25.8 nm (blue, 327 comb lines, 98.6 fs pulse duration), respectively.

Next, we systematically analyze the phase fluctuations of the soliton-based K- and X-band microwave carriers. The measurement setup is shown in Figure 3.11 a. The soliton pulse stream is driven by a CW external cavity diode laser (Toptica CTL). After the microresonator, the excess CW pump light is rejected using a narrow-band optical notch filter before photodetection of the

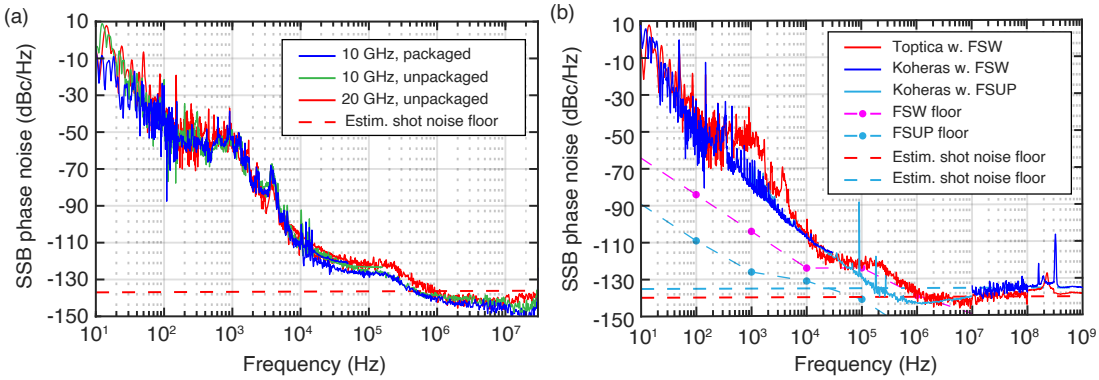

Figure 3.12: **Phase noise analysis of microwave signal generated via Si_3N_4 microresonators.** **a** Phase noise measurement of 10 and 20 GHz microwave carriers (packaged and non-packaged). **b** Phase noise comparison when pumping the Si_3N_4 using different lasers (Toptica and Koheras) to correlate different noise mechanisms.

soliton repetition rate on a fast InGaAs photodiode (Discovery Semi. DSC40) whose output electrical signal is fed to a phase noise analyzer (PNA, Rohde & Schwarz FSW43). The soliton repetition rates around 9.78 GHz are characterized in the free-running state, i.e., neither the laser frequency and power nor the microresonator is actively stabilized. A slow frequency modulation at ~5 Hz rate is observed, likely caused by the unstable chip coupling using suspended lensed fibers, susceptible to vibrations. We glue ultrahigh numerical aperture (UHNA) fibers to increase the coupling stability to the chip using a photonic packaging technique (subsection 3.9.4).

Figure 3.12 a shows the measured free-running phase noise of the 9.78 GHz soliton repetition rate before and after packaging (Figure 3.16 a) the same chip, in comparison with the phase noise of a K-band soliton in an unpackaged 19.6 GHz FSR chip. Note that in the case of the unpackaged 19.6 GHz soliton, though lensed fibers are used to couple light into and out of the chip, the power transmitted through the chip is actively stabilized, which is to mimic the case of a packaged chip with stable fiber-chip coupling. The packaging reduces the microwave phase noise at low offset frequencies < 30 Hz, yet at higher offset frequencies, the phase noise reduction is minimum. Furthermore, no prominent phase noise difference between the unpackaged 19.6 and 9.78 GHz solitons is observed. In the following, we focus only on the unpackaged 19.6 GHz soliton to further investigate the source of the observed phase noise.

The laser phase noise is measured and correlated with the soliton repetition rate noise to investigate the role of laser noise in the generated microwave signal. The conversion of optical to microwave noise is estimated as −55 dB (see SI, [24]). When the soliton is driven by the Toptica laser, as shown in the red curves in Figure 3.12 a and b, the noise feature within 100 Hz – 10 kHz offset frequency is caused by the Toptica laser phase noise, while the step-like feature within 20 kHz – 1 MHz is caused by the FSW43 noise floor. In a different case, when the soliton is driven by a fiber laser (Koheras AdjustiK) featuring a lower phase noise level, the soliton phase noise is reduced as shown in the blue curve in Figure 3.12 d. An additional PNA (Rohde &

Schwarz FSUP, with cross-correlations) is used here to overcome the FSW43 device limitation which however results in the phase noise within 200 kHz – 10 MHz falling marginally below the shot noise floor, likely caused by parasitic anti-correlation effects in the FSUP [211]. Our analysis shows that, when using the fiber laser, the main phase noise limitation is the laser relative intensity noise (RIN) for offset frequencies < 1 MHz, with a contribution from the impact of the thermo-refractive noise (TRN) [212] in Si_3N_4 on the cavity-pump detuning at offset frequencies between 10 – 100 kHz (see SI, [24]). The microwave carrier's absolute single-sideband (SSB) phase noise power spectral density reaches ~ -80 dBc/Hz at 1 kHz offset Fourier frequency, ~ -110 dBc/Hz at 10 kHz and ~ -130 dBc/Hz at 100 kHz. The pump lasers mainly limit our current soliton phase noise performance; thus further phase noise reduction can be achieved using lasers with lower phase noise and RIN.

3.9 Optical packaging for soliton generation

Silicon nitride microresonators fabricated using other processes that do not feature high-Q as shown here, or high-Q microresonators with lower FSR may still require high input power well above 100 mW. Meanwhile, waveguides and microresonators based on other material platforms such as $LiNbO_3$ [213, 209] and AlN [208] show rich nonlinear physics and can be used to build integrated electro-optic modulators [62], which is challenging to achieve on Si_3N_4 due to the absence of effective χ^2 nonlinearity. However, compared with Si_3N_4, these waveguide platforms typically have a much higher loss (lower microresonator Q) due to the fabrication constraint, thus again, high power is needed to induce prominent nonlinear processes based on these platforms. Moreover, most practical applications based on soliton require ~ -10 dBm power per line for 100 GHz or lower FSR microresonator, which needs over-coupling (κ_{ex}>3×κ_0, [21]) the microresonator leading to higher threshold power. To this end, we also developed a generic, robust packaging technique to build a compact module for chip-based nonlinear photonics that could be implemented either alone with a ULN laser or with an optical amplifier. The critical feature distinguishing our packaging technique from other solutions is the high-power handling capability, which is central for soliton microcomb generation (see section 2.11). To the best of our knowledge, such a high-power packaging solution or similar ones has been largely unexplored in the past, due to the strict misalignment tolerance (< 1 μm) and high-power operation (> 150 mW) [13] (section 2.9). A 2-cm-long ultrahigh numerical aperture (UHNA) fiber of ~ 4.1 μm mode field diameter is used to mode-match the fiber mode to the inverse taper mode on the Si_3N_4 chip facet, and is spliced with a single-mode fiber (SMF, SMF-28) fiber with ~ 1 dB splicing loss (see, section 2.4 & Figure 2.4 b) [214]. Fiber-chip-fiber through coupling efficiency of 15% is achieved using the UHNA fiber (including the splicing loss). The splicing loss is minimized by performing a multiple arc discharge, allowing the UHNA fiber core to expand for adiabatic mode conversion. The fiber is aligned to the chip input facet mechanically, and then a drop of epoxy is dispensed at the fiber-chip interface using an accurate pneumatic valve. One important aspect of the packaging is to keep the initial drop size as small as possible (Figure 3.13 a, inset), to avoid extra loss due to dimensional changes which occur during the glue curing. After dispensing the

glue, UV curing is performed in 3 steps with different UV light intensities for optimal curing performance: 100 mW/cm^2 for 0.5 - 1 min, 200 mW/cm^2 for 1 - 3 min and 300 mW/cm^2 for 3 - 5 min (see for more detail section 2.9). After UV curing, the packaged device is tested for long-term stability with input laser power below 1 mW to show the robustness of the packaged device (similar to the one in, Figure 2.10).

3.9.1 THz Microresonator - first generation

A microresonator with a repetition rate of 1 THz is packaged to demonstrate the feasibility of Si_3N_4 based optical comb generation. A THz soliton microcomb can be generated with an input power below 500 mW [3]. The key point before packaging is to characterize the device and package better-performing devices. Initial measurements showed that resonators are critically coupled with narrow linewidth resonances with intrinsic $\kappa_0/2\pi$ around 44 MHz. This high Q – factor enables comb generation with a few tens of mW input power.

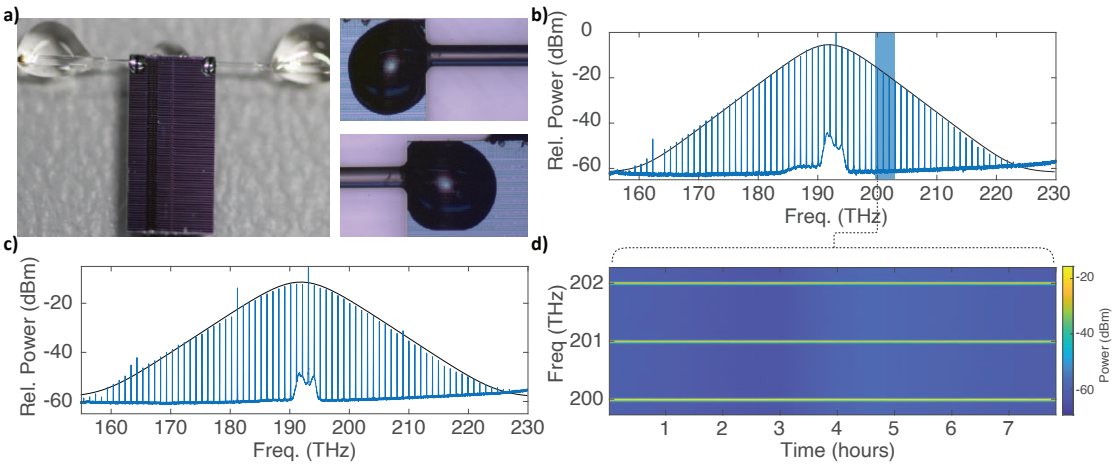

Figure 3.13: **Soliton generation in packaged 1 THz Si_3N_4 microresonators. a** A packaged THz microresonator with a magnified view of optical epoxy at the chip facet. The packaged chip is placed on the glass slab. The UHNA fiber is glued to the glass slab away from the chip facet to stabilize the joined UHNA fiber. **b & c** Soliton in a packaged device at an input power of 500 mW (b) and 1.2 W (c). The single soliton state is tuned from the multi-soliton state by tuning the laser towards a lower wavelength. No active locking is used to remain in the soliton state. **d** Stability of the generated soliton in the THz microresonator (b) shows that the soliton state can be maintained for more than 5 hours. This shows the importance of integration, as there is no need to align the fiber again actively.

After initial characterization, the next goal is the generation of soliton in a packaged device. A THz microresonator, as shown in Figure 3.13 a, is packaged using the method described in the above section (in detail in section 2.9). The device dimensions are as follows: resonator width is 1.52 (1.61) µm, waveguide width is 0.6 (0.6) µm, and distance between resonator and waveguide is 0.95 (0.95) µm (Figure 3.13 c (b)). The coupling efficiency of the microresonator before and

[3] Depending upon the coupling efficiency, Q-factor, and nonlinearity of the resonators.

after the packaging is around 13.8% and 12 %, respectively. After complete curing, the device is pumped using the setup described in Figure 3.1. At high power, around 1 to 2 % coupling degradation is observed, which can be related to the temperature increase at the interface of chip facets. A single soliton is observed in the packaged device. A single soliton state is achieved from a multi-soliton state by backward tuning of the wavelength [123]. No special active locking or tuning mechanism is used to tune into the soliton. The soliton state is observed at ~ 570 mW input power while coupling efficiency at this point is approximately 14.5% (Figure 3.13 b). Similarly, a single is generated in another packaged THz microresonator at an input power of ~ 1.2 W with a chip through coupling efficiency of 10 % (Figure 3.13 c).

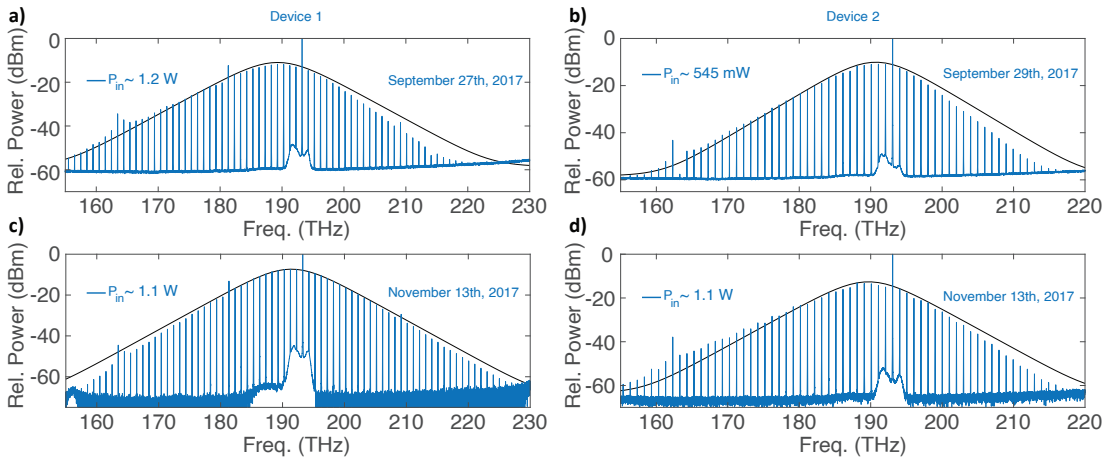

Figure 3.14: **Lifetime analysis of packaged THz Si_3N_4 microresonators.** Soliton generated in the same THz packaged devices but pumped on different days. **c & d** The soliton shown in a) is generated on September 27, 2017, with a coupling efficiency of 10 %. The soliton shown in c) is generated on November 13, 2017, with a coupling efficiency of 9.6 %. **c & d** The soliton shown in b) is generated on September 29, 2017, with the coupling efficiency of 14.3 %. The soliton shown in d) is generated on November 1, 2017, with a coupling efficiency of 11.6 %.

The next step is to check the stability of the generated soliton over time. After each minute, a spectrum is recorded on OSA. The device remained in the soliton state for > 7 hours while continuously pumping the device at ~ 570 mW, and no locking mechanism was used to remain in the soliton state. Long-term measurement proved the packaged device's robustness (Figure 3.13 d). No active alignment is needed once fibers are integrated into the chip compared to conventional lensed fiber-based coupling.

Packaged THz microresonators showed stability over time while showing the importance of packaging, as there is no need for active alignment during the experiment. Testing the performance of packaged microresonators over a long time (months) is equally important. This test will also give insight into the lifetime of cured glues and fiber misalignment over time due to pumping at high input power. A packaged microresonator shown in Figure 3.13 a is tested on two different days with a difference of 1.5 months. The soliton spectrums look similar as shown in Figure 3.14 (a & c, b & d). Figure 3.14 a and b solitons are generated at an input power of 1.2 W and 1.1 W.

The device is also pumped in between these days randomly.

Similarly, another packaged THz microresonator is tested for long-term stability. This device initially generated soliton with an input power of 545 mW as shown in Figure 3.14 b). But after one month, a soliton is generated at an input power of 1.1 W in the same device. A decrease of around 2.5 % is observed in coupling efficiency after one month. It is difficult to conclude if the decrease in coupling is due to the optical adhesive or the fiber shift due to thermal stress induced during pumping at high power. It can be associated with extra power required for soliton generation compared to the initial test (500 mW or more). At high input power, slight coupling degradation is observed.

3.9.2 100 GHz Microresonator - first generation

The 100 GHz microresonators are interesting for telecommunication, and distance measurement applications [83, 84, 86]. But low repetition rate devices require high power (0.5- 1.5 W) for generating a soliton due to higher effective mode volume ($V_{\text{eff}} = L * A_{\text{eff}}$, L is cavity length [4]). Moreover, generating a soliton at low-optical power is advantageous. However, as mentioned before, practical applications such as coherent communication and distance ranging still need a certain power level per comb line, e.g., > 20 µW per channel, for 50 channels at 100 GHz spacing. In addition, the conversion efficiency of bright dissipative soliton is less than two percent. In the next section, soliton generation in packaged devices with 100 GHz FSR will be demonstrated that is suitable for practical applications.

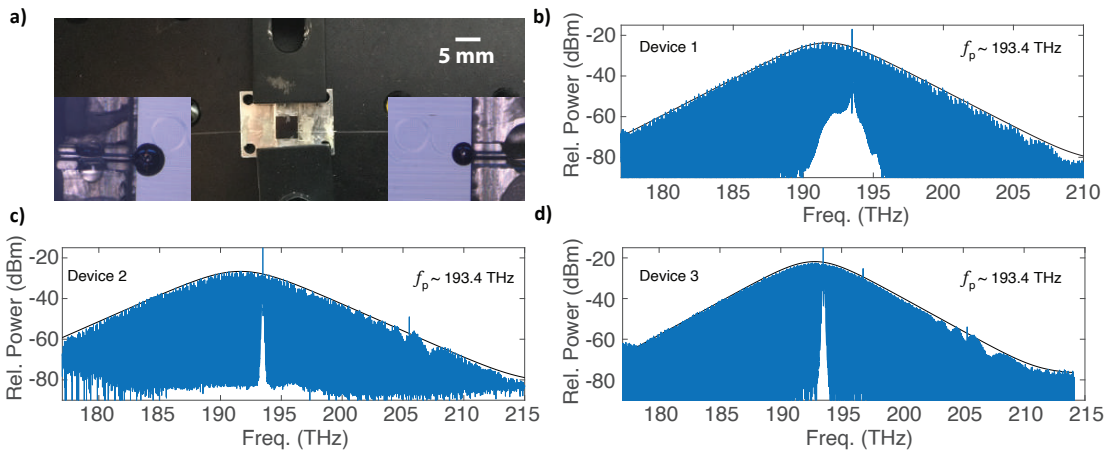

Figure 3.15: **Soliton generated in 100 GHz FSR packaged devices. a** One of the packaged devices mounted on an Al chip carrier (20 × 10 mm^2). The inset shows magnified views of the UHNA fibers and chip facets. **b, c, & d** A single soliton generated in three different Si_3N_4 microresonators. The soliton is generated by pumping resonance centered at 193.4 THz (1550 nm) in all microresonators. [* data taken by M. Karpov]

A custom-made aluminum mount is used for packaging the Si_3N_4 photonic circuits instead of the

[4] considering similar waveguide dimensions

glass slab, which is used for the initial test (subsection 3.9.1). After characterization of the Si_3N_4 microresonators, the chip is glued to Al mount with a dimension of 20×10 mm^2 (Figure 3.15, a). Similar packaging protocols have been followed, as mentioned in the previous chapter (see section 2.9). To demonstrate that the packaged device can generate a single soliton, a diode laser (Toptica CTL), along with an EDFA to amplify the power to overcome the coupling and the splicing losses, is used. A single soliton state is accessed in the packaged 99 GHz FSR microresonator with an input power exceeding 800 mW (Figure 3.15 b, c, & d). The reason for the high required threshold power (> 500 mW), in addition to 2 dB splicing loss, is that all these devices are over-coupled ($\kappa_{ex}/2\pi \sim 3 \times \kappa_0/2\pi$). The over-coupled microresonators lead to high power per comb lines at the expense of higher threshold power. Three over-coupled devices have been tested to verify package devices' stable soliton generation and high power stability for practical applications (Figure 3.15 b, c, & d). Moreover, these packaged devices have been used in applications such as optical circuit switching ([21], see chapter 5) and photonic parallel convolutional processing [26] (Figure 3.15).

3.9.3 100 GHz Microresonator - second generation

The accommodation and integration of chip-based devices into other photonic systems require packaging in a compact butterfly, traditionally used for laser diode packaging. Here, a commercially available butterfly module is utilized for packaging Si_3N_4 microresonators (Figure 3.16 a). In this particular butterfly package, the chip is glued to the Al carrier in a specific position such that the waveguide, which needs to be packaged, should align to the path in which the fiber is passed. Compared with the packaged chip shown in Figure 3.15 a, the movement along the horizontal axis is limited to the diameter of the butterfly pipe. However, these issues could be eliminated by using a custom-made butterfly package.

An ECDL and an EDFA to amplify the power are used to demonstrate that the packaged device inside the butterfly module can generate a single soliton. A single soliton state is accessed in the packaged 99 GHz FSR microresonator with an input power exceeding 150 mW (Figure 3.16 b). The packaged device can be operated in the single soliton state for a few hours without active stabilization (Figure 3.16 c).

3.9.4 10 GHz Microresonator - second generation

As mentioned in (section 3.8), the un-packaged fiber coupling leads to power drift impacting the phase noise of the microwave — a 9.78 GHz FSR Si_3N_4 microresonator is packaged to improve the coupling stability (Figure 3.16 a). After packaging the device inside a commercial butterfly package, it generates a single soliton at an input power of ~ 350 mW (Figure 3.16 b). Then, the device remained in a soliton state for over one hour without stabilization. In contrast, the unpackaged device is susceptible to vibrations, likely caused by the unstable chip coupling using suspended lensed fibers. To mitigate this effect, an acoustic-optic modulator (AOM) with a

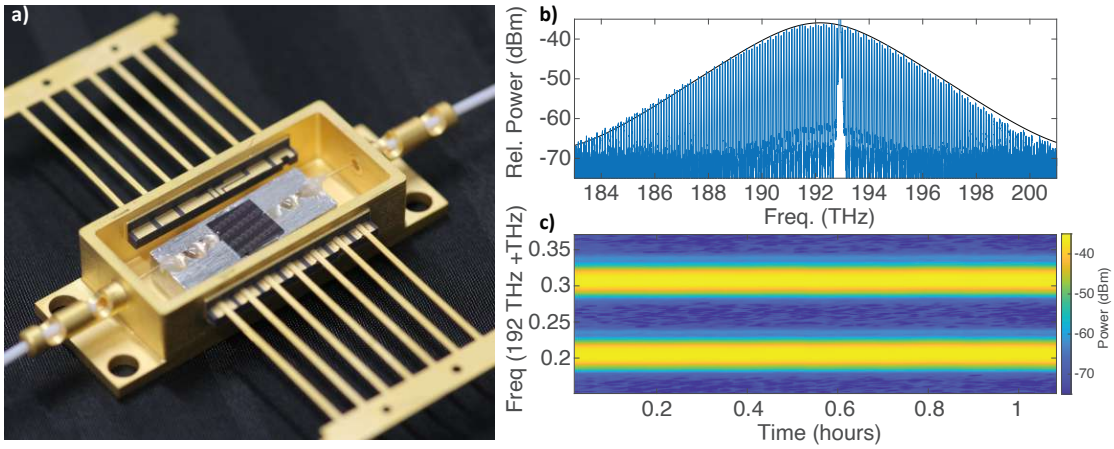

Figure 3.16: **Compact photonic packaging technique and its demonstration on Si_3N_4 microresonator chips for soliton microcomb generation. a** Photonic package of a Si_3N_4 chip using an ultrahigh numerical aperture (UHNA) fiber spliced with an SMF-28 inside a butterfly package. **b** A single soliton generation using the Toptica laser in a packaged device. **c** A long-term stability test in the packaged system showing two lines of a single soliton microcomb (spectrum in b). The soliton state is maintained for more than one hour without any active temperature stabilization (i.e., fully free running).

power servo based on a proportional-integral-derivative (PID) controller is used to stabilize the transmitted power through the chip and compensate for the coupling fluctuations. Furthermore, the detuning is also stabilized to remain inside the soliton for longer in the unpackaged device. Comparing the relative Allan deviation before and after packaging for the same 9.78 GHz FSR chip is shown in Figure 3.16 a (inset), proving that the chip packaging largely improves the soliton stability.

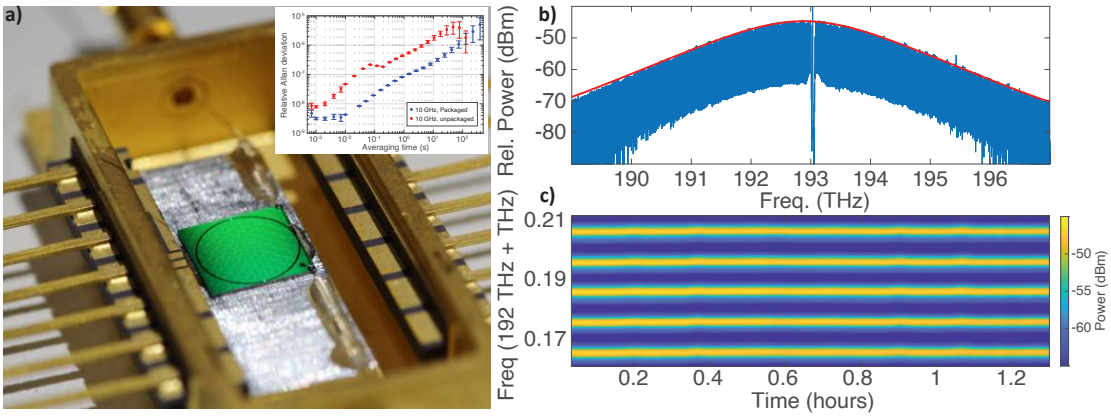

Figure 3.17: **Compact photonic packaging for soliton microcomb generation at a microwave repetition rate. a** Photonic package of a 10 GHz FSR Si_3N_4 chip using an ultrahigh numerical aperture (UHNA) fiber spliced with an SMF-28 inside a butterfly package. **b** Single soliton generation using the Toptica laser in a packaged device. **c** A long-term stability test in the packaged system showing five lines of a 10 GHz single soliton microcomb (spectrum in b). The soliton state is maintained for more than one hour without any active temperature stabilization (i.e., fully free running).

4 Electrically pumped photonic integrated soliton microcomb

In this chapter, the electrically-driven soliton microcomb by coupling an indium phosphide (III-V) multiple-longitudinal-mode laser diode chip to a high- Q Si_3N_4 microresonator is explained. We observe the formation of dissipative Kerr solitons, which is enabled by narrowing the diode laser linewidth via the injection-locking to the same microresonator. This approach, compatible with semiconductor laser diode technology, provides a route towards scalable manufacturing of microcombs as required for high-volume applications such as laser ranging or optical interconnects. The project is done in collaboration with a team of researchers from RQC (A. Voloshin, S. E. Agafonova & Prof. Michael L. Gorodetsky). The major part of the experimental work is conducted at EPFL by H. Guo and me, with substantial assistance from the RQC team. The Si_3N_4 microresonators are fabricated by J. Liu and characterized by me. The results of this work are published in Nature Communication [A. S. Raja*, A. Voloshin* et al., Nature Communications 10(1), 1-8 (2019) [1]] and a patent application is also filed [T.J. Kippenberg, M. L.Gorodetsky, A. S. Raja, H. Guo. US11513419B2 (2023)].

4.1 Background

Laser frequency combs have revolutionized frequency metrology and timekeeping and can be used in various optical technologies. Advances are underway that allow dramatic miniaturization of optical combs using Kerr nonlinear optical microresonators that enable broadband and coherent optical combs to be generated from a continuous wave laser. Such microcombs provide unprecedented form factor, low power and broad bandwidth, wafer-scale fabrication compatibility and can potentially allow combs to be field deployed outside of research laboratories. Towards this end, microcombs have already been applied in dual-comb spectroscopy [174], low-noise microwave generation [96], advanced telecommunication [84], ultrafast ranging [86, 215], and astrophysical spectrometer calibration [85, 216]. The full photonic integration of soliton microcombs in a single, compact, and electrically-driven package would allow mass-manufacturable devices compatible with emerging high-volume applications such as laser-based

[1] *equal contributions

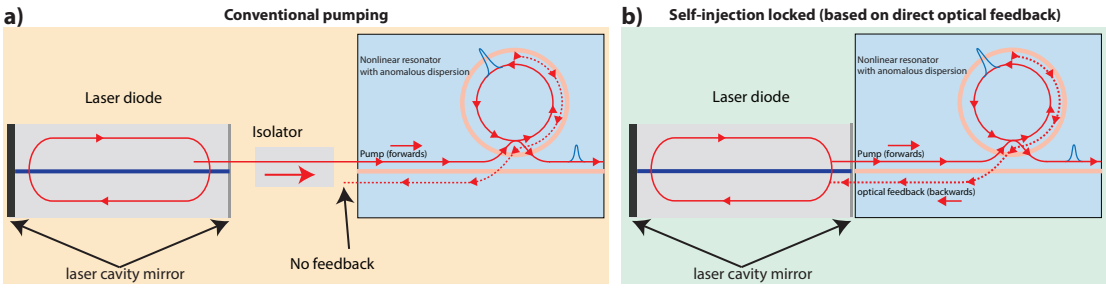

Figure 4.1: **Difference between conventional pumping and self-injection locking based generation of the optical frequency comb. a** In the conventional pumping method, light travels in one direction from laser to microresonator (forward). The optical feedback generated via the intrinsic scattering of microresonators is blocked with an isolator. **b** In self-injection locking-based pumping, Si_3N_4 microresonator reflects a portion of the light that travels backward into a semiconductor laser. This fast optical feedback stabilizes the laser and assists soliton generation if an optimum phase is achieved. Self-injection locking requires a feedback element external to the primary laser cavity.

ranging (LIDAR), or sources for dense wavelength division multiplexing for data center-based optical interconnects. Via advances in silicon photonics, such a level of integration has been achieved for lasers [3], modulators [217], and a wide range of passive and active elements which are already commercially available. Photonic integration of soliton microcombs requires not only the integration of nonlinear high-Q microresonators on-chip but also an on-chip solution for the narrow linewidth seed lasers with output power levels sufficient for soliton initiation and any laser tuning mechanism used in the soliton excitation process [218, 124, 82, 219]. Photonic integration of high-Q microresonators suitable for soliton formation has advanced significantly, in particular using Si_3N_4 – a CMOS-compatible material used as a capping layer [69]. The platform possesses several advantageous properties, including a high Kerr nonlinearity, large flexibility for dispersion engineering, outer-space compatibility [219], and a large bandgap ($\sim$ 5eV), thus free from two-photon absorption in the telecommunication band. All these advantages facilitate soliton formation in Si_3N_4 microresonators [82]. In a related effort, ultrahigh-Q SiO_2 air-clad microresonators have recently been integrated with Si_3N_4 waveguides for soliton generation [34]. Efforts to combine integrated photonic microresonators with chip-scale lasers, such as those developed in silicon photonics, have recently been made[51]. Yet, these and other approaches are still optically pumped with stand-alone bulk laser modules and typically employ additional amplifiers for soliton initiation to overcome coupling losses and the low Q-factors of integrated photonic resonators. Likewise, at the time of this study, silicon photonics-based lasers are compounded by the threshold of soliton formation that typically exceeds the laser's output power (mW scale). Advances in the fabrication of high-Q Si_3N_4 photonic integrated microresonators (intrinsic $Q_0 > 1 \times 10^7$) [60, 36, 77] suggest that electrically driven microcombs that employ chip-scale laser diodes – compatible with scalable manufacturing – may become viable.

In the following part, an electrically-driven, current-initiated soliton microcomb is shown that

significantly simplifies photonic integration. The integrated device has a volume of ca. 1cm^3 and uses a commercially available semiconductor laser diode chip. This device consumes less than 1 Watts of electrical power and produces a soliton microcomb with sub-100-GHz line spacing. By using high-Q ($Q_0 > 1 \times 10^7$) photonic chip-scale Si_3N_4 microresonators fabricated using the photonic Damascene reflow process [77, 27], in conjunction with a multiple-longitudinal-mode (multi-frequency) Fabry-Pérot InP laser diode chip, we observe self-injection locking [134, 97] in a regime where solitons are formed concurrently. Self-injection locking is passive feedback that sends a portion of the light back from the third-order nonlinear anomalous dispersion resonator to the laser cavity, which, in response, will adjust to the external optical feedback (Figure 4.1 b). In contrast, conventional soliton generation approaches did not utilize this effect (Figure 4.1 a). While self-injection locking is a phenomenon known to increase laser coherence, which can be implemented using high-Q microresonators. Such self-injection locking with concurrent soliton formation has recently been demonstrated for bulk ultrahigh-Q crystalline MgF_2 resonators (DFB [96], multi-frequency laser diode [98]). The current tuning of the laser diode can induce transitions from the injection-locking-based single-longitudinal-mode lasing (×1000 fold reduction of linewidth), to Kerr frequency combs, breather soliton formation, followed by stable multiple and single DKS formation in the integrated microresonator. Heterodyne measurements demonstrate the low-noise nature of the generated soliton states. Such an electrically-driven photonic chip-based soliton microcomb demonstrated here, provides a solution for integrated, unprecedentedly compact optical comb sources suitable for high-volume applications.

4.2 Fabrication and characterization of Si_3N_4 microresonator chip

The photonic integrated Si_3N_4 chips used in this particular study are fabricated by using the photonic Damascene reflow process [77]. Waveguide and resonator patterns were defined by deep-UV stepper lithography and transferred to the SiO_2 preform via dry etching. A preform reflow step was used to reduce the waveguide sidewall roughness caused by dry etching [59, 77], allowing for ultra-smooth waveguides and leading to high-Q factors for the microresonators. Optimized chemical mechanical polishing (CMP) allows precise control of the waveguide height to 750 ± 20 nm, measured over the full 4-inch wafer scale. No top cladding was deposited onto the Si_3N_4 waveguides. The precise dimension control by the lithography (mainly in the waveguide width) and CMP (in height) enables samples of the same design to have identical geometry at different positions on the wafer.The microresonator is coupled to the bus waveguide on the chip through the evanescent field. Light is coupled onto the Si_3N_4 chip via double inverse nanotapers [166] on the bus waveguides at both the input and output facets, i.e., from the laser diode chip to the microresonator chip and from the microresonator chip to a lensed fiber which collects the comb spectrum. In addition, the bus waveguide's geometry is designed to achieve a high coupling ideality with reduced parasitic losses [172].

The microresonator dispersion can be extracted by calibrating the transmission spectrum by a standard optical frequency comb [74, 115]. The dispersion of the microresonator is represented

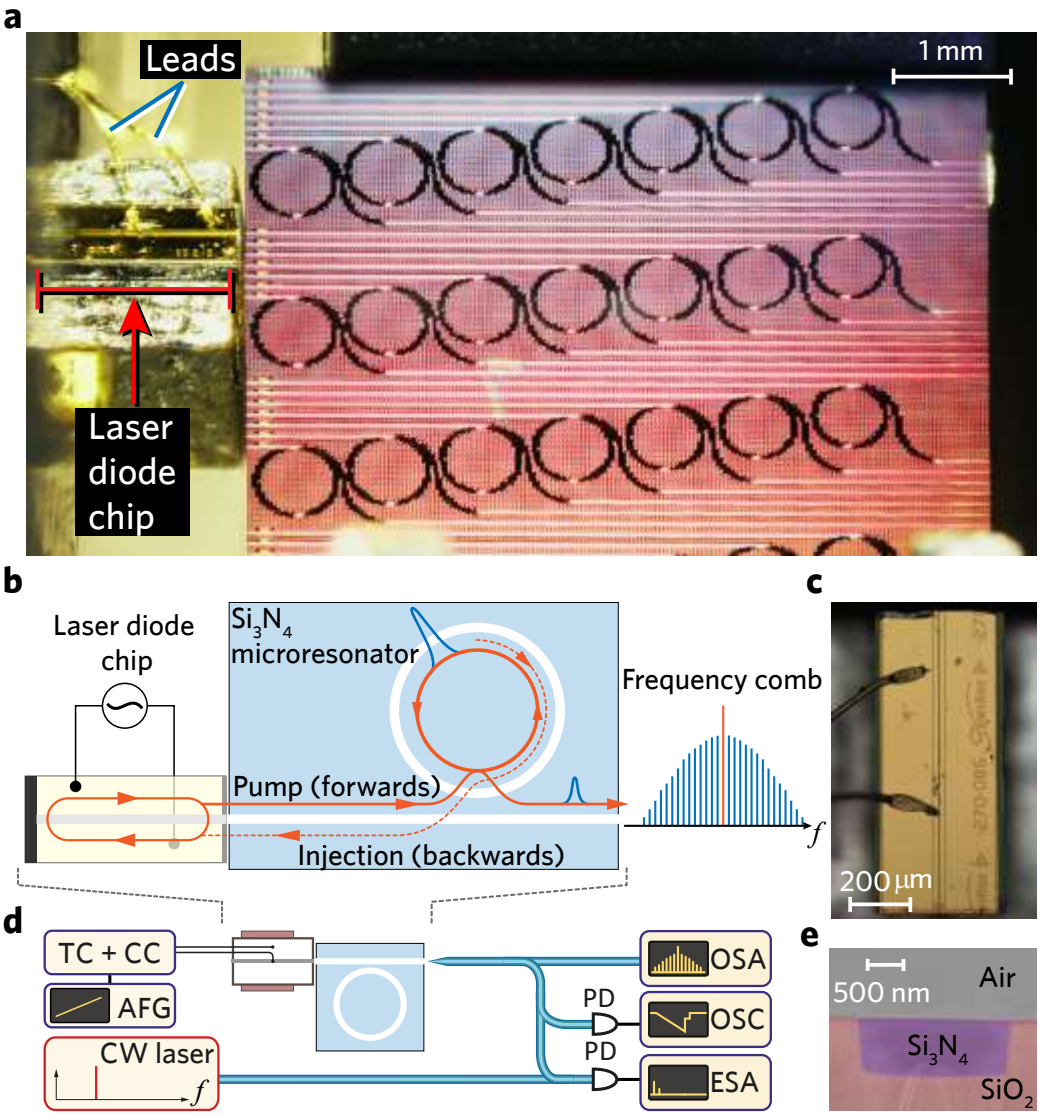

Figure 4.2: **Principle of an ultra-compact, laser-injection-locked soliton Kerr frequency comb.** **(a)** Close-range photo of the experimental setup, in which the laser diode chip is butt-coupled to a Si_3N_4 photonic chip, which contains several microresonators. **(b)** Schematic representation of the laser-injection-locked soliton Kerr frequency comb. An InP multi-frequency laser diode chip is directly butt-coupled to a Si_3N_4 photonic chip with a microresonator. **(c)** An optical image of the InP laser diode chip showing the magnified view. **(d)** Sketch of the experimental setup. The microresonator device output is characterized both in the optical domain using an optical spectral analyzer, and in the radio frequency (RF) domain using an electrical-signal spectral analyzer. In addition, to assess the coherence of the frequency comb, we employ a heterodyne beatnote measurement to a selected comb tooth with a narrow-linewidth reference laser. TC: temperature control module. CC: current control module. AFG: arbitrary function generator. OSA: optical spectral analyzer. OSC: oscilloscope. ESA: electrical-signal spectral analyzer. **(e)** False-colored scanning electron micrograph (SEM) image of the waveguide cross-section. The Si_3N_4 waveguide (blue) has no top SiO_2 cladding but only side and bottom SiO_2 cladding (red).

in terms of resonant frequency deviation with respect to a linear grid, namely:

$$D_{\text{int}} = \omega_\mu - (\omega_0 + \mu D_1) = \sum_{m\geq 2} \frac{\mu^m D_m}{m!} \tag{4.1}$$

where ω_μ is the physical resonant frequencies of the microresonator. A central resonance (to which the laser is injection locked) is given the index $\mu = 0$. $D_1 = 2\pi \times \text{FSR}$ is the repetition frequency (section 1.3). The second order element D_2 is the group velocity dispersion (GVD) of the microresonator, and $D_2 > 0$ represents the anomalous GVD. When the dispersion is described to the second order, the dissipative and nonlinear optical resonator can be described by the Lugiato-Lefever equation [121], which is equivalent to the coupled mode equation (section 1.5,section 1.6). Each resonance is fitted using the model based on coupled mode theory [109, 110] from the transmission spectrum (subsection 1.2.1). The resonance linewidth reflects the total loss rate (κ) of the microresonator, which consists of both the intrinsic loss rate (κ_0) and the external coupling rate κ_{ex}, i.e., $\kappa = \kappa_0 + \kappa_{\text{ex}}$. To extract the intrinsic Q-factor (Q_0), highly under-coupled microresonators are measured, i.e. $\kappa_{\text{ex}} \to 0$.

In this work, there are three sets of Si_3N_4 microresonators in terms of different FSRs: $\sim$ 1 THz, $\sim$ 150 GHz, and < 100 GHz. The microresonator corresponding to results shown in Figure 4.3 (f) has: $Q_0 \approx 6 \times 10^6$, FSR = 1.02 THz, $D_2/2\pi \approx 188$ MHz, for fundamental TE mode. The microresonator width is 1.53 m. The microresonator corresponding to results shown in Figure 4.4 has: $Q_0 \approx 6.5 \times 10^6$, FSR = 149 GHz, $D_2/2\pi \approx 3.90$ MHz (fundamental TE mode), the microresonatore width is 1.58 m. The microresonators corresponding to results shown in Figure 4.5 have: $Q_0 \approx 8.2 \times 10^6$, (for Figure 4.5(d)) FSR = 88.6 GHz, $D_2/2\pi \approx 1.10$ MHz (fundamental TE mode), the microresonator width is 1.58 m; (for Figure 4.5(e)) FSR = 92.4 GHz, $D_2/2\pi \approx 1.56$ MHz (fundamental TE mode), the microresonator width is 1.58 m.

Such high Q-factors have already enabled direct soliton comb generation in microresonators without amplification of the seed laser [27] (as shown in section 3.4). The threshold power for parametric oscillation can be as low as sub-milli-Watt (critical coupled), which is calculated as:

$$P_{\text{th}} = \frac{\kappa^2 n^2 V_{\text{eff}}}{4\omega c n_2} \tag{4.2}$$

where n is the refractive index, V_{eff} indicates the effective modal volume, ω is the angular frequency of light, c the speed of light in vacuum, and n_2 is the nonlinear refractive index. For Si_3N_4 microresonators with FSR $\sim$ 1 THz, we have $n \approx 1.9$, $V_{\text{eff}} \approx 1.5 \times 10^{-16}\ m^3$, and $n_2 \approx 2.4 \times 10^{-19}$ m^2/W. Hence, the threshold power is as low as $P_{\text{th}} \approx 0.62$ mW.

4.3 Experimental setup and technique

Figure 4.2 illustrates the approach taken in this work. A multi-frequency Fabry-Pérot laser diode chip (InP) is directly butt-coupled to a Si_3N_4 photonic chip [Figure 4.2(a,b)]. The butt-coupling

scheme gives an overall insertion loss of ~ 6 dB (diode-chip-lensed fiber), with a double inverse tapered structure for the light input/output coupling [166]. When the frequency of the light emitted from the laser diode coincides with a high-Q resonance of the Si_3N_4 microresonator, laser self-injection locking can take place. The process occurs due to the bulk and surface Rayleigh scattering in the microresonator, which injects a fraction of light back into the diode [97]. This provides frequency-selective optical feedback to the laser, leading to single-frequency operation and a significant reduction of the laser linewidth.

A key step for our approach is to match the optical power requirement for soliton generation to that of the laser diode. This is achieved by employing high-Q Si_3N_4 microresonators fabricated using the photonic Damascene process, featured with a novel and crucial reflow step [77], allowing for ultra-smooth waveguide sidewalls that enable high-Q factors ($Q_0 > 1 \times 10^7$) across the entire L band (more details in section 4.2).

The Fabry-Pérot laser diode we employ in the experiments is centered at 1530 nm, and its emission spectrum without self-injection locking is shown in Figure 4.3(b). The mode spacing is 35 GHz, determined by the Fabry-Pérot cavity length. The overall maximum optical output power is ~ 100 mW when applying a current of ~ 350 mA to the diode. The electrical power consumed by the laser diode is less than 1 W. Figure 4.3(c) shows the heterodyne beatnote of the free-running laser diode mode with the reference laser (Toptica CTL1550, short-time linewidth ~ 10 kHz), which is fitted with the Voigt profile (Appendix A), revealing both a Gaussian linewidth of 60 MHz and an estimated short-time linewidth of 2 MHz.

4.4 Self-injection-locking phenomena

We first studied self-injection locking of the laser diode chip to the photonic chip-based microresonator. This is achieved by tuning the current of the laser diode, which not only changes the optical output power, but also shifts the lasing frequency via the carrier dispersion effect. Initially, the laser diode coupled to the Si_3N_4 chip operates multi-frequency [Figure 4.3(b)], a regime where none of the high-Q microresonator modes is frequency-matched with the multi-mode laser emission of the diode. By shifting the lasing frequency of the diode via current tuning, we observe that the initially multi-frequency emission spectrum switches to single-mode operation, indicative of self-injection locking. Figure 4.3(d) demonstrates that the lasing frequency coincides with a selected resonance of the microresonator, and we also observe injection locking occurring for several resonances [155]. We note that all resonances, which give rise to the laser self-injection locking, feature mode splitting as a result of backscattering [cf. the inset in Figure 4.3(d)]. The back-coupling rate for the measured resonance, extracted from its mode-splitting profile, is $\gamma/2\pi = 118$ MHz (section 4.2). The presence of this back-coupling leads to an amplitude reflection coefficient (r) from the passive microresonator on resonance:

$$r \approx \frac{2\eta\Gamma}{1+\Gamma^2}, \tag{4.3}$$

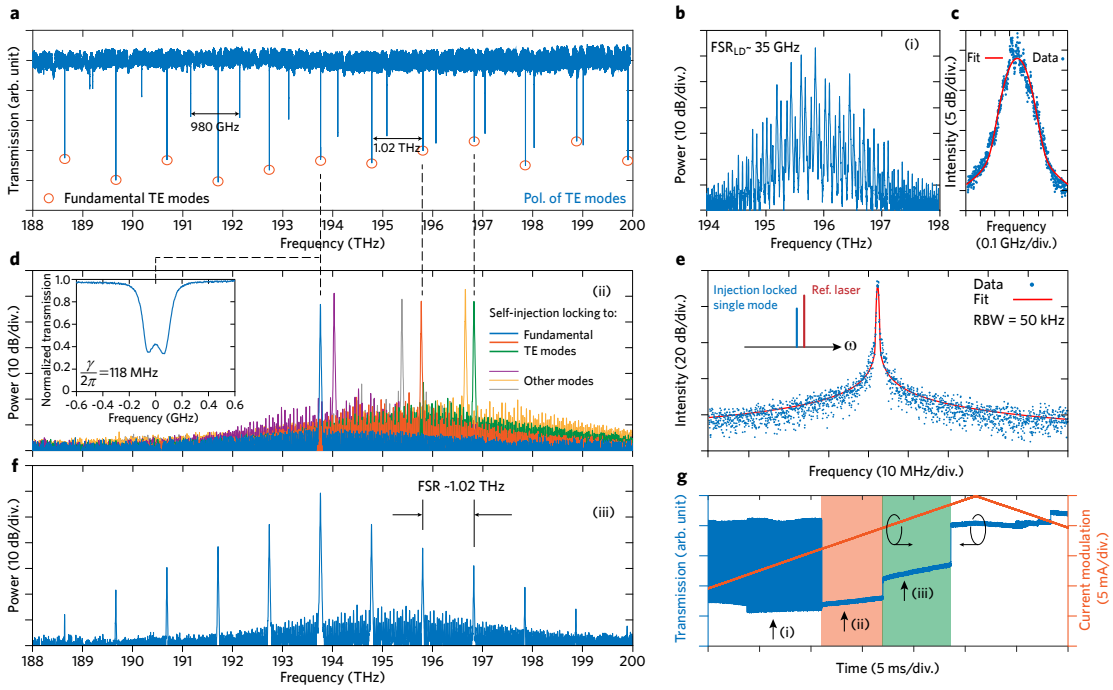

Figure 4.3: **Electrically pumped soliton microcomb via laser-injection-locked soliton formation.** **(a)** Transmission spectrum of a Si_3N_4 microresonator of 1.02 THz FSR, featuring two sets of resonances: the fundamental transverse electric (TE) mode family (marked by red circles) and one high-order TE mode family. **(b)** The laser spectrum of the multi-frequency laser diode chip used in this experiment corresponds to state i in **(g)**. **(c)** Measured and fitted heterodyne beat signal between the free-running laser diode and a narrow-linewidth reference laser (Toptica CTL1550, short-time linewidth ~ 10 kHz), showing 60 MHz full width at half maximum (FWHM) of Voigt profile. **(d)** (state ii in **(g)**): Spectra of single-longitudinal mode that is injection-locked to a selected resonance of the microresonator. **(f)** (state iii in **(g)**): Spectrum of the Kerr frequency comb that stems from the laser injection locking. Inset: One resonance of the fundamental TE mode showing mode splitting due to backscattering, with the estimated 118 MHz coupling strength ($\frac{\gamma}{2\pi}$) between the forward and backward propagating modes. **(e)** Heterodyne beat signal between the injection-locked laser and a narrow-linewidth reference laser. The measured beat signal is fitted with Voigt profile with FWHM ~ 186 kHz (Appendix A). RBW: Resolution bandwidth. **(g)** Typical transmitted power trace measured at the chip output facet, by current modulation imposed on the laser diode, in which different states are marked: (i) Noisy, multi-frequency lasing without injection locking; (ii) Laser injection locking to a microresonator resonance, and simultaneous formation of low-noise single-longitudinal-mode lasing (the orange region); (iii) Formation of Kerr frequency comb(the green region).

where $\eta = \kappa_{ex}/\kappa$ characterizes coupling efficiency ($\kappa = \kappa_0 + \kappa_{ex}$, with $\eta = 1/2$ corresponding to critical coupling, and $\eta \approx 1$ corresponding to strong overcoupling), and $\Gamma = \gamma/\kappa$ is the normalized mode-coupling parameter that describes the visibility of the resonance split. According to Ref.

[157] this reflection can initiate self-injection locking, and give rise to a narrow linewidth of:

$$\delta\omega \approx \delta\omega_{\text{free}} \frac{Q_{\text{LD}}^2}{Q^2} \frac{1}{16r^2(1+\alpha_g^2)}, \tag{4.4}$$

where $Q = \omega/\kappa$ is the microresonator quality factor, $\omega/2\pi$ is the light frequency, $\delta\omega_{\text{free}}/2\pi$ is the linewidth of the free running laser. The phase-amplitude coupling factor α_g is the linewidth enhancement factor, given by the ratio of the variation of the real refractive index to the imaginary refractive index of the laser diode active region in response to a carrier density fluctuation [220] and takes typical values from 1.6 to 7. The InGaAsP/InP multiple quantum well laser diode has $\alpha_g = 2.5$. The laser diode quality factor Q_{LD} can be estimated as $Q_{\text{LD}} \approx \frac{\omega\tau_d R_o}{1-R_o^2}$, where R_o is the amplitude reflection coefficient of the output laser mirrors, and τ_d is the laser cavity round trip. The laser diode's reflection coefficient is a parameter and given by the laser diode manufacturer as $R_o = \sqrt{0.05}$ as well as $\alpha_g = 2.5$. Other experimentally determined parameters are $\kappa/2\pi \approx 110$ MHz, $\gamma/2\pi \approx 118$ MHz, $\eta \approx 0.64$, $\Gamma \approx 1$, and $\tau_d = 1/\text{FSR}_{\text{diode}} = 1/(35\,\text{GHz}) = 28.6$ ps. The theoretical estimation for the narrowed linewidth is $\delta\omega/2\pi \sim 0.1$ kHz. We next compare these theoretical estimates of the self-injectioned locked linewidth to experiments. The linewidth of the self-injection-locked single-longitudinal-mode laser is measured by a heterodyne measurement [see Figure 4.3(e)]. The lineshape is fitted with a Voigt profile, which represents a convolution of Lorentzian and Gaussian lineshape (see, Appendix A), yielding a Gaussian contribution to the linewidth of 186 kHz. The estimated Lorentzian contribution amounts to 0.7 kHz, describing the wings of the measured beatnote. Self-injection locking leads to a narrowing of the white noise of the laser diode (Equation 4.4) [157]. Therefore, this value should be compared with the Lorentzian contribution in the Voigt profile (i.e. 0.7 kHz) corresponding to a more than 1000-fold reduction in the linewidth.

Injection locking occurs also in the case where the laser cavity and microresonator are detuned from each other due to "injection pulling", and as outlined below, is imperative to generate DKS using self-injection locking. Injection pulling is a result of a slight phase difference between the laser emission and its feedback, leading to imperfect locking [157]. The locking range is defined as the frequency range over which the laser diode emission self-injection locks to the high-Q microresonator resonance and follows the expression [157]:

$$\Delta\omega_{\text{lock}} \approx r\sqrt{1+\alpha_g^2}\frac{\omega}{Q_{\text{LD}}}. \tag{4.5}$$

The theoretically estimated locking range exceeds $\Delta\omega_{\text{lock}}/2\pi \approx 30$ GHz.

4.5 Kerr frequency comb generation via self-injection-locking

Experimentally, we can access this effect by tuning the current of the laser diode, allowing the laser frequency to be changed concurrently with the self-injection locking, providing thereby a frequency scan over the resonance – a prerequisite for DKS formation [218]. In the current study,

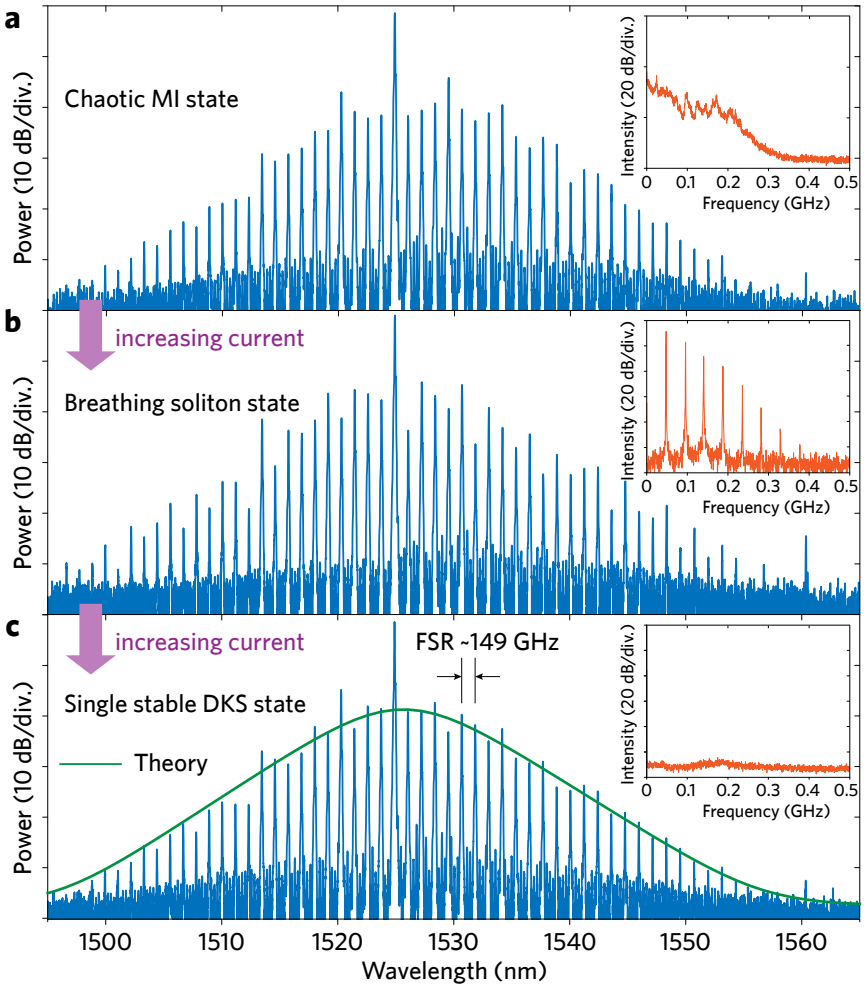

Figure 4.4: **Soliton comb generation with self-injection locking.** Evolution of Kerr frequency comb in the regime of laser self-injection locking, from noisy state in the operation regime of modulation instability (MI) **(a)** to breathing state **(b)**, and eventually to a low-noise state **(c)** showing the formation of a dissipative Kerr soliton (DKS) in the microresonator, where the spectrum is a hyperbolic secant envelope (green-solid line showing the fitting of the spectral envelope). Each inset shows the low-frequency radio frequency (RF) spectrum corresponding to each state. The current imposed to the diode is initially set ~ 300 mA and the increase to evoke the transitions is within 1 mA. The Si_3N_4 microresonator in this measurement has a free spectral range (FSR) of 149 GHz.

the proper phase for optimum locking range is achieved by adjusting the position of the laser diode using the translation stage. Figure 4.3(g) shows the optical output power (transmission) trace as a function of the current tuning, where self-injection locking is deterministically observed. An initial chaotic power trace [state (i) in Figure 4.3(g)] is switched to a step-like pattern [state (ii) in Figure 4.3(g), the orange marked region]. The average output power reduces during the switching since the self-injection leads to single-longitudinal-mode operation, with

enhanced power being coupled into the high-Q resonance of the Si_3N_4 microresonator. Most significantly, upon further tuning the current, a second step-like pattern in the power trace is observed [state (iii) in Figure 4.3(g), the green marked region], corresponding to the formation of a (low noise) Kerr frequency comb. Indeed, at high optical power levels (typically setting the current to be ~ 300 mA), Kerr comb generation was observed upon tuning the current, as shown in Figure 4.3(f). This phenomenon relies critically on the Q-factor of the Si_3N_4 microresonator, allowing sub-mW threshold power for parametric oscillations.

4.6 DKS with an electronically detectable mode spacing

We next investigated if self-injection locking can also be observed in devices with an electronically detectable mode spacing (149 GHz, and < 100 GHz), and critically if it can also enable operation in a regime where DKS are formed concurrently. Figure 4.4(a) shows the self-injection-locked Kerr comb generation in a microresonator with an FSR of 149 GHz. Significantly, not only were Kerr combs observed but also switching into the DKS regime [218]. Upon self-injection locking, and via current tuning we first excite a Kerr comb in a low-coherence state, as evidenced by the noise in the low-frequency RF spectrum [inset in Figure 4.4(a)]. We emphasize that for such low repetition rates the amplitude noise is still a valid indicator of the frequency comb's coherence, in contrast to terahertz mode spacing resonators where the noise can be located at high RF frequencies (> 1 GHz) [52]. Importantly, we observe, that upon increasing the current to the diode further ($\mathcal{O}$(mA)), which leads to a laser detuning increase by injection pulling, the low-coherence comb state is turned into an intermediate oscillatory state. That can be identified as a breather DKS [Figure 4.4(b)] [47], where the soliton exhibits periodic oscillations. The RF spectrum shows the breathing frequency at ~ 490 MHz exhibiting harmonics, see inset in Figure 4.4(b). Such soliton breathing dynamics, i.e. breather DKS, have been studied previously [47], and in particular the breathing frequency depends on the laser detuning. The observation of a DKS breathing state demonstrates that the injection pulling enables operation in the effectively red-detuned regime, required for soliton generation. Further increasing the laser current, we observe a transition to a low-noise comb state, demonstrating the formation of stable DKS as shown in Figure 4.4(c). In addition, the spectral envelope of the frequency comb exhibits a secant-squared profile, corresponding to a single soliton circulating in the resonator, with the breathing oscillations absent from the RF spectrum [inset in Figure 4.4(c)]. This transition, which we induce here by current tuning only, has been achieved in previous work by tuning the laser over the resonance from the blue to the effectively red detuned side [218]. Most significantly, to corroborate operation in the soliton state we verify the coherence via a heterodyne beatnote measurement [221]. The heterodyne beatnote of a soliton comb tooth with a narrow linewidth reference laser is shown in Figure 4.5(c). The measured heterodyne beatnote linewidth is comparable to that of the injection-locked laser [cf. Figure 4.3(e)], i.e. the Gaussian linewidth is 201 kHz and the estimated short-time Lorentzian linewidth (that describes the wings of the beatnote only) is 1 kHz. These values indicate no degradation of the coherence during the process of soliton comb generation via laser self-injection locking.

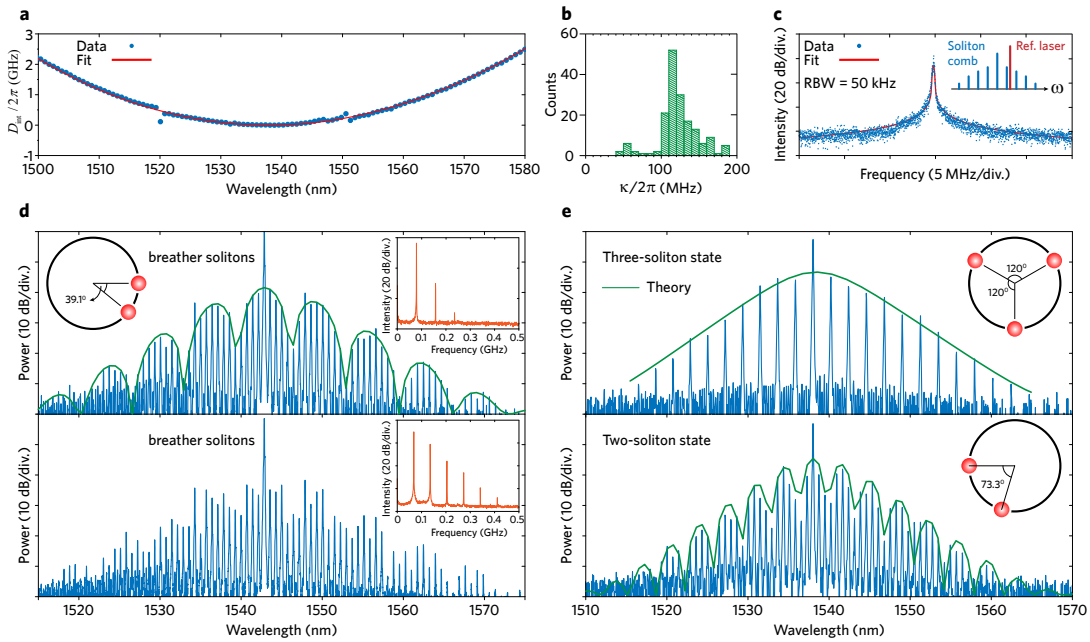

Figure 4.5: **Laser injection-locked multiple breathing and dissipative Kerr solitons.** **(a)** Measured and fitted dispersion landscape in a Si_3N_4 microresonator (cross-section 1.58×0.75 m^2), which has the FSR = 92.4 GHz, and the second order dispersion element indicating the anomalous group velocity, $D_2/2\pi \approx 1.56$ MHz. **(b)** Histogram of resonance linewidths that are $\sim$ 110 MHz, corresponding to a loaded Q-factor $\sim 1.8 \times 10^6$. **(c)** Heterodyne beat signal between the sideband of soliton Kerr frequency comb and the narrow-linewidth reference laser. The measured beat signal is fitted with Voigt profile with full width at half maximum (FWHM) $\sim$ 201 kHz (Appendix A). RBW: Resolution bandwidth. **(d, e)** Showcase of multiple dissipative solitons formed in Si_3N_4 microresonators, in the breathing state **(d)** as well as in the low-noise stable soliton state **(e)**, the fitting of the spectrum envelope (green-solid lines) further shows the relative position of solitons circulating in the micro-ring cavity (Schematic insets). The low-frequency RF spectra corresponding to breather solitons are also shown as insets. Spectra in **(d)** and **(e)** are generated in Si_3N_4 microresonators with a free spectral range (FSR) of $\sim$ 88 GHz and $\sim$ 92 GHz, respectively.

Moreover, DKS formation via laser self-injection locking was also observed in Si_3N_4 microresonators with FSRs below 100 GHz, an electronically detectable repetition rate, where due to the high Q-factors ($Q_0 \sim 8 \times 10^6$) enabled by the photonic Damascene reflow process, soliton combs could still be generated [27]. Figure 4.5(a,b) show a dispersion measurement of the microresonator, where the FSR is read as 92.4 GHz. The parabolic dispersion profile shows quadratic contribution from an anomalous group velocity dispersion (GVD) to be: $D_2/2\pi \approx 1.56$ MHz, centered at a wavelength $\sim$ 1540 nm. The loaded resonance linewidth $\kappa/2\pi$ is ca. 110 MHz [Figure 4.5(b)], corresponding to an over-coupled regime of the microresonator (the intrinsic loss rate is $\kappa_0/2\pi < 30$ MHz). In these types of microresonators, multiple dissipative solitons are observed, shown in Figure 4.5(d,e), not only in the breathing state but in the low-noise stable soliton

state as well. The spectral envelope reveals a multi-soliton state as a result of interfering Fourier components of the solitons. By fitting these spectral envelopes (Appendix A), we can resolve the number of solitons and estimate their relative positions, illustrated as insets in Figure 4.5(d,e). The overall transmitted optical power, consisting of both the comb power and the residual pump power, is measured ~ 11 mW. Multiple DKS in the microresonator with FSR ~ 92.4 GHz are generated when applying a current ~ 280 mA to the diode chip, corresponding to an optical output power of ~ 50 mW. The output power is measured as ~ 11 mW, collected by using a lensed fiber at the output chip facet, indicating a coupling efficiency of ~ 22% (overall insertion loss −6.6 dB). The optical power in the bus waveguide is estimated to be ~ 23.5 mW, which has been demonstrated sufficient to excite DKS in high-Q Si_3N_4 microresonators [27] (section 3.4).

In comparison with a recent report of integrated soliton microcomb[99] concurrent to this report, our scheme alleviates the need for on-chip Vernier filters, as well as for thermal heaters for soliton tuning[94], which increase power consumption (30 mW per heater[99]) and add complexity in the fabrication process and soliton initiation. Controlling only the current applied to the laser diode, the soliton states are generated in a compact form with low cost and significant simplification in terms of the fabrication process and experimental setup.

Discussion

In summary, we have demonstrated a route to an ultra-compact, cost-effective soliton frequency comb in photonic integrated Si_3N_4 microresonators, via laser self-injection-locking with off-the-shelf laser diodes. We observed power-efficient soliton combs in microresonators with different FSRs, particularly for FSR below 100 GHz. This approach offers a dramatic reduction in size, cost, and weight, and also offers simplified heterogeneous integration, in particular as no wafer bonding is required unlike for silicon photonic III-V lasers. This approach provides a route to scalable manufacturing of soliton microcombs for future high-volume applications.

5 Ultrafast optical circuit switching for data centers using integrated soliton microcombs

This chapter will show ultrafast optical circuit switching using an integrated soliton microcomb as the multi-wavelength source and SOAs as switching elements. This work is done in collaboration between EPFL and Microsoft Research Cambridge under the umbrella of the Swiss Joint Research Center - Microsoft. In addition, this work demonstrates the benefits of a fully packaged soliton microcomb module (contributed by M. Karpov and X. Fu), which was shipped to Cambridge to perform the experiments. I performed circuit-switching experiments with S. Lange and K. Shi in Cambridge during the 3-month internship. Moreover, a system-level analysis is performed to show the feasibility of soliton microcomb technology compared to tunable lasers.

5.1 Introduction

The recent growth in data center traffic due to emerging applications such as machine learning, resource disaggregation, and large-scale data analytics, poses tight requirements on the network regarding low latency, high bandwidth, and high scalability. Current data center networks comprise a multi-tier fabric of electrical switches and optical transceivers that consume a significant power, which is expected to exacerbate due to the slowdown of Moore's law [222, 223]. These optical transceivers are discrete components with a large footprint, mainly performing the opto-electronic-opto (O-E-O) conversion and consuming a lot of power. Further, the complexity in port scaling and power budget reduction of electronics switches poses a significant challenge to meet the dynamic changes in the future data centers [222].

Optical circuit switching (OCS) has been proposed as an alternative technology to overcome these challenges; it can provide high bandwidth and low network latency (due to the lack of buffers in the network core), and by allowing for a flat data center topology, the network can be more energy-efficient as fewer electrical switches and transceivers are required [225]. In OCS the servers are optically interconnected directly without needing the opto-electronic-opto (O-E-O) conversion. Micro-electro-mechanical (MEMS) based OCS systems are commercially available with the possibility of high port counts ($\sim$ 1000 ports) [226, 227]. Indeed, CALIENT

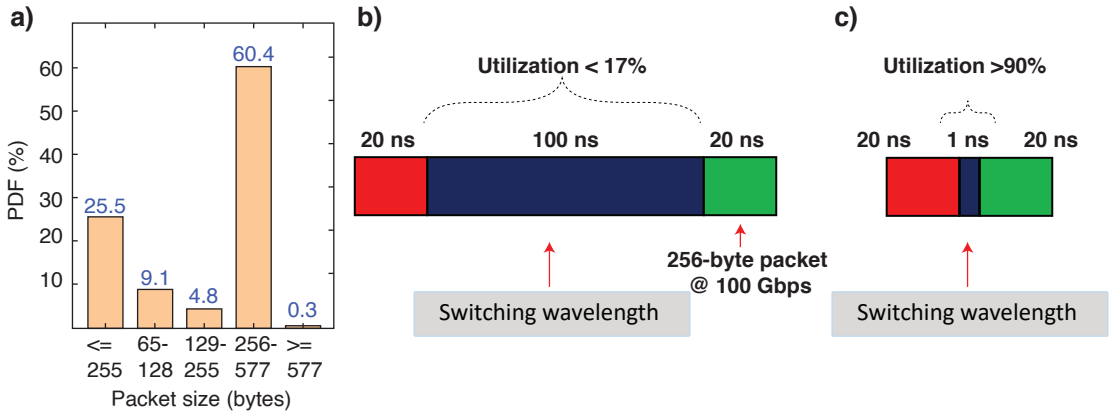

Figure 5.1: **The need for fast optical circuit switching**. **a** Packet size distribution of data center workload showing 97% data packets have a size of < 576 bytes. While more than 40% of data packets are < 256 bytes requiring switching between each packet after ~ 20 ns. figure adapted from [224] **b** The resources are underutilized if the switching between packets is around 100 ns (256 bytes data block transmitted at 100 Gbps). **c** The efficient utilization of resources requires switching at ≤ 1 ns.

has already shipped>500.000 optical connections globally for data center applications. However, MEMS-based OCS architectures suffer from slow switching time (~ ms), which can result in severe bandwidth under-utilization (Figure 5.1 b). Some emerging workloads are characterized by very small packets, e.g., in a recent key-value store application, more than 97% of the packets have a size of 576 bytes or less [224] (Figure 5.1). Assuming today's 20-Gbps speeds, it takes <30 ns to transmit a 256-byte packet (Figure 5.1 b). Therefore, achieving a reconfiguration overhead lower than 10% would require a nanosecond switching time (Figure 5.1 c).

Many photonic chip-based techniques have been used to demonstrate the fast optical switching (ns), such as semiconductor optical amplifiers(SOAs) [233], electro-absorption modulators (EAMs) [234], and Mach–Zehnder interferometers (MZIs) [235, 236] (Figure 5.2). The arrayed waveguide grating routers (AWGRs) [237, 238], in conjunction with a tunable laser (TL), is a promising optical circuit switching technology as the core of the network is passive. This improves fault tolerance and is also beneficial for future scaling because, unlike today's electrical switches, the core may not need to be upgraded when data rates increase. However, state-of-the-art tunable lasers with custom drivers can have a tuning latency of 10 ns or higher [239, 240]. In comparison, custom lasers and drivers have been combined to achieve a latency of around 5 ns [241, 242], which makes them unsuitable for our targets. A recent proposal addresses this issue by showing that using a disaggregated laser architecture in which the wavelength generation is decoupled from the wavelength selection, it is possible to achieve sub-nanosecond laser tuning time [243, 244]. One possible implementation of this architecture relies on a discrete bank of lasers as a multi-wavelength source and a wavelength selector containing photonic integrated arrayed waveguide grating (AWG) and SOAs. The SOAs are preferred as switching elements due to fast and lossless switching, chip-scale integration, and high extinction ratio [233].

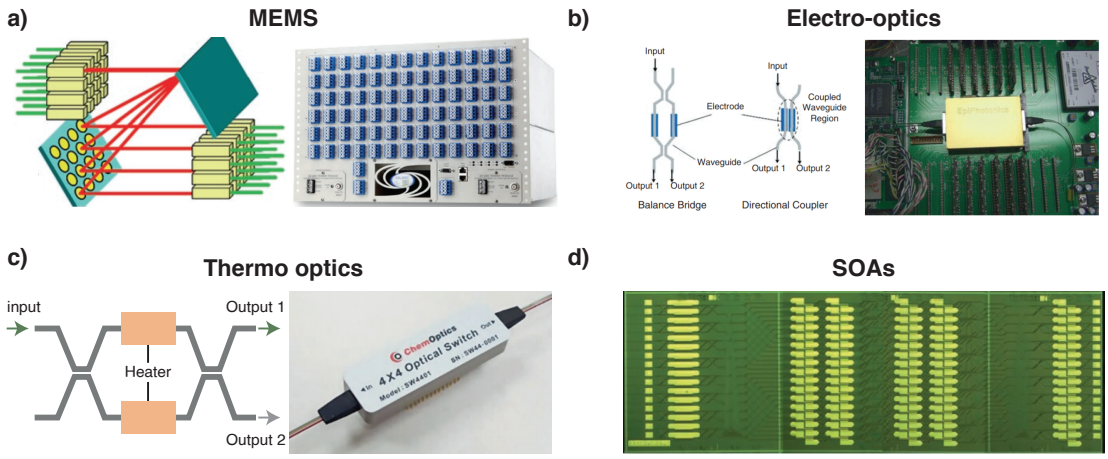

Figure 5.2: **Different photonic-based optical switching module proposed and implemented for optical circuits switching**. **a** A micro-electro-mechanical system (MEMs) based solution for switching by steering optical beams in a pre-defined direction for rerouting. This commercially available architecture can be scaled to *sim* 1,000 of ports. However, it suffers from slow switching time (~ ms). **b** By modulating the phase of light in one path of the Mach Zehnder interferometer, the light path can be directed from one waveguide to another. The system can be scaled higher number of ports with high switching speed (> ns). However, the platform is in the development phase ($LiNbO_3$) to minimize losses that become critical when scaling to a higher number of ports. **b** Similarly, the phase of light can be modified by applying local heat via a metallic heater and can be implemented on low-loss platforms such as Si and Si_3N_4. But, some of the obstacles are the cross-talk when scaling to a higher number of channels and low-switching speed (*sim* ms). **d** Semiconductor optical amplifiers are another possible candidate to transmit and block light paths at ns-time scale by applying current. The yield of fabrication is not high. Figure adapter from. (a [228, 229]), (b, [229, 230], (c, [231, 229]) and (d, [232])

5.2 Soliton-based multi-wavelength source - advantages

In this work, a disaggregated tunable transceiver that uses photonic chip-based soliton microcombs as a multi-wavelength source, which are generated in high-quality (Q) microresonators exhibiting third-order nonlinearity ($\chi^{(3)}$) and anomalous dispersion [18, 43], is proposed and experimentally demonstrated. The soliton microcombs have been used in many system-level applications, for example, distance ranging (LiDAR) [86, 215, 87], microwave photonics [245, 246, 247, 248], optical coherence tomography (OCT) [89, 88], and coherent communication [84, 249, 250]. The remarkable improvements in the losses of high-confinement Si_3N_4 integrated waveguides, a widely used platform for integrated photonics [79, 251], allows the generation of solitons using the on-chip laser [99, 98, 19]. The broadband-bandwidth operation across C- and L-bands, precise spacing control to match ITU frequency grid (50/100 GHz), low power consumption, and wafer-scale scalability make the soliton microcomb an attractive solution for an ultra-fast wavelength switched system in comparison with a bank of lasers [84]. Further, no extra guard band is required for frequency stabilization or to align each comb channel to the frequency grid.

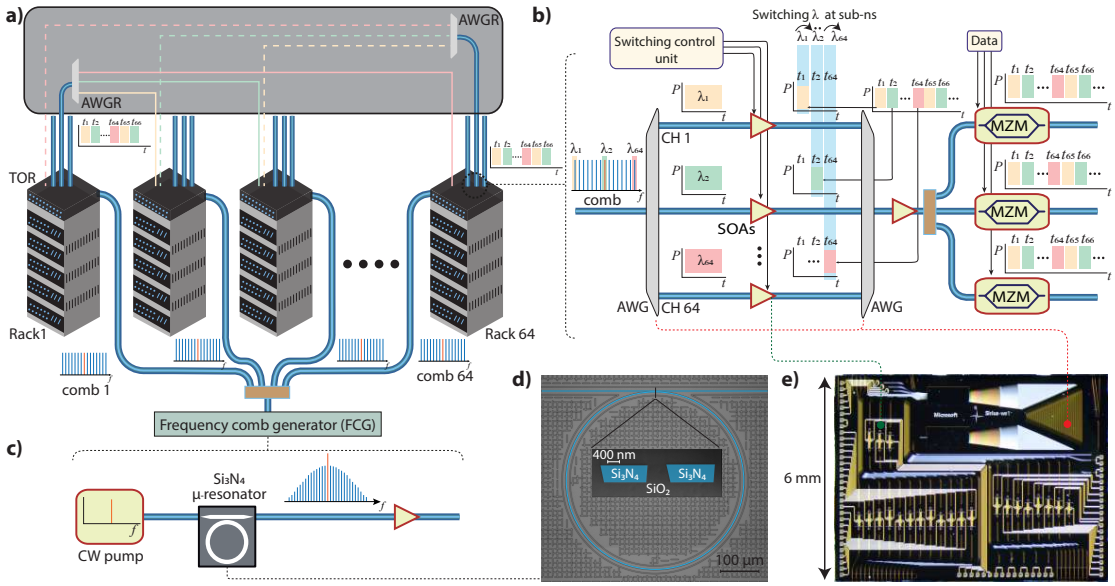

Figure 5.3: **Concept of optical circuit switching (OCS) using a photonic chip-based Si_3N_4 soliton microcomb and semiconductor optical amplifiers (SOAs).** **a)** Interconnection of 64 racks via an arrayed waveguide grating router (AWGR) for implementing fast OCS. In this model, distinct wavelengths are assigned to each rack at each time slot. At each receiver, a 10 to 20 nanosecond (ns) time slot is assigned for each rack on a round-robin basis for data transmission. The switching module is placed on the top of rack (TOR) switch. A single comb source which is post-amplified via cascaded amplifiers to attain high optical power per line can be distributed among many racks. The 64 individual combs (comb1, ..., comb 64) split from a central frequency comb generator (FCG) can be distributed across 64 different racks as a multi-wavelength laser, making this architecture more power-efficient and flexible. The multiple data-carrying optical carriers are routed using a passive AWGR to the assigned racks. **b)** Each comb channel is transmitted to SOAs after de-multiplexing, where a control signal (turning on/off current) is applied to switch between the comb channels at sub-ns. The comb channels (10-ns slots) are encoded with data using Mach-Zehnder modulators (MZMs) and transmitted to the relevant racks. The multiple MZMs shown here indicate that this architecture can be scaled further to establish links between more racks. **c)** The multi-wavelength source based on the chip-scale soliton microcomb is generated by pumping with a single laser. Microscope images of a Si_3N_4 microresonator **(d)** and a photonic chip **(e)** containing an AWG and SOAs. The inset in **(d)** shows a false color SEM image of a Si_3N_4 microresonator's coupling section.

A key advantage of the disaggregated transceiver design is that the multi-wavelength comb source can be shared across many (e.g., 64) nodes (racks or servers) in parallel instead of using 64 separate comb sources, using a split-and-amplify architecture (Figure 5.3a). The source can thus be treated as a shared infrastructure element, such as the power source in today's data centers. This allows for an appealing division of functionality since the power consumed by the comb source is amortized as the end-to-end system's power efficiency converges to the amplifiers' efficiency while allowing for a high-quality and stable light source that can be rapidly wavelength-tuned (section 5.7).

5.3 Optical circuit switching architecture based on soliton microcomb.

Figure 5.3 shows the OCS architecture containing the soliton microcomb, SOAs, AWGs in the switch, and AWGRs to route the data across many racks. The link between two racks is only established via a single wavelength (comb tooth) in specific time slots ($t_{64}, t_{128}, ...$) as shown in Figure 5.3a. The soliton microcombs provide many coherent optical carriers assigned to distinct racks. The switching operation is performed by applying a control signal on the SOAs, e.g., the switching from t_1 to t_2 data slot is done by applying an on signal to the second SOA and off signals to all other SOAs. A trigger signal from an external reference clock is used to align the switching control and data-encoding units. This architecture allows further parallelization of different resources by sharing the soliton across many racks and modulators for power efficiency and parallel data transmission, respectively (Figure 5.3a & b). The multi-wavelength source is generated by pumping a packaged Si_3N_4 microresonator fabricated using the photonic Damascene reflow [77, 27] process enabling a mean intrinsic Q-factor (Q_0) of > 15 million. The designed microresonators are over-coupled ($\kappa_{ex} \sim 4 \times \kappa_0$) with an FSR of 99.5 GHz and intrinsic linewidth of 15 MHz [27]. The waveguides have a dimension of 1500×900 nm^2. The double inverse nano tapers are used to facilitate the light coupling in, and out of the chip [166].

A compact fiber laser (Koheras BASIK) is amplified using an EDFA. Then, amplified spontaneous emission (ASE) noise is filtered out using a narrow optical bandpass filter. The Si_3N_4 chip is packaged by splicing the ultrahigh numerical aperture (UHNA) fiber with standard SMF-28 fiber with chip through (fiber-chip-fiber) 15% coupling efficiency [20] (section 2.9). A single soliton is initiated at an input power of ~ 450 mW in the bus waveguide by applying a custom-designed ramp voltage. The deterministic soliton initiation and backward tuning (Figure 5.4b) are controlled via a computer interface. The power conversion from CW-pump to single soliton is ~ 2.1 % in the current device. An intrinsically coherent single soliton state is preferred due to low line-to-line power variation in 3 dB bandwidth (smooth spectral). Figure 5.5 c) shows the absolute power and optical signal-to-noise ratio (OSNR) of the lines of the individual comb after post-amplification. Around 25 channels in the C-band have a power of more than -18 dBm and an OSNR of 34 dB. The four channels around the pump mode centered at 1550 nm (CH 32) have a lower OSNR due to residual ASE noise. This can be avoided either by using a narrower optical bandpass filter or by using the drop-port of the microresonators to couple out the soliton instead of the through port. The post-amplified soliton as shown in Figure 5.4c is de-multiplexed using a 100G spaced 48-channel AWG (~ 1525 nm-1564 nm) providing 30 dB isolation. The switching control unit supplies the bias currents and electrical switching signals to the SOAs. A negative voltage is applied to drive the SOAs at the zero-level. The current flowing through the SOAs at the zero-level was around 1 A. To optimize the switching between two different channels, the upcoming channel starts switching on while the current channel is still switching off. The extinction ratio (ER) appears to be degraded since the signal intensity shows the sum of the channels and does not drop to the zero-level during the switching event. The ER of the waveform in Figure 5.4d is ~ 15 dB. It is difficult to estimate actual ER as the signal was measured using a

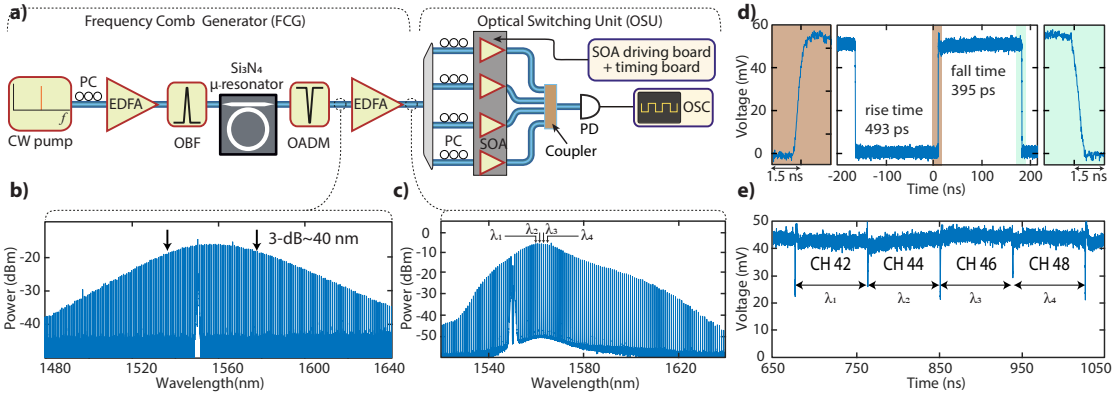

Figure 5.4: **Experimental demonstration of sub-ns optical circuit switching (OCS) of single and four different microcomb channels. a)** A packaged Si_3N_4 microresonator is pumped using a continuous wave (CW) pump amplified via an erbium-doped fiber amplifier (EDFA) to generate a soliton microcomb. A soliton state is initiated via forward tuning. After filtering the pump using an optical add-drop multiplexer (OADM), a low-noise amplifier is used to amplify the soliton comb further. The post-amplified comb is de-multiplexed using a 48-channels 100G AWG, and the individual comb channels are routed to semiconductor amplifiers (SOAs) controlled via a custom-designed switching board. The output signal is detected using a photodiode (PD) and recorded on an oscilloscope (OSC). PC, polarization controller; OBF, (narrow) optical bandpass filter. **b)** A single soliton spectrum with 3 dB bandwidth around 40 nm and no post-amplification. **c)** Post-amplified soliton spectrum with maximum power up to -4 dBm in comb lines close to the pump line (1550 nm). **d)** The 10%×90% rise and fall time of 493 ps and 395 ps respectively for single comb channel (CH 37: 1554.9 nm). The left and right insets show the zoomed-in view of rising and falling signals. **e)** The four different microcomb channels simultaneously switching at sub-ns time scale with wavelength separation ~ 4.9 nm. A guard zone of ~ 2.56 ns allows smooth switching between two adjacent channels. The ER is lower in comparison with **d)** as signal intensity does not drop to zero while switching between adjacent channels (see Methods, Switching control unit). CH-42: 1558.988 nm, CH-44: 1560.613 nm, CH-46: 1562.238 nm, and CH-48: 1563.863 nm.

sampling scope and zero level of signal is buried in noise. This unit also controls the clock and time synchronisation of the switching signals. A time synchronization having less than 100 ps accuracy is achieved in current study [244]. The individual comb channels are initially switched using discrete SOAs with a small-signal gain ~ 11-13 dB at 1550 nm. Figure 5.4d shows a 10% – 90% rise and fall times of 493 ps and 395 ps, respectively, for a single microcomb carrier centered at 1555 nm (CH 37 of AWG) when applying a current of 120 mA to operate the SOA. Similarly, more than 20 comb channels (1540 nm - 1564 nm) in C-band are tested individually to show sub-ns switching (Figure 5.5 a & b). All these comb channels are used to perform the optical circuit switching using discrete SOAs with the setup shown in Figure 5.4 a. The 10% - 90% rise and fall times are less than 520 ps. Even though not tested due to the unavailability of an L-band AWG, the current results indicate that more than 40 comb channels could also be used.

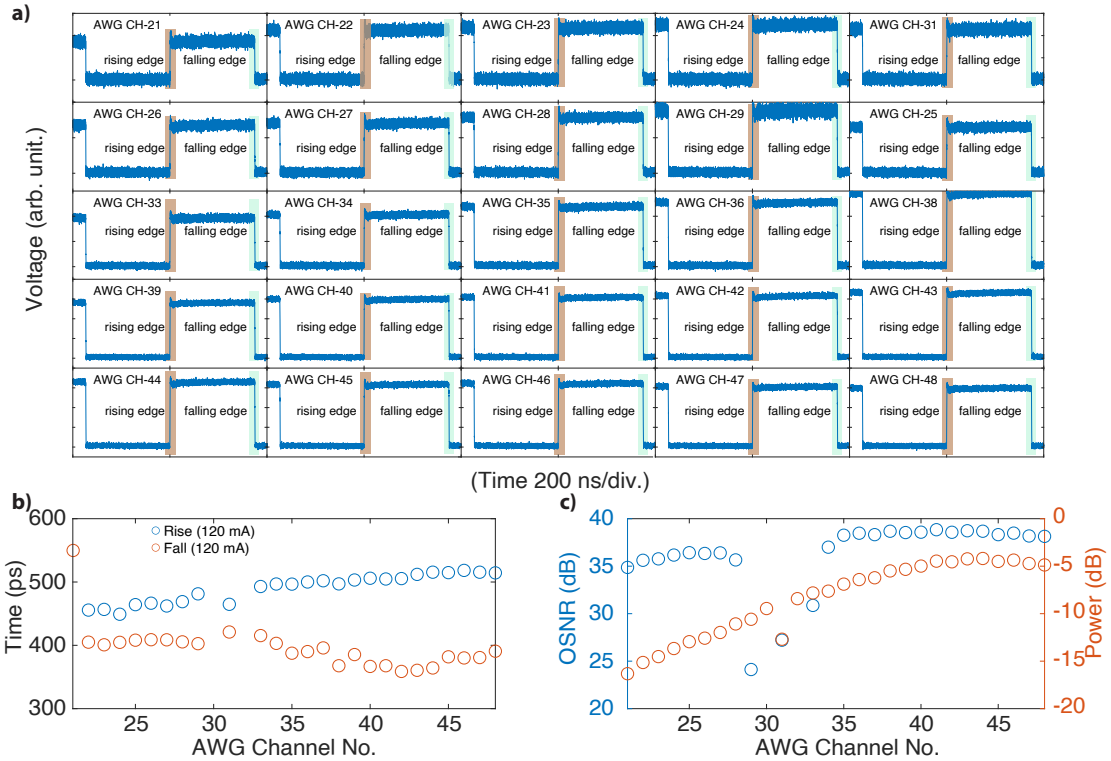

Figure 5.5: **The power, optical signal to noise ratio (OSNR), and individual channel switching characterization of soliton microcomb. a)** The ultrafast switching demonstration of ~ 24 channels lying in the C-band. Each channel's rising and falling edge is indicated in the shaded region. **b)** The 10% - 90 % rise and fall times of around ~ 24 channels lying in the C-band with a maximum switching time of less than 520 ps while using discrete semiconductor optical amplifiers (SOAs). **c)** The optical power of different channels in the C-band is up to -4 dBm. The OSNR of two channels around CH 32 (pump mode, ~ 1550 nm) is degraded due to ASE noise. The remaining 23 channels have an OSNR of > 34 dB.

5.4 Ultra-fast wavelength switching and data transmission via discrete SOAs.

Fast switching within four comb channels is performed for a proof-of-concept system-level demonstration. Figure 5.4e shows sub-ns switching between 4 different comb channels with a wavelength separation of ~ 5.6 nm. A guard zone of 2.56 ns allows smooth switching between adjacent comb channels while an external reference clock (timing board) aligns the different switching signals. Distinct currents are applied to the SOAs to achieve a constant output power and to compensate for the non-uniform comb power per line or SOA's gain (Figure 5.4e). While the sub-ns switching of four channels with a maximum 20 nm separation has been demonstrated, the maximum channel separation is mainly limited by the optical band-pass filter(OBF) (Figure 5.6 c & d). The sub-ns switching between two (Figure 5.6 a) and four (Figure 5.6 b) different comb channels having a maximum separation of more than 20 nm. The variations in comb channel

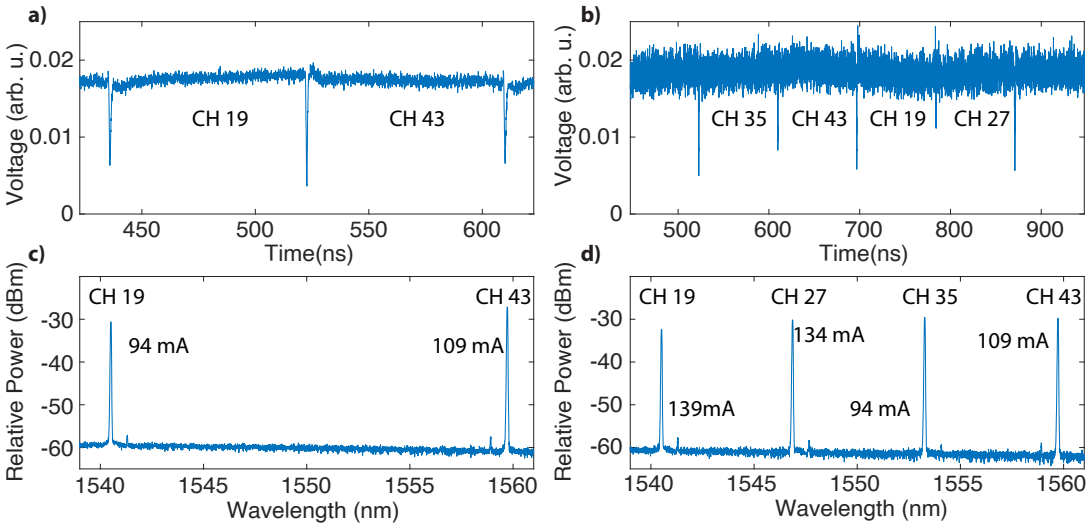

Figure 5.6: **The fast wavelength switching between two and four comb channels spanning 20 nm. a)** The simultaneous switching of two comb channels (centered at ~ 1540 and 1560 nm) using discrete SOAs. **b)** The simultaneous switching of four different comb channels using discrete SOAs. The limitation of the wavelength span in the current system is due to an optical bandpass filter used to reject channels in the next order of free spectral range from C-band AWG. **c & d** The optical spectrum measured after the SOAs covering 20 nm. Different currents (94 mA & 109 mA in c, 94 mA, 134 mA, 139 mA & 109 mA in d) are applied to each SOAs to equalize the optical power after SOAs.

power and SOAs gain are compensated by applying different biasing currents to each SOA. A biasing current of 94 mA, 109 mA, 139 mA, and 134 mA is applied to the SOAs connected to AWG channels 35, 43, 19, and 27, respectively (Figure 5.6 c & d).

In the following experiment, we show 25 Gbps non-return to zero (NRZ) and 50 Gbps four-level pulse amplitude modulation (PAM-4) burst mode data transmission while switching between four comb channels using the setup shown in Figure 5.7b. The four optical carriers after switching are further amplified to overcome the insertion loss (~ 7dB) of the 20 GHz Mach-Zehnder modulator (MZM) which is operating at the quadrature point. In addition to eliminating comb channels in the next-order FSR of the AWG, the OBF is utilized to suppress the out-of-band SOA and EDFA amplified spontaneous emission (ASE) noise. The burst mode sequence at 25 GBaud symbol rate, generated by the arbitrary waveform generator is applied to the MZM with a random sequence of 2^{15}- and 2^{16}-bits for NRZ and PAM-4 respectively. The electrical waveform is amplified using a trans-impedance amplifier (TIA) after detecting it on a fast photodiode having 50 GHz bandwidth. The amplified waveform is acquired using a real-time oscilloscope with 160 GSamples/s sampling rate. The digital signal processing (DSP), explained in detail in ref [243], is performed offline to obtain the bit error ratio (BER). The received optical power (ROP) vs. (BER) of the system, as shown in Figure 5.7c, is characterized by changing the optical power of incoming waveform via a variable optical attenuator (VOA). A BER of below 5×10^{-5}, which is the threshold for forward

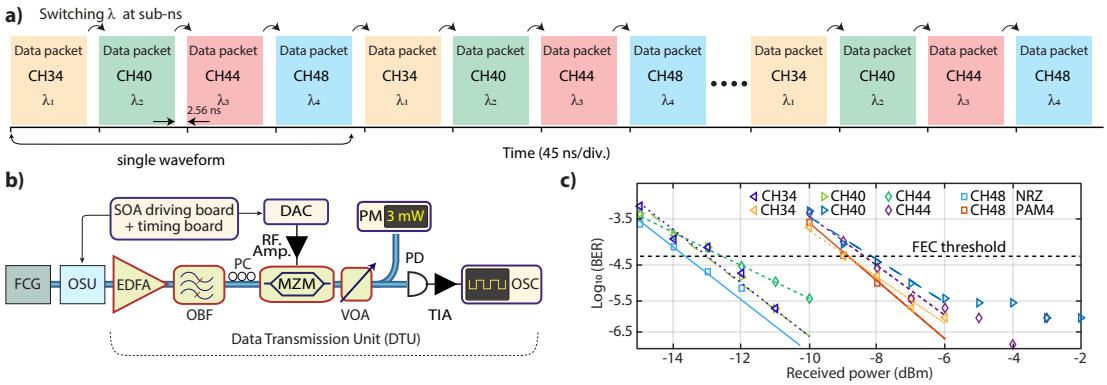

Figure 5.7: **Experimental demonstration of burst mode NRZ and PAM-4 transmission using discrete SOAs while switching. a)** A stream of multiple data packets showing data transmission along with sequential switching between the four comb channels. A single burst waveform sequence consists of header, payload, and guard zone containing 32, 1024, and 64 symbols respectively. **b)** The signal after the frequency comb generator (FCG) and the optical switching unit (OSU) is amplified using a compact EDFA to compensate for losses of the 20 GHz Mach-Zehnder modulator (MZM). Then, it is filtered out using a wide-band optical bandpass filter (OBF) (~ 20 nm) to reject amplified spontaneous emission (ASE) noise from the SOAs and the EDFA. The data is encoded on the modulator using an arbitrary waveform generator (DAC). A fast photodiode (PD) is used to detect the signal. The electrical signal is amplified using a trans-impedance amplifier (TIA) and finally captured by an OSC. **c)** The bit error ratio (BER) of four different comb channels while switching between them, using different modulation formats non-return to zero (NRZ) and four-level pulse amplitude modulation (PAM-4). A performance below forward error correction (FEC) threshold is achieved for NRZ and PAM-4 for a received optical power of ~ -12 dBm and ~ -8 dBm, respectively. CH-34: 1552.524 nm, CH-40: 1557.363 nm, CH-44: 1560.606 nm, and CH-48: 1563.863 nm.

error correction (FEC) in data center transmission systems corresponding to the KP4 FEC [252], is achieved for both NRZ and PAM-4 at a ROP of ~ -12 dBm and ~ -8 dBm respectively. The BER error floor for PAM4 at a ROP of > -6 dBm emerges due to ASE and AWG crosstalk.

5.5 Photonic integrated circuit based optical switching and data transmission.

Next, integrated Indium phosphide (InP) chip-based SOAs and AWG are used to show 25-Gbps NRZ burst mode data transmission along with fast OCS using a soliton microcomb. Figure 5.8b shows the photonic integrated circuit (PIC) based wavelength selector PIC with a dimension of 6 mm × 8 mm. The reflection of the light from the high-reflection (HR) coated facet allows simultaneous utilization of an AWG with 32×50 GHz separated channels as multiplexer and de-multiplexer. This simplifies the wavelength alignment procedure and reduces the footprint of the device. The InP-based wavelength selector PIC incorporates 23 SOAs, of which four are used as references. The other 19 SOAs are connected to a 1x32 AWG which acts as a multiplexer and

demultiplexer. One of the PIC facets is high-reflection coated so that the light is reflected back through the SOAs and AWG to the input waveguide. The reflective single AWG design reduces the footprint compared to two AWGs and avoids wavelength misalignment of the AWGs. The wavelength selector PIC was designed using the JEPPIX foundry and fabricated at Fraunhofer HHI. The wavelength alignment of the comb channels to the AWG is performed by changing the temperature of the PIC, resulting in seven comb channels matching with the AWG. This can also be realized by changing the temperature of the Si_3N_4 chip. Figure 5.8c shows the optical spectrum of the AWG-aligned comb channels indicating a >20 dB isolation with adjacent channels. Initially, PIC's 10% – 90% rising and falling times is characterized by performing simultaneous switching between two comb channels. The maximum (minimum) experimentally observed switching time is ~ 820 ps (~ 375 ps). Moreover, the overshoot in the switching signal, as seen in Figure 5.8d, arises due to impedance mismatch between the SOAs on-chip electrodes and the RF probes [243]. Then, a burst mode data transmission demonstration with 25-Gbps NRZ modulation is performed. A BER below FEC threshold is obtained when switching between two-channels with different combinations for a ROP > -11 dBm. While channels 40 and 41 have approximately the same optical power, channel 41 shows better BER performance as the crosstalk from channel 41 to 40 is about 8 dB lower than the crosstalk from channel 40 to 41. The PAM-4 burst mode transmission demonstration requires further improvement in the output power of the comb due to low in- and out-coupling in a packaged Si_3N_4. The main reason behind the low coupling efficiency (15 %) is an additional 2 dB splicing loss between UHNA and SMF-28 fiber, which can be reduced to < 0.2 dB by using state-of-art splicing instruments [253] (Figure 2.4). Similarly, the AWG crosstalk and insertion loss of the PIC can be further improved along with the utilization of lower FSR microcomb (25/50 GHz) to enhance the overall performance of this architecture. Nevertheless, the current results show the potential of a soliton microcomb as a suitable multi-wavelength source for 25 GBd NRZ burst mode transmission along with fast switching.

5.6 System level analysis

Regarding the power consumption, the current multi-wavelength source consumes a total electrical power of ~ 30 W (section 5.7), providing more than 60 carriers, having an optical power > -20 dBm (~ 500 mW electrical power per carrier). The electrical power consumption can be improved down to < 193 mW per carrier (15.5 W total) by reducing the splicing loss between UHNA and SMF fibers [253], implementing on-chip actuators [93] instead of a bulk temperature controller and using a power-efficient, compact distributed feedback (DFB) laser as CW pump [99, 19]. Optimizing the microresonator dispersion design makes it possible to generate 122 comb channels with an optical power > -14 dBm without needing any post-amplification [84]. Similarly, an optimized amplifier utilization with an amplifier for C- and L-band would give a comb with an optical power per line ~ 13 dBm in the C- and L- bands mentioned in SI of ref. [84].

More importantly, this high-power comb source can be shared among multiple racks by adding a hierarchy of passive optical splitters and amplifiers for better power and resource utilization

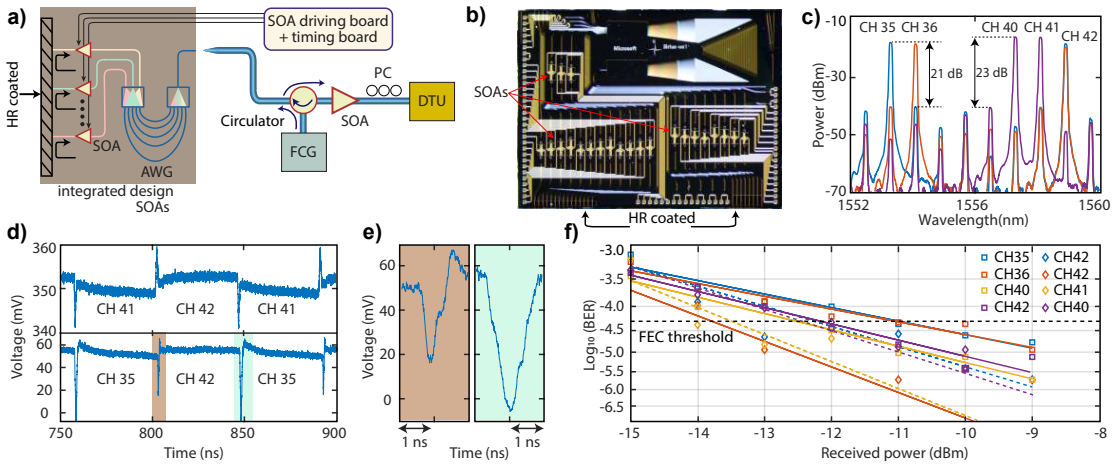

Figure 5.8: **Sub-ns optical circuit switching (OCS) and data transmission using on-chip SOAs and on-chip AWG along with soliton microcomb. a)** Schematic of the setup used to perform the OCS and data transmission. The multi-wavelength optical carriers, generated via the frequency comb generator (FCG), are coupled to an InP chip containing an AWG and SOAs via an optical circulator. The coupled optical carriers are aligned to the AWG by changing the temperature of InP chip. The aligned carriers are transmitted to integrated SOAs; if one of them is biased, then the AWG channel (waveguide) connected to that particular SOA is reflected from the high-reflection coated facet of the chip while non-biased SOAs block the light. The reflected-back channels are coupled back via an anti-reflection coated optical fiber for encoding the information using the data transmission unit (DTU). **b)** Microscope image of PIC showing the SOAs (red arrows) and AWG. **c)** Optical spectrum of comb channels with different spacing while switching after the InP chip indicating more than 20 dB isolation with adjacent AWG channels (cross talk). The red curve shows CH 36 and 42 with 4.8 nm wavelength spacing, the blue curve CH 35 and 42 (5.6 nm) and the purple curve CH 40 and 41 (0.8nm). **d)** The sub-ns wavelength switching between two different comb channels using on-chip SOAs. The overshoot in the switching signal is due to impedance mismatch between the high-speed radio-frequency (RF) probes and the on-chip electrodes. This effect can be minimized by optimizing the drive signal. **e)** The left and right figures show the zoomed-in view of switching signals between two different comb channels (CH35 and CH 42). **f)** The bit error ratio (BER) performance of the 25 GBd NRZ PIC-based switching system for different combinations of two comb channels.

(Figure 5.3a). The soliton microcomb source distributed among 32 racks provides carriers with P_{opt} ~ -4 dBm while consuming ~ 2.57 W (1.115 W) electrical power per rack by using a state-of-the-art commercial EDFA (on-chip amplifier [254]) making it a highly power-efficient and flexible solution for the data center (Figure 5.9). More broadly, the flexibility of sharing the comb across many racks, with the fast wavelength selection done on the rack itself, means that the overall electrical power efficiency per channel approaches the power efficiency of the EDFAs with the comb power as only a small contributor. This indicates that an optimized shared comb source would consume a comparable electrical power to other multi-wavelength source solutions, including recent techniques that use a bank of tunable lasers as a multi-wavelength source [255, 244]. Since the wavelength tuning is done on the bank of tunable lasers itself, sharing it between multiple racks would lead to an increased complexity when synchronizing the wavelength switching between the racks, due to the varying time delays between the bank of tunable lasers and the racks. As a matter of fact, one tunable laser bank per rack would be more optimal for a time-multiplexed solution [255], which would require at least 2×32 tunable lasers for switching between 32 racks instead of a single amplified comb chip. Moreover, a comb does not require additional complex algorithms for fast switching and wavelength stabilization, thus offering an appealing division of functionality by leveraging a complex yet highly shared light source.

5.7 Soliton microcomb power consumption

In this section, a detailed power consumption analysis is carried out to understand the system's performance and to provide possible ways to improve it further. The multi-wavelength soliton microcomb is generated using the setup shown in Figure 5.4 a. A compact KOHERAS BASIK fiber laser is used to pump the microresonator, which consumes approximately 1.5 W electrical power when operated at low optical power (~ 1 mW). A high-power BKtel erbium-doped optical amplifier (EDFA) providing a gain of up to 34 dB is used mainly to overcome the coupling losses. A single soliton is accessed at a power of 1.2 W at the input fiber (450 mW in bus waveguide), while a high-power EDFA operated at a power of 1.8 W compensates the additional 1.5 dB insertion loss (IL) of a narrow band optical bandpass filter. The high-power EDFA consumes around 24 W of electrical power. A thermoelectric cooler (TEC) based control loop is implemented to stabilize the temperature, actuating on the Si_3N_4 chip and consuming ~ 0.5 W of electrical power. After filtering out the pump, the soliton is further amplified using a low noise EDFA which consumes 4 W electrical power. The total electrical power consumed by the multi-wavelength source is 30 W, and each carrier's electrical power is around 500 mW (60 carriers in C- and L-bands suitable for switching and data transmission).

Table 1: Electrical power consumption (current system)	
Components	Power consumed
Laser	1.5 W
TEC	0.5 W
High power EDFA	24 W
Low-noise EDFA (post amplification)	4 W
Total	30 W

As mentioned in the main text, the main origin of excess power consumption is the lower coupling efficiency into the packaged Si_3N_4 microresonator arising due to splicing loss between the ultrahigh numerical aperture (UHNA) and SMF-28 fibers (1 dB per facet). The coupling efficiency can be improved > 50% by using an optimized mode converter and by reducing the splicing loss between the UHNA-SMF fibers [253, 166] (see Figure 2.4). These improvements allow the generation of solitons at an input power of 0.8 W, including 1 dB loss from the optical bandpass filter. In addition, a more compact, power-efficient (electrical power ~ 0.5 W), and on-chip laser can be used to generate the soliton microcomb without requiring lasers with a stabilized module [99, 19]. Similarly, a monolithic piezoelectric or an integrated heater element can stabilize the soliton, ensuring long-term operation and reducing the power consumption to the range of nW to few-mW (TEC, 0.5 W) [93, 94]. These improvements, such as using an on-chip laser, optimized coupling and on-chip actuation, will reduce the system's power consumption down to 15.5 W (193 mW per carrier). Also, it will give access to more than 80 optical carriers as output coupling will be increased around twice. The optimization of the microresonators' different design parameters (as shown in the supplementary information of ref. [84]) such as coupling strength (κ_{ex}) and second-order dispersion (D_2) eliminates the need for post-amplification of comb lines. This will reduce the power consumption down to 13 W for more than 114 carriers in the C and L bands.

Table 2: Electrical power consumption ($P_{opt.}$ ~ 13 dBm /line)	
Components	Power consumed
Laser (DFB)	0.5 W
High power EDFA	11 W
Low-noise EDFA (post-amplification, C- and L-bands)	8 W
High power EDFA (post-amplification, C- and L-bands)	63 W
Total	82.5 W
Per-server (sharing between 32)	2.57 W

Besides, the comb source can be shared across many servers or transceivers as a parallel multi-

wavelength source. As pointed out in ref. [84] supplementary information, it is possible to generate the soliton microcomb in C and L-band with ~ 13 dbm power per carrier while using two additional C- and L-band amplifiers. This particular source can be distributed among 32 servers using a 1×32 splitter with an average insertion loss of around 17 dB. Each server will have a soliton microcomb source with -4 dBm power per carrier for independent wavelength switching. The total electrical power consumed by the whole system and each server is around 82.5 W and 2.57 W, respectively. The power efficiency can be improved to 37 W for the whole system and 1.15 W for each server by using the on-chip amplifier [254]. This makes microcomb-based wavelength sources a more flexible and power-efficient solution for optical circuit switching in the data center.

Next, we evaluated the OSNR of a single comb generator shared between 32 nodes while a single node provides 4x122 individual connections (Figure 5.9). The following analytical expressions are used to estimate the OSNR.

$$OSNR = \frac{\mathrm{P_{out}}}{\mathrm{P_{ASE}}}, \tag{5.1}$$

where $\mathrm{P_{out}}$ and $\mathrm{P_{ASE}}$ are the output power and the ASE noise of a single comb channel after being amplified by an amplifier or a SOA. The amplified output power of each comb channel after EDFA is given by $\mathrm{P_{out}} = \mathrm{G}P_{comb}$, where G is gain. The ASE noise power is given by $\mathrm{P_{ASE}} = h\nu B_{\mathrm{ref}}(FG - 1)$ and h is the Planck constant, ν is the optical frequency of comb channel, F is the noise figure of an EDFA and B_{ref} is the reference bandwidth for noise measurement (12.5 GHz). The total gain (G) and noise figure (F) of the system consisting of a chain of amplifiers is given by

$$G_{\mathrm{t}} = \prod_{\mathrm{n=1}}^{\mathrm{N}} \alpha_{\mathrm{n}} G_{\mathrm{n}} \tag{5.2}$$

$$F_{\mathrm{t}} = \frac{1}{G_{\mathrm{t}}} + \left(F_1 + \frac{F_2}{G_1\alpha_1} + \frac{F_3}{G_1\alpha_1 G_2\alpha_2} + ... + \frac{F_n}{\prod_{\mathrm{n=1}}^{\mathrm{N-1}} \alpha_{\mathrm{n}} G_{\mathrm{n}}} \right) \tag{5.3}$$

Where α is the power transmission factor of the passive component ($0 < \alpha < 1$) while G_1, G_2, ..., G_n and F_1, F_2, ..., F_n are gain and noise figure of individual amplifier respectively. An optimized high-power comb source could provide carriers with maximum and minimum OSNR of ~ 39 dB ($\mathrm{P_{comb}}$= -12 dBm) and ~ 35 dB ($\mathrm{P_{comb}}$= -16 dBm) before data encoding via MZM (Figure 5.9) indicating better OSNR can be achieved in comparison with current results. The variation in OSNR is due to the varying power of comb lines in ~ 3 dB bandwidth. The variation in OSNR can be reduced and further improved by optimizing the ratio of κ_{ex} and κ_0 and second-order

dispersion.

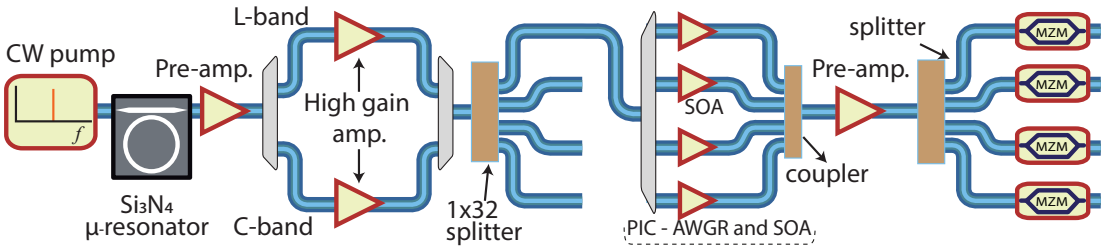

Figure 5.9: **The experimental setup to generate the comb lines having 13 dBm power per line to be shared across multiple nodes and transmitters.** The soliton microcomb after the Si_3N_4 chip is amplified using a low noise pre-amplifier ($G \sim 12$dB, F(noise figure) $\sim 4.5 - 5$) [256]. The pre-amplified microcomb is separated into C and L bands via demux (Insertion loss (I.L.) $\sim$ 0.5 dB) and then amplified using high gain amplifiers ($G \sim 20 - 25$dB, F(noise figure) $\sim 5.5 - 6$) [256]. The post-amplified soliton is further split into 32 channels using a 1x32 splitter (I.L. $\sim$ 17 dB). One of the split channels is transmitted through AWGR (I.L. $\sim$ 4 - 6 dB) and SOAs ($G \sim 10$dB, F(noise figure) ~ 6) for fast optical wavelength switching [257]. The signal is further amplified using a low noise amplifier ($G \sim 12$dB, F(noise figure) $\sim 4.5 - 5$) after switching to shared across multiple transmitters (MZM).

5.8 Summary

This work demonstrates the possibility of achieving nanosecond optical circuit switching using a chip-based microcomb for future power-efficient and low-latency data centers. More than twenty individual comb channels in C-band having a power > -20 dBm are switched at < 520 ps using discrete SOAs. The optical circuit switching system with 25-GBd NRZ and PAM-4 burst mode data transmission is shown while switching between different comb channels. Further, a PIC containing on-chip SOAs and an AWG is implemented to show sub-ns switching (<900 ps) and 25-GBd NRZ transmission. The current demonstration can provide a route for a fully integrated, fast-tunable transceiver providing dense carriers for wavelength switching to meet future cloud workloads' power and latency requirements.

6 Integrated photonics enables continuous-beam electron phase modulation

This chapter will discuss a new technological approach to facilitate electron-photon interactions in the continuous-wave regime using a transmission electron microscope (TEM) and photonic integrated circuits based on Si_3N_4. This work brings coherent electron-light interactions out of the realm of ultrafast electron microscopy into conventional electron microscopy. The two main challenges to perform the Inelastic electron-light scattering using photonic integrated structures are the following: first, the optimum photonic chip design allowing smooth interaction with free-electron while maintaining the high-Q essential for resonance enhancement, and second, the efficient light coupling in- and out-of photonic chip during interaction with free-electron inside TEM. In this project, I designed, characterized, and developed the new packaging protocol for this experiment. The experiment was performed at the University of Goettingen. The results are published in Nature [J.-W. Henke*, A.S. Raja*, et al Nature, 600(7890), 653-658 (2022) [1]].

6.1 Introduction

Electron beams are the basis for some of the most precise spatial imaging and chemical analysis methods ubiquitously used across science: material science [258], condensed matter Physics, and Biology [259]. The rapid advancement of electron microscopy epitomizes our growing ability to characterize the structure and function of nanoscale materials, devices and biological systems. Beyond stationary imaging, the advent of in-situ and time-resolved electron microscopy allow for the observation of transient phenomena, and non-equilibrium dynamics [260, 261, 262, 263]. These functionalities are achieved by interfacing standard TEM with a custom-designed ultra-fast laser module [264]. In the form of photon-induced near-field electron microscopy (PINEM) [265], ultrafast transmission electron microscopy (UTEM) permits quantitative, high-resolution imaging of nano-optical fields [266, 267, 268, 269]. The coupling of free electrons with optical fields is utilized for spatial and temporal beam shaping of the electrons through processes such as the Kapitza-Dirac effect [270] and inelastic electron-light scattering [265]. The underlying process of stimulated inelastic electron-light scattering (IELS) involves energy transfer

[1] * equal contribution

between localized optical excitations and free electrons, modifying the state of the electron by generating discrete photon sidebands. The corresponding longitudinal phase modulation of the electronic wavefunction at optical frequencies is quantum-coherent in nature [178, 271], and thus can be used for the coherent control of electron quantum states in space [272, 273, 274, 275] and time [276, 277, 278]. Recent theoretical works suggest that such modulated electron beams enable an electron-mediated transfer of optical coherence, predicting the generation of coherent cathodoluminescence, the resonant excitation of two-level systems, and superradiance from sequential electrons [279, 280, 281, 282, 283]. These developments imply a future close integration of electron microscopy with coherent optical spectroscopy, with opportunities in local quantum control and enhanced sensing.

Harnessing coherent electron-light interactions for scientific and technological applications is hampered by its usual limitation to the ultrafast regime. Recent works implemented IELS [284, 285], a ponderomotive laser phase plate [286] and an attosecond modulator [287] at high continuous-wave powers. To date, low coupling efficiencies and structural damage have limited inelastic scattering to weak interactions in standard TEM (CW-regime).

Recent demonstrations using dielectric microcavities such as microspheres [177] and photonic crystal cavities (PhC) [268], indicate that resonant field enhancement has the potential for an increased interaction per unit of optical power. Despite the use of phase matching and resonant amplification in dielectric laser accelerators [288], prism geometries [289, 290] or free-space coupled whispering gallery mode microresonators [177], achieving strong phase modulation of an electron beam has remained out of reach of regular electron microscopes.

Photonic integrated circuits provide improved flexibility, scalability, compactness, and robustness compared to bulky optics for tailoring electron-light interactions. Recently, inverse-designed photonic integrated circuits have been shown in on-chip particle accelerators, demonstrating keV-level electron acceleration [291]. However, the strong electron-light interaction still requires high peak power pulsed light sources, and quantum coherence of the interaction remains obscure. High quality-factor photonic integrated microresonator is a promising candidate for demonstrating quantum-coherent electron-light interactions at low optical power, via cavity enhancement and phase matching the optical phase velocity with the electron velocity. In particular, Si_3N_4 based CMOS-compatible integrated platform has gained much attention due to its ultra-low loss propagation [37, 38, 28] and has been implemented to perform many linear and nonlinear photonics.

In the following section, highly efficient electron-photon interactions in the continuous-wave regime, using an electron microscope and photonic integrated circuits based on Si_3N_4 are shown. Our setup (Figure 6.1) allows for an electron beam to interact with the co-propagating evanescent field of a microresonator waveguide in the object plane of a transmission electron microscope (TEM). In addition, fiber-coupled microresonators allow light investigation after electrons interact with the empty cavity or cavity pumped externally.

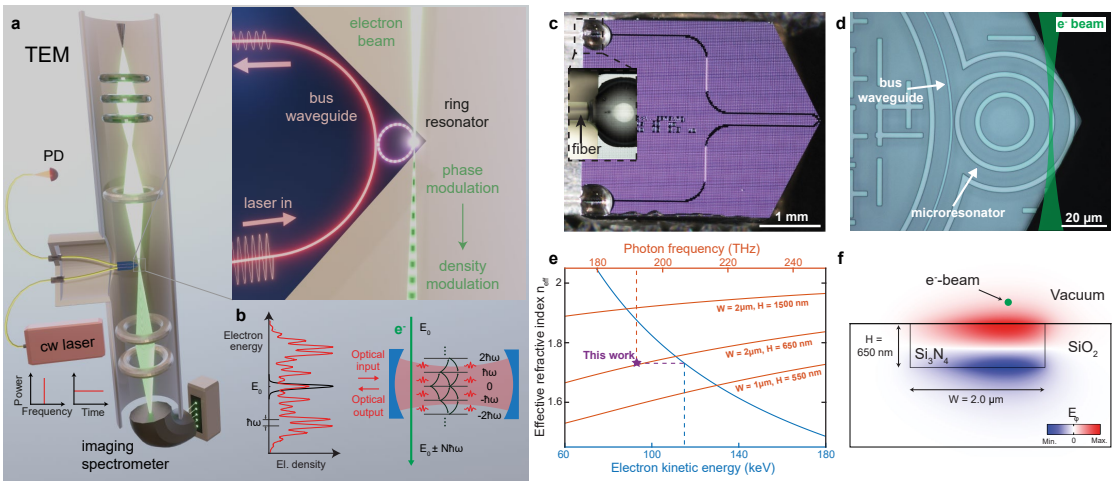

Figure 6.1: **Principle of continuous-wave (CW) photonic-chip-based optical phase modulation of free-electron beams. a)** Rendering of the experimental setup including the electron microscope and a fiber-coupled Si_3N_4 photonic chip-based microresonator. **b)** Left: During interaction with the laser-driven cavity mode, the initially narrow electron spectrum (black) develops discrete sidebands at integer multiples of the photon energy (red). Right: In a cavity quantum electro-dynamical (cQED) depiction, the cavity photons induce transitions between the free-electron energy ladder states. **c)** Photograph of the fiber-coupled Si_3N_4 photonic chip mounted on a customized TEM holder. The triangular-shaped chip edge minimizes undesired electron-substrate interactions. (inset: optical fiber glued to the input waveguide). **d)** Optical microscope image of the photonic chip showing the bus waveguide and the microresonator. The electron beam (green path, not to scale) traverses the microresonator parallel to the chip surface. **e)** Frequency-dependent effective index of the fundamental quasi-TM microresonator mode (red). The integrated on-chip platform allows for achieving phase matching at different electron kinetic energies (blue, 90-145 keV) either by changing the dimensions of the Si_3N_4 waveguide or operating at different optical frequencies. For the waveguide shown in f), phase matching is achieved between the optical mode at ~ 193.5 THz (corresponding to a wavelength of ~ 1550 nm) and the free electrons at ~ 115 keV. **f)** Finite element simulation of the E_φ distribution of the fundamental quasi-TM mode of microresonator (green dot: exemplary electron trajectory pointing into the page).

6.2 Free-electron cavity-photon interaction

The electron-photon interaction at the photonic chip (schematic in Figure 6.1) is described by the Hamiltonian [292, 293] (see SI of Ref. [22])

$$H_{\text{int}} = \frac{e}{2m}(\hat{p}\cdot\hat{A} + \hat{A}\cdot\hat{p}) = \hbar g_0 \hat{a}\hat{b}^\dagger + \hbar g_0^* \hat{a}^\dagger \hat{b}. \tag{6.1}$$

While the length gauge is usually chosen for localized quantum systems in cavity quantum electrodynamics (cQED) [294], the above velocity gauge is a natural choice for free electrons at finite momentum $\hat{p}$ in an electromagnetic field with vector potential $\hat{A}$. The interaction between the optical mode ($\hat{a}$: annihilation operator) and an electron ($\hat{b}$: electron-energy ladder operator,

see SI of Ref. [22]) is characterized by the vacuum coupling rate g_0 [292, 293], determined by the mode distribution and the matching of electron group and optical phase velocities:

$$g_0 = \eta \sqrt{\frac{e^2 v_e^2}{2\epsilon\hbar\omega V}}. \tag{6.2}$$

Here e is the electron charge, v_e the electron group velocity, ϵ the optical permittivity, ω the optical frequency, and V the effective optical mode volume. The phase matching condition is manifested in the coefficient $\eta = \int dz e^{-i\Delta_{k\cdot z}} u(z)/L$ defined by the optical mode profile function $u(z)$ describing the electric field component along the electron trajectory, linked to the vector potential by $\hat{A} = \hat{A}(z) = \sqrt{\frac{\hbar}{2\epsilon\omega V}}(u(z)a + u^*(z)a^\dagger)$, and the electron wavenumber change $\Delta k = \omega/v_e$ upon photon absorption and emission [271, 295]. The scattering matrix, summarizing the effect of the interaction on both the electron and the cavity, is given by $S = \exp\left(-ig_0\tau\hat{a}\hat{b}^\dagger - \text{h.c.}\right)$ [292]. An empty cavity, therefore, allows for electron-driven photon generation [296, 292, 297] in a spontaneous Cherenkov or Smith-Purcell like process [298], and with coherence properties of transition radiation known from so-called coherent cathodoluminescence [299]. Populated by a coherent state $|\alpha\rangle$ from a laser, the free-electron-photon interaction reduces to a dimensionless coupling parameter $g = i\tau\alpha g_0$, where $|\alpha|^2 = n_c$ is the mean intracavity photon number, and $\tau = L/v_e$ is the electron's transit time over the interaction region L, and the scattering operator becomes a displacement operator acting on the electron state. The interaction produces electron energy sidebands separated from the initial energy E_0 by integer multiples of the photon energy $N\hbar\omega$ ($N \in \mathbb{Z}$), with populations following the Bessel functions of the first kind, $P_N = J_N(2|g|)^2$ [295, 178]. In a position representation, the interaction imprints a sinusoidal phase modulation onto the electron wavefunction [295], which upon dispersive propagation will result in a density modulation of the electron beam [276, 277, 278].

6.3 Chip-based integrated photonics platform

To facilitate high interaction strengths, we use photonic chip-based Si_3N_4 microresonators, a platform with many important features including radiation-hardness, high power handling [82], extremely low propagation losses (below 1 dB/m at 1550 nm) [28] and flexibility to engineer dispersion for phase matching. The Si_3N_4 microresonators employed here enable phase matching at different electron energies by modifying the waveguide geometry (Figure 6.1e), while various established integrated platforms can further extend the phase matching range in electron energy and optical frequency. The light is coupled into and out of the Si_3N_4 photonic chip on one edge, while the microresonator is placed on the other edge. To avoid cutting the electron beam by the substrate (see Figure 6.1c), the near edge is clipped and forms a tight supporting triangle. A bus waveguide (dimensions 800 nm × 650 nm) is used to evanescently couple the light into the multimode microresonator (dimensions 2 µm × 650 nm) to achieve a better coupling ideality [172]. The inverse-taper waveguides [166] are used to facilitate efficient light coupling via ultrahigh numerical aperture (UHNA-7) fibers (mode field diameter ~ 3.2 µm at 1550 nm). For

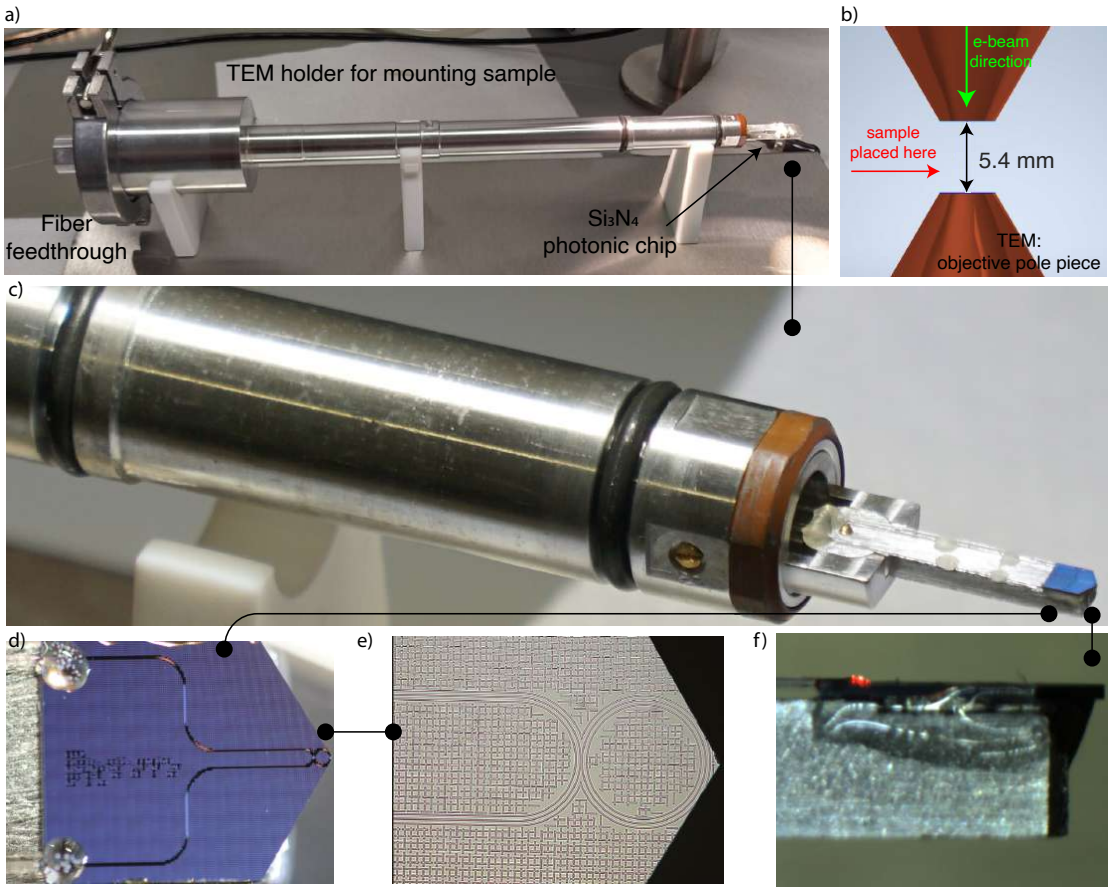

Figure 6.2: **The procedure of sample transfer to a transmission electron microscope (TEM) and Si_3N_4 sample design protocol. a** A TEM sample holder with a length of 32 cm and diameter of ~ 5 mm posing restriction on chip design. The Si_3N_4 microresonators are packaged on a custom-designed chip carrier mount and later transferred to the TEM sample holder. **b** The objective pole piece of TEM where the Si_3N_4 sample is placed. **c** The packaged sample is mounted on a TEM sample holder. **d** The microscope image of packaged Si_3N_4 microresonator. **e** The Si_3N_4 microresonator is placed on the edge of photonic chip, as shown in the zoom-in image. **e** The chip is initially glued to the chip carrier using UV-cured epoxy before fiber interfacing.

operation in the TEM, the photonic structure is packaged via UHNA fibers (see Figure 6.1c & section C.5). A 2-3 cm long UHNA-7 fiber having a thermally expandable core is spliced to standard single-mode fiber (SMF-28) with a splicing loss of < 0.2 dB. A chip through-coupling efficiency (fiber-chip-fiber) of > 25 % is achieved using the UHNA-7 fiber. The photonic packaging is done by first aligning the UHNA-7 fiber via a custom-built holder to optimize the coupling. Then, a small drop of epoxy (~ 150 µm, Figure 6.1 b) is dispensed using a precise pneumatic valve and cured using a UV lamp in four small time steps (~ 2 to 5 minutes). A long-term (~ 1-2 days) coupling stability test is performed at low optical power by monitoring the transmitted light. The broadband characterization of the microresonators is done by employing a widely tunable diode laser. The transmission spectrum is calibrated using a self-referenced optical

frequency comb and Mach-Zehnder interferometer (MZI) [115]. The resonance is fitted using models explained in the subsection 1.2.1 to extract $\kappa_0/2\pi$ (intrinsic loss rate), $\kappa_{ex}/2\pi$ (external coupling loss rate), and $\gamma/2\pi$ (mode coupling rate) for both quasi-TE and quasi-TM mode families. The mean intrinsic linewidth is ~ 110-120 MHz ($Q_0 \sim 1.75 \times 10^6$) for quasi-TM mode family. The cavity resonance center at ~ 1549 nm is critical coupled with $\kappa_0/2\pi = 112$ MHz and $\kappa_{ex}/2\pi = 139$ MHz ($Q \sim 0.77 \times 10^6$). Additionally, in this study, samples with normal dispersion ($D_2 < 0$) are employed to prevent nonlinear effects and explore the interaction of resonantly enhanced fields within a linear regime.

In the current study, we design a ring microresonator (cross-section: 2 µm × 650 nm) to provide phase matching at an optical frequency of ~193 THz ($\lambda \sim$ 1549-nm) for a target electron energy of 115 keV. The effective refractive index (n_{eff}) and the mode profile of the Si_3N_4 microresonator are calculated via finite-element-method (FEM) simulations (COMSOL Multiphysics) (see Figure 6.1f). Mode analysis is performed for the two-dimensional axially symmetric model with the cross-section of the microresonator. Figure 6.1f shows a FEM simulation of the quasi-TM mode profile in terms of its major contributing field component E_φ along the electron propagation direction. The Si_3N_4 core has a rectangular cross-section with width W and height H. The microresonator has a SiO_2 bottom cladding and an air (vacuum) top cladding. The refractive index of Si_3N_4 used in the simulation is obtained from in-house ellipsometry measurement and found to be $n_K = 1.9923$ (J.A. Woollam), while the refractive index of SiO_2 is obtained from ref. [300] as $n_M = 1.4440$. Owing to the small mode area and considerable evanescent field component, we predict a vacuum coupling rate of $g_0/2\pi \sim 10^{11}$ Hz over an interaction time of $\tau \sim 10^{-13}$ s (interaction length: $L \sim 19$ µm). The microresonator's high-Q factor enables a unity coupling constant $g \sim 1$[2] at a coupled optical power of $P = n_c\hbar\omega\kappa \sim 1$ µW, where $\kappa/2\pi = 390$ MHz is the measured cavity decay rate inside of the electron microscope (the intrinsic quality-factor of $Q_0 \sim 0.74 \times 10^6$ is slightly degraded in the microscope) [see section 7.1].

6.3.1 Fabrication of Si_3N_4 based photonic circuit for electron beam manipulation

The microresonators used in this study are fabricated using the photonic Damascene process [59, 28]. A 4-inch silicon substrate with 4 µm thick thermal wet SiO_2 cladding is used. The substrate is coated with deep-ultraviolet (DUV) photoresist, and microresonators and bus waveguides are patterned on the substrate via DUV stepper photolithography (248 nm KrF excimer laser). The pattern is then dry-etched into the SiO_2 cladding using C_4H_8/O_2/He etchants, to create waveguide preforms. Stoichiometric Si_3N_4 film is deposited on the patterned substrate via low-pressure chemical vapor deposition (LPCVD), to fill the waveguide preforms and to form the waveguide cores. Afterward, etch-back and chemical-mechanical polishing [28] are used to planarize the substrate and to remove excess Si_3N_4. The entire substrate is further annealed at 1200°C to remove the residual hydrogen content in Si_3N_4, to reduce hydrogen-induced absorption loss in Si_3N_4 waveguides. This high-temperature annealing is critical to fabricate low propagation losses waveguides at telecommunication bands around 1550 nm. No top SiO_2 cladding is added on top

[2]The coupling constant g is a complex number; for simplicity, in the following, we use g in place of $|g|$.

of the Si_3N_4 waveguides, such that the electron beam can interact with the optical mode. Finally, photolithography with alignment is used to precisely position the Si_3N_4 microresonator close to the chip edge (within a distance smaller than 10 µm, key for aligning the electron beam to the Si_3N_4 microresonator) (Figure 6.2 e & Figure 6.1 d). Deep reactive-ion etching is used to separate the entire substrate into hundreds of individual dies / chips for the following die-level integration with fibers.

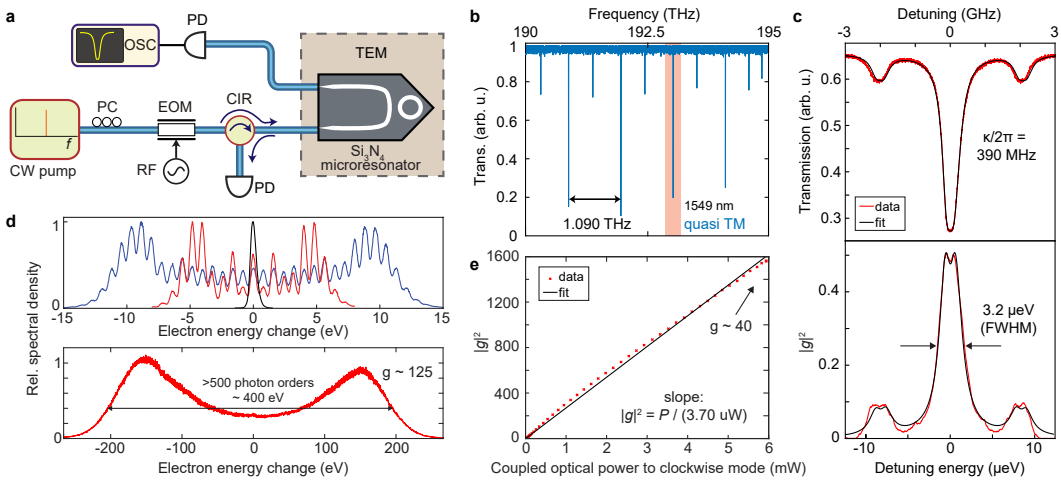

Figure 6.3: **Simultaneous optical and electron spectroscopy of a high-Q microresonator mode. a)** A continuous-wave (CW) is used to excite the quasi-TM mode of the Si_3N_4 microresonator by using a polarization controller (PC). The relative optical frequency is calibrated by imparting sidebands (±2GHz) via an electro-optical phase modulator (EOM). The total transmitted and back-reflected light is detected to calibrate the power coupled into the clockwise propagating mode (CIR: circulator, PD: photodiode, OSC: oscilloscope, TEM: transmission electron microscope, RF: radio-frequency synthesizer). **b)** Normalized transmission scan of the microresonator quasi-TM mode measured outside of the TEM with a Q-factor of $\sim 0.77 \times 10^6$ ($\kappa_0/2\pi = 112$ MHz, $\kappa_{ex}/2\pi = 139$ MHz) and a free spectral range (FSR) of ~ 1.090 THz (see Methods for *in-situ* optical characterization). **c)** Simultaneously measured optical transmission at the output waveguide (top) and $|g|^2$ retrieved from the electron energy spectra (bottom) during interaction of the electron-beam with the evanescent cavity field. The measured $|g|^2$ trace follows the power coupled to the clockwise mode and a slight splitting is present due to modal coupling. **d)** Example electron energy spectra for low (top; $g = 0$ (black), $g \approx 3.5$ (red) and $g \approx 6.7$ (blue)) and high (bottom, $g \approx 125$) optical power. **e)** $|g|^2$ varies linearly with optical power coupled to the clockwise mode of the cavity (slope: $|g|^2 = P/3.70\,\mu$W).

6.4 Combined optical and electron spectroscopy

The packaged sample is transferred into the TEM using a custom holder with vacuum fiber feed-throughs. The fibers connected to the microresonator chip are fed through the hollowed pipe part of the holder (Figure 6.2 a, b, & c). The T-shaped base holding the photonic chip is mounted on an adapter that allows for the placement of the entire structure in the object plane of

the field-emission TEM (Figure 6.2 b& c). Parallel to the surface, the electron beam passes by the waveguide and interacts with the confined optical mode (Figure 6.1a inset). After traversing the structure, the electron kinetic energy distribution is characterized with an imaging electron spectrometer. Electron spectroscopy (Figure 6.3) is implemented in LowMAG STEM mode (indicated magnification: 1000x) at 120 keV electron energy, achieving an electron focal spot size of about 25 nm (FWHM) with a beam semi-convergence angle of 1.1 mrad (100 µm condenser aperture, Figure 6.3d) and 0.45 mrad (40 µm condenser aperture, Figure 6.3c (lower panel) and e), respectively. The STEM focal plane is set in the middle of the microresonator. The lateral beam position relative to the chip is software-controlled (Filter Control, CEOS GmbH) via an external scan generator (USG, TVIPS GmbH). Single spectra are recorded with an integration time of 100 ms (Figure 6.3d). Electron spectroscopy with fast sweeps of the laser frequency is captured by an event-based hybrid pixel detector (EM CheeTah T3, Timepix3 ASIC, 1.56-ns timing precision) and discrete binning in time (100 µs windows, Figure 6.3c,e). The electron beam was either positioned about 30 nm over the microresonator surface, such that no clipping or beam distortion was observed (Figure 6.3d) or at a distance of 380 nm from the microresonator surface (Figure 6.3c and e), as estimated from the optical power in the bus waveguide and the exponential decay of the optical mode.

We first investigate the strength of the coupling parameter g using a focused electron probe, recording electron spectra while scanning the laser over a photonic microresonator resonance employing the setup depicted in Figure 6.3a. The transmission spectrum, displayed in Figure 6.3b, shows the quasi-TM microresonator modes spaced by a free spectral range (FSR) of 1.090 THz.

The optical setup used to perform the spectroscopy in the TEM is shown in Figure 6.3a. The setup is driven by a CW-laser (Toptica CTL 1550), with a maximal power of 40 mW, a tunable wavelength from 1510 nm to 1630 nm, and a linewidth below 10 kHz. The laser is coupled to an electro-optic modulator (EOM) that allows for frequency calibration of the transmission scan and the dependence of g on the detuning from the resonance frequency. A polarization controller is used to align the input light to the microresonator's quasi -TE or -TM mode. An optical circulator is used to probe the light reflected from the microresonator due to bulk and Rayleigh surface scattering responsible for splitting clockwise and counterclockwise cavity modes. The optical transmission and reflection are measured simultaneously to calibrate intracavity power coupled to the clockwise mode.

Figure 6.3c shows simultaneous optical and in-situ electron spectroscopy of the laser-excited microresonator mode. The resonance's spectral line shape is analyzed by recording the transmitted optical power and extracting g for varying frequency detuning (Figure 6.3c). An electro-optical modulator (EOM, driven at 2.0 GHz) generates sidebands that can be observed in the transmission spectrum to calibrate the optical frequency. The laser is tuned to a single optical mode at ~1549.4 nm ($\kappa/2\pi$ = 390 MHz). The focused electron beam (120-keV beam energy, 25-nm focal spot size, 1-mrad convergence semi-angle) is centered just above the surface of the microresonator to record electron spectra for a stationary beam. The optical transmission trace, formed by the interference of the input light with the light coupled out from the clockwise-propagating resonator

mode, exhibits a full-width-half-maximum of 560 MHz (total line width $\kappa/2\pi = 390$ MHz, see SI). Interestingly, the electron spectra, sensitive only to the intra-cavity power stored in the clockwise-rotating, copropagating optical mode, display a double-peaked structure originating from coupling power to the frequency degenerate counterclockwise mode [110]. The differences in width and shape between the optical and electron spectroscopic measurements are explained by the interference in the optical transmission channel with the input field, and both curves can be fitted consistently in one model as presented in section C.6 (Figure C.7 a).

Harnessing the high-Q intracavity enhancement, we observe strong populations P_N in multiple photon orders N, reaching a previously inaccessible regime for a continuous laser light source and electron beam (Figure 6.3d). The coupling parameter g is retrieved from the spectra, while the optical power coupled to the clockwise-propagating mode is determined from the recorded optical transmission and reflection data (Figure 6.3e). Theory predicts that $|g|^2$ is proportional to the photon number n_{cw} of the clockwise mode optical cavity mode. The intracavity photon numbers are varied by sweeping the laser frequency through the optical resonance to find the $|g|^2$ dependence on optical power. The $g(t)$ value is extracted for each time step of the sweep, t, by fitting the measured electron spectrum, and the intracavity photon number $n_{\mathrm{cw}}(t)$ is measured from the optical transmission signal using the steady state Langevin equation. By binning the $|g(t)|^2$ trace in 20 ms steps and plotting it against the coupled optical power in the clockwise mode $P = \kappa\hbar\omega n_{\mathrm{cw}}(t)$, we obtain the power sweep curve shown in Figure 6.3(e).

We observe the expected linear dependence $|g|^2 = P/3.70\,\mu\mathrm{W}$ of the coupling on the coupled clockwise optical power. From this, we find a value of 5.35 µW required for a suppression of the electron zero energy-loss peak at $g \sim 1.2$ and a value of $g \sim 40$ for an optical power of about 6 mW. For an optical power of ~ 38 mWin the bus waveguide, we generate > 500 photon sidebands ($g \sim 125$, see Figure 6.3d). While state-of-the-art dielectric laser accelerators (DLAs) achieve the highest peak acceleration gradients for sub-relativistic electron beams using femtosecond lasers [288, 301], our approach enables continuous acceleration with $330\,\mathrm{keV/(m \cdot mW)}$ of micro-bunched electron beams [276, 302]. In terms of the input peak optical power required, this is a 4-orders-of-magnitude improvement in efficiency over free-space coupled dielectric structures [290, 177]. [3] Moreover, the integrated photonics approach allows for controlled interaction with a single optical mode, as described in the following.

6.5 Mode imaging and phase matching

The implementation of chip-based high-Q optical microresonators as efficient electron phase modulators requires insights into the real-space scattering distribution. For this purpose, an energy-filtered transmission electron microscopy (EFTEM) using collimated TEM-illumination is used to image the interaction across the cavity mode near-field. These measurements enable imaging of individual sideband populations with a high spatial resolution (Figure 6.4 & Figure 6.5).

[3] Note a recent study presenting continuous-wave IELS in the context of DLA posted at the same time as our work [303].

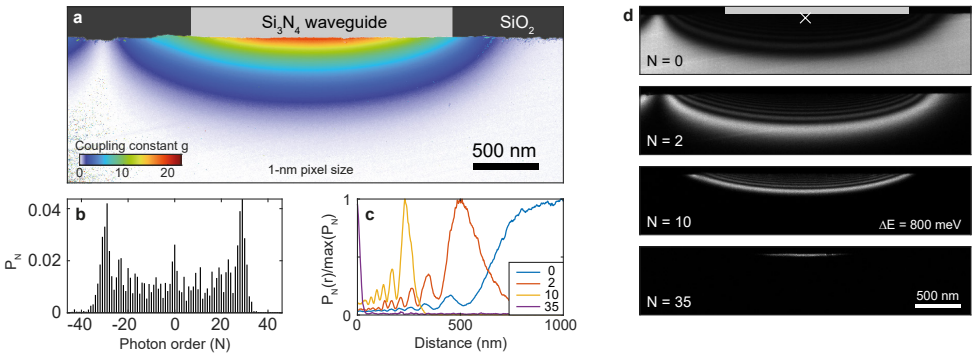

Figure 6.4: **High-resolution hyperspectral imaging of the quasi-TM microresonator mode. a)** Spatial map of the coupling constant g at phase-matching condition (115-keV electron energy) with a 1-nm image resolution. **b)** Exemplary electron spectrum retrieved from energy filtered spatial map (position indicated by cross in d)). **c)** Photon order-dependent sideband population as a function of the distance to the chip surface. **d)** Energy-filtered images of selected photon sidebands N (indicated). The energy window has a width of 800 meV and the position of the microresonator is indicated in grey.

Employing an imaging energy filter (800-meV energy pass band), we record spatial maps of the discrete sideband populations P_N (Figure 6.4d, see Methods). At each image pixel a photon-order resolved spectrum is extracted (Figure 6.4b) and the coupling parameter g is retrieved with a 1-nm spatial resolution (Figure 6.4a), lifting previously encountered signal-to-noise ratio limitations in PINEM by using a continuous electron beam (about 3-4 orders of magnitude higher electron flux). The distance-dependent sideband occupations (Figure 6.4c) reveal a strong and high-contrast modulation, indicating the absence of spatial and temporal averaging. We note that a three-dimensional momentum transfer typically accompanies IELS [272, 274], however, in the current experiment, these transverse deflections are not limiting the resolution for in-focus imaging. The transverse deflection of the electron beam upon passing by the microresonator structure is estimated. For an electron energy of 120 keV, a photon energy of about 0.8 eV (corresponding to a wavelength of 1550 nm) and assuming $E_\varphi = E_z$ (i.e. electron-photon scattering above a straight waveguide), a single photon scattering would lead to a deflection of $\sim 1.5\,\mu$rad. Accordingly, in the case of multi-photon exchange with $N = 250$, as shown in Figure 6.3 d of the main text, a deflection of < 0.4 mrad is expected. The STEM camera length was chosen for the measurements presented here to enable full beam transmission through the angle-limiting aperture into the spectrometer.

The microresonator waveguide is designed to match the phase velocity of the excited optical mode with the group velocity of electrons at an energy around ~115 keV. Figure 6.5 shows the spatial pattern of the electron-light coupling near the ring-shaped microresonator (Figure 6.5a). The electron-energy dependent near field maps reveal an oscillatory modulation of g along the chip surface (Figure 6.5c) and an amplitude change with electron energy (Figure 6.5b). At phase matching, the spatial distribution of g closely resembles the electric field configuration of the excited quasi-TM mode (see Figure 6.4a), and the most efficient coupling is achieved for a

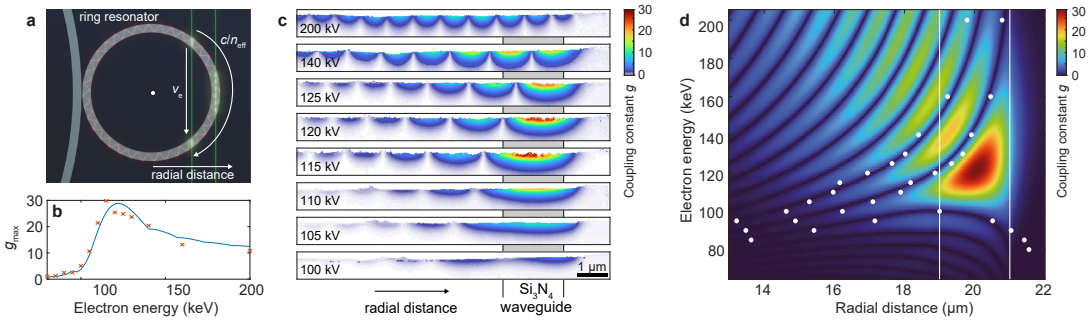

Figure 6.5: **Phase-matching and Ramsey-type interference. a)** Geometry (side view) of the electron beam passing by the photonic chip and interacting with the quasi-TM microresonator mode. The double interaction and phase-shifts between light and electron wave lead to a characteristic spatial distribution of the coupling constant g due to Ramsey-type interference. **b)** Comparison of experimental (red dots, cf. c)) and numerically simulated (blue line, cf. d)) maximum coupling parameter g as a function of electron kinetic energy. **c)** Quantitative g-maps for variable electron energy, showing the spatial distribution and amplitude of the electron-light interaction. The radial position of the Si_3N_4 waveguide is indicated. **d)** Numerical simulation of g as a function of electron energy and lateral position just above the surface. The white dots overlay the experimentally observed minima as retrieved from c) (80-200 kV electron beam energy, waveguide position marked by white lines).

beam passing the periphery of the ring (tangent line). Trajectories further to the center of the microresonator (secant line) are governed by two sequential interactions with the microresonator mode. This results in Ramsey-type constructive or destructive interference that depends on the relative phase of both individual interactions [304].

From the electric field distribution in the cross-section $(r,\ \tilde{z})$ (Figure 6.1 f), the complex electric field along the electron trajectory $E_{\text{traj}}(r,\tilde{z},z)$, related to the physical field by $E_{\text{physical}} = \text{real}[E_{\text{traj}}]$, can be determined via $E_{\text{traj}}(r,\tilde{z},z) = E_\varphi(r,\tilde{z})\cos(z/r) + E_r(r,\tilde{z})\sin(z/r)$. The coupling constant $g(r,\tilde{z},E)$ is then found by evaluating $g = \frac{e}{2\hbar\omega}\int_{-\infty}^{\infty} E_{\text{traj}}(r,\tilde{z},z)\exp(-i\frac{\omega}{v_e}z)\mathrm{d}z$ [295, 178] for different electron energies E, where $v_e = c\sqrt{1 - 1/(1+E/m_0c^2)^2}$ is the relativistic electron velocity. Numerical FEM simulations of the optical mode profile (Figure 6.5d,), considering the electron trajectory through the near-field and the microresonator power enhancement, closely reproduce the experimental observations including the position of the minima in g (white dots). Excellent agreement is achieved for the electron energy dependence of the maximum of g (Figure 6.5b). In contrast to nanoscale-confined optical fields, a steep cutoff in electron-light coupling is found below ~100 keV beam energy, because the optical mode is devoid of higher-momentum electric field components. At high electron energies, the coupling strength reaches a plateau, which enables broadband temporal phase plates for TEM. Besides enhancing the total coupling via a larger interaction time, an increase in microresonator radius will further sharpen the phase matching condition in energy.

6.6 Summary

In summary, we demonstrate highly efficient, phase-matched and single-optical-mode interaction of free electrons with photonic chip-based high-Q microresonators, driving transitions at micro-Watt continuous optical pump power. Based on simultaneous *in-situ* optical and electron measurements, this cQED-type setting yields a quantitative understanding of the interaction and electron energy gain spectroscopy at the μeV level. Our approach may enable a seamless integration of temporal phase plates in electron microscopy over a broad range of energies, with various applications in advanced longitudinal and transverse electron beam shaping for high-fidelity attosecond metrology and sub-cycle probing, beam blanking and high-frequency beam modulation. Coherent beam separation in the optical field may enable new variants of inelastic electron holography, and sequential interactions will provide sensitivity enhancements in coherent electron spectroscopy. The present study provides a missing link for realizing various theoretical concepts in free-electron cQED by establishing full control over the optical input and output channels of a single confined integrated microresonator mode coupled to an electron beam.

7 Interaction of electron with nonlinear dissipative states

This chapter will extend the discussion of the electron beam interaction with multiple nonlinear dissipative states (primary, secondary, modulation instability, multiple soliton, soliton crystal, and single soliton). Pumping the Si_3N_4 microresonator exhibiting anomalous dispersion allows probing of the nonlinear states (intra-cavity). The soliton pulse's intense peak power could pave the way for ~ keV-wide inelastic electron scattering leading to an ultracompact photonic integrated accelerator. Moreover, the initial part of this chapter will discuss the mitigation of charging effects leading to electron beam deflection. I was mainly responsible for sample design, characterization, soliton generation experimental design, and packaging with assistance from Y. Yang, J. Kappert, and J.-W. Henke. I also took part in conducting experiments at the University of Göttingen for this study. Currently, a publication is under preparation summarizing the results of this work [Y. Yang*, J.-W. Henke*, Arslan S. Raja*, F J. Kappert* et al. "Free Electron Interaction with Nonlinear Optical States." In preparation, 2023. [1]].

7.1 Mitigation of charging issues

When an electron beam is passed over the surface of Si_3N_4 chip, a considerable amount of charging effects are observed, even when a small microresonator is used (radius is ~ 20 m). The accumulation of charges on the surface of dielectric materials such as Si_3N_4 and SiO_2 leads to the deflection of the beam. A relatively small microresonator structure is implemented for ease of operation and strong field enhancement inside the cavity due to higher finesse for the first set of experiments (chapter 6). However, the bigger microresonators (radius ~ 113 m) are more suitable for coherent cathodoluminescence (CL) generation due to longer interaction length [106]. In addition, soliton generation experiments are performed in a microresonator with a free spectral range (FSR) of 200 GHz, 100 GHz, and 50 GHz. The soliton generation in the microresonator with 1 THz FSR could not be achieved due to a higher loss (bending radius) and weak anomalous dispersion (limitation due to height). So, in addition to soliton generation for electron beam interaction, the major focus is laid on improving the charging issues to ensure measurements for

[1] * equal contribution.

a longer duration or structures.

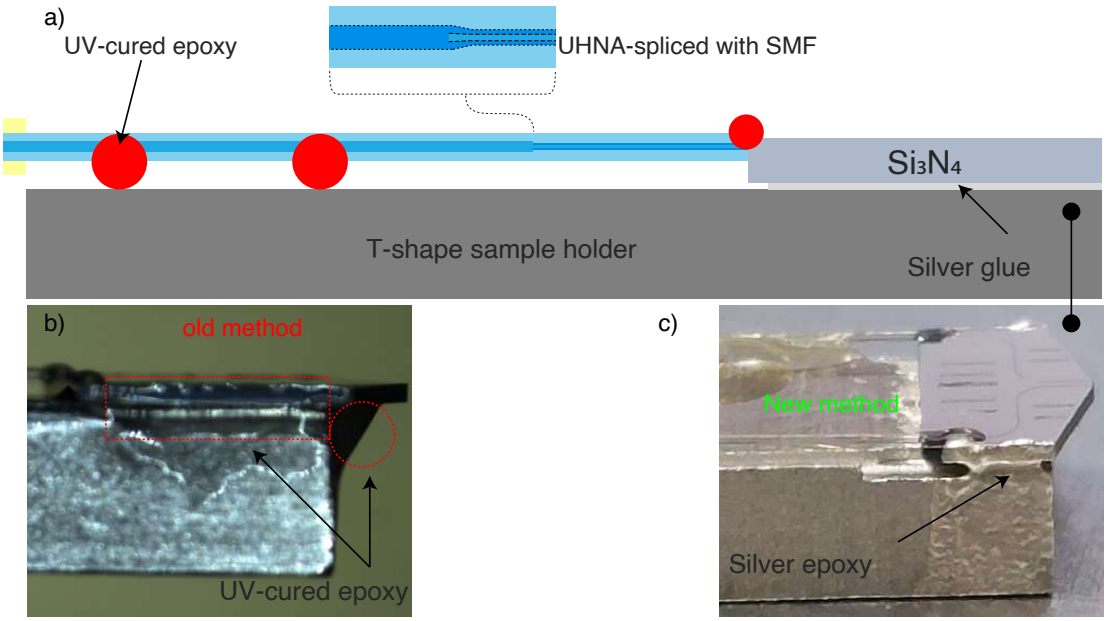

Figure 7.1: **The principle of gluing photonic chip to T-shaped chip carrier.** **a** In the modified sample mounting procedure to the T-shape chip carrier, UV-cured epoxy is only used for attaching the fiber to the chip facet and carrier. **b** An example of chip gluing to a T-shape sample holder via UV-cured epoxy on the side and front edge of the chip. **c** In the modified mounting procedure, a silver paste compatible with vacuum protocols of the transmission electron microscope (TEM) is used to attach the chip. In addition, the bottom surface of Si_3N_4 is also glued via silver epoxy.

7.1.1 Silver epoxy

The initial idea to minimize the charging effects is not to use UV-cured polymer glue on the T-shape carrier for chip adhesion. The initial set of experiments utilizes a large amount of polymer-based glue to attach the chip to the carrier, leading to charging, as found in the first study (chapter 6, section 6.3). Electrically conductive epoxy is used to reduce the charging, compatible with the transmission electron microscope (TEM) operations (vacuum). First, a thin layer of silver epoxy is applied to the surface of the T-shape holder, and then Si_3N_4 is placed on top of it. After ensuring that Si_3N_4 chip is mounted in a straight position, a slight push from the top side of the chip is performed via a Teflon tweezer. Then chip is cured at 80°C for ~ 10 minutes for temporary adhesion. Afterward, the silver paste is applied to the side of the chip as indicated in the Figure 7.1 b carefully. This step is done via needle, which carries a small amount of silver epoxy to avoid putting glue on the surface of the waveguide. However, this step can be avoided as the adhesion via the bottom silver paste is strong enough. But, the purpose of this paste is to make a connection with the top surface of Si_3N_4 chip, which will be coated with a thin metallic layer (subsection 7.1.3). Once the silver paste is applied to the side of the chip, it is cured at 80°C for > 1 hour for curing.

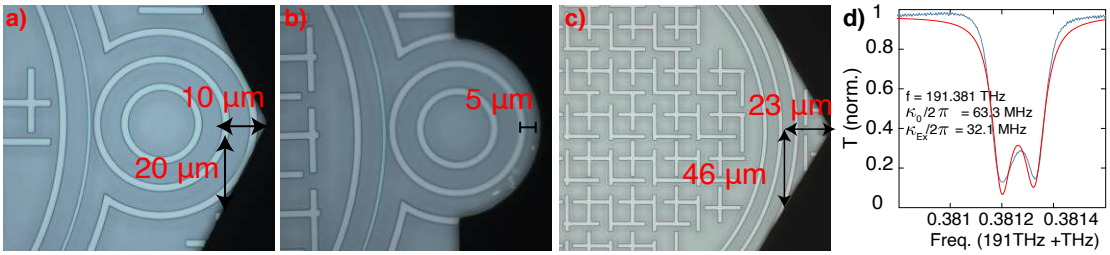

Figure 7.2: **Excess oxide removal on the right edge of Si_3N_4 microresonator to reduce the charging due dielectric materials.** **a** The first chip design is triangular-shape around the Si_3N_4 microresonator. Charging is not severe for relatively smaller rings (radius ~ 20 m). **a** In the modified chip pattern, a semi circle with radius ($Radius_{microresonator}$ + 5 m) is implemented, leading to reduced SiO_2 around Si_3N_4 waveguide. **c** In 200 GHz microresonators (radius ~ 113 m), the charging becomes a major issue in experimental studies, especially for measurements requiring longer duration. **d** The linewidth of the chip shown in b with modified semicircle chip shape, indicating that placing Si_3N_4 close to the chip edge does not degrade the Q-factor (quasi-TM mode).

7.1.2 Optimizing the chip structure

This section discusses the further optimization of the chip structure, mainly removing excess SiO_2 close to the microresonator. The first designed structure consists of a triangular shape at the edge of Si_3N_4 to provide mechanical stability and avoid clipping of e-beam. As seen in the Figure 7.2 a, e-beam travels ~ 20 m before interacting at the edge of the Si_3N_4 ring. The excess SiO_2 around Si_3N_4 waveguide is around ~ 200 m^2. While in the case of 200 GHz, the e-beam needs to travel 46 m before interaction at the edge and excess SiO_2 around waveguide is ~ 1058 m^2. A modified chip structure is introduced to reduce dielectric material close to the interaction region, as shown in the Figure 7.2b. A semi circle-based chip leads to Si_3N_4 microresonator at 5 m from the chip facet with minimum SiO_2 at the exterior surface (Figure 7.2 b). The 5 m value is chosen by considering the misalignment tolerance that can affect the fabrication yield. Moreover, the modified chip shape did not impact the Q-factor of the microresonator. The Figure 7.2 d shows the measured linewidth 1 THz microresonator (Figure 7.2) for quasi-TM mode with total linewidth $\kappa/2\pi$ ~ 95.3 MHz.

7.1.3 Coating thin layer of metal

Further improvements to reduce the charging issue are focused on coating the full part of the photonic chip with a thin metal layer, excluding the Si_3N_4 waveguide and some part of SiO_2 (4 m in the vicinity of Si_3N_4 waveguide, red arrows in Figure 7.3 b & d). In addition to coating the metal, small holes (via) are etched in multiple locations of the chip till the bottom Si layer conducts the electron to Si (Figure 7.3 a, b, c, & e)). To avoid blocking the electron beam due to the additional metal layer, a 100 nm of SiO_2 layer is removed to ensure that the beam can efficiently interact on the top of Si_3N_4 waveguide (Figure 7.3 b & d). The distance between the

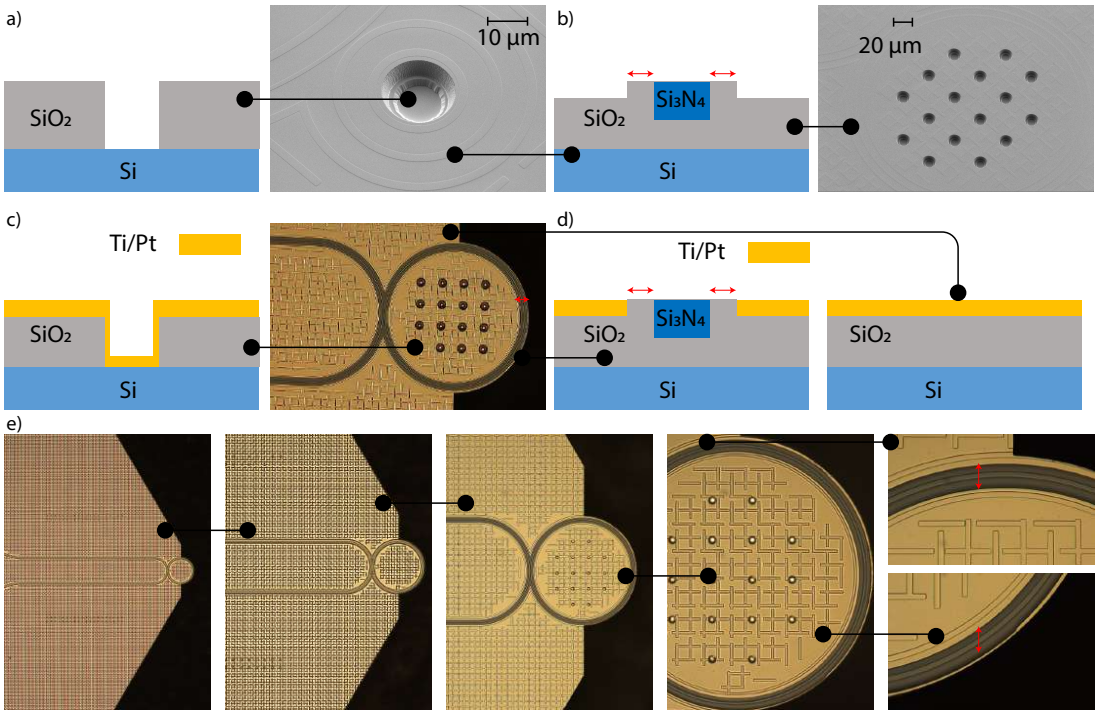

Figure 7.3: **Thin metal layer deposition on Si_3N_4 & SiO_2 chip to improve overall conductivity of electron to reduce the charging further. a** After the chip fabrication, in some parts the chip SiO_2 are etched till layer which can transfer an electron to Si layer via metal. **b** Similarly, a thin layer of SiO_2 is removed to ensure after metal deposition, it does not block *e*-beam (see d). **c** The via-hole after metal deposition provides an electrical connection between Si and the top metal layer. **d** Left, Si_3N_4 waveguides along with SiO_2 in its surroundings (red arrows) are not coated with metal layers. **e)** The microscope images of metal-coated photonic structure with semi circle chip pattern at different magnifications. The red arrows indicate the part where the chip surface is not coated with a metal layer to avoid additional losses. SEM image credit: Rui and Zheru.

metal and Si_3N_4 is swept in the range of 2, 5, 6 m to access the fabrication tolerance and losses. During the metalization process, a misalignment in the range of 2-3 m is observed due to the mask. Indeed, the chip in which the metal layer is placed 2 m away from Si_3N_4 waveguide, the metal approximately touches the Si_3N_4 (see Figure 7.4 c). Moreover, the linewidth measurement indicates that intrinsic linewidth $\kappa_0/2\pi$ is increased from ~ 50-60 MHz to 1.3 GHz in quasi-TM mode. In addition, an overall lower linear transmission is observed in this sample due to the presence of metal in close vicinity of Si_3N_4 waveguide. However, No prominent additional losses are observed in chips having the distance between the metal and Si_3N_4 waveguide is $\geq$ 5 m.

The metal-coated structure was first tested in a scanning electron microscope (SEM) to observe the charging at the waveguide level (Figure 7.4 d). The part of the chip that is not covered with metal (Si_3N_4/SiO_2) showed strong local charging. At the same time, there is no charging on top of the metal surface. A similar behavior is observed when a metal-coated Si_3N_4 chip is transferred to TEM (Figure 7.4 e). However, reducing the SiO_2 around the microresonator

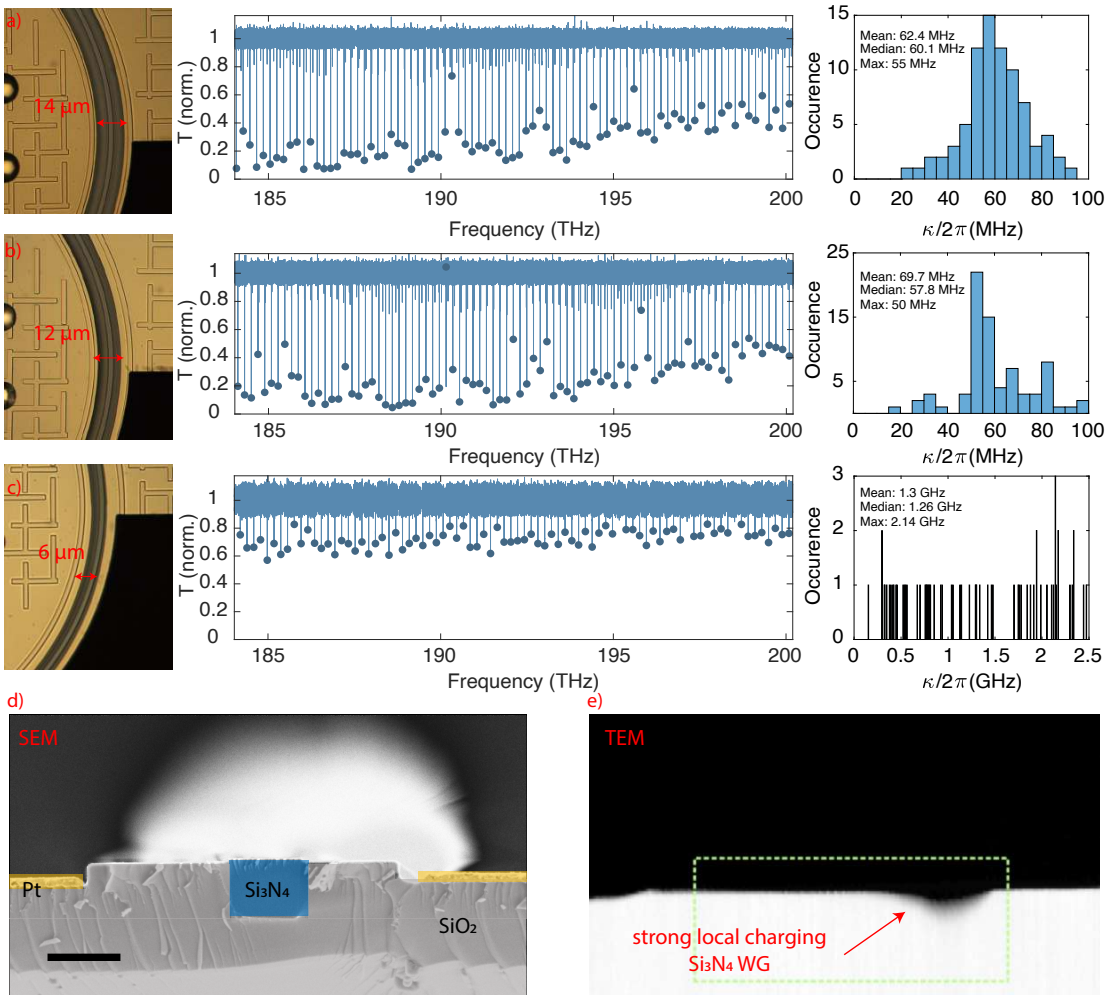

Figure 7.4: **Trsansmission characterization of the Si_3N_4 microresonator by varying the distance of the metal layer from the waveguide edge. a** The distance between metal and Si_3N_4 waveguide's edge is ~ 6 m (both sides, WG width ~ 2 m, total ~ 14 m). The microresonator exhibits intrinsic linewidth $\kappa_0/2\pi$ ~ 60 MHz, showing no additional losses occur due to metal presence. **a** Similarly, chip with the distance between the metal and waveguide is ~ 5 m exhibits intrinsic linewidth $\kappa_0/2\pi$ ~ 55-65 MHz. **a** While chip with the distance between the metal and waveguide is ~ 2 m shows intrinsic linewidth > 1.25 GHz. Here, metal is misaligned by ~ 1 m to the left side leading to higher losses. **d** False color image of Si_3N_4, SiO_2 and Pt(metal) interface taken via scanning electron microscope indicating local charging on dielectric surfaces (Si_3N_4 waveguide and SiO_2). **e** Dark-field image taken using a transmission electron microscope shows the presence of charging on the waveguide surface.

and adding a thin metal layer on the chip substantially improve the charging even though local charging still exists. These changes enable the utilization of bigger microresonators 100 GHz (Radius ~ 227 m) and racetracks resonators.

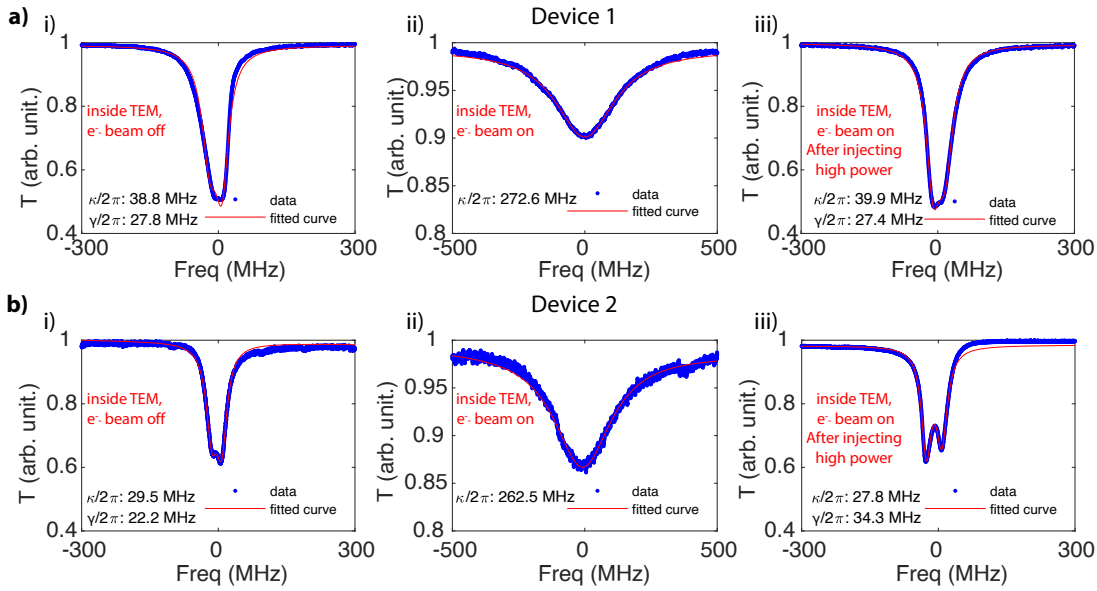

Figure 7.5: **Linewidth measurements to investigate the additional loss when putting Si_3N_4 sample inside TEM. a,i** When a packaged sample is placed inside TEM, the microresonator does not show additional losses when the electron beam is blocked or off. **a,ii** After an electron beam is brought in close vicinity of Si_3N_4 microresonator, an increase in linewidth is observed. **a,iii** However, when the high optical power is coupled to Si_3N_4 microresonator, the cavity's linewidth recovers to its original position. **b,i** A similar trend is observed in another sample that did show any extra loss when the beam is off. **b,ii** In contrast, cavity loss becomes higher when the beam is close to the waveguide. **b,iii** Eventually, the loss recovers when putting a high-power CW light inside the cavity.

7.1.4 Q-degradation

One of the other key challenges regarding soliton generation inside TEM is the degradation of the Q factor. The threshold power for parametric oscillations scales inversely with Q^2 ($P_{th} \propto 1/Q^2$). As mentioned in the last chapter, in the first study (see chapter 6): degradation of the Q-factor from 0.77×10^6 to 0.49×10^6, resulting in an additional increase in total linewidth (~ 150 MHz), is observed when the sample is transferred into the TEM, which could be related to some charging, strain or contamination of the resonator chip.

Here, a more thorough investigation is performed to get insight into possible causes. A Q-factor measurement is performed after packaging, the sample transferring to the holder, and inside TEM (before and after exposure to the beam). When the electron beam is either blocked or off, no significant changes in the linewidth of packaged Si_3N_4, microresonators are observed after inserting the sample inside TEM via holder (Figure 7.5 a, i). Interestingly, as soon as the beam is placed close to Si_3N_4 surface, the resonance shifts and becomes ~ 7× broader (272.6 MHz) (Figure 7.5 a, iii). This means that the device now requires 49× more optical power to generate soliton. However, when a relatively high pump power (~ 300 mW) is coupled to the

microresonator, the linewidth of the microresonator recovers (Figure 7.5 a, iii). A similar trend is observed in another sample (Figure 7.5 b (i-iii))). The possible cause could be the mid-trap states in Si_3N_4 leading to this loss. Unfortunately, the cycle of linewidth recovery via high power is random. Sometimes, it works more than three times on one device, while another device gets damaged permanently after recovering one time. A more detailed analysis needs to be performed, such as analyzing the surface for damage or the formation of some external materials.

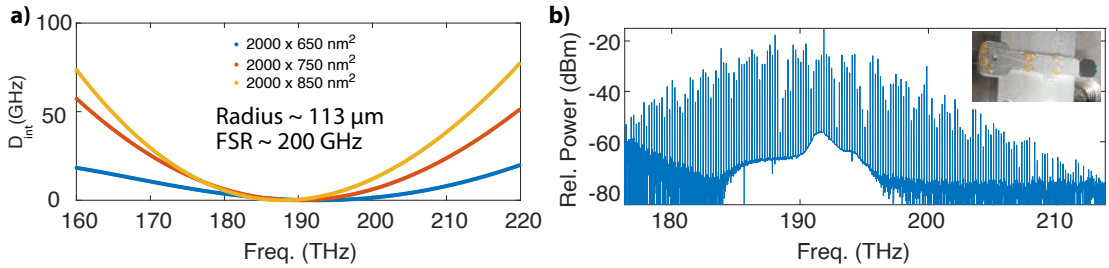

Figure 7.6: **Soliton generation in 200 GHz FSR microresonator via forward scanning (laser's PZT)** **a** The simulated integrated dispersion D_{int} showing the impact thickness variation of air-cladded Si_3N_4 waveguide. A relatively strong second-order dispersion element (D_2) is achieved by increasing the height to ~ 850 nm. However, more thick Si_3N_4 leads to a more confined optical mode and a weaker evanescent field in the air. **b** A multi-soliton initiated via laser PZT (forward scanning) at an input power of ~ 800 mW in packaged 200 GHz FSR Si_3N_4 microresonator. A green light is observed when the multi-soliton state is generated due to the third harmonic generation (inset).

7.2 Soliton generation via PZT - outside TEM

The first wafer designed for electron-beam phase modulation contains a waveguide with a dimension of 2 × 0.650 m^2 (width × height), meeting the requirement for phase matching at 110-120 keV. The waveguide (1 THz) exhibits normal dispersion to avoid nonlinear conversion, allowing electron beam interaction with a single mode, as presented in the chapter 7. However, the multimode interaction requires a microresonator with anomalous dispersion. For this purpose, a lower FSR microresonator (200 GHz) is designed with height ~ 650 nm, which exhibits a weaker D_2. Figure 7.6 a shows simulated integrated dispersion of air cladded Si_3N_4 microresonator with radius of 113 m for three different height (650,750 & 850 nm). As the height is increased, the integrated dispersion becomes stronger. Initially, soliton generation is performed in a microresonator with $D_1/2\pi$ ~ 200 GHz and $D_2/2\pi$ ~ 3.07 MHz. The Si_3N_4 waveguide with a height of 670 nm is chosen to find a balance between anomalous dispersion and evanescent field for interaction with electrons. For soliton generation experiments, quasi-TE (average intrinsic linewidth ~ 25-40) is preferred due to a relatively higher Q-factor than quai-TM mode (average intrinsic linewidth ~ 45-65). However, a multi-soliton state is observed at an input power ~ 800 mW while pumping mode centered ~ 1562.5 nm (f_p ~ 191.867 THz) (Figure 7.6 b). Moreover, the soliton or multi-soliton initiation is difficult below 1555 nm due to strong thermal effects in this sample. The spectrum shown in Figure 7.6 b is generated by scanning the laser PZT by

implementing the setup shown in Figure 3.1.

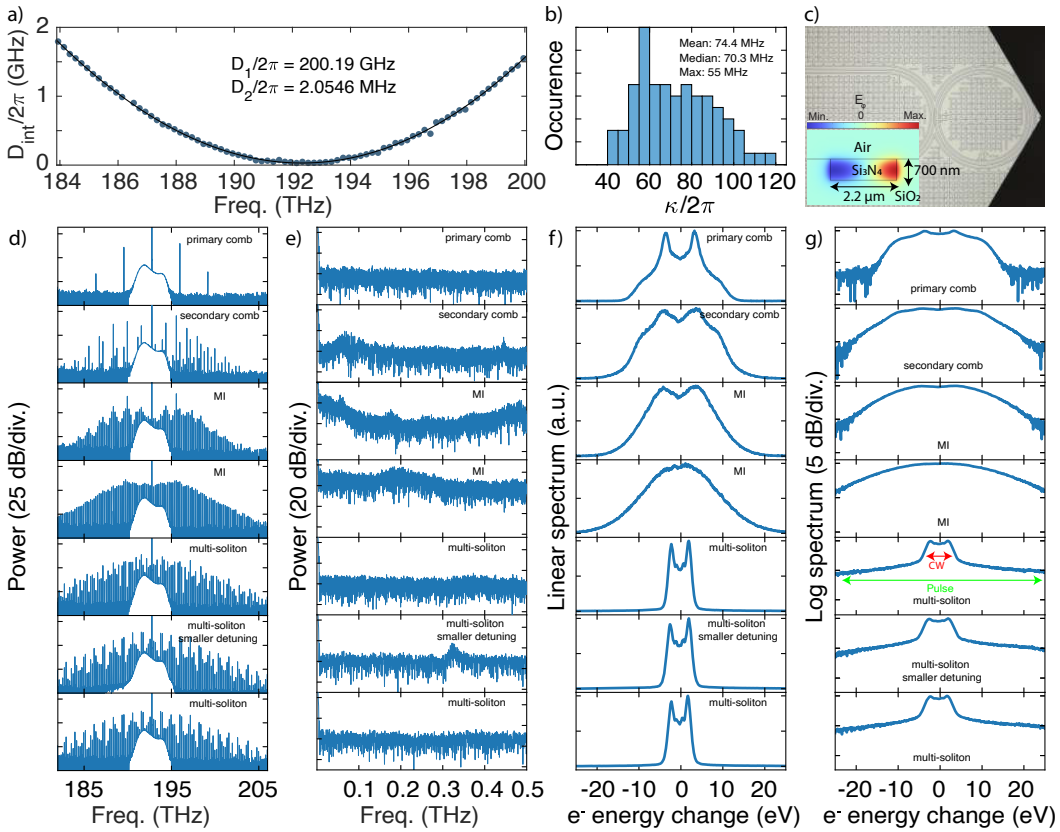

Figure 7.7: **Interaction of multiple lines generated via nonlinear frequency conversion in a Si_3N_4 microresonators with a 200 keV electron beam.** **a** The integrated dispersion of Si_3N_4 with FSR ~ 200 GHz and second order dispersion element $D_2/2\pi \sim 2.05$ MHz for quasi-TE mode is measured by calibrating the spectrum against the full reference fiber frequency comb. **b** The intrinsic linewidth distribution with a mean value of 55 MHz. **c** The microscope image of Si_3N_4 without any additional metal layer and semi circle chip shape. Inset: Finite element simulation of the E_φ distribution of the fundamental quasi-TE mode of microresonator. **d** A set of multiple nonlinear states either generated via manual tuning (primary comb, secondary comb, MI) or performing a single scan over the resonance (multi-soliton states). **e** The low radio-frequency (RF) intensity noise measurement to verify the multiple states. **f** The electron scattering spectrum after interacting with states mentioned in (d). The primary and secondary combs show additional wings due to newly generated frequency lines. While the chaotic state leads to a Gaussian shape electron scattering spectrum in which width varies depending upon detuning (weak or strong modulation instability state), deviating from pure phase modulation with two sideband lobes. When the multiple dissipative pulses inside the cavity interact with an electron, a typical CW inelastic electron scattering is observed with a small contribution from the pulse (not evident in linear scale). The logarithmic scale inelastic electron scattering for different states. Along with CW IELS, a much wider electron scattering (covering the full detector window) is observed arising due to the pulse nature of soliton.

7.3 Soliton generation inside TEM and interaction with electron beam

The next goal is to generate the soliton inside the TEM to study the dynamics of the interactions of nonlinear dissipative states with an electron beam. Due to strong thermal effects, the soliton generation is performed via dual parallel Mach–Zehnder modulator-based techniques, providing access to fast scanning (10 - 250 kHz, section 3.3) of pump mode. For the first feasibility experiment, a Si_3N_4 microresonator with free spectral range (FSR) of 200 GHz, $D_2/2\pi \sim$ and mean $\kappa_0/2\pi \sim 60$ MHz (Figure 7.7 a & b). The Si_3N_4 microresonator surrounding is not covered with a metal layer in this wafer (old wafer, wafer ID D66 (internal naming convention), Figure 7.7 c). Even though the phase matching for CW mode centered at 192 THz is around 110 keV for this microresonator. Due to ease of operation related to beam and spectrometer alignment, the measurements are performed at 200-keV. Moreover, the purpose of the first study is to understand the possible challenges of the soliton generation inside the TEM, and even phase mismatch interaction can provide impactful insight into the interaction of the soliton. Phase-matched interaction will lead to a relatively wider scattering of electrons.

As mentioned, inside TEM, soliton generation is done via DP-MZM as shown in the Figure 7.7 d (bottom three spectrum). The multiple soliton states are generated at ~ 730 mW optical power, the maximum available power that could be coupled to the chip (erbium-doped fiber power ~ 1W). This limits the achieving the longer existence range of soliton [46]. After adjusting the beam current (1.8 A) and aligning the beam on the top of Si_3N_4 waveguide, the inelastic electron scattering spectrums (Figure 7.7 f) are measured while simultaneously measuring the optical and electrical spectrum (low RF- intensity noise, Figure 7.7 d & e). In these measurements, the soliton generation is achieved at ~ 2× higher optical power than the required to generate soliton outside the TEM. Later measurements found that when the electron beam is close (~ 100 nm) to the surface of the microresonator, it affects the resonance hindering the soliton initiations even though slightly above threshold initiation power is injected into microresonators.

However, after interacting with the nonlinear states, the initial measurements provide valuable insight into the IELS. First, we look at primary comb interaction with the CW-electron beam at 200 keV. In addition to pure sideband modulation with two humps around zero loss peak arising from a central strong CW pump, a hump on both sides is observed (Figure 7.7 f). Further increasing the detuning, a secondary comb is observed, leading to a more scattering of electrons. When a modulation instability state is generated, a Gaussian-shape IELS spectrum is observed [303], and the IELS spectrum gets wider when further tuning into resonance (stronger MI). The multi-soliton state yields an IELS spectrum similar to the single line. However, it becomes evident after plotting the IELS spectrum on a logarithmic scale that the IELS spectrum contains two parts CW (marked as red in Figure 7.7 g) and pulse part, which is marked green. The scattered electrons are wider than the CW part due to the pulse nature of the multiple solitons, which contain strong peak power. While the strength (or the number of scattered electrons) is weaker as we measured the average spectrum, and the soliton pulse interacts with electrons for shorter time

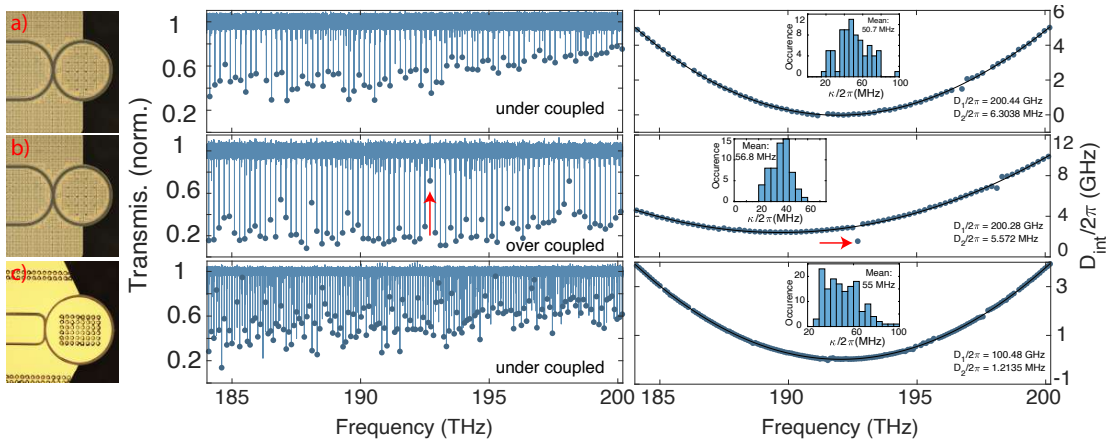

Figure 7.8: **Characterization overview of Si_3N_4 microresonator used for probing the interaction of an electron beam with soliton pulse and multiple frequencies generated via nonlinear frequency conversion.** **a** left: The optical microscope image of 200 GHz Si_3N_4 with metal layer and semicircle clipping. middle: A tunable laser diode calibrated against the optical frequency comb performs the normalized transmissions scan. right: The integrated dispersion calculated from transmission scan with $D_2 \sim 6$ MHz. **b** left: The optical microscope image of Si_3N_4 with metal layer and semi circle clipping. middle: The normalized transmissions scan of over coupled 200 GHz Si_3N_4 microresonator. Right: The integrated dispersion calculated from transmission scan with $D_2 \sim 5.5$ MHz. The red arrow indicates only the mode that generated the soliton; the mode crossing facilitates the soliton generation. **c** left: The optical microscope image of Si_3N_4 with metal layer and semi circle clipping. middle: The normalized transmissions scan of 100 GHz Si_3N_4 microresonator. Right: The integrated dispersion calculated from transmission scan with $D_2 \sim 1.21$ MHz.

intervals in comparison CW part. The electron scattered by soliton pulses covers the full range of the electron spectrometer, and the noise floor is outside the range of the electron spectrometer. In the first measurement run, the vector network analyzer is not used (due to unavailability) to study the impact of detuning, which is linked to the pulse duration. A link between the bandwidth of scatter electrons and pulse duration can be established by studying the detuning-dependent properties.

7.4 Electron-soliton interaction, second generation

The following sections focus on the interaction of electron and soliton with improved Si_3N_4 microresonators with stronger D_2 (higher waveguide height, ~ 750 nm) and metal coating to reduce charging. In addition, some important parameters such as detuning and breathing frequencies are measured via VNA and ESA further to understand the interaction of electron beam with soliton pulse. As mentioned above, the Si_3N_4 sample performance degrades when inserted inside the TEM. Even though the Q-factor recovers when injection of high optical power, samples usually degrade permanently after performing measurements for a couple of days; this

process is random, e.g., some samples never recover even after being put inside TEM for the first time.

In comparison with Si_3N_4 microresonator in section 7.3, the current devices are coated with a metal layer. In addition, they have reduced SiO_2 area (semicircle chip, Figure 7.8 a, b & c) to reduce the charging. Figure 7.8 a & b show the characterization data of 200 GHz of under-couple and over-couple for quasi-TE mode respective. The devices feature anomalous dispersion $D_2/2\pi \sim 6.3$ MHz and $D_2/2\pi \sim 5.5$ MHz corresponding height of $Si_3N_4 \sim 800$ nm and 750 nm respectively. The intrinsic linewidth ($\kappa_0/2\pi$) is around ~ 55 MHz. The over-coupled 200 GHz microresonator exhibits $\kappa_{ex}/2\pi \sim 100$ MHz (total linewidth, $\kappa/2\pi \sim 150$ MHz), requiring input power > 1 W to generate a single soliton (estimation based on under couple device, $P_{th} \sim 120$ mW & $\kappa/2\pi \sim 35$ MHz). However, a single soliton is initiated in this device at ~ 212 mW in a mode close to mode crossing (Figure 7.8 b, red arrow)[196]. In addition to 200 GHz, the interaction of solitons and free electrons is studied for 100 GHz (Figure 7.8 c). A single soliton in these samples is generated at an input power of ~ 187 mW (a), 262 mW (b), and 346 mW (c) by scanning laser via DP-MZM at a speed of 250 kHz. A single soliton generation could not be achieved in section 7.3 in previous measurements.

After inserting the sample inside TEM, a low-magnification scanning TEM mode (x5000 nominal magnification) is used with a focused electron beam of < 25 nm spot size, and a low convergence angle (40 µm condenser aperture) are used to scan parallel to the chip surface. The focus of the electron beam is adjusted by using a sharp triangular tip placed at the edge of Si_3N_4 microresonator. After roughly aligning the beam while pumping the microresonator in a single-mode regime (absence of nonlinear conversion), tilt alignment is adjusted by improving the contrast of Ramsay fringes (see in last chapter 6, Figure 6.5). The electron energy distribution is measured using a post-column energy filter with 64 eV dispersion, effectively measuring 32 eV around the central zero loss peak (ZLP). The width of ZLP is around 1.1 eV, measured via a hybrid pixel electron detector. The pixel-to-size (m) calibrations are performed with the help of reference measurements.

The results from 3 different chips are summarized in Figure 7.9. The 200keV electron beam is shown to interact with multiple nonlinear states. As observed in the first experiment, the primary comb features a hump on both sides in addition to central modulation to CW-components (more prominent in Figure 7.9 b & c). The CW part contribution becomes narrow in the IELS spectrum due to the conversion of the pump into primary combs. When the laser is further tuned in the forward direction to get a modulation instability state (MI), the IELS spectra resemble a Gaussian shape. No prominent CW part is visible in this regime due to strong newly generated frequency modes around the pump. A single soliton states yield an electron scattering spectrum with two parts; a central CW part and a broad pulse part. As mentioned earlier, while explaining similar time average multi-soliton broader electron scattering spectrum. A single soliton state leads to a similar IELS spectrum.

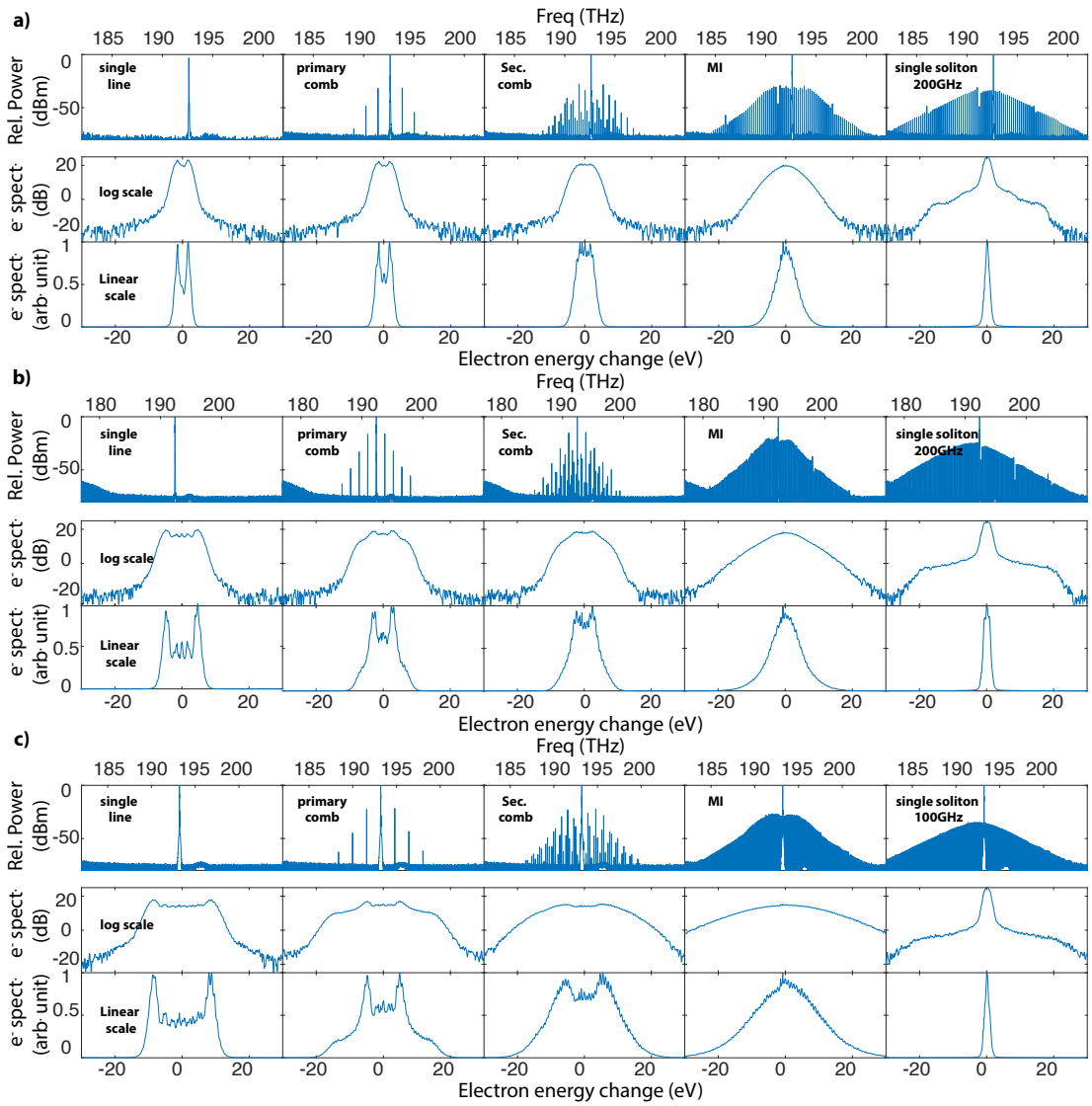

Figure 7.9: **Interaction of multiple frequency lines generated via nonlinear frequency conversion in a Si_3N_4 microresonators with a 200 keV electron beam.** The time average interaction of CW electron beam with single mode, primary comb, secondary combs, modulation instability (MI), and single soliton for three different microresonators (**a** 200 GHz, **b** 200 GHz & **c** 100 GHz). The top row shows the optical spectrum generated inside TEM, the middle row shows the logarithmic scale inelastic electron scattering spectrum, and the bottom row shows the linear scale IELs spectrum. All three microresonator features approximately similar electron scattering spectra for specific optical states.

7.4.1 Spatial dependence of nonlinear states

Scanning the focus electron beam linearly over a small region across the Si_3N_4 microresonator records a spatial map of electron scattering. As shown in the previous chapter, Si_3N_4 microresonator showed a Ramsey-type interference due to the double interactions of the electron beam

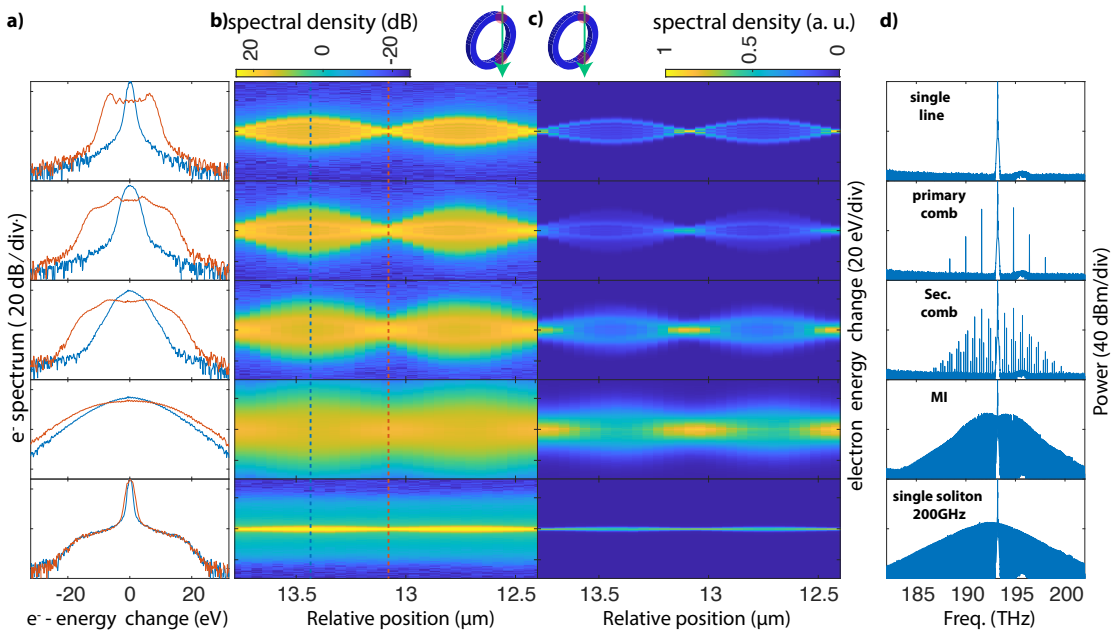

Figure 7.10: **Spatial dependence of nonlinear states with electron accelerating at 200 keV by scanning. a** The spectrum slices taken from spatial maps shown in **b** to compare the electron scattering spectrum at an antinode (blue) and a node (orange) point of Ramsey type interference of CW to other nonlinear dissipative states. The spatial maps in linear (**c**) and logarithmic scale (**b**) are recorded by scanning the beam across ~ 1.39 m region (radial). CW-mode shows typical Ramsey-type interference arising due to double interactions of an electron with a microresonator (as indicated in the top side of b). The primary comb features a slightly broader IELS spectrum at the node and anti-node (CW-contribution is reduced). The secondary comb further broadens the IELS spectrum at node and antinode locations. However, Ramsey disappears as the phase of all modes can not be canceled. The weak CW Ramsey is observed in the soliton state, while the pulse part shows no interference (due to single interaction). **d** The corresponding optical spectrum of different optical states is generated by tuning the laser frequency.

with optical fields (or waveguide, see Figure 7.10b top part). This interference pattern contains multi-level Rabi oscillation, as shown in Figure 7.10 a & c (top image). When laser frequency is further tuned inside resonance, optical parametric oscillations lead to the generation of primary combs. The primary combs lead to additional scattering of electrons around the central CW part due to newly generated light. The spatial map node point contains some contributions from new primary combs lines (Figure 7.10 a (red spectrum slice) & b (red dashed lines). However, the anti-node contains scattered electrons due to the CW part (central part) and the side portion arising due to comb lines. The tuning into the secondary comb state further enhances these effects. The node point in the spatial map contains slightly broader electron scattering as some modes' phases can not be compensated for destructive interference. The modulation instability state spatial dependence becomes blurred as the number of modes and relative power increase. Interestingly, the node point (CW- spatial map) scattering is relatively strong, and a slight difference is observed compared to the anti-node point. A single soliton state spatial map contains a weak interference

from the CW part (in the center) and a constant low-intensity spectrum across the 1.39 m region.

In another sample (200 GHz FSR), the radial distance scanning is performed with more data points to capture dependence in detail (Figure 7.11). The single line, primary combs and modulation instability states feature similar as explained before. However, the soliton and soliton breather states feature an interference pattern inside the plateau due to pulse scattering (around the weak CW part, Figure 7.11 a & b black arrow). The spectrum slices at the node and antinode show a hump on the soliton scattering part. This hump arises due to the double interaction of the soliton pulse with the electron pulse. The electron accelerating at 200 keV travels at 0.7c while the soliton pulse travels at 0.5c. In certain regions of the microresonator, there is the possibility of the soliton pulse double interaction (e.g., trailing edge and leading edge). Moreover, the interaction of the breather soliton is studied. First, a slightly strong CW part is observed compared to soliton with higher effective detuning, further validating the origin of the central part. At the same time, the plateau part possesses narrower energy bandwidth compared to the soliton state due longer pulse.

7.4.2 Detuning dependent soliton interaction with electron beam

In the next section, a detailed study analysis is performed to probe the interaction of the soliton pulse with the electron, focusing mainly on detuning. The soliton bandwidth (alternatively pulse duration) links with effective detuning. For this purpose, two approaches are used: discrete detuning (manual) and continuous detuning (by scanning via AFG continuously within the soliton existence range [87, 93]).

7.4.3 Discrete detuning dependent measurements

In the first approach, a single soliton is initiated by scanning over the resonance via SSB. Then soliton detuning is changed by changing the laser wavelength via internal PZT. The effective detuning ($\delta\omega = 2\pi\Delta$) is linked to minimal pulse duration(τ) as follows [46],

$$\tau \approx \frac{1}{D_1}\sqrt{\frac{D_2}{2\delta\omega}}, \tag{7.1}$$

whereas $D_1/2\,\pi$ is FSR, $D_2/2\,\pi$ is second order dispersion element and $\delta\omega$ is the effective detuning. Similarly, the average comb power scale linearly with the square root of effective laser detuning. Generally, it is difficult to measure the effective detuning directly due to the shifting of the cavity during the soliton generation process. By performing weak phase modulation of the pump through a VNA, the effective detuning of the soliton state can be probed without perturbation [123]. Adjusting the laser wavelength manually, a discrete set of detuning points is measured (Figure 7.12 b) within the soliton existence range (typical soliton existence range $\sim 10 \times \kappa/2\pi$). As evident from Equation 7.1, the soliton spectrum gets broader (shorter pulse) at higher effective

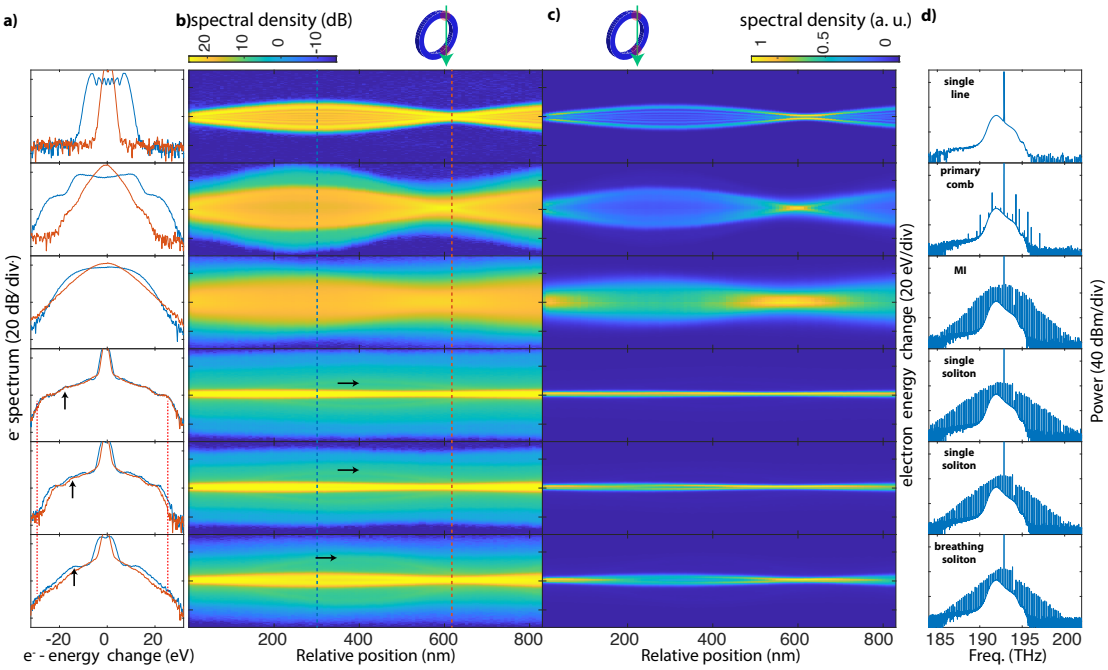

Figure 7.11: **Spatial dependence of nonlinear states with electron accelerating at 200 keV by scanning. a** The spectrum slices taken from spatial maps shown in **b** to compare the electron scattering spectrum at an antinode (blue) and a node (orange) point of Ramsey type interference of CW to other nonlinear dissipative states. The spatial maps in linear (**b**) and logarithmic scale (**c**) are recorded by scanning the beam across ~ 1.39 m region (radial). CW-mode shows typical Ramsey-type interference arising due to double interactions of an electron with a microresonator (as indicated in the top side of b). The primary comb features a slightly broader IELS spectrum at the node and anti-node (CW-contribution is reduced). The secondary comb further broadens the IELS spectrum at node and antinode locations. However, Ramsey disappears as the phase of all modes can not be canceled. The weak CW Ramsey is observed in the soliton state, while the pulse part shows no interference (due to single interaction). A breather soliton is initiated by reducing the effecting detuning, leading to a relatively stronger central CW part. In addition, a weaker soliton plateau is observed due to longer pulse duration. **d** The corresponding optical spectrum of different optical states is generated by tuning the laser frequency.

detuning) and is shown in Figure 7.12 a & d. The larger effective detuning (Δ_3, blue) lead to a larger plateau in electron due to a shorter electron pulse (higher peak power). However, the CW component became weaker due pump moving away from cavity resonance (Figure 7.12 c inset). For more qualitative analysis, the maximum dimensionless coupling parameter $|g_{\max}|$ is calculated after fitting the electron scattering spectrum by using the following expression

$$g = CW + P_{\text{peak}} \frac{1}{cosh(x/width)} \tag{7.2}$$

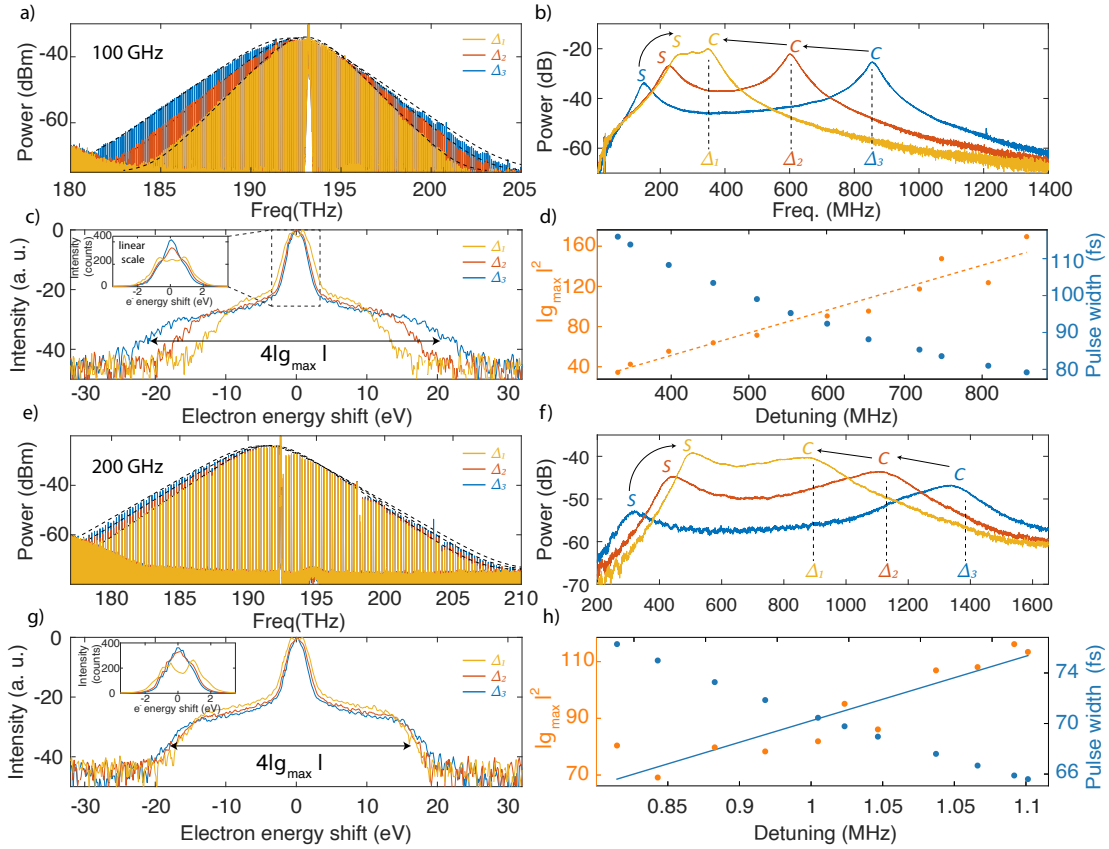

Figure 7.12: **The interaction of electron beam with single soliton state at different effective detuning.** **a** The 100 GHz FSR soliton spectra acquired at three different effective detunings (Δ) as indicated in(Δ_1,Δ_2,Δ_3). **b** Double resonance response of soliton ($\mathscr{S}$) and cavity ($\mathscr{C}$) by scanning phase-modulated sidebands via vector network analyzer (VNA). This allows for determining the effective detuning, which is directly linked to the spectral width of the soliton spectrum (pulse duration). **a** The corresponding electron scattering spectra at three detunings (Δ_1,Δ_2,Δ_3). The main figure indicates the broadening of the plateau at higher effective detuning (or shorter pulse). However, the inset shows linear electron spectrums (2.5 eV to 2.5 eV) showing CW component dependence on effective detuning. **d** The dependence of dimensionless coupling parameter $|g_{\max}|^2$ and soliton pulse duration on the effective pump detuning. The pulse width is estimated by fitting the soliton spectrum, while $|g_{\max}|^2$ is obtained by fitting the electron spectrum at different pump detuning. **e** The 100 GHz FSR soliton spectra acquired at three different effective detunings (Δ) as indicated in(Δ_1,Δ_2,Δ_3) with corresponding VNA (**f**) and electron spectrum (**g**). The detuning dependent dimensionless coupling parameter $|g_{\max}|^2$ estimated after fitting the spectrum shows shorter pulsed lead to broader electron scattering.

where CW is a continuous wave part and $\frac{1}{cosh(x/width)}$ (P_{peak} is peak power and width is pulse duration) is pulse part. The expression is similar to the steady-state solution of the LLE equation ([305], section 1.6). And the fitting is done after averaging the coupling strengths $|g_i|$ ($g(x,y) = -\frac{e}{2\hbar\omega_0}\int_{-\infty}^{+\infty} E_z(x,y,z')e^{-i\frac{\omega_0}{v}z'}\,dz'$) over entire intra-cavity field. Finally, the electron spectrum is determined by the weighted average of IELS spectra corresponding to the different values $|g_i|$

in the distribution, which are given by a comb of sidebands of intensity $P_N = J_N(2|g_i|)^2$ and Gaussian shape [178]. A linear relation between effective detuning and fitted $|g_{\max}|$ values is observed, further indicating broader IELS with a shorter pulse (high peak power). A similar measurement is also performed on a 200 GHz FSR Si_3N_4 (Figure 7.12 e, f,g & h). However, a linear trend can be seen in this measurement (Figure 7.12 h), but overall a deviation is observed ($R^2 \sim 84$ %).

7.4.4 Continous detuning dependent measurements

Further, a Timepix 3 (EM CheeTah T3, Amsterdam Scientific Instruments) electron detector is used to acquire time tagged (event-based) spectra [22, 106]. A ramp signal generated via AFG is fed to laser PZT enabling a continuous tuning of laser wavelength, eventually leading to cavity effective detuning scan if ensuring scan is performed within soliton existence range. The trigger signal from AFG is sent to Timepix 3 time-to-digital converters (TDC) to achieve synchronization. The acquired spectrums are time average (overlap on top of each other) over the integration time to get the single spectrum. Compensating for an electron beam jitter related to 50 Hz noise in the laboratory, the center of mass of the electron spectra in each time bin is shifted to coincide with the zero electron energy change.

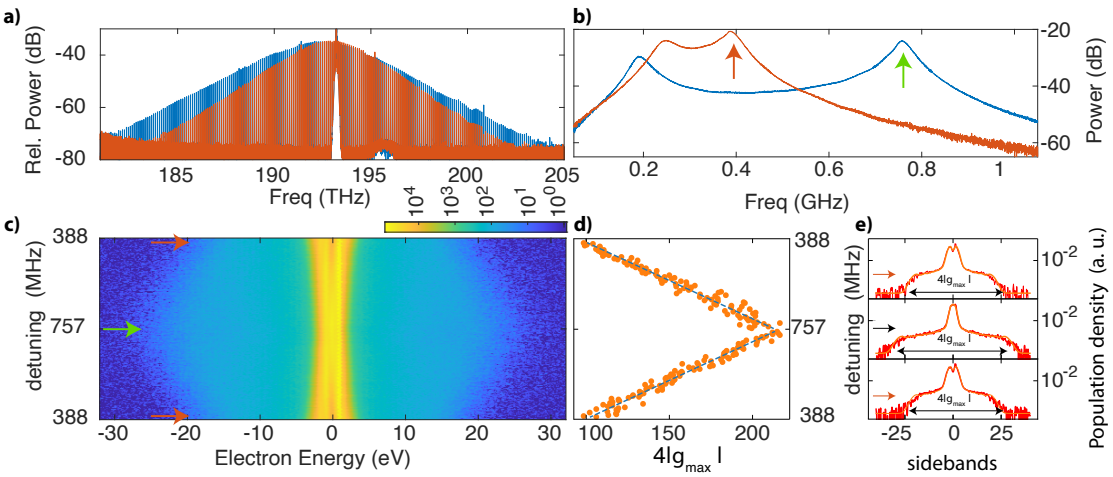

Figure 7.13: **Continous scanning of detuning within soliton existence range via an external AFG. a** The optical spectrum measured at the minimum and maximum of the ramp signal. **b** The corresponding soliton ($\mathscr{S}$) and cavity ($\mathscr{C}$) response measurements. The ramp signal enables tunning of detuning between two $\mathscr{S}$ (marked by orange and black arrows) resonances continuously at the speed of 1 Hz. The total detuning excursion achieved with this method is around ~ 370 MHz. **c** The histogram is calculated after averaging out the measured spectra within integration time. The spectrum in the logarithmic scale shows the modulation of the IELS spectrum via detuning. **d** All 200 spectra in the histogram are fitted using a model explained in Equation 7.2 to calculate the maximum dimensionless coupling parameter ($|g_{\max}|$). The $|g_{\max}|$ scale linearly with the detuning which is changed via AFG. **e** The fitted IELS spectrum at three different points in the histogram (**c**).

Figure 7.13 summarizes the results obtained with this approach—first a ramp signal with V_{PP} ~ 1.1 V is applied to laser PZT. The voltage is applied after initiating the solitons station via DP-MZM (external scanning) and then adjusting the effective detuning to an optimum point such that applying the ramp signal does not lead to going out of the soliton state. A VNA signal is recorded at the maximum and the minimum peak voltage to calibrate the scan from the voltage in frequency (Figure 7.13 b). Moreover, the optical spectrums are also measured to cross verify the detuning properties (Figure 7.13 a). A trigger signal from the same AFG, driving the laser PZT, is injected into the Timepix detector to synchronize. Figure 7.13 c shows a histogram of electron scattering when scanning the laser inside the existence range. The spectrum is linked with effective detuning (Δ), matching well with a trend observed in the last measurement. Each spectrum is fitted with a model explained in Equation 7.2 (Figure 7.13 e) to quantify further the measurement and relation between detuning and $|g_{\max}|$ is calculated. Indeed, the $|g_{\max}|$ scale linearly with the detuning (Figure 7.13 d). These measurements establish a link between the broadening of the electron spectrum and soliton state pulse width and verify the plateau part of electron scattering is due to the soliton state.

In addition, time tagged measurement further allows probing intra-cavity states while continuously scanning the laser. This allows continuous mapping different properties of nonlinear states without tuning into specific states. For this purpose, we utilize the trigger signal from AFG driving the DP-MZM instead of laser PZT. In order to reach a meaningful level of electron counts per 8 ns time bin, spectra are accumulated over repetitive scans of the optical frequency (acquisition time 10 s, corresponding to 2.5×10^6 scans). Figure 7.14 a,b,&c report overview of these measurements performed on three different Si_3N_4 microresonators and at two scanning speed (150 & 250 kHz). The average electron spectra manage to capture multiple states' properties. A continuous scan across the resonance is performed (red to blue and blue to red) during the measurements, and multiple generated light oscilloscope traces are captured to link different nonlinear states with the IELS spectrum. A similar trend is also observed here, such as the broadening of electrons due to primary combs, Gaussian shape spectrum in MI state, and strong CW along with wider low-intensity plateau linking with soliton states (single and multiple).

7.5 Interaction with multi-soliton states

In this part, interaction with multiple solitons is discussed. In addition, with the help of backward switching, a single soliton state is initiated from three soliton states via backward switching to compare interactions in the same experimental condition for better understanding. First, a three-soliton state is initiated by performing a scan over-the-resonance with the help of DP-MZM (Figure 7.15a, top panel). An IELs spectrum similar to a single soliton (strong CW central part and weak broader plateau) is observed. Afterward, a two-soliton state is generated via backward switching by reducing the laser wavelength. A plateau with weak electron counts (intensity) is measured as electrons effectively interact for less time (two pulses instead of three), leading to low electron scattering counts. Finally, a single soliton is initiated by reducing the wavelength further (Figure 7.15a, bottom panel). This leads to even weaker electron counts in

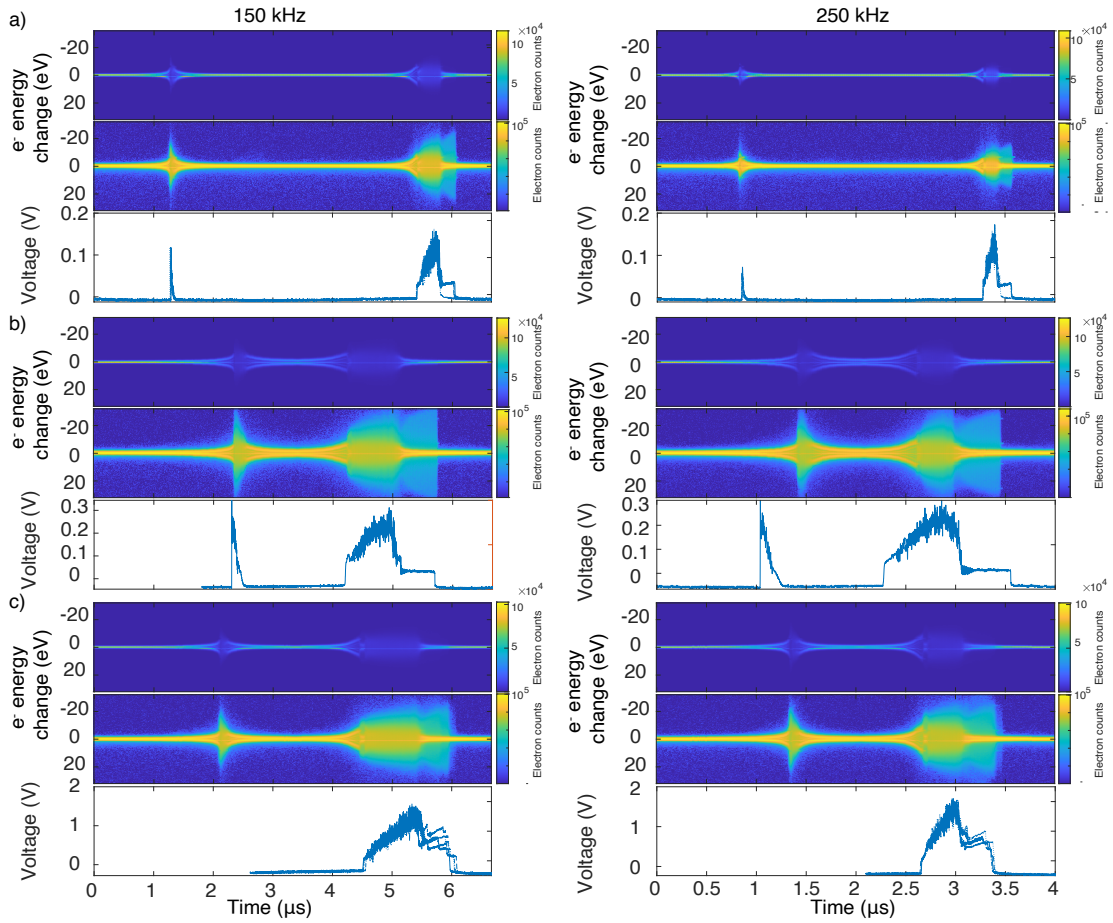

Figure 7.14: **The histogram IELS maps while scanning the cavity continuously via DP-MZM. a** A linear (top) and logarithmic (middle) scale IELS spectrogram showing scattering counts for different nonlinear states of 200 GHz Si_3N_4 microresonator. Multiple generated light traces overlayed to map different stated properties with the IELS spectrum. **a** IELS spectrogram for over-coupled 200 GHz Si_3N_4 microresoantor and generated light traces. **c** IELS spectrogram for 100 GHz Si_3N_4 microresoantor and generated light traces.

the plateau as interaction time is shorter than two and three solitons. The current study relied on the time-averaged interaction of soliton in CW-TEM mode; multiple soliton states could be interesting to study synchronizing the electron pulse and soliton to enhance the interaction.

7.6 Interaction at different electron energies (200 keV and 120 keV)

All the results reported previously are measured at 200 keV, providing a key insight into the electron interactions with nonlinear states. The soliton pulse requires phase matching around ~ 85-100 keV as it travels with group velocity ($n_g \sim 2.1$), requiring some modifications in standard settings instruments (beam and spectrogram). However, the interaction of nonlinear dissipative states with an electron beam accelerating at 120 keV is performed to see the impact of operating

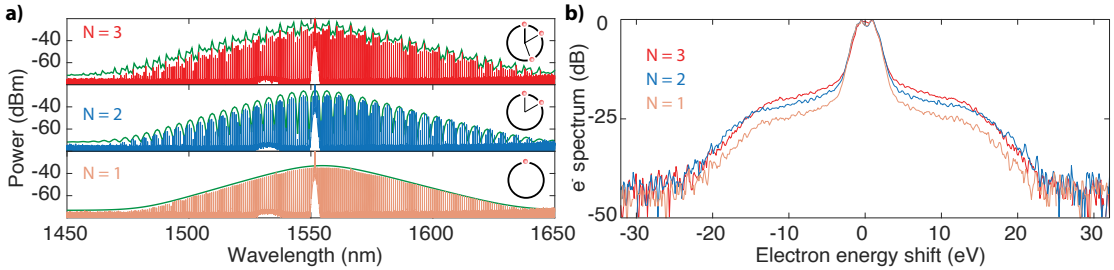

Figure 7.15: **Electron beam interaction with multiple solitons states. a** A set of three different 200 GHZ FSR soliton states, first a three soliton state is initiated by performing a single scan across the resonance (panel). The relative position of the soliton is extracted by fitting the optical spectrum (inset). Then, by decreasing the laser wavelength, a two soliton state is initiated. Finally, a single soliton state is generated by decreasing the laser wavelength further. **b** The IELS for three soliton states, no change in width is observed (detuning is kept constant for all states). However, the strength of the plateau (number of scattered electrons) gets higher with a higher number of soliton states.

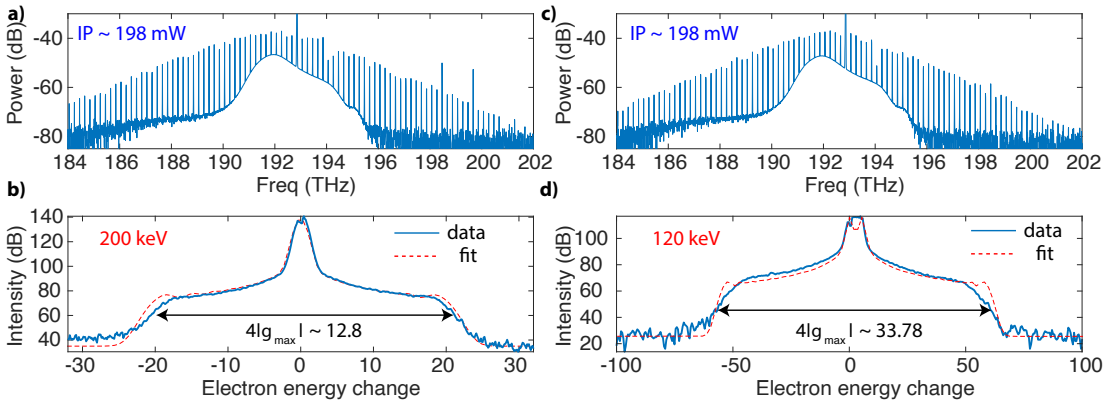

Figure 7.16: **Soliton interaction with electron beam at different electron accelerating voltages. a** The optical spectrum of 200 GHz FSR Si_3N_4 microresonator generated at 198 mW of input power. **b** The IELS spectra after being modulated by a single soliton at 200 keV. The data is fitted using the model explained in Equation 7.2. **c** The optical spectrum of 200 GHz FSR Si_3N_4 microresonator generated at 198 mW of input power (same device as shown in **a**). **b** The measured (blue) and fitted (dashed red) IELS spectra after interaction with a single soliton state at 120 keV.

closer to phase matching points on the same device along with similar states and input power levels (Figure 7.16 a & c). Figure 7.16 shows IELS and optical spectrum performed at two different electron energies. As expected, the 120 keV beams lead to more efficient interaction than 200 keV—a 2.6× higher $|g_{\max}|$ is observed for 120 keV.

7.6.1 Power dependence

In the last section, a study on optical power is performed. Even though soliton initiation is ~ 190 mW, soliton can be generated at relatively higher power (~ 300 mW). Figure 7.17 show two different single soliton states (a & c) generated at two different optical powers (**a** 198 mW & **c** 295 mW). The higher power leads to a broader soliton spectrum in frequency domain and hence a shorter soliton pulse. As expected, the soliton generated at a higher led to a broader IELS with $4|g_{\max}| \sim 60$ compared to lowe power soliton with $4|g_{\max}| \sim 33$—a 1.5 × increase in optical power lead to an increase of 1.7 × in $|g_{\max}|$. Even though the g scale with the square root of optical power P ($g \propto |E|$). Some other factors, such as detuning impacting the pulse duration, need to be considered. In addition, a detuning-dependent spectral broadening of IELS is studied for higher power cases with higher detuning leading to a wider scattering spectrum in plateau region (Figure 7.17 e & f).

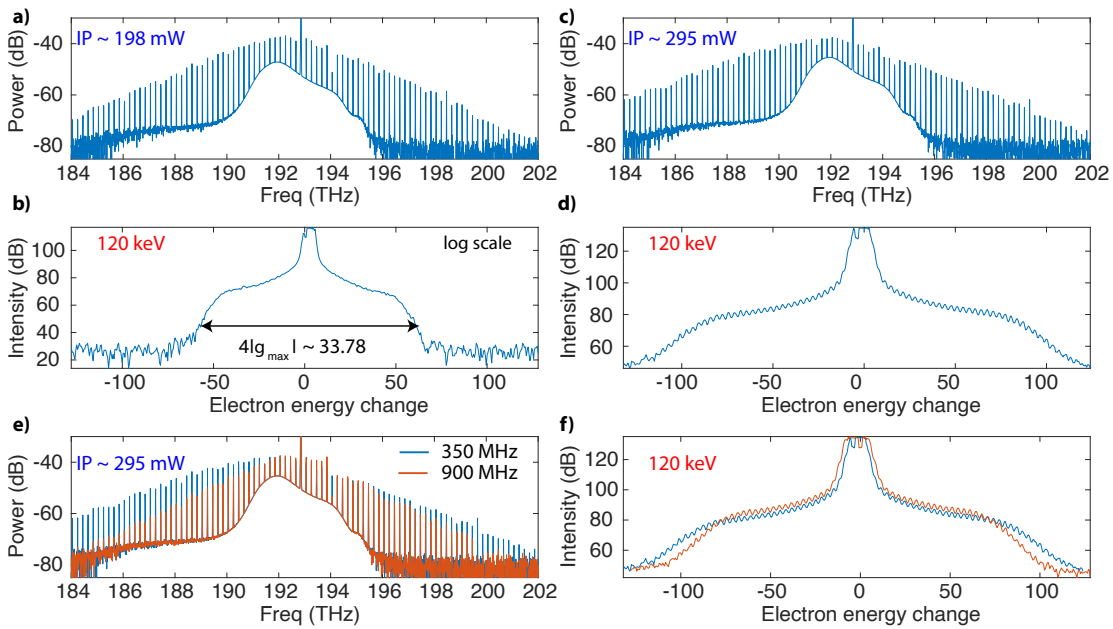

Figure 7.17: **Soliton initiated at different optical power to probe the scattering bandwidth. a** Optical spectrum of single in 200 GHz FSR Si_3N_4 generated at input power ~ 198 mW and the corresponding modulated electron beam spectra (**b**) showing a $|g_{\max}|$ of ~ 8.4 at 120 keV. **c** A soliton spectrum generated at an input power of ~ 295mW with higher comb power lines and higher 3 dB bandwidth. **c** The IELS spectrum shows a wider plateau part covering the full range of 256 eV spectrometer. **e** The optical spectrum generated at two different detunings ($\Delta \sim 350$ and 900 MHz) at an input power of 295 mW. **f** A tuning in spectral width of IELS is observed due to varying soliton pulse duration.

7.7 Summary

Our study further consolidates the modulation of electron beams via integrated photonics and eliminates the massive pulse source to tailor electron beam properties. In addition, the current study could potentially lead to arbitrary electron waveform generation by utilizing multiple nonlinear dissipative states. Current work provides an acceleration gradient of $\sim$ 7 Mev/m while operating in a single soliton regime, which is on par with state-of-the-art RF- accelerators and integrated photonic-based-on-chip laser accelerators. However, the phase-matching interaction can further optimize the performance of such a toolkit for tailoring the electron beam. Moreover, the fast modulation of the electron via pulse (in plateau) can provide the gating of the electron source at a variable 10-1000 GHz repetition rate.

8 Summary and Outlook

8.1 Summary

This chapter is focused on summarizing the results of the current study. The thesis aims to miniaturize Si_3N_4 based photonic devices for multiple linear and nonlinear applications. For miniaturization, two approaches are taken: first is based on self-injection-effect demonstration on an integrated platform. This led to a hybrid integrated electrically driven soliton microcomb based on a multi-frequency-laser diode [19]. The second approach is implemented for a more generic photonic packaging that can be transferred to other platforms and applications, as shown in the current thesis. The main idea of packaging Si_3N_4 microresonator is to demonstrate the applicability of soliton microcomb outside the lab environment, e.g., optical circuit switching for the data centers. To achieve this milestone, much time is devoted to establishing a packaging technique that can work at higher optical power to generate soliton [20]. Moreover, a cost-effective fiber-based mode convertor is used to couple light into the Si_3N_4 waveguide. In parallel, splicing loss between UHNA and SMF fibers is optimized to increase coupling efficiency.

In addition, this study's first application demonstration takes advantage of soliton; a thorough study is done on design, characterization, and soliton generation without amplifier [27], at microwave repetition rate [24] and via AlN-actuation [93]. These studies enable a good understanding of soliton microcomb. Afterward, the combination of experimental understanding of soliton and generic optical packaging led to the demonstration of ultra-fast circuit switching in conjunction with InP-based SOAs and AWGR. The study indicated the potential of microcomb technology as a multi-wavelength source for datacenter by carefully performing a system-level analysis of power and scalability [21].

The generic packaging protocol further demonstrated electron and photon interactions showing the importance of integration ([22, 106]). Moreover, unconventional packaging and sample design requirements validate the reliability of packaging built at the start of the current thesis. The study shows that interfacing a photonic integrated microresonator inside a transmission electron microscope (TEM) leads to efficient interaction without needing pulse electrons, making

this approach more generic (not limited to ultra-fast TEM). Moreover, the efficient light coupling, achieved by optimizing the splicing loss of UHNA-fiber with SMF, leads to electron-photon pairs entanglement [106]. In the last part, the interaction of the electron beam with the dissipative structure is studied, consolidating the established high-power packaging protocols as soliton is generated inside the TEM. Electron beam modulation via nonlinear intra-cavity dissipative states provides rich dynamics of the beam shaping and efficient interactions.

In addition to the main applications mentioned above as part of the current study, fiber pigtailed Si_3N_4 photonics integrated circuit facilitates the demonstration of integrated photon-pair source [25], on-chip accelerometer, photonic parallel convolution [26] and study of Brillouin scattering [81].

8.2 Outlook

8.2.1 Photonic packaging

The generic packaging protocol works relatively well for high-power applications. It can be further optimized by automatizing certain parts, e.g., after dispensing the epoxy at the chip-fiber facet; most of the time, it leads to drift of fiber needing realignment, which is tricky for high viscosity epoxies due to resistance. The current experimental study provides a good understanding of which epoxies work relatively well for high-power, low-temperature, and vacuum applications. This can be extended to a fiber array solution based on SMF-28; however, requiring mode engineering to relax the misalignment tolerance. As shown in section C.4, the coupling achieved via chip-based convertors is not good. The option of UHNA or chip-based mode converter array [1] becomes more feasible if the on-chip mode engineering is done optimally to have better mode overlap allowing > 80% coupling per facet.

8.2.2 electron photon interaction

Generic platform: Various integrated photonics platforms have been used for controlling manifold quantum systems [306, 307, 308, 309, 310, 311, 312, 313, 314, 315, 316]. The current Si_3N_4-based electron beam phase modulation demonstration could be potentially extended to other well-established photonic integrated platforms showing the broader applicability [22, 106]. Finite element method-based simulations are performed to calculate the n_{eff} of the microresonators with different materials by sweeping the frequency and changing the waveguide height. The width of the waveguide is kept at 1.5 m for all materials (Figure 8.1). Differently shaded regions are calculated by performing simulations at two waveguide heights (e.g., solid light-red line GaP: 1500 x 800 nm^2, dashed light-red line GaP: 1500 x 400 nm^2). It is possible to achieve phase matching for electron kinetic energies ranging from 30 to 180 keV by using different established integrated photonic platforms (AlGaAs [71, 317], GaP [318], 4H-SiC [319], Diamond [57], $LiNbO_3$ [320], Si_3N_4 [65], Hydex [65, 321]). Some other prominent platforms, such as Si [322],

AlN [70], Ta_2O_5 [323], and SiO_2 [34] are not shown due to overlapping phase matching, but could also be considered for implementing the electron beam phase modulation. In addition to phase matching, other important parameters that also need to be considered are linear propagation loss, light coupling into the chip and optical power handling.

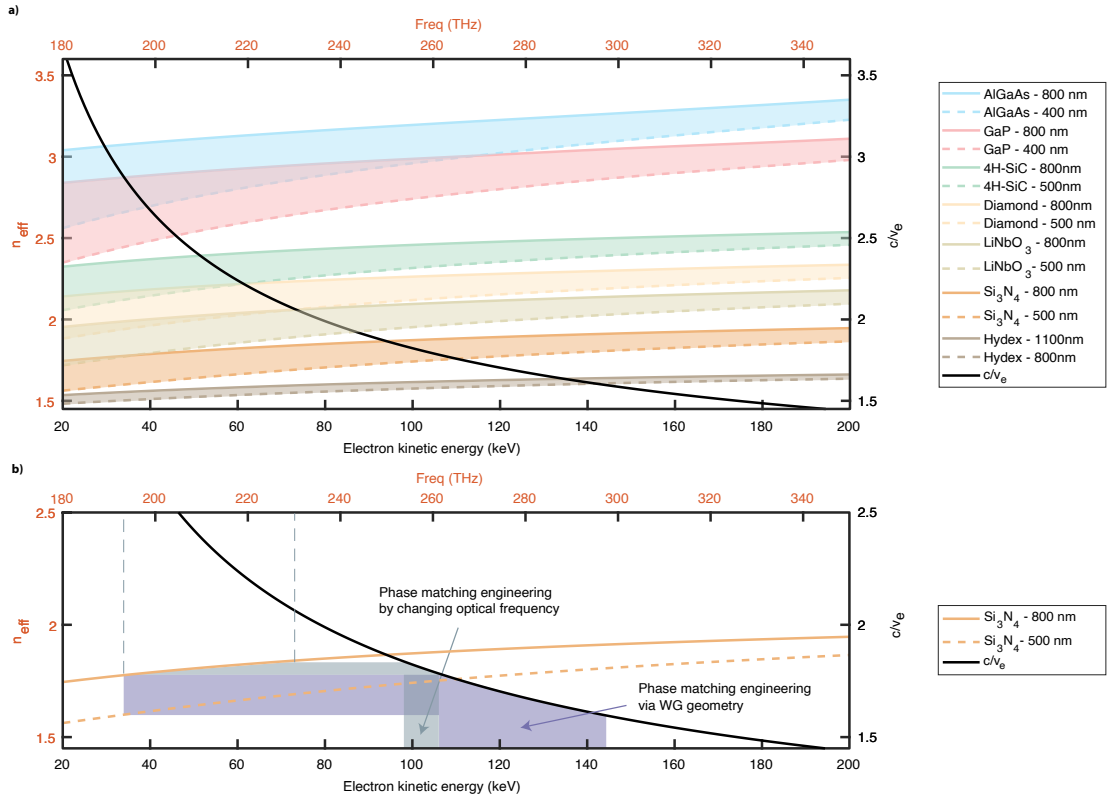

Figure 8.1: **Phase matching conditions for different materials and optical frequencies. a)** For each electron, the electron velocity determines a phase-matched refractive index value accessible through a wide range of optical frequencies and material platforms by engineering the waveguide geometry. The possible simulated regions of the microresonators' effective index (quasi-TM mode) with 50 m radius for different materials are achieved by varying either the waveguide dimensions (height) or the optical frequency. Each shaded region shows a possible operating regime for a single integrated platform. Si_3N_4 could provide phase matching from 95 to 145 keV, while phase matching below 80 keV could be implemented using $4H - SiC$ or $LiNbO_3$. b) The two shaded regions show phase-matching windows for geometry or frequency tuning. The light purple region can be reached by changing the Si3N4 waveguide height from 800 nm to 500 nm while operating at a single frequency (193 THz). The gray-shaded region can be reached by changing the optical frequency from ~193 THz to 230 THz.

Extenstion to other TEM instruments: The platform built as a part of the study performed in the current thesis related to electron-photon interactions (more details in chapter 6 & chapter 7,

[22, 23, 106]), has been already extended to other instruments, such as Titan Themis [324][1]. This could allow realizing a true electron comb (separated sidebands) as the initial electron beam energy (source) width is ~ 100 meV compared to 0.8 to 1.1 eV used in current work. The initial measurements are currently underway.

Synchronize electron soliton interaction: The next possible avenue for further understanding soliton interaction with the free electron beam can be done using a pulse source. Current CW-TEM-based studies provide rich insight into interactions with nonlinear intracavity fields. However, if proper synchronization is achieved, the pulse electron could lead to a longer interaction time (subject to phase matching in addition). It could potentially provide a deeper insight into interactions of multi-soliton states. The pulse laser source utilized to perform the photoemission has a typical repetition rate of ~ tens of MHz. A lower repetition rate soliton is desirable for better phase locking between signals at different frequency ranges (photoemission laser ~ 10 MHz, soliton ~ 25 - GHz). In the case of CW pumping, a fast photodiode can detect the repetition rate. Alternatively, a pulse pumping [54] method can be used to generate the soliton, and the signal RF-synthesizer (electro-optics combs [54, 55, 56]) can be directly used for locking. Regarding the soliton generation at a lower repetition rate, section C.8 shows solitons generated inside TEM at 50 GHz FSR.

Versatile structure: The current study can be further extended by designing two uncoupled microresonators to probe attosecond pulse generation [276] (Figure 8.2 c, d & e). This could be implemented by driving the first cavity via an external laser providing phase modulation to the electron beam. After the phase modulation, the electron can interact with empty second microresonators. It can also potentially lead to the transfer of coherence to free electrons from optics, as highlighted in Ref. [283]. Similarly, a racetrack microresonator can be designed for longer interaction length; the current work is focused on circular ring interaction, where effective interaction length (or time τ) is relatively small. The dimension coupling parameter scale with interaction time τ ($g = i\tau\alpha g_0$), while g_0 scale inversely with effective mode volume (V_{eff}). A trade-off need to be considered for such a structure.

8.2.3 Ultra-fast optical circuit switching

Central unit for parallelization: As highlighted in the previous chapter (chapter 5), a potential next step would be to design a microcomb module providing 13-dbm power per comb line and distributed across 16 servers. The proposed would take advantage of the split and share policy to further ensure the advantage of a soliton-based multi-wavelength laser source. This would require designing an optimal dispersion of Si_3N_4 (e.g., over-coupled). In addition, the dark soliton-based combs could be further considered, which possess higher conversion efficiency and provide low line-to-line power variations [325]. The current study [21] utilized a single MZM modulator for encoding the data; it can also be made parallel by using more than one modulator [244].

[1] in collaboration with LUMES

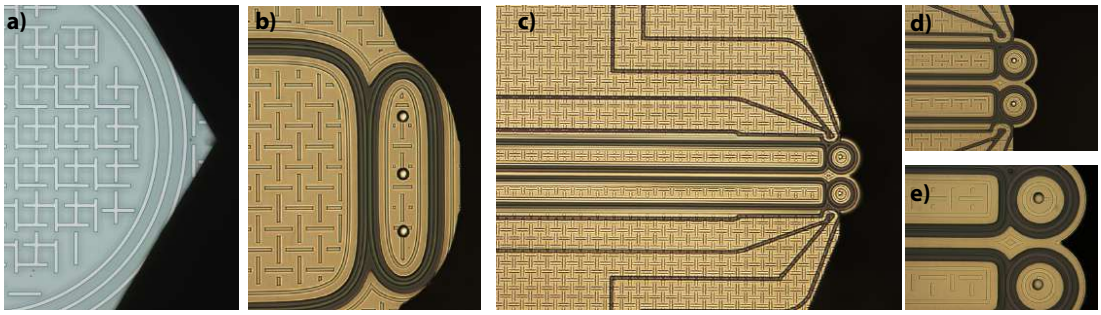

Figure 8.2: **New possible photonic design implementation to study efficient electron-photon interaction. a)** A 200 GHz microresonator used for soliton photon interaction and cathode luminescence (CL, electron-photon pair generation). **b** A race track microresonator for longer interaction length with a free electron. **c** Two 1 THz microresonators (not coupled to each other) are placed at 5 m distance from each other. **d & e** The zoomed-in image of the double microresonator structure.

8.2.4 Self-injection-locking

Multi-frequency laser diode: Even though after the first demonstration of electrically driven soliton microcombs systems (multi-frequency diode and gain chip) [19, 99], DFB laser-based soliton generation via optical feedback has gained more interest due to more deterministic injection locking and soliton generation [101, 100, 37, 6]. However, achieving single-frequency mode operation along with linewidth narrowing at different wavelengths gained a lot of interest. Indeed, a recent demonstration from our group extended the self-injection of multi-frequency laser to near UV and green wavelength range [156] (Figure 1.10). Moreover, a similar demonstration is done at multiple wavelengths ranging from 400 to 780 nm by utilizing fast optical feedback [159]. Even a self-injection locked laser is shown at the mid-IR region around 3 m ([160]), further indicating the potential of this scheme.

A Heterodyne beat signal fitting and soliton fitting

A.1 Heterodyne beat signal and fitting function

The heterodyne measurement is used to assess the coherence of the generated soliton comb, as its lineshape reveals the frequency noise spectral density with respect to the reference laser. When the VNA response is difficult to measure [123] e.g., for self-injection locked soliton, this method can be used to access the coherence of the solution state. However, this method is a useful indicator for low repetition rate devices; more precautions must be taken for high repetition rates soliton (1 THz) [52]. In fact, the frequency noise may consist of both the white noise (resulting in a Lorenztian lineshape) and the flicker noise (corresponding to a Gaussian lineshape). Therefore, we employ the Voigt profile [326] to fit the beat signal, which represents the convolution of the Lorenztian ($L(f)$) and the Gaussian ($G(f)$) lineshapes, i.e.:

$$V(f) = \int_{-\infty}^{+\infty} G(f';\sigma)L(f-f';,\psi)df', \tag{A.1}$$

$$G(f;\sigma) = \frac{\exp^{-f^2/2\sigma^2}}{\sigma\sqrt{2\pi}}, \tag{A.2}$$

$$L(f;\psi) = \frac{\gamma}{\pi(f^2+\psi^2)}, \tag{A.3}$$

where f indicates the frequency shift with respect to the center of the beat signal, in the radio frequency domain, and σ and ψ scale the linewidth. To initiate the fitting we assume that, on the wings of the beat profile, the signal is mostly contributed by the white noise that determines the instantaneous linewidth described by ψ. In contrast, around the center of the beat profile, the signal is also contributed by flicker noise depending on e.g. the acquisition time of the ESA, as well as the stability of the current or temperature controller. This part of the noise is scaled by σ. The full width at half maximum (FWHM) of the Gaussian lineshape is then $\Delta f_G = 2\sigma$ and

$\Delta f_{\mathrm{L}} = 2\psi$ for the Lorentzian.

A.2 soliton comb spectral fitting

It is known that N identical solitons circulating in the resonator produce a spectral interference on the single soliton spectrum [218, 82]:

$$S^{(N)}(\mu) = S^{(1)}(\mu)\left(N + 2\sum_{j\neq l}\cos\left(\mu(\phi_j - \phi_l)\right)\right) \tag{A.4}$$

Here $\phi_i \in [0, 2\pi]$ is the position of the i-th pulse along the cavity roundtrip, μ is the comb mode index relative to the pump laser frequency and $S^{(1)}(\mu)$ is the spectral envelope of a single soliton following an approximate secant hyperbolic squared:

$$S^{(1)} \approx A\,\mathrm{sech}^2\left(\frac{\mu - \mu_c}{\Delta\mu}\right) \tag{A.5}$$

where A is the power of the comb lines near the pump and $\Delta\mu$ is the spectral width of the comb (in unit of comb lines) and μ_c is the central mode of the soliton (to account for soliton recoil or self frequency shift). Knowing the comb repetition rate f_r, the spectral width (or pulse duration) can be retrieved: $\Delta f = f_r\,\Delta\mu$.

The spectral envelope of the single or multiple soliton states are fitted using the following procedure: First, the peaks $\tilde{S}(\mu)$ constituting the frequency comb are detected and labeled with their relative mode index from the pump μ, and the pump mode is rejected. The number of solitons N is estimated by taking the inverse Fourier transform of this spectrum, which yields the autocorrelation of the intracavity waveform, and detecting its peaks [82]. The set of fitting parameters $\{A, \Delta\mu, \mu_c, \phi_i | i \in [\![2, N]\!]\}$ is defined accordingly (the position of one soliton is arbitrarily set to zero) and the expression (A.4) is fitted to the experimental points $\tilde{S}(\mu)$. When N solitons are perfectly equispaced, the repetition is multiplied by N and the single soliton expression can be fitted on every N line.

B Scalability for ultra-fast optical circuit switching

B.1 Scalability of optical circuit switching module proposed in chapter 5

To scale to thousands of nodes, we can take advantage of the fact that today's servers or top-of-the-rack (ToR) switches comprise multiple channels. For example, the recently-announced NVDIA Ampere A100 GPU [327], supports 2.4 Tbps of bandwidth by combining 48 channels, each operating at 50 Gbps. Therefore, assuming 40 wavelengths and SOAs per transmitter, we can connect up to 48 x 40 =1,920 other nodes. If instead, we consider a rack-based deployment, the latest ToR switches [328] have 512 SERDESes (i.e., 256 uplinks) that could allow interconnecting up to 256 x 40 = 25,600 racks, which is an order of magnitude higher than the number of racks in even large data centers today. However, this also means that a node is directly connected to any other node in the data center through only one of its uplink channels. To ensure that any pair of nodes can still communicate with their full bandwidth, the network routes traffic between any pair of nodes through all other nodes in the network. Such detour routing imposes a throughput overhead, although the throughput can be at most 2× worse than an ideal switch and, thus, can be compensated by doubling the per-node network bandwidth. Furthermore, detour routing offers several advantages. It obviates the need for explicitly scheduling network traffic, which has been a key bottleneck for practical and deployable optical switching in the data center. More comprehensive details of this network architecture and the trade-offs imposed by topology and routing choice are presented in a separate paper [244]. Increasing the number of nodes in the current system would require using soliton microcomb and AWG with lower FSR. Soliton microcombs operating at a repetition rate of 10 GHz have been demonstrated [248]. Similarly, InP-based AWG with 100 × 10 GHz has been shown [329] indicating scaling feasibility in the future. In the current architecture, the SOAs scale with N^2 where N is the number of nodes if a single transmitter (MZM) is used. Here we propose to use multiple transmitters (MZM) on each node (figure 1 b, main text) to reduce N^2 scaling. This allows scaling the flat network without being limited by the low yield of large-scale InP devices. Detailed analysis on the scalability optical network is explained in ref [244].

B.1.1 FSR matching of switching unit and microcomb

It is important to match the FSR of both soliton microcomb and AWG to standard ITU grid spacing for precise aligning of channels while the central channel can be aligned via thermal tuning. In the current demonstration (chapter 5), the FSR mismatch is $\sim$ 0.5 GHz (soliton microcomb), which can be further improved by using an optimized design that is more tolerant to fabrication errors [330] and improved fabrication [35]. InP-based AWG is a standard module that is designed (JEPPIX foundry) and fabricated at the commercial foundry (Fraunhofer HHI), providing precise control over FSR.

C Optical packaging for electron-photon interaction and Transmission electron microscope

C.1 Transmission electron microscope

One of the current study's applications revolves around the free electron's interaction with the photon required using a transmission electron microscope [331]. A basic instrument overview is given in Figure C.1. Historically, TEMs are used for the imaging and spectroscopy of materials in transmission mode by taking advantage of the short wavelength of electrons. An electron gun emits an electron beam, which is accelerated at 30 to 300 keV. Then a set of electromagnetic lenses collimate or focuses the divergent electron beam. Then focus or collimated beam interacts with a thin sample (transparent for electron beam). After interaction with a thin sample, the electron beam is sent to the detector for imaging with the help of an objective lens. To achieve temporal resolution, an external pulse laser system is interfaced with standard TEM, known as ultrafast TEM (UTEM)[264].

C.2 Long-term coupling stability

The input and output power monitoring of the packaged device for data shown in the Figure 2.10 (Figure C.2) is performed to understand the fluctuations in coupling efficiency.

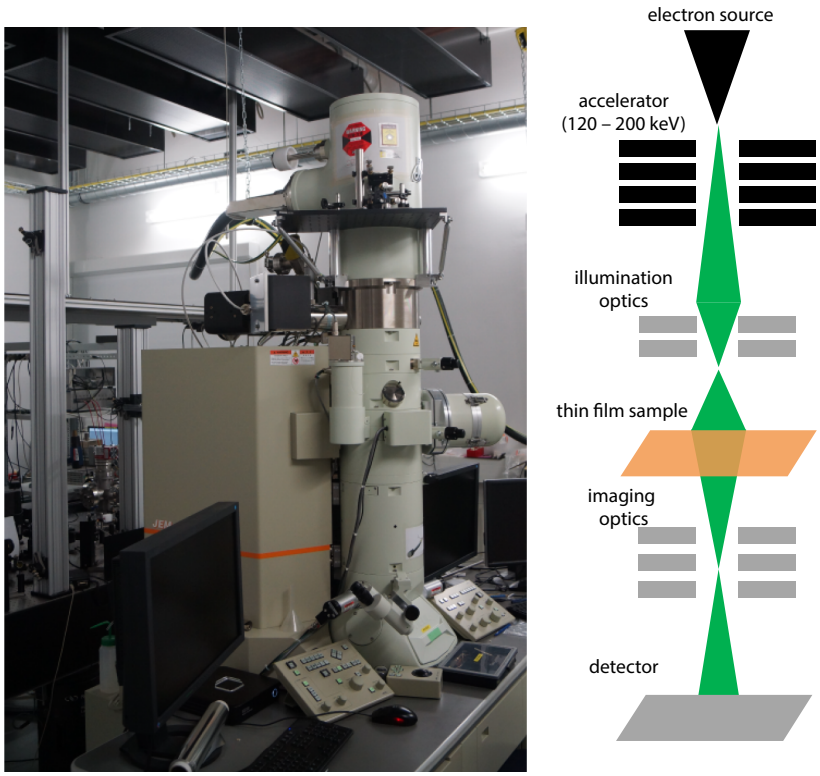

Figure C.1: Transmission electron microscope general working principle. Left: The image of modified TEM (ultrafast TEM) at the University of Goettingen. Right: Electrons emitted by the source are accelerated in the column of the TEM. The electron beam is then focused using electromagnetic lenses at the sample plane. Then electrons are directed towards the detector via electromagnetic lenses after passing through the sample. Image Credit: Armin Feist.

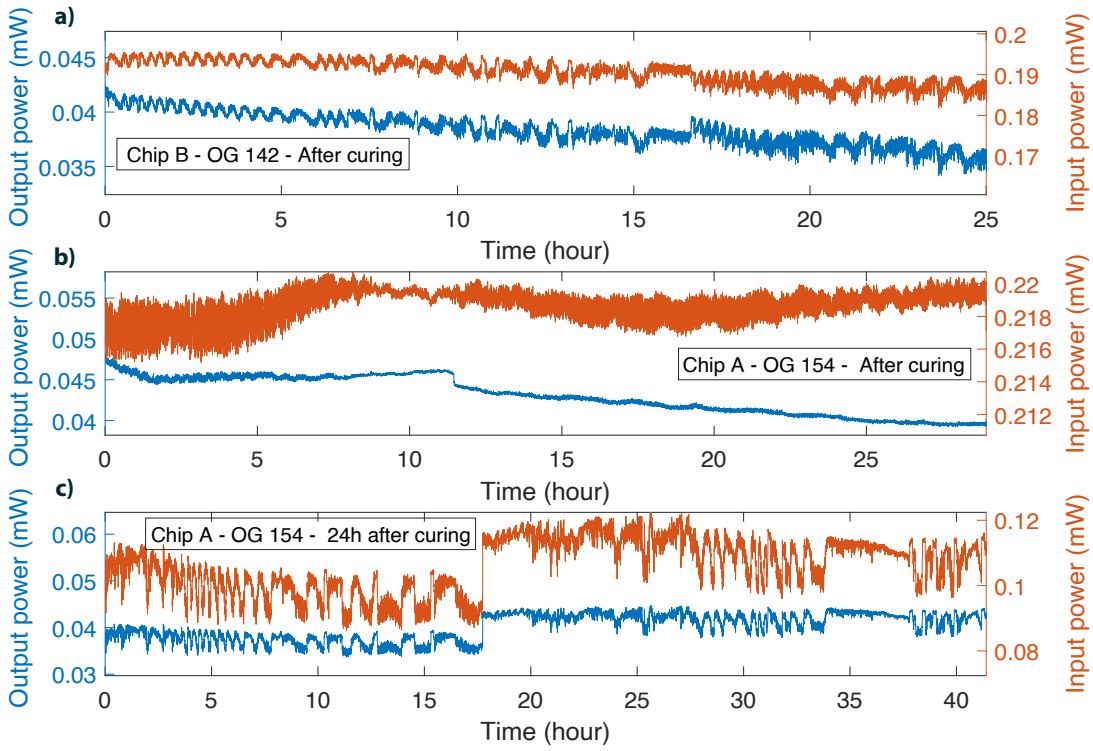

Figure C.2: **The post-curing coupling monitoring of packaged chips.** The coupling efficiency of both chips degrades (2-3 %) during the initial 24 hours (**a & b**). This coupling drift comes from stress on fiber due to cured epoxy or changes in epoxy properties post-curing. **c** The packaged chip coupling stabilizes after 24 hours of epoxy curing. The fluctuations in output power follow the changes in input power.

C.3 Fiber Inlet

To minimize the loss due to linear shrinkage and epoxy in the path of the light, an inlet (U-groove) structure on the chip is implemented. The epoxy can be dispensed away from the chip facet, but the fibers are still glued to the chip, hence providing better adhesion. Linear shrinkage-based fiber drifts during curing might be compensated due to the presence of the glue on both sides of the fiber (Figure C.3 a). Inlets with the width of 250 m, two times fiber diameter, have been tested, providing freedom of active alignment. The structure is 62.5 m wider on each fiber side to dispense the epoxy. Wider spacing means a large drop size of the glue is needed to join the fiber. However, this might lead to the spreading of glue all over the inlet. In addition, lens fibers could be used to package photonic chips for efficient light coupling (Figure C.3 b). More importantly, the U-inlet structure packaging could provide more stable coupling for extreme conditions due to drift caused by changing the temperature. Particularly, in this scheme, the light cannot interact with glue, and hence optically packaged devices can be operated at even higher input power (> 3-W).

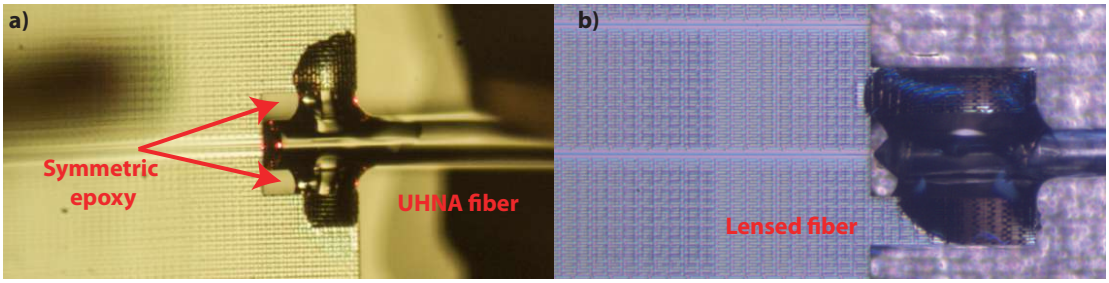

Figure C.3: Si_3N_4 microresonator chip with inlet structure. **a** The dispensing away from the chip facet minimizes the coupling drift during the curing (24 hours). This structure also provides better stability to the fiber due to symmetric glue. Furthermore, the light does not have to propagate through the glue to avoid damage at extremely high optical power (> 3 W). **b** A lensed fiber-based optical packaging can also be done using U-inlets. The glue can not cover the front of the fiber diminishing the focusing effect.

C.4 Packaging of Si_3N_4 sample using commercial mode convertor [1]

Fiber array-based packaging allows the parallelization of chip packaging. Passively aligned packaging processes are generally preferred as they could lead to relatively large scale without needing too many resources at a lower cost [17]. This is easier to implement in SMF-28-based fiber array (e.g., with grating coupler) as misalignment tolerances are higher (~ μm range). However, implementing this solution via a smaller mode field diameter (< 3 - 4 μm) is difficult due to small misalignment tolerance (< 0.25 μm). A small project in collaboration with STMicroelectronics is done to explore a fiber array-based packaging solution. The fiber packaging uses the SiO_2 waveguide-based mode converter (Figure C.4 b, inset). However, a

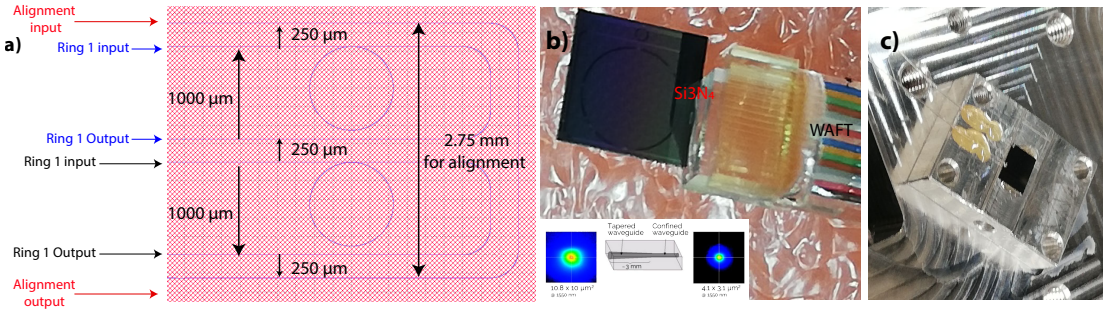

Figure C.4: **Optical packaging using on-chip mode convertor. a** The Si_3N_4 photonic chip is designed to meet the requirement for fiber array packaging. The between different waveguides is a multiple of 250 μm. The alignment waveguide (outer loop waveguide) is automatically aligned coupling in Ring 1 and Ring 2 waveguides. **b** A packaged sample in conjunction with chip-based mode convertor [1]. The inset shows the principle of mode conversion from SMF-28 fiber (10 μm) to 4 μm via tapering [image adapted from [1]]. **c** In house packaging of Si_3N_4 chip shown in **a** using UHNA-fiber spliced with SMF (see section C.5).

coupling of up to 12.5 % in a set of more than ten chips is observed (10 chips showed coupling lower than 9%), while the coupling of the same devices with the help of lensed fiber is around 30 %. This is due to the slightly bigger mode field diameter than lensed fiber (WAFT: 4 μm $\times$ 3 μm, & lensed fiber: 2.5 μm $\times$ 2.5 μm). In addition, misalignment could also provide additional loss (both in Si_3N_4 waveguide and mode converter offset from the pitch of 250 μm). Due to lower coupling achieved in these measurements, a custom solution is built to optimize the light coupled into the Si_3N_4 photonic devices for electron-photon interactions (see, section C.5). The packaging is done via an external company [332]. The packaged device using an in-house scheme (Figure C.4 c) yielded a coupling efficiency of $\sim$ 23 %, two times higher than the WAFT fiber-array-based solution.

C.5 Packaging of Si_3N_4 sample for electron-photon interaction and fitting models

The Si_3N_4 photonic structure designed for electron-photon interactions differs from the conventionally designed one. The conventional design requires a coupling from both sides of the chip, facilitating testing and other experimental activities. A simple solution is to use a fiber array to couple the light, but they suffer from higher coupling loss due to bigger mode field diameter and misalignment (pitch of 250 μm). To achieve a higher coupling efficiency, which is one desired coupling light out of the microresonator generated via cathode luminescence [106], a custom solution is designed (Figure C.5). The first iteration of the experiment is brute force, utilizing commercial stages and fiber holder (Figure C.5 a). The first design is optimum for characterization, where fiber mounted on a fiber holder does not need to be removed once attached. But it complicates the packaging process as removing fiber from the stage is difficult due to limited space (see, Figure C.5 a, red arrow). To eliminate this issue, a custom holder is designed using

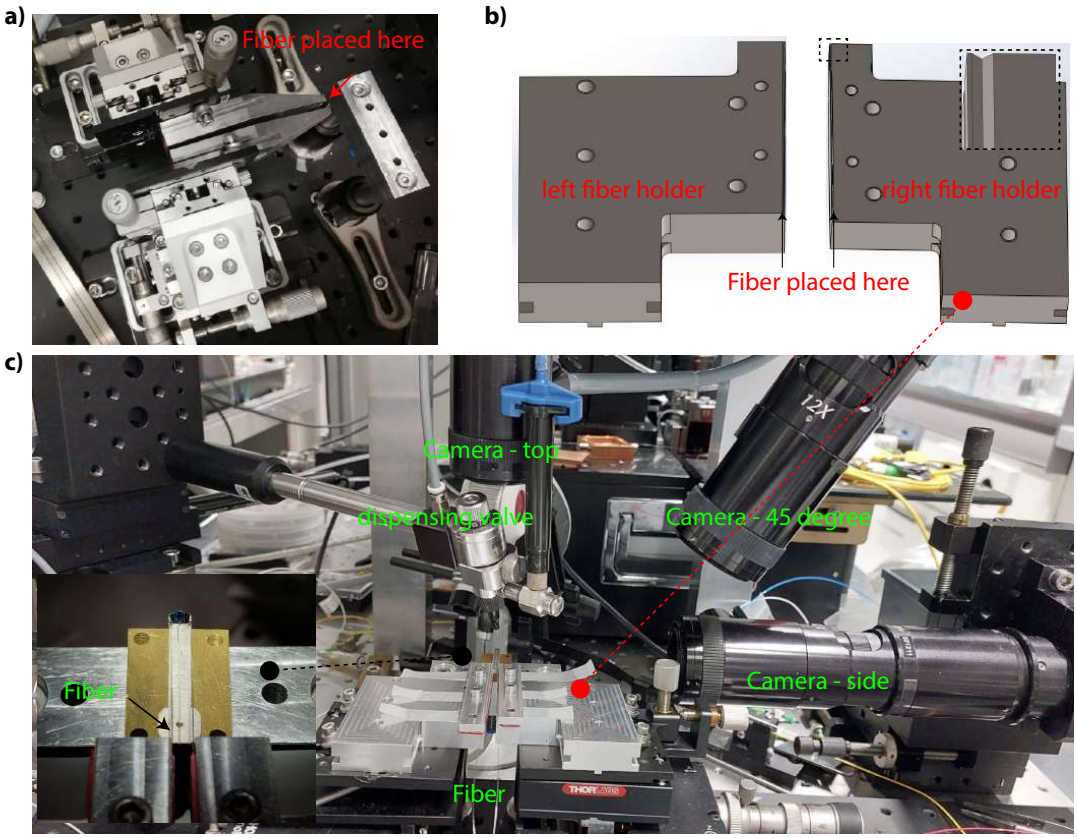

Figure C.5: **Optical setup for characterization and pacakging for Si_3N_4 devices for electron photon interaction. a** The first iteration for testing the sample with a coupling on the same side of the photonic chip utilized commercial fiber holders and customized stages. **b** A custom-designed fiber holder that allows coupling via discrete fibers with a spacing of ~ 0.5 mm. A V-groove is made on the edge to support both fibers (lensed or UHNA) to obtain higher coupling efficiencies. **c** Modified optical setup used for packaging Si_3N_4 photonic integrated circuit for electron-photon interactions. A set of multiple cameras to assist with a vision for coupling optimization and gluing the fiber. A dispensing valve attached to the motorized stage is used to put a small drop of epoxy. Inset: The Si_3N_4 sample is placed on an Al chip carrier designed to fit the TEM holder. To facilitate the sample handling, Al chip carrier is further mounted on the Cu-sample carrier.

Solidworks [171]. Figure C.5 b shows the 3D images of the fiber holder designed to optimize the packaging process. A custom V-groove is designed to hold the fiber on edge (Figure C.5 b, inset) [1]. The modified optical setup (see, Figure 2.7 used for conventional chip packaging) is shown in the Figure C.5 c with an additional camera placed on the side for better vision control for placing a syringe of top fiber at chip for gluing. The dispensing valve is attached to the motorized stage, which is brought close to the chip after coupling optimization. For alignment, the top fiber camera is used. At the same time, the fibers are aligned via 3-axis nano max stages with fine distance tunning via PZT. The same optical setup is used for characterizing the chip.

[1]The fiber holder is fabricated by EPFL mechanical workshop, supervised by Thomas Alfred.

C.6 Transmission and Reflection calibration

The surface Rayleigh or bulk scattering in the microresonator leads to the coupling of clockwise (a_{cw}) and counter-clockwise (a_{ccw}) modes [109]. Assuming both modes have degenerate frequencies ω with modal coupling rate γ, the Hamiltonian of the microresonator system reads

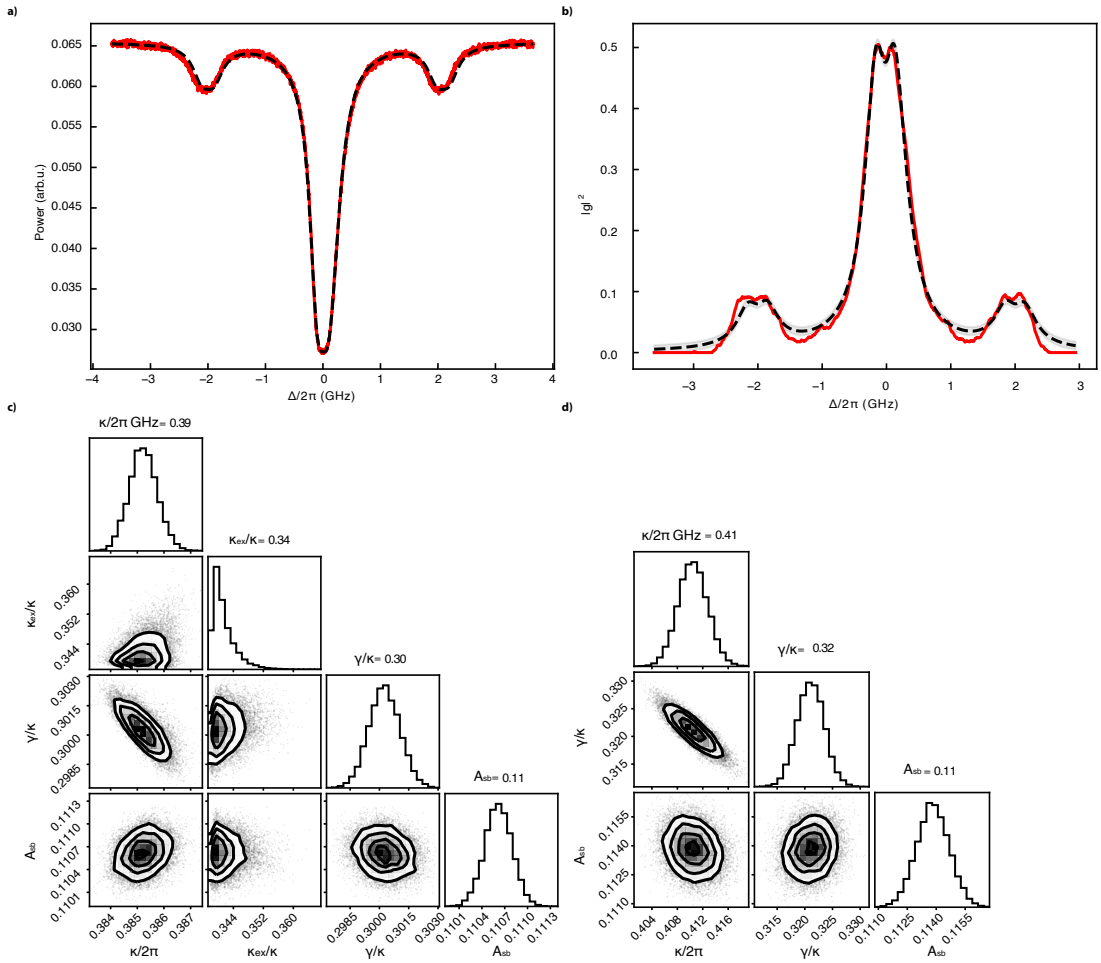

Figure C.6: **a)** An optical transmission scan measured at the output of the chip is fitted using Eq.(C.7). The sidebands, generated via an electro-optic modulator, are used to calibrate the frequency. **b)** Fitting to the fitted g frequency sweep using Eq.(C.10). Note that the frequency sweep line shape difference near the resonance is due to the frequency degenerate counter-clockwise optical mode coupling. **c,d)** The Markov chain Monte Carlo random walk corner plot of the fitting to the optical data and the fitted g data. The fitted system key parameters (cavity decay rate κ, splitting ratio γ/κ, sideband ratio A_{sb}) of the two frequency sweeps are all within 7% discrepancy, indicating great consistency between the optical and electron spectroscopic measurements. Also, strong correlation between the fitted γ and κ is observed for both fittings, indicating the necessity of applying the coupled modes model to extract the cavity decay rate correctly.

$$H = \hbar\omega(a_{\mathrm{cw}}^{\dagger}a_{\mathrm{cw}} + a_{\mathrm{ccw}}^{\dagger}a_{\mathrm{ccw}}) + \hbar\gamma(a_{\mathrm{cw}} + a_{\mathrm{cw}}^{\dagger})(a_{\mathrm{ccw}} + a_{\mathrm{ccw}}^{\dagger}). \tag{C.1}$$

Considering the laser's frame with frequency $\omega_l = \omega + \Delta$, under the rotating wave approximation, the Hamiltonian reads

$$H = -\hbar\Delta(a_{\mathrm{cw}}^{\dagger}a_{\mathrm{cw}} + a_{\mathrm{ccw}}^{\dagger}a_{\mathrm{ccw}}) + \hbar\gamma(a_{\mathrm{cw}}a_{\mathrm{ccw}}^{\dagger} + a_{\mathrm{cw}}^{\dagger}a_{\mathrm{ccw}}). \tag{C.2}$$

After considering coupling to the bus waveguide with rate κ_{ex} and losses to the environment with rate κ_0, this results in the Langevin equation (ignoring vacuum fluctuation)

$$\dot{a}_{\mathrm{cw}} = (-\kappa/2 + i\Delta)a_{\mathrm{cw}} - i\gamma a_{\mathrm{ccw}} + \sqrt{\eta\kappa}a_{\mathrm{cw,in}} \tag{C.3}$$

$$\dot{a}_{\mathrm{ccw}} = (-\kappa/2 + i\Delta)a_{\mathrm{ccw}} - i\gamma a_{\mathrm{cw}}, \tag{C.4}$$

where $\kappa = \kappa_{\mathrm{ex}} + \kappa_0$ describes the total loss rate and $\eta = \kappa_{\mathrm{ex}}/\kappa$ denotes the coupling efficiency. The stationary solution of the intracavity fields can be easily obtained as

$$a_{\mathrm{cw}} = \frac{-\sqrt{\eta\kappa}a_{\mathrm{cw,in}}}{-\kappa/2 + i\Delta + \frac{\gamma^2}{-\kappa/2+i\Delta}} \tag{C.5}$$

$$a_{\mathrm{ccw}} = \frac{-i\gamma a_{\mathrm{cw}}}{-\kappa/2 + i\Delta}. \tag{C.6}$$

The cavity transmission, reflection and dissipation are then obtained from the input-output formalism $\mathscr{O}_{\mathrm{out}} = \mathscr{O}_{\mathrm{in}} - \sqrt{\kappa_{\mathrm{ex}}}\mathscr{O}$,

$$P_{\mathrm{t}}/\hbar\omega = |a_{\mathrm{cw,out}}|^2 = |a_{\mathrm{cw,in}} - \sqrt{\eta\kappa}a_{\mathrm{cw}}|^2 \tag{C.7}$$

$$P_{\mathrm{r}}/\hbar\omega = |a_{\mathrm{ccw,out}}|^2 = |-\sqrt{\eta\kappa}a_{\mathrm{ccw}}|^2 \tag{C.8}$$

$$P_{\mathrm{diss}}/\hbar\omega = |-\sqrt{(1-\eta)\kappa}a_{\mathrm{cw}}|^2 + |-\sqrt{(1-\eta)\kappa}a_{\mathrm{ccw}}|^2. \tag{C.9}$$

And the intracavity photon numbers are simply

$$n_{\mathrm{cw}} = \left|\frac{-\sqrt{\eta\kappa}}{-\kappa/2 + i\Delta + \frac{\gamma^2}{-\kappa/2+i\Delta}}\right|^2 \dot{n}_{\mathrm{cw,in}} \tag{C.10}$$

$$n_{\mathrm{ccw}} = \left|\frac{-i\gamma}{-\kappa/2 + i\Delta}\right|^2 n_{\mathrm{cw}}. \tag{C.11}$$

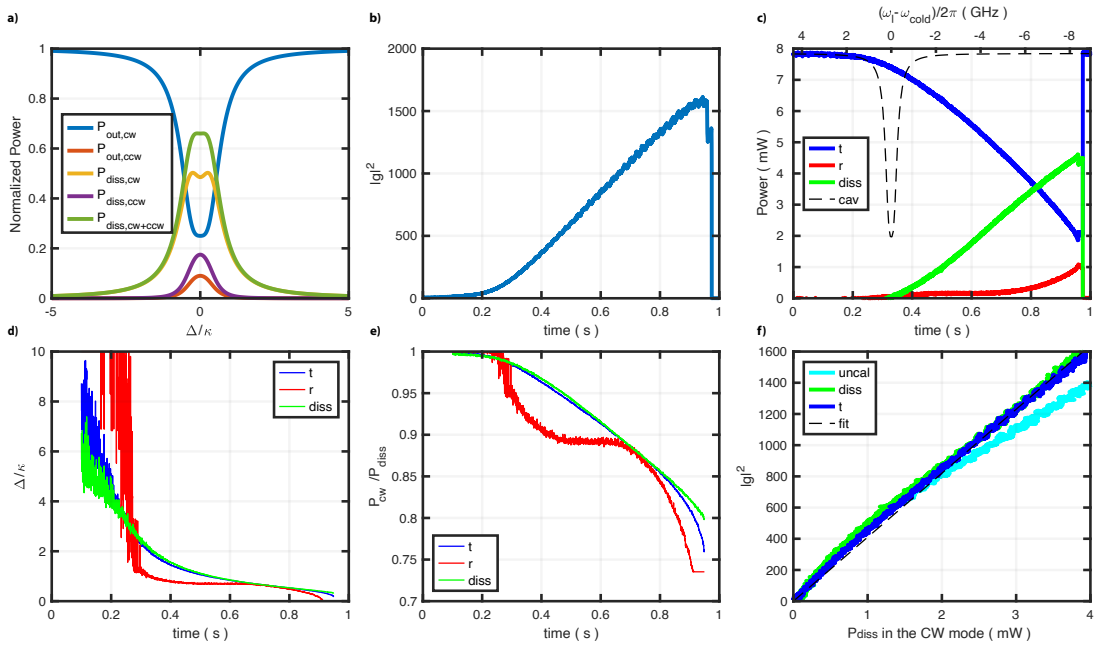

Figure C.7: **a)** Simulated power distribution in the optical system when the pump is along clockwise direction, generated using parameters fitted from the frequency sweep measurement shown in Fig.C.6. **b)** $|g|^2$ scan where each point is obtained after fitting the electron energy distribution. **c)** Experimentally measured optical signal of the cavity transmission (blue), reflection (red), and dissipation (green). The resonance-shaped (black dashed) curve shows the inferred cold cavity transmission without thermal absorption and Kerr nonlinearity-induced cavity frequency shift, which is present in the triangular-shaped (blue) curve due to high input power ($\sim > 50\mu$W). **d)** Calibrated detuning $\Delta(t)$ based on the experimentally measured optical signal in (c). **e)** Calibrated correction factor $P_{\text{diss,cw}}/P_{\text{diss}}$ from the detuning plot (d). The reflection calibration is empirically erroneous. This effect can be attributed to the etalon formed by the chip facets, by which the transmission signal is less affected. **f)** The calibrated dissipated power in the clockwise mode shows linear relation with $|g|^2$ from different measurement channels (transmission and dissipation).

Eq.(C.7) and (C.10) are used for fitting the frequency sweep of the optical transmission $P_t(\Delta)$. The frequency sweep fitting was done using the Markov chain Monte Carlo (MCMC) methods [333], with the optical sidebands $\pm\Omega_{\text{sb}}$ and absorption induced cavity frequency shift $\chi_{\text{th}}P_{\text{diss}}(\Delta)$ included in the models. The fitting function is $F_{\text{fit}}(\Delta) = \sum_{n=-1,0,1} F_i(\Delta+n\Omega_{\text{sb}}+\chi_{\text{th}}P_{\text{diss}}(\Delta))$, where F_i is either P_t for optical measurement or n_a for measurement of the electron-light coupling g. The fitting results are shown in Fig.C.6, and the fitted system parameters show great consistency between the two distinct measurements. These data demonstrate continuous-wave electron energy gain spectroscopy (EEGS) [334, 335] at an extraordinarily narrow spectral feature of only 3.2 µeV in width (FWHM; 1 µeV peak separation). The electron-light coupling constant g is extracted by fitting the shape and amplitudes of the individual spectral sidebands N with a comb of Voigt-peaks and normalized occupations $P_N = J_N(2|g|)^2$. For details on the fitting procedure, see [178, 177]. By considering the change of the coupling constant g as a function of frequency detuning, the

optical linewidth can be extracted and the achievable energy resolution in electron energy-gain spectroscopy is ultimately limited by the laser linewidth. The concept can be transferred to arbitrary high-Q optical modes, with previously demonstrated spectral linewidths below $\kappa/2\pi \sim$ 10 MHz [28]. In comparison, state-of-the-art monochromated EELS probes material excitations with a zero-loss peak (ZLP) of sub-10-meV energy width [336, 337, 338].

For the power sweep calibration, Eq.(C.7), (C.10) and (C.11) are used for calibrating the clockwise dissipated power $\tilde{P}_{\mathrm{diss},cw}(t)$. The detuning $\tilde{\Delta}(t)$ was extracted from the experimentally measured $\tilde{P}_{\mathrm{t}}(t)$ (Figure C.7(b), suffers the least from background noise) using the fitted resonator parameters (κ, η, γ) from the frequency sweep (Figure C.7(a)(c)). Then the clockwise dissipated power $\tilde{P}_{\mathrm{diss},cw}(t)$ (Figure C.7(e)) was calibrated from the experimentally measured transmission power $\tilde{P}_{\mathrm{t}}(t)$ and the calibrated $\tilde{\Delta}(t)$ by $\tilde{P}_{\mathrm{diss},cw}(t) = \frac{P_{\mathrm{diss},cw}(\Delta(t))}{P_{\mathrm{t}}(\Delta(t))}\tilde{P}_{\mathrm{t}}(t)$. We later calculate the characteristic coupled optical power $P = n_{\mathrm{cw}}\hbar\omega\kappa$ by scaling the dissipated power $P = \frac{\kappa}{\kappa_0} \times \tilde{P}_{\mathrm{diss},cw}$, and plot it against the fitted coupling constant $|g(t)|^2$ (Figure C.7f), one could find the linear relation as is expected in theory. The observable oscillations in the linear dependence of $|g|^2$ on the clockwise dissipated power are related to a 50 Hz noise in the beam position leading to variations in electron-light coupling strength. To eliminate this 50 Hz noise, we binned the retrieved coupling strength in time intervals of 20 ms.

C.7 Modified sample for electron soliton interaction

The setup mentioned in section C.5 is suitable for characterizing and packaging chips for electron-photon interaction. However, it requires a substantial modification to test the soliton generation while pumping the microresonator at high optical power (e.g., safety protection, modified chip holder with clamping). Moreover, testing the soliton after packaging the chip is not an optimum solution as it requires multiple steps. In this direction, a modified chip design is developed that facilitates the integration of chips into the standard pumping station in our group. In the modified design, a drop port waveguide (direction coupler) is placed in the bus waveguide allowing 5 to 10 % tapping of light on the other side of the chip. The directional coupler is designed using standard Lumerical simulation. This project is concerned with probing intra-cavity nonlinear dissipative states; a small on-chip light tapping does not impact the experiment—furthermore, the light is tapped after interaction with the microresonator to avoid additional power penalty to nonlinear threshold power.

C.8 50 GHz Soliton generation inside TEM

In chapter 7, most results discuss the soliton interaction with 200 GHz and 100 GHz FSR Si_3N_4 devices. Soliton states are observed in even lower FSR Si_3N_4 microresonators with 50 GHz FSR in both mode families (quasi-TE [single and multisoliton] and quasi-TM [multi-soliton]) inside the TEM (Figure C.9). However, unfortunately, due to stronger charging and hanging metal parts in the vicinity of the microresonator waveguide, a proper dataset could not be obtained. The

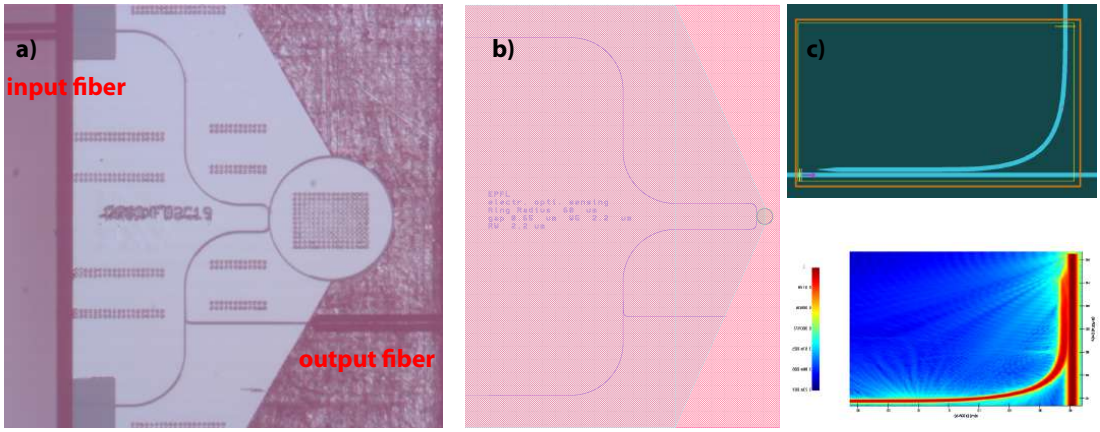

Figure C.8: **Modified sample designed for soliton photon interactions. a** Microscope image of Si_3N_4 chip with lensed fiber coupled from the different side of the chip facilitating with soliton generation before packaging. **b** The GDS design of the chip with modified clipping on edge for electron soliton interactions. **c** Time domain FDTD simulation to design a coupler 10% light coupled to the auxiliary waveguide.

lower FSR cavities are interesting for the pulse pumping scheme [54], which could pave the way for synchronized interaction between electron and photon by locking the soliton and laser used for photoemission of the electron from the TEM tip. The current study is focused on average interaction where electron pulse only interacts for a short time compared to weak CW-part.

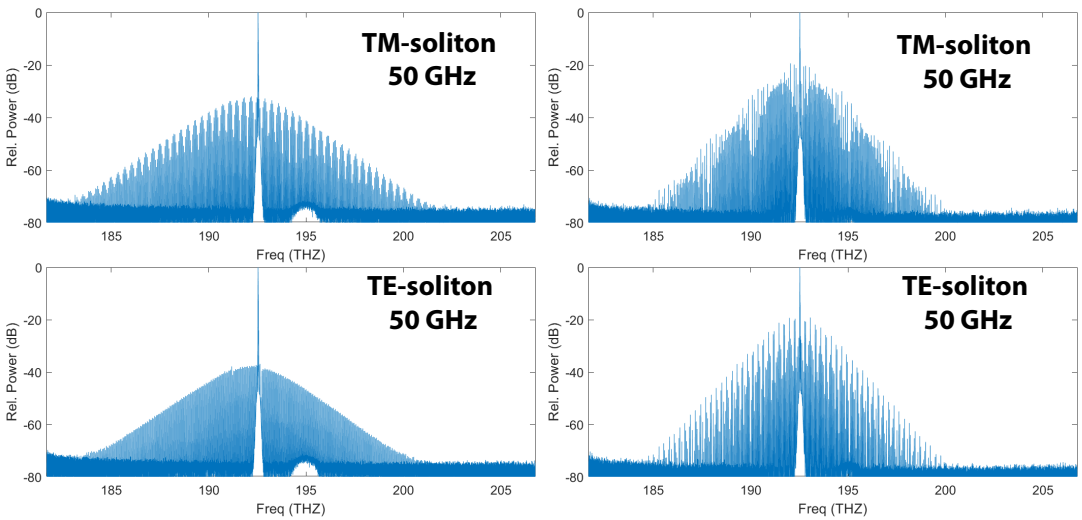

Figure C.9: **Overview of 50 GHz soliton states in a sample designed for electron-photon interaction.** Top row: Multiple soliton states generated in 50 GHz FSR Si_3N_4 microresonator by pumping at quasi-TM mode. Bottom row: A single soliton and multiple solitons generated in same Si_3N_4 microresonators in quasi-TE mode.

D Packaging facilitated applications

D.1 Application demonstration facilitated by packaging

This section will present a short overview of applications that took advantage of optical packaging protocols established as part of the current thesis. In these projects, I was mainly responsible for packaging, design, and characterization of Si_3N_4 samples, while the actual experiments were performed by my colleagues leading the project. However, these demonstrations emphasize the importance of photonics packaging, enabling a wider range of applications.

D.1.1 An Integrated Photon-Pair Source with Monolithic Piezoelectric Frequency Tunability

An entangled photon-pair source at telecom wavelengths, based on a packaged Si_3N_4 microresonator, with monolithically integrated piezoelectric frequency tuning, is demonstrated. The light is coupled directly into the bus waveguide on the chip through an ultrahigh numerical aperture (UHNA) fiber pigtailed to the chip (Figure D.1 a). When the laser is brought on resonance, the laser couples evanescently into the microresonator via the bus waveguide, generating signal and idler photons through spontaneous four-wave mixing (SFWM) at each mode supported by the cavity. This leads to the generation of a photon frequency comb with a frequency spacing ~200 GHz, matching the free spectral range (FSR) of the microresonator. The device itself is an over-coupled device with an average intrinsic linewidth ~40 MHz and total linewidth ~200 MHz.

D.1.2 High-Resolution Accelerometer by Stress-optic Modulation based on photonic integrated circuit

Optical accelerometers are important for self-driving cars, virtual reality headsets, and navigation applications. This work demonstrated a monolithically integrated optomechanical accelerometer based on a Silicon Nitride (Si_3N_4) optical microring resonator that senses acceleration via the stress-optic effect. A large proof mass allows sub-μg resolution at the mechanical resonance. It

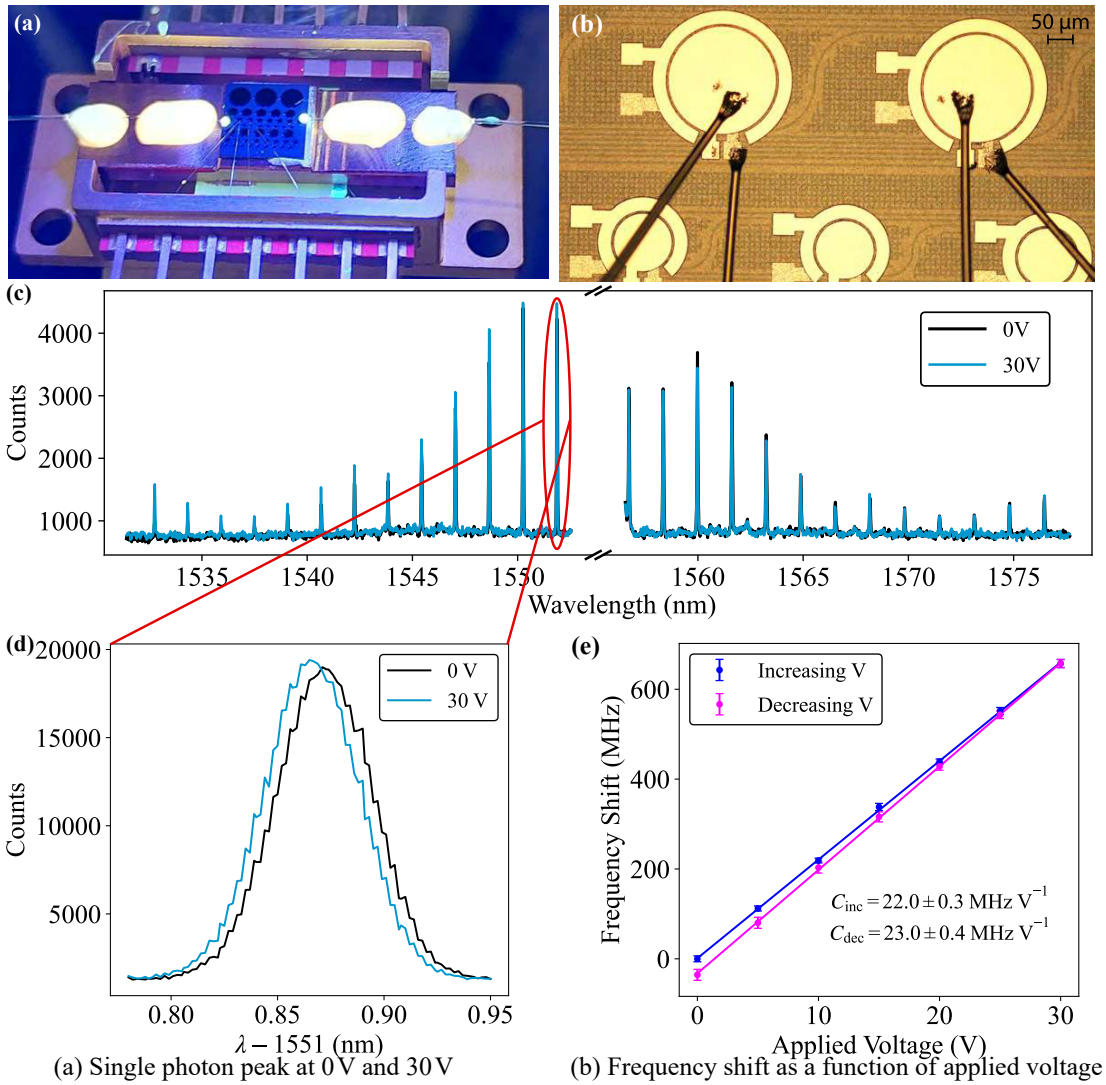

(a) Single photon peak at 0 V and 30 V (b) Frequency shift as a function of applied voltage

Figure D.1: **Integrated photon-pair source based on packaged Si_3N_4 microresonator, which is heterogeneously integrated with AlN for frequency tuning. a** An optically and electrically packaged Si_3N_4 photonic device. **b** The wire bonding to electrical pads for applying an external voltage to the control cavity. **c** Photon pairs generated in Si_3N_4 when the cavity is subject to two different voltages (0 & 30 V). **d** A single photon shift induced by changing voltage on AlN actuator. **e** When changing the voltage (forward & backward), a hysteresis is observed. Figure adapted from [25].

measures the transmitted light passing through the microring resonator, enabling the cascading of sensor arrays.

In addition, optically packaged Si_3N_4 microresonators are used for demonstrating convolutional processing [26] and electron-photon pair generation [106].

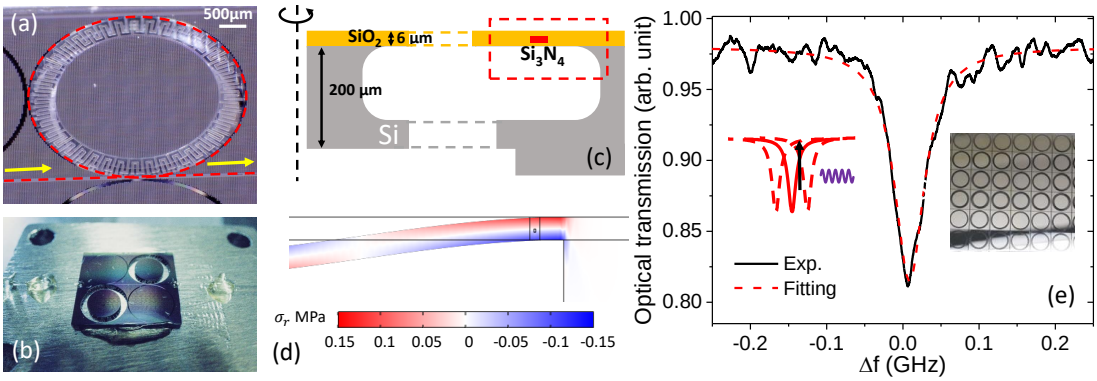

Figure D.2: (a) Optical microscope image of a 3mm diameter, 200 μm thick accelerometer with integrated Si_3N_4 microring resonator (red dashed line). The white scale bar is 500μm. (b) Optical image of a UHNA-fiber epoxy-connected sensor. (c) Cross-section of the accelerometer (not to scale) rotationally symmetry with respect to the black dashed line. (d) FEA simulation of the radial stress σ_r under one gravity of the region in the red dashed box in (c). (e) Normalized transmission of one optical resonance (black) with Lorentz fitting (red). Figure adapted from [H. Tian, A. S. Raja et al, CLEO 2023.].

Bibliography

[1] Teemphotonics, https://www.teemphotonics.com/.

[2] D. Liang and J. E. Bowers, Nature Photonics **4**, 511 (2010).

[3] A. W. Fang, H. Park, O. Cohen, R. Jones, M. J. Paniccia, and J. E. Bowers, Optics Express **14**, 9203 (2006).

[4] D. Thomson, A. Zilkie, J. E. Bowers, T. Komljenovic, G. T. Reed, L. Vivien, D. Marris-Morini, E. Cassan, L. Virot, J.-M. Fédéli, *et al.*, Journal of Optics **18**, 073003 (2016).

[5] J. Van Campenhout, P. Rojo-Romeo, P. Regreny, C. Seassal, D. Van Thourhout, S. Verstuyft, L. Di Cioccio, J. Fedeli, C. Lagahe, and R. Baets, Optics express **15**, 6744 (2007).

[6] C. Xiang, J. Liu, J. Guo, L. Chang, R. N. Wang, W. Weng, J. Peters, W. Xie, Z. Zhang, J. Riemensberger, *et al.*, Science **373**, 99 (2021).

[7] M. Pantouvaki, P. Verheyen, G. Lepage, J. De Coster, H. Yu, P. De Heyn, P. Absil, and J. Van Campenhout, in *39th European Conference and Exhibition on Optical Communication (ECOC 2013)* (IET, 2013) pp. 1–3.

[8] Q. Xu, B. Schmidt, S. Pradhan, and M. Lipson, nature **435**, 325 (2005).

[9] L. Agazzi, J. D. Bradley, M. Dijkstra, F. Ay, G. Roelkens, R. Baets, K. Worhoff, and M. Pollnau, Optics express **18**, 27703 (2010).

[10] Y. Liu, Z. Qiu, X. Ji, A. Lukashchuk, J. He, J. Riemensberger, M. Hafermann, R. N. Wang, J. Liu, C. Ronning, *et al.*, Science **376**, 1309 (2022).

[11] H. Li, S. Zhang, Z. Zhang, S. Zuo, S. Zhang, Y. Sun, D. Zhao, and Z. Zhang, Nanomaterials **10**, 1683 (2020).

[12] Y. Su, Y. Zhang, C. Qiu, X. Guo, and L. Sun, Advanced Materials Technologies **5**, 1901153 (2020).

[13] L. Carroll, J.-S. Lee, C. Scarcella, K. Gradkowski, M. Duperron, H. Lu, Y. Zhao, C. Eason, P. Morrissey, M. Rensing, S. Collins, H. Hwang, and P. O'Brien, Applied Sciences **6**, 426 (2016).

[14] G. Roelkens, D. Van Thourhout, and R. Baets, Optics Express **14**, 11622 (2006).

[15] M. Asaduzzaman, M. Bakaul, S. Skafidas, and M. R. H. Khandokar, IBP 2015 - 2015 IEEE International Broadband and Photonics Conference , 31 (2015).

[16] V. R. Almeida, R. R. Panepucci, and M. Lipson, Opt. Lett. **28**, 1302 (2003).

[17] T. Barwicz, T. W. Lichoulas, Y. Taira, Y. Martin, S. Takenobu, A. Janta, H. Numata, E. L. Kimbrell, J.-w. Nah, B. Peng, R. Leidy, M. Khater, S. Kamlapurkar, S. Engelmann, P. Fortier, and N. Boyer, Ofc , 4 (2017).

[18] T. J. Kippenberg, A. L. Gaeta, M. Lipson, and M. L. Gorodetsky, Science **361**, 10.1126/science.aan8083 (2018).

[19] A. S. Raja, A. S. Voloshin, H. Guo, S. E. Agafonova, J. Liu, A. S. Gorodnitskiy, M. Karpov, N. G. Pavlov, E. Lucas, R. R. Galiev, A. E. Shitikov, J. D. Jost, M. L. Gorodetsky, and T. J. Kippenberg, Nature Communications **10**, 1 (2019).

[20] A. S. Raja, J. Liu, N. Volet, R. N. Wang, J. He, E. Lucas, R. Bouchandand, P. Morton, J. Bowers, and T. J. Kippenberg, Opt. Express **28**, 2714 (2020).

[21] A. S. Raja, S. Lange, M. Karpov, K. Shi, X. Fu, R. Behrendt, D. Cletheroe, A. Lukashchuk, I. Haller, F. Karinou, *et al.*, Nature communications **12**, 5867 (2021).

[22] J.-W. Henke, A. S. Raja, A. Feist, G. Huang, G. Arend, Y. Yang, F. J. Kappert, R. N. Wang, M. Möller, J. Pan, *et al.*, Nature **600**, 653 (2021).

[23] Y. Yujia, H. Jan-Wilke, R. Arslan Sajid, K. F Jasmin, G. Huang, A. Germaine, Q. Zheru, F. Armin, W. Rui Ning, T. Aleksandr, T. Alexey, R. Claus, and T. J. Kippenberg, In preparation **XX**, XXX (2023).

[24] J. Liu, E. Lucas, A. S. Raja, J. He, J. Riemensberger, R. N. Wang, M. Karpov, H. Guo, R. Bouchand, and T. J. Kippenberg, Nature Photonics **14**, 486 (2020).

[25] T. Brydges, A. S. Raja, A. Gelmini, G. Likhachev, A. Petitjean, H. Tian, R. N. Wang, S. A. Bhave, H. Zbinden, T. J. Kippenberg, *et al.*, arXiv preprint arXiv:2210.16387 (2022).

[26] J. Feldmann, N. Youngblood, M. Karpov, H. Gehring, X. Li, M. Stappers, M. Gallo, X. Fu, A. Lukashchuk, A. Raja, *et al.*, Nature **589**, 52 (2021).

[27] J. Liu, A. S. Raja, M. Karpov, B. Ghadiani, M. H. Pfeiffer, B. Du, N. J. Engelsen, H. Guo, M. Zervas, and T. J. Kippenberg, Optica **5**, 1347 (2018).

[28] J. Liu, G. Huang, R. N. Wang, J. He, A. S. Raja, T. Liu, N. J. Engelsen, and T. J. Kippenberg, Nature Communications **12**, 2236 (2021).

[29] R. Holzwarth, T. Udem, T. W. Hänsch, J. Knight, W. Wadsworth, and P. S. J. Russell, Physical review letters **85**, 2264 (2000).

[30] M. T. Murphy, T. Udem, R. Holzwarth, A. Sizmann, L. Pasquini, C. Araujo-Hauck, H. Dekker, S. D'Odorico, M. Fischer, T. W. Hänsch, and A. Manescau, Monthly Notices of the Royal Astronomical Society **380**, 839 (2007), arXiv:0703622 [astro-ph] .

[31] T. Udem, R. Holzwarth, and T. W. Hänsch, Nature **416**, 233 (2002).

[32] P. Del'Haye, A. Schliesser, O. Arcizet, T. Wilken, R. Holzwarth, and T. J. Kippenberg, Nature **450**, 1214 (2007).

[33] A. A. Savchenkov, A. B. Matsko, V. S. Ilchenko, and L. Maleki, Optics Express **15**, 6768 (2007).

[34] K. Y. Yang, D. Y. Oh, S. H. Lee, Q.-F. Yang, X. Yi, B. Shen, H. Wang, and K. Vahala, Nature Photonics **12**, 297 (2018).

[35] J. Liu, G. Huang, R. N. Wang, J. He, A. S. Raja, T. Liu, N. J. Engelsen, and T. J. Kippenberg, Nature communications **12**, 1 (2021).

[36] X. Ji, F. A. S. Barbosa, S. P. Roberts, A. Dutt, J. Cardenas, Y. Okawachi, A. Bryant, A. L. Gaeta, and M. Lipson, Optica **4**, 619 (2017).

[37] W. Jin, Q.-F. Yang, L. Chang, B. Shen, H. Wang, M. A. Leal, L. Wu, M. Gao, A. Feshali, M. Paniccia, *et al.*, Nature Photonics **15**, 346 (2021).

[38] M. W. Puckett, K. Liu, N. Chauhan, Q. Zhao, N. Jin, H. Cheng, J. Wu, R. O. Behunin, P. T. Rakich, K. D. Nelson, *et al.*, Nature communications **12**, 934 (2021).

[39] M. H. P. Pfeiffer, J. Liu, A. S. Raja, T. Morais, B. Ghadiani, and T. J. Kippenberg, Optica **5**, 884 (2018).

[40] A. Haboucha, W. Zhang, T. Li, M. Lours, A. N. Luiten, Y. L. Coq, and G. Santarelli, Opt. Lett. **36**, 3654 (2011).

[41] T. Herr, K. Hartinger, J. Riemensberger, C. Y. Wang, E. Gavartin, R. Holzwarth, M. L. Gorodetsky, and T. J. Kippenberg, Nature Photonics **6**, 480 EP (2012).

[42] A. L. Gaeta, M. Lipson, and T. J. Kippenberg, Nature Photonics **13**, 158 (2019).

[43] T. Herr, V. Brasch, J. D. Jost, C. Y. Wang, N. M. Kondratiev, M. L. Gorodetsky, and T. J. Kippenberg, Nature Photonics **8**, 145 (2013).

[44] H. Guo, M. Karpov, E. Lucas, A. Kordts, M. H. P. Pfeiffer, V. Brasch, G. Lihachev, V. E. Lobanov, M. L. Gorodetsky, and T. J. Kippenberg, Nature Physics **13**, 94 (2016).

[45] M. Karpov, M. H. P. Pfeiffer, J. Liu, A. Lukashchuk, and T. J. Kippenberg, Nature Communications **9**, 1146 (2018).

[46] E. Lucas, H. Guo, J. D. Jost, M. Karpov, and T. J. Kippenberg, Phys. Rev. A **95**, 043822 (2017).

[47] E. Lucas, M. Karpov, H. Guo, M. L. Gorodetsky, and T. J. Kippenberg, Nature Communications **8**, 736 (2017).

[48] D. C. Cole, E. S. Lamb, P. Del'Haye, S. A. Diddams, and S. B. Papp, Nature Photonics **11**, 671 (2017).

[49] M. Yu, J. K. Jang, Y. Okawachi, A. G. Griffith, K. Luke, S. A. Miller, X. Ji, M. Lipson, and A. L. Gaeta, Nature communications **8**, 14569 (2017).

[50] P. Del'Haye, A. Coillet, T. Fortier, K. Beha, D. C. Cole, K. Y. Yang, H. Lee, K. J. Vahala, S. B. Papp, and S. A. Diddams, Nature Photonics **10**, 516 (2016).

[51] D. T. Spencer, T. Drake, T. C. Briles, J. Stone, L. C. Sinclair, C. Fredrick, Q. Li, D. Westly, B. R. Ilic, A. Bluestone, N. Volet, T. Komljenovic, L. Chang, S. H. Lee, D. Y. Oh, M.-G. Suh, K. Y. Yang, M. H. P. Pfeiffer, T. J. Kippenberg, E. Norberg, L. Theogarajan, K. Vahala, N. R. Newbury, K. Srinivasan, J. E. Bowers, S. A. Diddams, and S. B. Papp, Nature **557**, 81 (2018).

[52] M. H. P. Pfeiffer, C. Herkommer, J. Liu, H. Guo, M. Karpov, E. Lucas, M. Zervas, and T. J. Kippenberg, Optica **4**, 684 (2017).

[53] X. Liu, Z. Gong, A. W. Bruch, J. B. Surya, J. Lu, and H. X. Tang, Nature communications **12**, 5428 (2021).

[54] E. Obrzud, S. Lecomte, and T. Herr, Nature Photonics **11**, 600 EP (2017).

[55] M. H. Anderson, R. Bouchand, J. Liu, W. Weng, E. Obrzud, T. Herr, and T. J. Kippenberg, Optica **8**, 771 (2021).

[56] M. H. Anderson, W. Weng, G. Lihachev, A. Tikan, J. Liu, and T. J. Kippenberg, Nature communications **13**, 4764 (2022).

[57] B. J. M. Hausmann, I. Bulu, V. Venkataraman, P. Deotare, and M. Lončar, Nature Photonics **8**, 369 (2014).

[58] I. Grudinin, A. Savchenkov, A. Matsko, D. Strekalov, V. Ilchenko, and L. Maleki, IQEC, International Quantum Electronics Conference Proceedings **2005**, 380 (2005).

[59] M. H. P. Pfeiffer, A. Kordts, V. Brasch, M. Zervas, M. Geiselmann, J. D. Jost, and T. J. Kippenberg, Optica **3**, 20 (2016).

[60] Y. Xuan, Y. Liu, L. T. Varghese, A. J. Metcalf, X. Xue, P.-H. Wang, K. Han, J. A. Jaramillo-Villegas, A. A. Noman, C. Wang, S. Kim, M. Teng, Y. J. Lee, B. Niu, L. Fan, J. Wang, D. E. Leaird, A. M. Weiner, and M. Qi, Optica **3**, 1171 (2016).

[61] H. Hu, F. Da Ros, F. Ye, M. Pu, K. Ingerslev, E. Porto da Silva, M. Nooruzzaman, Y. Amma, Y. Sasaki, T. Mizuno, Y. Miyamoto, L. Ottaviano, E. Semenova, P. Guan, D. Zibar, M. Galili, K. Yvind, L. K. Oxenløwe, and T. Morioka, Conference on Lasers and Electro-Optics (CLEO) , JTh4C.1 (2016).

[62] C. Wang, M. Zhang, M. Yu, R. Zhu, H. Hu, and M. Loncar, Nature Communications **10**, 978 (2019).

[63] Y. He, Q.-F. Yang, J. Ling, R. Luo, H. Liang, M. Li, B. Shen, H. Wang, K. Vahala, and Q. Lin, Optica **6**, 1138 (2019).

[64] D. J. Wilson, K. Schneider, S. Hoenl, M. Anderson, T. J. Kippenberg, and P. Seidler, arXiv (1808.03554v2).

[65] D. J. Moss, R. Morandotti, A. L. Gaeta, and M. Lipson, Nature photonics **7**, 597 (2013).

[66] Y. Okawachi, M. Yu, B. Desiatov, B. Y. Kim, T. Hansson, M. Lončar, and A. L. Gaeta, Optica **7**, 702 (2020).

[67] L. He, M. Zhang, A. Shams-Ansari, R. Zhu, C. Wang, and L. Marko, Optics letters **44**, 2314 (2019).

[68] L. Razzari, D. Duchesne, M. Ferrera, R. Morandotti, S. Chu, B. E. Little, and D. J. Moss, Nature Photonics **4**, 41 EP (2009).

[69] J. S. Levy, A. Gondarenko, M. A. Foster, A. C. Turner-Foster, A. L. Gaeta, and M. Lipson, Nature Photonics **4**, 37 (2010).

[70] H. Jung, C. Xiong, K. Y. Fong, X. Zhang, and H. X. Tang, Optics letters **38**, 2810 (2013).

[71] M. Pu, L. Ottaviano, E. Semenova, and K. Yvind, Optica **3**, 823 (2016).

[72] M. Yu, Y. Okawachi, A. G. Griffith, N. Picqué, M. Lipson, and A. L. Gaeta, Nat. Commun. **9**, 1869 (2018).

[73] A. Pasquazi, M. Peccianti, Y. Park, B. E. Little, S. T. Chu, R. Morandotti, J. Azaña, and D. J. Moss, Nature Photonics **5**, 618 (2011).

[74] P. Del'Haye, A. Schliesser, O. Arcizet, T. Wilken, R. Holzwarth, and T. J. Kippenberg, Nature **450**, 1214 (2007).

[75] H. Lee, T. Chen, J. Li, K. Y. Yang, S. Jeon, O. Painter, and K. J. Vahala, Nature Photonics **6**, 369 (2012).

[76] A. G. Griffith, R. K. Lau, J. Cardenas, Y. Okawachi, A. Mohanty, R. Fain, Y. H. D. Lee, M. Yu, C. T. Phare, C. B. Poitras, *et al.*, Nature communications **6**, 6299 (2015).

[77] M. H. P. Pfeiffer, C. Herkommer, J. Liu, T. Morais, M. Zervas, M. Geiselmann, and T. J. Kippenberg, *IEEE Journal of Selected Topics in Quantum Electronics*, IEEE Journal of Selected Topics in Quantum Electronics **24**, 1 (2018).

[78] J. S. Levy, A. Gondarenko, M. A. Foster, A. C. Turner-Foster, A. L. Gaeta, and M. Lipson, Nature Photonics **4**, 37 EP (2009).

[79] D. J. Moss, R. Morandotti, A. L. Gaeta, and M. Lipson, Nature Photonics **7**, 597 (2013).

[80] S. Kim, K. Han, C. Wang, J. A. Jaramillo-Villegas, X. Xue, C. Bao, Y. Xuan, D. E. Leaird, A. M. Weiner, and M. Qi, Nature Communications **8**, 372 (2017).

[81] F. Gyger, J. Liu, F. Yang, J. He, A. S. Raja, R. N. Wang, S. A. Bhave, T. J. Kippenberg, and L. Thévenaz, arXiv **1908.09815** (2019).

[82] V. Brasch, M. Geiselmann, T. Herr, G. Lihachev, M. H. P. Pfeiffer, M. L. Gorodetsky, and T. J. Kippenberg, Science **351**, 357 (2016).

[83] J. Pfeifle, V. Brasch, M. Lauermann, Y. Yu, D. Wegner, T. Herr, K. Hartinger, P. Schindler, J. Li, D. Hillerkuss, *et al.*, Nature photonics **8**, 375 (2014).

[84] P. Marin-Palomo, J. N. Kemal, M. Karpov, A. Kordts, J. Pfeifle, M. H. P. Pfeiffer, P. Trocha, S. Wolf, V. Brasch, M. H. Anderson, R. Rosenberger, K. Vijayan, W. Freude, T. J. Kippenberg, and C. Koos, Nature **546**, 274 (2017).

[85] E. Obrzud, M. Rainer, A. Harutyunyan, M. H. Anderson, M. Geiselmann, B. Chazelas, S. Kundermann, S. Lecomte, M. Cecconi, A. Ghedina, E. Molinari, F. Pepe, F. Wildi, F. Bouchy, T. J. Kippenberg, and T. Herr, arXiv:1712.09526 (2017).

[86] P. Trocha, M. Karpov, D. Ganin, M. H. P. Pfeiffer, A. Kordts, S. Wolf, J. Krockenberger, P. Marin-Palomo, C. Weimann, S. Randel, W. Freude, T. J. Kippenberg, and C. Koos, Science **359**, 887 (2018).

[87] J. Riemensberger, A. Lukashchuk, M. Karpov, W. Weng, E. Lucas, J. Liu, and T. J. Kippenberg, Nature **581**, 164 (2020).

[88] P. J. Marchand, J. Riemensberger, J. C. Skehan, J.-J. Ho, M. H. Pfeiffer, J. Liu, C. Hauger, T. Lasser, and T. J. Kippenberg, Nature Communications **12**, 1 (2021).

[89] X. Ji, X. Yao, A. Klenner, Y. Gan, A. L. Gaeta, C. P. Hendon, and M. Lipson, Opt. Express **27**, 19896 (2019).

[90] J. Stone, T. Briles, T. Drake, D. Spencer, D. Carlson, S. Diddams, and S. Papp, arXiv:1708.08405 (2017).

[91] S. Zhang, J. M. Silver, L. Del Bino, F. Copie, M. T. Woodley, G. N. Ghalanos, A. Ø. Svela, N. Moroney, and P. Del'Haye, Optica **6**, 206 (2019).

[92] T. Wildi, V. Brasch, J. Liu, T. J. Kippenberg, and T. Herr, Optics letters **44**, 4447 (2019).

[93] J. Liu, H. Tian, E. Lucas, A. S. Raja, G. Lihachev, R. N. Wang, J. He, T. Liu, M. H. Anderson, W. Weng, S. A. Bhave, and T. J. Kippenberg, Nature **583**, 385 (2020).

[94] C. Joshi, J. K. Jang, K. Luke, X. Ji, S. A. Miller, A. Klenner, Y. Okawachi, M. Lipson, and A. L. Gaeta, Opt. Lett. **41**, 2565 (2016).

[95] W. LIANG, V. ILCHENKO, A. SAVCHENKOV, A. MATSKO, D. SEIDEL, and L. MALEKI, Optics letters **35**, 2822 (2010).

[96] W. Liang, D. Eliyahu, V. S. Ilchenko, A. A. Savchenkov, A. B. Matsko, D. Seidel, and L. Maleki, Nature Communications **6**, 7957 (2015).

[97] V. Vassiliev, V. Velichansky, V. Ilchenko, M. Gorodetsky, L. Hollberg, and A. Yarovitsky, Optics Communications **158**, 305 (1998).

[98] N. G. Pavlov, S. Koptyaev, G. V. Lihachev, A. S. Voloshin, A. S. Gorodnitskiy, M. V. Ryabko, S. V. Polonsky, and M. L. Gorodetsky, Nature Photonics **12**, 694 (2018).

[99] B. Stern, X. Ji, Y. Okawachi, A. L. Gaeta, and M. Lipson, Nature **562**, 401 (2018).

[100] A. S. Voloshin, N. M. Kondratiev, G. V. Lihachev, J. Liu, V. E. Lobanov, N. Y. Dmitriev, W. Weng, T. J. Kippenberg, and I. A. Bilenko, Nature communications **12**, 235 (2021).

[101] B. Shen, L. Chang, J. Liu, H. Wang, Q.-F. Yang, C. Xiang, R. N. Wang, J. He, T. Liu, W. Xie, *et al.*, Nature **582**, 365 (2020).

[102] R. Voelkel, K. J. Weible, and M. Eisner, Spie **8169**, 81690C (2011).

[103] J. H. Song, H. N. J. Fernando, B. Roycroft, B. Corbett, and F. H. Peters, Journal of Lightwave Technology **27**, 1533 (2009).

[104] H. Schröder, L. Brusberg, R. Erxleben, I. Ndip, M. Töpper, N. F. Nissen, and H. Reichl, Proceedings - Electronic Components and Technology Conference , 1647 (2010).

[105] C. Li, K. S. Chee, J. Tao, H. Zhang, M. Yu, and G. Q. Lo, Optics Express **22**, 24235 (2014).

[106] A. Feist, G. Huang, G. Arend, Y. Yang, J.-W. Henke, A. S. Raja, F. J. Kappert, R. N. Wang, H. Lourenço-Martins, Z. Qiu, *et al.*, Science **377**, 777 (2022).

[107] K. J. Vahala, Nature **424**, 839 EP (2003).

[108] H. A. Haus, *Waves and Fields in Optoelectronics. Prentice-Hall Series in Solid State Physical Electronics.* (1984).

[109] M. L. Gorodetsky, A. D. Pryamikov, and V. S. Ilchenko, J. Opt. Soc. Am. B **17**, 1051 (2000).

[110] T. J. Kippenberg, S. M. Spillane, and K. J. Vahala, Optics Letters **27**, 1669 (2002).

[111] J. Zhu, Ş. K. Özdemir, L. He, and L. Yang, Optics Express **18**, 23535 (2010).

[112] S. Spillane, T. Kippenberg, O. Painter, and K. Vahala, Physical review letters **91**, 043902 (2003).

[113] A. Kordts, M. H. P. Pfeiffer, H. Guo, V. Brasch, and T. J. Kippenberg, Opt. Lett. **41**, 452 (2016).

[114] P. Del'Haye, O. Arcizet, M. L. Gorodetsky, R. Holzwarth, and T. J. Kippenberg, Nature Photonics **3**, 529 (2009).

[115] J. Liu, V. Brasch, M. H. P. Pfeiffer, A. Kordts, A. N. Kamel, H. Guo, M. Geiselmann, and T. J. Kippenberg, Optics Letters **41**, 3134 (2016).

[116] J. Leuthold, C. Koos, and W. Freude, Nature Photonics **4**, 535 (2010).

[117] C. Koos, *Nonlinear Optics (NLO)(http:// www. ipq.kit.edu)* (2017).

[118] . Haim Suchowski, . * Kevin O'Brien, . * Zi Jing Wong, . * Alessandro Salandrino, and Xiaobo Yin, 1, 2 Xiang Zhang1, Science **342**, 1223 (2013).

[119] T. J. Kippenberg, R. Holzwarth, and S. A. Diddams, Science **332**, 555 (2011).

[120] L. Deych, Physical Review A - Atomic, Molecular, and Optical Physics **84**, 1 (2011).

[121] L. A. Lugiato and R. Lefever, Phys. Rev. Lett. **58**, 2209 (1987).

[122] F. Leo, S. Coen, P. Kockaert, S.-P. Gorza, P. Emplit, and M. Haelterman, Nature Photonics **4**, 471 (2010).

[123] H. Guo, M. Karpov, E. Lucas, A. Kordts, M. H. P. Pfeiffer, V. Brasch, G. Lihachev, V. E. Lobanov, M. L. Gorodetsky, and T. J. Kippenberg, Nature Phys. **13**, 94 (2017).

[124] J. R. Stone, T. C. Briles, T. E. Drake, D. T. Spencer, D. R. Carlson, S. A. Diddams, and S. B. Papp, Phys. Rev. Lett. **121**, 063902 (2018).

[125] V. Brasch, M. Geiselmann, M. H. P. Pfeiffer, and T. J. Kippenberg, Opt. Express **24**, 29312 (2016).

[126] G. Lihachev, J. Riemensberger, W. Weng, J. Liu, H. Tian, A. Siddharth, V. Snigirev, V. Shadymov, A. Voloshin, R. N. Wang, *et al.*, Nature communications **13**, 3522 (2022).

[127] B. Li, W. Jin, L. Wu, L. Chang, H. Wang, B. Shen, Z. Yuan, A. Feshali, M. Paniccia, K. J. Vahala, *et al.*, Optics Letters **46**, 5201 (2021).

[128] G. Hadley, IEEE Journal of Quantum Electronics **22**, 419 (1986).

[129] R. W. Drever, J. L. Hall, F. V. Kowalski, J. Hough, G. Ford, A. Munley, and H. Ward, Applied Physics B **31**, 97 (1983).

[130] E. D. Black, American journal of physics **69**, 79 (2001).

[131] M. Kourogi and M. Ohtsu, Optics communications **81**, 204 (1991).

[132] V. Velichanskii, A. Zibrov, V. Kargopol'tsev, V. Molochev, V. Nikitin, V. Sautenkov, G. Kharisov, and D. Tyurikov, Sov. Tech. Phys. Lett.(Engl. Transl.);(United States) **4** (1978).

[133] G. Agrawal, IEEE Journal of Quantum Electronics **20**, 468 (1984).

[134] B. Dahmani, L. Hollberg, and R. Drullinger, Optics Letters **12**, 876 (1987).

[135] E. Patzak, H. Olesen, A. Sugimura, S. Saito, and T. Mukai, Electronics Letters **22**, 938 (1983).

[136] C. E. Wieman and L. Hollberg, Review of scientific instruments **62**, 1 (1991).

[137] E. M. Belenov, V. Velichanskiu, A. S. Zibrov, V. Nikitin, V. A. Sautenkov, and A. V. Uskov, Soviet Journal of Quantum Electronics **13**, 792 (1983).

[138] A. Hemmerich, C. Zimmermann, and T. Hänsch, Applied optics **33**, 988 (1994).

[139] H. Olesen, S. Saito, T. Mukai, T. Saitoh, and O. Mikami, Japanese Journal of Applied Physics **22**, L664 (1983).

[140] S. Saito, O. Nilsson, and Y. Yamamoto, IEEE Journal of Quantum Electronics **18**, 961 (1982).

[141] L. Ricci, M. Weidemüller, T. Esslinger, A. Hemmerich, C. Zimmermann, V. Vuletic, W. König, and T. W. Hänsch, Optics communications **117**, 541 (1995).

[142] B. Volodin, S. Dolgy, E. Melnik, E. Downs, J. Shaw, and V. Ban, Optics letters **29**, 1891 (2004).

[143] G. J. Steckman, W. Liu, R. Platz, D. Schroeder, C. Moser, and F. Havermeyer, IEEE Journal of Selected Topics in Quantum Electronics **13**, 672 (2007).

[144] H. Li and H. Telle, IEEE journal of quantum electronics **25**, 257 (1989).

[145] L. Hollberg and M. Ohtsu, Applied physics letters **53**, 944 (1988).

[146] P. Laurent, A. Clairon, and C. Breant, IEEE Journal of Quantum Electronics **25**, 1131 (1989).

[147] Y. Zhao, Q. Wang, F. Meng, Y. Lin, S. Wang, Y. Li, B. Lin, S. Cao, J. Cao, Z. Fang, *et al.*, Optics Letters **37**, 4729 (2012).

[148] H. Patrick and C. Wieman, Review of scientific instruments **62**, 2593 (1991).

[149] R. Adler, Proceedings of the IRE **34**, 351 (1946).

[150] F. Wei, F. Yang, X. Zhang, D. Xu, M. Ding, L. Zhang, D. Chen, H. Cai, Z. Fang, and G. Xijia, Optics express **24**, 17406 (2016).

[151] V. V. Vasil'ev, V. L. Velichansky, M. L. Gorodetskii, V. Il'chenko, L. Holberg, and A. V. Yarovitsky, Quantum electronics **26**, 657 (1996).

[152] V. Vassiliev, S. Il'ina, and V. Velichansky, Applied Physics B **76**, 521 (2003).

[153] B. Sprenger, H. G. Schwefel, Z. Lu, S. Svitlov, and L. Wang, arXiv preprint arXiv:1208.0244 (2012).

[154] W. Liang, V. S. Ilchenko, D. Eliyahu, A. A. Savchenkov, A. B. Matsko, D. Seidel, and L. Maleki, Nature Communications **6**, 7371 (2015).

[155] R. R. Galiev, N. G. Pavlov, N. M. Kondratiev, S. Koptyaev, V. E. Lobanov, A. S. Voloshin, A. S. Gorodnitskiy, and M. L. Gorodetsky, Opt. Express **26**, 30509 (2018).

[156] A. Siddharth, T. Wunderer, G. Lihachev, A. S. Voloshin, C. Haller, R. N. Wang, M. Teepe, Z. Yang, J. Liu, J. Riemensberger, *et al.*, Apl Photonics **7**, 046108 (2022).

[157] N. M. Kondratiev, V. E. Lobanov, A. V. Cherenkov, A. S. Voloshin, N. G. Pavlov, S. Koptyaev, and M. L. Gorodetsky, Optics Express **25**, 28167 (2017).

[158] R. Lang and K. Kobayashi, IEEE journal of Quantum Electronics **16**, 347 (1980).

[159] M. Corato-Zanarella, A. Gil-Molina, X. Ji, M. C. Shin, A. Mohanty, and M. Lipson, Nature Photonics , 1 (2022).

[160] E. Shim, A. Gil-Molina, O. Westreich, Y. Dikmelik, K. Lascola, A. L. Gaeta, and M. Lipson, Communications Physics **4**, 268 (2021).

[161] a. Z. Subramanian, S. Selvaraja, P. Verheyen, a. Dhakal, K. Komorowska, and R. Baets, ECIO, Stiges, Spain **19**, 5 (2012).

[162] C. Koos and W. Freude, *Optical Waveguides and Fibers Lecture Notes (http:// www. ipq.kit.edu)* (2017).

[163] G. Ren, S. Chen, Y. Cheng, and Y. Zhai, Optics Communications **284**, 4782 (2011).

[164] K. Kawase, J.-i. Shikata, H. Minamide, K. Imai, and H. Ito, Applied Optics **40**, 1423 (2001).

[165] A. Delage, S. Janz, D. X. Xu, D. Dalacu, B. Lamontagne, and A. L. Bogdanov, Photonics North , 204 (2004).

[166] J. Liu, A. S. Raja, M. H. P. Pfeiffer, C. Herkommer, H. Guo, M. Zervas, M. Geiselmann, and T. J. Kippenberg, Optics Letters **43**, 3200 (2018).

[167] Lumerical inc.

[168] A. Taflove and S. C. Hagness, *Computational Electrodynamics: The Finite-Difference Time-Domain Method*.

[169] K. Yee, Numerical solution of initial boundary value problems involving Maxwell's equations in isotropic media (1966).

[170] K. S. Yee and J. S. Chen, IEEE Transactions on Antennas and Propagation **45**, 354 (1997).

[171] solidworks, https://www.solidworks.com/de.

[172] M. H. P. Pfeiffer, J. Liu, M. Geiselmann, and T. J. Kippenberg, Physical Review Applied **7**, 024026 (2017).

[173] J. Riemensberger, N. Kuznetsov, J. Liu, J. He, R. N. Wang, and T. J. Kippenberg, Nature **612**, 56 (2022).

[174] M.-G. Suh, Q.-F. Yang, K. Y. Yang, X. Yi, and K. J. Vahala, Science **354**, 600 (2016).

[175] B. Lomsadze and S. T. Cundiff, Science (New York, N.Y.) **357**, 1389 (2017).

[176] X. Han, W. Fu, C.-L. Zou, L. Jiang, and H. X. Tang, Optica **8**, 1050 (2021).

[177] O. Kfir, H. Lourenço-Martins, G. Storeck, M. Sivis, T. R. Harvey, T. J. Kippenberg, A. Feist, and C. Ropers, Nature **582**, 46 (2020).

[178] A. Feist, K. E. Echternkamp, J. Schauss, S. V. Yalunin, S. Schäfer, and C. Ropers, Nature **521**, 200 (2015).

[179] U. H. Fischer-Hirchert, *Photonic Packaging Sourcebook: Fiber-Chip Coupling for Optical Components, Basic Calculations, Modules* (2015) pp. 1–325.

[180] C. Minkenberg, R. Krishnaswamy, A. Zilkie, and D. Nelson, IET Optoelectronics **15**, 77 (2021).

[181] V. Snigirev, A. Riedhauser, G. Lihachev, M. Churaev, J. Riemensberger, R. N. Wang, A. Siddharth, G. Huang, C. Möhl, Y. Popoff, *et al.*, Nature **615**, 411 (2023).

[182] A. Shams-Ansari, D. Renaud, R. Cheng, L. Shao, L. He, D. Zhu, M. Yu, H. R. Grant, L. Johansson, M. Zhang, *et al.*, Optica **9**, 408 (2022).

[183] Y. Yang, M. Yu, Q. Fang, J. Song, X. Tu, P. G. Q. Lo, and Rusli, Proceedings - Electronic Components and Technology Conference **2016-Augus**, 483 (2016).

[184] N. Lindenmann, G. Balthasar, D. Hillerkuss, R. Schmogrow, M. Jordan, J. Leuthold, W. Freude, and C. Koos, Optics express **20**, 17667 (2012).

[185] SchaefterKirchhoff, https://rb.gy/hiilmz.

[186] A. Liang, L. Hu, and Z. Liang, Optics and Photonics Journal **5**, 151 (2015).

[187] M. Fung, K. S. Tsang, J. Cheung, Y. Tsang, V. Ho, K. L. Lui, and R. Man, ICOCN 2016 - 2016 15th International Conference on Optical Communications and Networks , 15 (2017).

[188] vytran, https://www.thorlabs.com/newgrouppage9.cfm?objectgroup_id=9355.

[189] Furukawa, https://www.furukawa.co.jp/splicer/en/product/s179a.html.

[190] A. Martínez-Rios, I. Torres-Gómez, D. Monzon-Hernandez, O. Barbosa-Garcia, and V. M. Duran-Ramirez, Revista Mexicana de Fisica **56**, 80 (2010).

[191] A. Clements, Product Guide , 18 (2006).

[192] Nordson, http://www.nordson.com/en.

[193] A. Youssefi, I. Shomroni, Y. J. Joshi, N. R. Bernier, A. Lukashchuk, P. Uhrich, L. Qiu, and T. J. Kippenberg, Nature Electronics **4**, 326 (2021).

[194] F. Lecocq, F. Quinlan, K. Cicak, J. Aumentado, S. Diddams, and J. Teufel, Nature **591**, 575 (2021).

[195] X. Yi, Q.-F. Yang, K. Y. Yang, M.-G. Suh, and K. Vahala, Optica **2**, 1078 (2015).

[196] C. Bao, Y. Xuan, D. E. Leaird, S. Wabnitz, M. Qi, and A. M. Weiner, Optica **4**, 1011 (2017).

[197] P. A. Morton and M. J. Morton, J. Lightwave Technol. **36**, 5048 (2018).

[198] V. Nicolas, Y. Xu, Y. Qi-Fan, S. E. J., M. P. A., Y. K. Youl, V. K. J., and B. J. E., Laser & Photonics Reviews **12**, 1700307 (2018).

[199] S. Zhang, J. M. Silver, L. D. Bino, F. Copie, M. T. M. Woodley, G. N. Ghalanos, A. Ø. Svela, N. Moroney, and P. Del'Haye, Optica **6**, 206 (2019).

[200] R. J. Jones and J.-C. Diels, Physical review letters **86**, 3288 (2001).

[201] T. M. Fortier, M. S. Kirchner, F. Quinlan, J. Taylor, J. Bergquist, T. Rosenband, N. Lemke, A. Ludlow, Y. Jiang, C. Oates, *et al.*, Nature Photonics **5**, 425 (2011).

[202] M. Takamoto, F.-L. Hong, R. Higashi, and H. Katori, Nature **435**, 321 (2005).

[203] B. Yao, S.-W. Huang, Y. Liu, A. K. Vinod, C. Choi, M. Hoff, Y. Li, M. Yu, Z. Feng, D.-L. Kwong, *et al.*, Nature **558**, 410 (2018).

[204] H. Tian, J. Liu, B. Dong, J. C. Skehan, M. Zervas, T. J. Kippenberg, and S. A. Bhave, arXiv **1907.10177** (2019).

[205] C. Xiong, W. H. P. Pernice, X. Sun, C. Schuck, K. Y. Fong, and H. X. Tang, New Journal of Physics **14**, 095014 (2012).

[206] H. Jung, K. Y. Fong, C. Xiong, and H. X. Tang, Opt. Lett. **39**, 84 (2014).

[207] X. Liu, C. Sun, B. Xiong, L. Wang, J. Wang, Y. Han, Z. Hao, H. Li, Y. Luo, J. Yan, T. Wei, Y. Zhang, and J. Wang, ACS Photonics **5**, 1943 (2018).

[208] Z. Gong, A. Bruch, M. Shen, X. Guo, H. Jung, L. Fan, X. Liu, L. Zhang, J. Wang, J. Li, J. Yan, and H. X. Tang, Opt. Lett. **43**, 4366 (2018).

[209] Z. Gong, X. Liu, Y. Xu, M. Xu, J. B. Surya, J. Lu, A. Bruch, C. Zou, and H. X. Tang, Opt. Lett. **44**, 3182 (2019).

[210] Q.-F. Yang, X. Yi, K. Y. Yang, and K. Vahala, Optica **3**, 1132 (2016).

[211] C. W. Nelson, A. Hati, and D. A. Howe, Review of Scientific Instruments **85**, 024705 (2014).

[212] G. Huang, E. Lucas, J. Liu, A. S. Raja, G. Lihachev, M. L. Gorodetsky, N. J. Engelsen, and T. J. Kippenberg, arXiv **1901.07112v1** (2019).

[213] Y. He, Q.-F. Yang, J. Ling, R. Luo, H. Liang, M. Li, B. Shen, H. Wang, K. Vahala, and Q. Lin, arXiv **1812.09610v1** (2018).

[214] S. F. Preble, M. L. Fanto, J. A. Steidle, C. C. Tison, G. A. Howland, Z. Wang, and P. M. Alsing, Phys. Rev. Applied **4**, 021001 (2015).

[215] M.-G. Suh and K. J. Vahala, Science **359**, 884 (2018).

[216] M.-G. Suh, X. Yi, Y.-H. Lai, S. Leifer, I. S. Grudinin, G. Vasisht, E. C. Martin, M. P. Fitzgerald, G. Doppmann, J. Wang, D. Mawet, S. B. Papp, S. A. Diddams, C. Beichman, and K. Vahala, Nature Photonics **13**, 25 (2019).

[217] W. M. J. Green, M. J. Rooks, L. Sekaric, and Y. A. Vlasov, Optics Express **15**, 17106 (2007).

[218] T. Herr, V. Brasch, J. D. Jost, C. Y. Wang, N. M. Kondratiev, M. L. Gorodetsky, and T. J. Kippenberg, Nature Photonics **8**, 145 (2014).

[219] V. Brasch, Q.-F. Chen, S. Schiller, and T. J. Kippenberg, Optics Express **22**, 30786 (2014).

[220] C. Henry, IEEE Journal of Quantum Electronics **18**, 259 (1982).

[221] S. T. Cundiff and J. Ye, Rev. Mod. Phys. **75**, 325 (2003).

[222] H. Ballani, P. Costa, I. Haller, K. Jozwik, K. Shi, B. Thomsen, and H. Williams, in *Optical Fiber Communication Conference* (OSA, 2018) p. W1C.3.

[223] Q. Cheng, M. Bahadori, M. Glick, S. Rumley, and K. Bergman, Optica **5**, 1354 (2018).

[224] K. Clark, H. Ballani, P. Bayvel, D. Cletheroe, T. Gerard, I. Haller, K. Jozwik, K. Shi, B. Thomsen, P. Watts, H. Williams, G. Zervas, P. Costa, and Z. Liu, in *2018 European Conference on Optical Communication (ECOC)* (2018) pp. 1–3.

[225] L. P. Barry, J. Wang, C. McArdle, and D. Kilper, in *Optical Switching in Next Generation Data Centers*, edited by F. Testa and L. Pavesi (Springer International Publishing, 2018) pp. 23–44.

[226] S. Han, T. J. Seok, N. Quack, B.-w. Yoo, and M. C. Wu, in *Optical Fiber Communication Conference (2014), paper M2K.2* (Optical Society of America, 2014) p. M2K.2.

[227] J. Kim, C. Nuzman, B. Kumar, D. Lieuwen, J. Kraus, A. Weiss, C. Lichtenwalner, A. Papazian, R. Frahm, N. Basavanhally, D. Ramsey, V. Aksyuk, F. Pardo, M. Simon, V. Lifton, H. Chan, M. Haueis, A. Gasparyan, H. Shea, S. Arney, C. Bolle, P. Kolodner, R. Ryf, D. Neilson, and J. Gates, IEEE Photonics Technology Letters **15**, 1537 (2003).

[228] Calient, https://www.calient.net/.

[229] Q. Huang, Optical Switching in Next Generation Data Centers , 203 (2018).

[230] Epiphotonics, http://epiphotonics.com/.

[231] Chemoptics, http://www.chemoptics.co.kr/kr/index.php.

[232] R. Stabile, A. Albores-Mejia, and K. Williams, Optics letters **37**, 4666 (2012).

[233] S. Tanaka, S.-H. Jeong, S. Yamazaki, A. Uetake, S. Tomabechi, M. Ekawa, and K. Morito, IEEE Journal of Quantum Electronics **45**, 1155 (2009).

[234] T. Segawa, M. Nada, M. Nakamura, Y. Suzaki, and R. Takahashi, in *39th European Conference and Exhibition on Optical Communication (ECOC 2013)* (2013) pp. 1–3.

[235] N. Dupuis, J. E. Proesel, H. Ainspan, C. W. Baks, M. Meghelli, and B. G. Lee, Optics Letters **44**, 3610 (2019).

[236] N. Dupuis, J. E. Proesel, N. Boyer, H. Ainspan, C. W. Baks, F. Doany, E. Cyr, and B. G. Lee, in *Optical Fiber Communication Conference Postdeadline Papers 2020 (2020), paper Th4A.6* (Optical Society of America, 2020) p. Th4A.6.

[237] Y. Yin, R. Proietti, X. Ye, C. J. Nitta, V. Akella, and S. J. B. Yoo, IEEE Journal of Selected Topics in Quantum Electronics **19**, 3600409 (2013).

[238] X. Xiao, Y. Zhang, K. Zhang, R. Proietti, and S. J. B. Yoo, in *2019 Conference on Lasers and Electro-Optics (CLEO)* (2019) pp. 1–2.

[239] O. A. Lavrova, L. Rau, and D. J. Blumenthal, Journal of lightwave technology **20**, 712 (2002).

[240] D. J. Blumenthal, B.-E. Olsson, G. Rossi, T. E. Dimmick, L. Rau, M. Masanovic, O. Lavrova, R. Doshi, O. Jerphagnon, J. E. Bowers, *et al.*, Journal of Lightwave Technology **18**, 2058 (2000).

[241] J. Simsarian, M. Larson, H. Garrett, H. Xu, and T. Strand, IEEE Photonics Technology Letters **18**, 565 (2006).

[242] A. C. Funnell, K. Shi, P. Costa, P. Watts, H. Ballani, and B. C. Thomsen, Journal of Lightwave Technology **35**, 4438 (2017).

[243] K. Shi, S. Lange, I. Haller, D. Cletheroe, R. Behrendt, B. Thomsen, F. Karinou, K. Jozwik, P. Costa, and H. Ballani, in *45th European Conference on Optical Communication (ECOC 2019)* (IET, 2019) pp. 1–4.

[244] H. Ballani, P. Costa, R. Behrendt, D. Cletheroe, I. Haller, K. Jozwik, F. Karinou, S. Lange, K. Shi, B. Thomsen, and H. Williams, in *Proceedings of the Annual Conference of the ACM Special Interest Group on Data Communication on the Applications, Technologies, Architectures, and Protocols for Computer Communication*, SIGCOMM '20 (Association for Computing Machinery, New York, NY, USA, 2020) p. 782–797.

[245] V. Torres-Company and A. M. Weiner, Laser & Photonics Reviews **8**, 368 (2014).

[246] J. Wu, X. Xu, T. G. Nguyen, S. T. Chu, B. E. Little, R. Morandotti, A. Mitchell, and D. J. Moss, IEEE Journal of Selected Topics in Quantum Electronics **24**, 1 (2018).

[247] M.-G. Suh and K. Vahala, Optica **5**, 65 (2018).

[248] J. Liu, E. Lucas, A. S. Raja, J. He, J. Riemensberger, R. N. Wang, M. Karpov, H. Guo, R. Bouchand, and T. J. Kippenberg, Nature Photonics **14**, 486 (2020).

[249] A. Fülöp, M. Mazur, A. Lorences-Riesgo, Ó. B. Helgason, P.-H. Wang, Y. Xuan, D. E. Leaird, M. Qi, P. A. Andrekson, A. M. Weiner, and V. Torres-Company, Nature Communications **9**, 1598 (2018).

[250] B. Corcoran, M. Tan, X. Xu, A. Boes, J. Wu, T. G. Nguyen, S. T. Chu, B. E. Little, R. Morandotti, A. Mitchell, and D. J. Moss, Nature Communications **11**, 2568 (2020).

[251] D. J. Blumenthal, R. Heideman, D. Geuzebroek, A. Leinse, and C. Roeloffzen, *Proceedings of the IEEE*, Proceedings of the IEEE **106**, 2209 (2018).

[252] IEEE Std 802.3bj-2014 (Amendment to IEEE Std 802.3-2012 as amended by IEEE Std 802.3bk-2013) , 1 (2014).

[253] P. Yin, J. R. Serafini, Z. Su, R.-J. Shiue, E. Timurdogan, M. L. Fanto, M. L. Fanto, and S. Preble, Optics Express **27**, 24188 (2019).

[254] P. W. Juodawlkis, J. J. Plant, W. Loh, L. J. Missaggia, F. J. O'Donnell, D. C. Oakley, A. Napoleone, J. Klamkin, J. T. Gopinath, D. J. Ripin, S. Gee, P. J. Delfyett, and J. P. Donnelly, IEEE Journal of Selected Topics in Quantum Electronics **17**, 1698 (2011).

[255] T. Gerard, C. Parsonson, Z. Shabka, P. Bayvel, D. Lavery, and G. Zervas, arXiv:2003.05489 [cs, eess] http://arxiv.org/abs/2003.05489 (2020).

[256] Optilab LLC https://www.optilab.com/optical-amplifier.

[257] L. Schares, R. Budd, D. Kuchta, F. Doany, C. Schow, M. Möhrle, A. Sigmund, and W. Rehbein, in *2015 European Conference on Optical Communication (ECOC)* (2015) pp. 1–3.

[258] P. A. Midgley and R. E. Dunin-Borkowski, Nature materials **8**, 271 (2009).

[259] R. Fernandez-Leiro and S. H. Scheres, Nature **537**, 339 (2016).

[260] A. H. Zewail, Science **328**, 187 (2010).

[261] R. M. van der Veen, O.-H. Kwon, A. Tissot, A. Hauser, and A. H. Zewail, Nature Chemistry **5**, 395 (2013).

[262] D. R. Cremons, D. A. Plemmons, and D. J. Flannigan, Nature Communications **7**, 11230 (2016).

[263] T. Danz, T. Domröse, and C. Ropers, Science **371**, 371 (2021).

[264] A. Feist, N. Bach, N. Rubiano da Silva, T. Danz, M. Möller, K. E. Priebe, T. Domröse, J. G. Gatzmann, S. Rost, J. Schauss, S. Strauch, R. Bormann, M. Sivis, S. Schäfer, and C. Ropers, Ultramicroscopy **176**, 63 (2017).

[265] B. Barwick, D. J. Flannigan, and A. H. Zewail, Nature **462**, 902 (2009).

[266] A. Yurtsever, R. M. van der Veen, and A. H. Zewail, Science **335**, 59 (2012).

[267] L. Piazza, T. Lummen, E. Quiñonez, Y. Murooka, B. Reed, B. Barwick, and F. Carbone, Nature Communications **6**, 6407 (2015).

[268] K. Wang, R. Dahan, M. Shentcis, Y. Kauffmann, A. Ben Hayun, O. Reinhardt, S. Tsesses, and I. Kaminer, Nature **582**, 50 (2020).

[269] M. Liebtrau, M. Sivis, A. Feist, H. Lourenço-Martins, N. Pazos-Pérez, R. A. Alvarez-Puebla, F. J. G. de Abajo, A. Polman, and C. Ropers, Light: Science & Applications **10**, 82 (2021).

[270] P. Kapitza and P. Dirac, in *Mathematical Proceedings of the Cambridge Philosophical Society*, Vol. 29 (Cambridge University Press, 1933) pp. 297–300.

[271] F. J. García de Abajo, Reviews of Modern Physics **82**, 209 (2010).

[272] G. M. Vanacore, I. Madan, G. Berruto, K. Wang, E. Pomarico, R. J. Lamb, D. McGrouther, I. Kaminer, B. Barwick, F. J. García de Abajo, and F. Carbone, Nature Communications **9**, 2694 (2018).

[273] G. M. Vanacore, G. Berruto, I. Madan, E. Pomarico, P. Biagioni, R. J. Lamb, D. McGrouther, O. Reinhardt, I. Kaminer, B. Barwick, H. Larocque, V. Grillo, E. Karimi, F. J. García de Abajo, and F. Carbone, Nature Materials **18**, 573 (2019).

[274] A. Feist, S. V. Yalunin, S. Schäfer, and C. Ropers, Physical Review Research **2**, 043227 (2020).

[275] F. J. García de Abajo and A. Konečná, Physical Review Letters **126**, 123901 (2021).

[276] K. E. Priebe, C. Rathje, S. V. Yalunin, T. Hohage, A. Feist, S. Schäfer, and C. Ropers, Nature Photonics **11**, 793 (2017).

[277] M. Kozák, N. Schönenberger, and P. Hommelhoff, Physical Review Letters **120**, 103203 (2018).

[278] Y. Morimoto and P. Baum, Nature Physics **14**, 252 (2018).

[279] A. Gover, R. Ianconescu, A. Friedman, C. Emma, N. Sudar, P. Musumeci, and C. Pellegrini, Reviews of Modern Physics **91**, 035003 (2019).

[280] A. Gover and A. Yariv, Physical Review Letters **124**, 064801 (2020).

[281] Z. Zhao, X.-Q. Sun, and S. Fan, Physical Review Letters **126**, 233402 (2021).

[282] V. Di Giulio, O. Kfir, C. Ropers, and F. J. García de Abajo, ACS Nano , acsnano.1c00549 (2021).

[283] O. Kfir, V. Di Giulio, F. J. G. de Abajo, and C. Ropers, Science Advances **7**, eabf6380 (2021).

[284] P. Das, J. Blazit, M. Tencé, L. Zagonel, Y. Auad, Y. Lee, X. Ling, A. Losquin, C. Colliex, O. Stéphan, F. García de Abajo, and M. Kociak, Ultramicroscopy **203**, 44 (2019).

[285] C. Liu, Y. Wu, Z. Hu, J. A. Busche, E. K. Beutler, N. P. Montoni, T. M. Moore, G. A. Magel, J. P. Camden, D. J. Masiello, G. Duscher, and P. D. Rack, ACS Photonics **6**, 2499 (2019).

[286] O. Schwartz, J. J. Axelrod, S. L. Campbell, C. Turnbaugh, R. M. Glaeser, and H. Müller, Nature Methods **16**, 1016 (2019).

[287] A. Ryabov, J. W. Thurner, D. Nabben, M. V. Tsarev, and P. Baum, Science Advances **6**, eabb1393 (2020).

[288] R. J. England, R. J. Noble, K. Bane, D. H. Dowell, C.-K. Ng, J. E. Spencer, S. Tantawi, Z. Wu, R. L. Byer, E. Peralta, K. Soong, C.-M. Chang, B. Montazeri, S. J. Wolf, B. Cowan, J. Dawson, W. Gai, P. Hommelhoff, Y.-C. Huang, C. Jing, C. McGuinness, R. B. Palmer, B. Naranjo, J. Rosenzweig, G. Travish, A. Mizrahi, L. Schachter, C. Sears, G. R. Werner, and R. B. Yoder, Reviews of Modern Physics **86**, 1337 (2014).

[289] M. Kozák, P. Beck, H. Deng, J. McNeur, N. Schönenberger, C. Gaida, F. Stutzki, M. Gebhardt, J. Limpert, A. Ruehl, I. Hartl, O. Solgaard, J. S. Harris, R. L. Byer, and P. Hommelhoff, Optics Express **25**, 19195 (2017).

[290] R. Dahan, S. Nehemia, M. Shentcis, O. Reinhardt, Y. Adiv, X. Shi, O. Be'er, M. H. Lynch, Y. Kurman, K. Wang, and I. Kaminer, Nature Physics **16**, 1123 (2020).

[291] N. V. Sapra, K. Y. Yang, D. Vercruysse, K. J. Leedle, D. S. Black, R. J. England, L. Su, R. Trivedi, Y. Miao, O. Solgaard, R. L. Byer, and J. Vučković, Science **367**, 79 (2020).

[292] O. Kfir, Physical Review Letters **123**, 103602 (2019).

[293] V. Di Giulio, M. Kociak, and F. J. G. de Abajo, Optica **6**, 1524 (2019).

[294] H. J. Kimble, Physica Scripta **T76**, 127 (1998).

[295] S. T. Park, M. Lin, and A. H. Zewail, New Journal of Physics **12**, 123028 (2010).

[296] X. Bendaña, A. Polman, and F. J. García de Abajo, Nano Letters **11**, 5099 (2011).

[297] N. Müller, V. Hock, H. Koch, N. Bach, C. Rathje, and S. Schäfer, ACS Photonics , acsphotonics.1c00456 (2021).

[298] J. Christopher, M. Taleb, A. Maity, M. Hentschel, H. Giessen, and N. Talebi, Nanophotonics **9**, 4381 (2020).

[299] A. Polman, M. Kociak, and F. J. García de Abajo, Nature Materials **18**, 1158 (2019).

[300] I. H. Malitson, Journal of the Optical Society of America **55**, 1205 (1965).

[301] K. J. Leedle, A. Ceballos, H. Deng, O. Solgaard, R. Fabian Pease, R. L. Byer, and J. S. Harris, Optics Letters **40**, 4344 (2015).

[302] S. V. Yalunin, A. Feist, and C. Ropers, Physical Review Research **3**, L032036 (2021).

[303] R. Dahan, A. Gorlach, U. Haeusler, A. Karnieli, O. Eyal, P. Yousefi, M. Segev, A. Arie, G. Eisenstein, P. Hommelhoff, and I. Kaminer, Science **373**, eabj7128 (2021).

[304] K. E. Echternkamp, A. Feist, S. Schäfer, and C. Ropers, Nature Physics **12**, 1000 (2016).

[305] T. Herr, K. Hartinger, J. Riemensberger, C. Y. Wang, E. Gavartin, R. Holzwarth, M. L. Gorodetsky, and T. J. Kippenberg, Nature Photonics **6**, 480 (2012).

[306] J. D. Thompson, T. G. Tiecke, N. P. de Leon, J. Feist, A. V. Akimov, M. Gullans, A. S. Zibrov, V. Vuletić, and M. D. Lukin, Science **340**, 1202 (2013).

[307] D. E. Chang, J. S. Douglas, A. González-Tudela, C.-L. Hung, and H. J. Kimble, Rev. Mod. Phys. **90**, 031002 (2018).

[308] N. V. Corzo, J. Raskop, A. Chandra, A. S. Sheremet, B. Gouraud, and J. Laurat, Nature **566**, 359 (2019).

[309] K. K. Mehta, C. D. Bruzewicz, R. McConnell, R. J. Ram, J. M. Sage, and J. Chiaverini, Nat. Nanotechnol. **11**, 1066 (2016).

[310] K. K. Mehta, C. Zhang, M. Malinowski, T.-L. Nguyen, M. Stadler, and J. P. Home, Nature **586**, 533 (2020).

[311] R. J. Niffenegger, J. Stuart, C. Sorace-Agaskar, D. Kharas, S. Bramhavar, C. D. Bruzewicz, W. Loh, R. T. Maxson, R. McConnell, D. Reens, G. N. West, J. M. Sage, and J. Chiaverini, Nature **586**, 538 (2020).

[312] I. Söllner, S. Mahmoodian, S. L. Hansen, L. Midolo, A. Javadi, G. Kiršanskė, T. Pregnolato, H. El-Ella, E. H. Lee, J. D. Song, S. Stobbe, and P. Lodahl, Nat. Nanotechnol. **10**, 775 (2015).

[313] P. Lodahl, S. Mahmoodian, and S. Stobbe, Reviews of Modern Physics **87**, 347 (2015).

[314] F. Liu, A. J. Brash, J. O'Hara, L. M. P. P. Martins, C. L. Phillips, R. J. Coles, B. Royall, E. Clarke, C. Bentham, N. Prtljaga, I. E. Itskevich, L. R. Wilson, M. S. Skolnick, and A. M. Fox, Nature Nanotech **13**, 835 (2018).

[315] J. C. Norman, D. Jung, Y. Wan, and J. E. Bowers, APL Photonics **3**, 030901 (2018).

[316] A. Sipahigil, R. E. Evans, D. D. Sukachev, M. J. Burek, J. Borregaard, M. K. Bhaskar, C. T. Nguyen, J. L. Pacheco, H. A. Atikian, C. Meuwly, R. M. Camacho, F. Jelezko, E. Bielejec, H. Park, M. Lončar, and M. D. Lukin, Science **354**, 847 (2016).

[317] L. Chang, W. Xie, H. Shu, Q.-F. Yang, B. Shen, A. Boes, J. D. Peters, W. Jin, C. Xiang, S. Liu, *et al.*, Nature communications **11**, 1 (2020).

[318] D. J. Wilson, K. Schneider, S. Hönl, M. Anderson, Y. Baumgartner, L. Czornomaz, T. J. Kippenberg, and P. Seidler, Nature Photonics **14**, 57 (2020).

[319] D. M. Lukin, C. Dory, M. A. Guidry, K. Y. Yang, S. D. Mishra, R. Trivedi, M. Radulaski, S. Sun, D. Vercruysse, G. H. Ahn, *et al.*, Nature Photonics **14**, 330 (2020).

[320] M. Zhang, C. Wang, R. Cheng, A. Shams-Ansari, and M. Lončar, Optica **4**, 1536 (2017).

[321] L. Razzari, D. Duchesne, M. Ferrera, R. Morandotti, S. Chu, B. Little, and D. Moss, Nature Photonics **4**, 41 (2010).

[322] M. Soltani, S. Yegnanarayanan, Q. Li, and A. Adibi, IEEE Journal of Quantum Electronics **46**, 1158 (2010).

[323] H. Jung, S.-P. Yu, D. R. Carlson, T. E. Drake, T. C. Briles, and S. B. Papp, Optica **8**, 811 (2021).

[324] Titan Themis, https://www.epfl.ch/research/facilities/cime/electron-microscopy/microscopes/titan/.

[325] A. Jørgensen, D. Kong, M. Henriksen, F. Klejs, Z. Ye, O. Helgason, H. Hansen, H. Hu, M. Yankov, S. Forchhammer, *et al.*, Nature Photonics , 1 (2022).

[326] G. M. Stéphan, T. T. Tam, S. Blin, P. Besnard, and M. Têtu, Phys. Rev. A **71**, 043809 (2005).

[327] NVIDIA A100 Tensor Core GPU Architecture, https://www.nvidia.com/content/dam/en-zz/Solutions/Data-Center/nvidia-ampere-architecture-whitepaper.pdf (2020).

[328] Broadcom, 25.6 Tb/s StrataXGS Tomahawk 4 Ethernet Switch Series, https://www.broadcom.com/products/ethernet-connectivity/switching/strataxgs/bcm56990-series (2020).

[329] F. M. Soares, N. K. Fontaine, R. P. Scott, J. H. Baek, X. Zhou, T. Su, S. Cheung, Y. Wang, C. Junesand, S. Lourdudoss, K. Y. Liou, R. A. Hamm, W. Wang, B. Patel, L. A. Gruezke, W. T. Tsang, J. P. Heritage, and S. J. B. Yoo, IEEE Photonics Journal **3**, 975 (2011).

[330] B. Ouyang, Y. Xing, W. Bogaerts, and J. Caro, Opt. Express **27**, 38698 (2019).

[331] D. B. Williams, C. B. Carter, D. B. Williams, and C. B. Carter, *The transmission electron microscope* (Springer, 1996).

[332] Inphotec, https://www.inphotec.it/.

[333] D. Foreman-Mackey, D. W. Hogg, D. Lang, and J. Goodman, PASP **125**, 306 (2013), 1202.3665 .

[334] F. J. G. de Abajo and M. Kociak, New Journal of Physics **10**, 073035 (2008).

[335] E. Pomarico, I. Madan, G. Berruto, G. M. Vanacore, K. Wang, I. Kaminer, F. J. García de Abajo, and F. Carbone, ACS Photonics **5**, 759 (2018).

[336] M. J. Lagos, A. Trügler, U. Hohenester, and P. E. Batson, Nature **543**, 529 (2017).

[337] J. A. Hachtel, J. Huang, I. Popovs, S. Jansone-Popova, J. K. Keum, J. Jakowski, T. C. Lovejoy, N. Dellby, O. L. Krivanek, and J. C. Idrobo, Science **363**, 525 (2019).

[338] X. Li, G. Haberfehlner, U. Hohenester, O. Stéphan, G. Kothleitner, and M. Kociak, Science **371**, 1364 (2021).

Arslan Sajid Raja

+41 77 921 64 19
rajaarslansajid@gmail.com
Lausanne, Switzerland

EDUCATION

Ph.D. in Photonics, Laboratory of Photonics and Quantum Measurements, École Polytechnique Fédérale de Lausanne (EPFL), Switzerland. June 2023

- Linear and nonlinear applications of miniaturized Si_3N_4 microresonators.
  Thesis advisor: Prof. Tobias Kippenberg.

M.S. in Optics and Photonics, Karlsruhe Institute of Technology (KIT), Germany. 2014 - 2017

- M.S. thesis: Optical packaging of Si_3N_4 microresonators for high power applications.
  Thesis advisor: Prof. Tobias Kippenberg.

B.S.c in Engineering Sciences, Ghulam Ishaq Khan Institute of Engineering Science and Technology (GIKI), Pakistan. 2010 - 2014

- B.S.c thesis: Control of industrial and agricultural applications via fiber.
  Thesis advisor: Prof. Hassan Sayyad.

SKILLS

Technical Skills	COMSOL, Lumerical, Matlab, Python, Zemax, SolidWorks, NLSE simulation
Experimental Skills	Fiber splicing via Vytran (dissimilar fiber) and standard splicer, Optical packaging, Intensive experience with lab instruments i.e. ECDL(laser), amplifier, signal analyzer (optical and electrical) etc.
Soft Skills	Teamwork (executed >4 projects while collaborating with industrial and academics teams, Communication (presented in conferences and workshop)
Language	English (Fluent)

EXPERIENCE

Research Intern May 2019 - July 2019
Microsoft Research *Cambridge, UK*

- System level demonstration of ultra-fast optical circuit using photonic integrated optical frequency comb.

Student Research Assistance Oct 2016 - Dec 2016
Hannover Optical Technologies, Leibniz Universität Hannover, Germany *Hannover, Germany*

- Higher order mode generation using Spatial Light Modulator (Simulation and experimental) and Grating assisted coupler characterization.

Student Research Assistance Feb 2016 - April 2016
Institute of Microstructure Technology, Karlsruhe Institute of Technology *Karlsruhe, Germany*

- Experimental characterization of polymer waveguide fabricated by fs-laser via 2-photon absorption.

Intern Aug 2015 - Nov 2015
Advanced Research Department, Rosenberger *Fridolfing, Germany*

- Simulation on integrated prism turn based design for coupling the light to SMF and MMF using Zemax and surface scattering analysis to improve the coupling efficiency.

PATENT APPLICATION

- T. Kippenberg, M. L.Gorodetsky, **Arslan S. Raja**, H. Guo."Generating optical pulses via a soliton state of an optical microresonator coupled with a chip based semiconductor laser."WO2020057716A1 & US20220050356A1 (2018)

- T. LaGrange, P. Cattaneo, F. Carbone, B. Weaver, A. Sapozhnik, Y. Yang, **Arslan S. Raja,** T. Kippenberg. 'Electron spectrometer calibration method ."Application submitted.

MAIN PUBLICATIONS

- **Arslan S. Raja*,** et al. "Electrically pumped photonic integrated soliton microcomb."Nature Communications 10(1), 1-8 (2019)
- **Arslan S. Raja*,** et al. "Ultrafast optical circuit switching for data centers using integrated soliton microcombs."Nature Communications 12(1), 1-7 (2021)
- Jan-Wilke Henke*,**Arslan S. Raja*,** et al. "Integrated photonics enables continuous-beam electron phase modulation."Nature, 600(7890), 653-658 (2022)
- J. Liu*, H. Tian*, E. Lucas*, **Arslan S. Raja*,** et al. "Monolithic piezoelectric control of soliton microcombs."Nature, 583(7816), 385-390 (2020)
- J. Liu*, E. Lucas*,**Arslan S. Raja*,** et al. "Photonic microwave generation in the X-and K-band using integrated soliton microcombs."Nature Photonics, 14(8), 486-491 (2020)
- J. Liu*, **Arslan S. Raja*,** et al. "Ultralow-power chip-based soliton microcombs for photonic integration."Optica, 5(10), 1347-1353 (2019)
- **Arslan S. Raja*,** et al. "Chip-based soliton microcomb module using a hybrid semiconductor laser."Optics Express, 28(3), 2714-2721 (2020)

*equal contribution